Separation and Purification Technology 215 (2019) 227–241

Contents lists available at ScienceDirect

Separation and Purification Technology

journal homepage: www.elsevier.com/locate/seppur

Elucidation and characterization of entropy effects in mixture separations with micro-porous crystalline adsorbents

Rajamani Krishna

Van 't Hoff Institute for Molecular Sciences, University of Amsterdam, Science Park 904, 1098 XH Amsterdam, the Netherlands

ARTICLE INFO

Keywords:
Selectivity reversal
Packing efficiencies
Saturation capacities
Lattice models
Entropy maximization

ABSTRACT

Separations of mixtures of xylene isomers, alkane isomers, linear alkanes, and linear alcohols using micro-porous crystalline adsorbents such as zeolites and MOFs are often carried out under conditions in which the pores are nearly saturated with guest molecules. Such separations are often dominated by factors other than the relative binding strengths of the constituents; the component that is preferentially adsorbed under pore saturation conditions is the guest molecule that has the higher saturation capacity, and packs more efficiently within the microporous channels. Higher saturation capacities, and packing efficiencies, arise from a wide variety of factors such as (a) smaller size, (b) shorter length, (c) smaller footprint, (d) commensurateness of molecular configuration with channel geometry. A common characteristic of all these separations is that at low pore occupancies, $\theta_{mix} < 0.5$, the separations are dominated by differences in binding strengths, and at pore occupancies $\theta_{mix} > 0.5$, the separations become increasing influenced by differences in saturation capacities. Remarkably, at pore saturation, i.e. $\theta_{mix} \approx 1$, the component that packs more poorly is virtually excluded. Statistical thermodynamics, and the Boltzmann expression $S = k_B \ln(W)$, applied to lattice models, are used to quantify and rationalize the influence of packing efficiencies, and the phenomena of selectivity reversals.

1. Introduction

Currently, the major focus in the development of novel metal–organic frameworks (MOFs) and zeolitic imidazolate framework (ZIFs) is on separations of *gaseous* mixtures such as CO_2/N_2 [1–3], N_2O/N_2 [4], CO_2/H_2 [3,5], CO_2/CH_4 [6,7], $H_2S/CO_2/CH_4$ [8], C_2H_2/CO_2 [9], $H_2/CO_2/CO/CH_4$ [6], Xe/Kr [10], C_2H_2/C_2H_4 [11,12], C_2H_4/C_2H_6 [13–17], C_3H_4/C_3H_6 [18], C_3H_6/C_3H_8 [14,19,20], O_2/N_2 [21,22], and N_2/CH_4 [22–24]. All these separations rely on the differences in binding strengths, and operate under conditions in which the fractional occupancy within the pores, $\theta_{mix} < 0.5$ [25]. There are however a large number of industrially important separations that operate under conditions in which the feed mixture exist in the liquid phase; this invariably implies that the fractional pore occupancy, θ_{mix}, will be close to unity. Industrially important mixture separations that operate at conditions close to pore saturation include: mixtures of xylene isomers [26,27], styrene/ethylbenzene [28,29], separation of alkane isomers [30–32], and separation of water/alcohol mixtures [25,33]. Mixture separations near pore saturation conditions are commonly driven by factors other than differences in binding strengths of guest molecules.

To set the scene, and define the objectives of the investigations to be reported in this article, consider the adsorption of binary mixtures of linear alkanes: methane/ethane, ethane/propane, propane/n-hexane, n-butane/n-hexane, and n-pentane/n-hexane in CHA zeolite. CHA is a cage type zeolite that consists of cages of volume 316 Å^3, separated by 3.8 Å × 4.2 Å 8-ring windows; Fig. 1(a) shows the pore landscape, along with snapshots of guest molecules within the cages. Fig. 1(b) presents Configurational-Bias Monte Carlo (CBMC) simulation data [34] on the mole fraction in the adsorbed phase of the shorter alkane, x_k, as a function of the cage occupancy of the mixture, θ_{mix}. In these CBMC simulations, the partial fugacities in the bulk fluid phase mixture (shorter alkane = k, longer alkane = l) were kept equal to each other, $f_k = f_l$, and the total mixture fugacity $f_t = f_k + f_l$ was varied over a wide range from 1 Pa to 10^8 Pa. For all five mixtures, we observe two common characteristic features. For $\theta_{mix} < 0.5$, the adsorbed phase is richer in the longer chain alkane that exerts larger van der Waals interactions with the pore walls. However, in all cases, at cage occupancies $\theta_{mix} > 0.6$, the adsorbed phase is richer in the shorter chain alkane. Remarkably, at $\theta_{mix} \approx 1$ the longer chain alkane is virtually excluded from the cages, and the adsorbed phase mole fraction of the shorter alkane is practically unity. Precisely analogous characteristics are observed for adsorption of binary mixtures of linear alcohols: methanol/ethanol, ethanol/propanol, 1-butanol/1-pentanol, ethanol/1-hexanol, and 1-butanol/1-hexanol in CHA; see CBMC simulation data [35], presented in Fig. 1(c). For all five mixtures, at cage occupancies $\theta_{mix} > 0.6$, the adsorbed phase is richer in the shorter alcohol. In

E-mail address: r.krishna@contact.uva.nl.

https://doi.org/10.1016/j.seppur.2019.01.014
Received 17 August 2018; Received in revised form 28 December 2018; Accepted 5 January 2019
Available online 07 January 2019
1383-5866/

Nomenclature

Latin alphabet

b_k	binding constant of k-mer, Pa^{-1}
b_l	binding constant of l-mer, Pa^{-1}
f_i	partial fugacity of species i, Pa
f_t	total fugacity of bulk fluid mixture, Pa
k	number of identical units occupied by k-mer, dimensionless
k_B	Boltzmann constant, 1.38×10^{-23} J molecule^{-1} K^{-1}
l	number of identical units occupied by l-mer, dimensionless
M	number of sites on lattice, dimensionless
N_k	number of k-mers, dimensionless
N_l	number of l-mers, dimensionless
n	number of species in the mixture, dimensionless
q_i	component molar loading of species i, mol kg^{-1}
$q_{i,sat}$	molar loading of species i at saturation, mol kg^{-1}
S	entropy, J mol^{-1} K^{-1}
T	absolute temperature, K
W	number of arrangements on lattice sites, dimensionless
x_i	component mole fraction in adsorbed phase, i, dimensionless
y_i	component mole fraction in bulk fluid phase, i, dimensionless

Greek letters

μ_i	molar chemical potential of component i, J mol^{-1}
θ_k	fractional occupancy of k-mer, dimensionless
θ_l	fractional occupancy of l-mer, dimensionless
θ_{mix}	occupancy of adsorbed mixture, $\theta_{mix} = \frac{\theta_k}{k} + \frac{\theta_l}{l}$, dimensionless
Ω	entropy factor, dimensionless

Subscripts

1	referring to component 1
2	referring to component 2
i	referring to component i
k	referring to k-mer
l	referring to l-mer

practice, high cage occupancies are guaranteed when operating with the bulk fluid phase in the liquid state. Experimental confirmation of the selectivity reversals is observed in the experiments reported by Remy et al. [36] for transient breakthroughs of liquid phase feed mixtures of ethanol/propanol, and ethanol/1-hexanol in a fixed bed adsorber packed with SAPO-34, that has the same structural topology as CHA. The component that is eluted first from the adsorber is the alcohol with the longer chain length.

For a quantitative determination of the component loadings, the Ideal Adsorbed Solution Theory (IAST) theory of Myers and Prausnitz [37] is the most commonly used approach [5,25,31,34,35,38]. As illustration, Fig. 2 presents comparison of the CBMC simulations of the mole fraction in the adsorbed phase of the shorter molecule, x_k, for methane/ethane, and 1-butanol/1-hexanol mixture adsorption with corresponding IAST calculations based on the unary isotherm fits. The IAST captures the selectivity reversal phenomena quantitatively for both mixtures; similar good agreement between the IAST and CBMC mixture simulations are obtained for adsorption of all other binary mixtures in CHA zeolite [34,35]; see Chapter 12 of Supplementary Material. The success of the IAST in capturing entropy effects is directly ascribable to the fact the theory is based on the concept that the spreading pressure for any component in the mixture equals the spreading pressures of that component determined from the unary isotherms; see detailed discussions in Chapter 4 of the Supplementary Material accompanying this publication. The spreading pressures, in turn, properly encapsulate the separate influences of both binding strengths and saturation capacities. Though entropy effects are properly captured by the IAST, there are some instances in which the quantitative agreement with CBMC mixture simulations are not perfect [39,40]. However, the IAST calculations are implicit in nature, and require robust numerical procedures for implementation in fixed bed adsorber codes [22,41,42].

The article has its focus on mixture separations at high occupancies, and has threefold objectives. The first objective is to demonstrate that selectivity reversals at high occupancies θ_{mix}, as observed in Fig. 1, are common characteristics of mixture adsorption in which the guest molecules have different saturation capacities, and that they manifest in materials with a wide variety of pore topologies and connectivities. The second objective is provide a physically intuitive explanation of the selectivity reversal phenomena using simple lattice models and concepts of statistical thermodynamics that originate from the Boltzmann expression for entropy, $S = k_B \ln(W)$; such physical insights are difficult to glean from use of the IAST. The third objective is to examine the applicability, and accuracy, of the recently developed model of van Assche et al. [43] for explicit calculations of the component loadings for adsorption of mixtures with different saturation capacities.

The Supplementary Material accompanying this article provides: (a) detailed structural information on all zeolites, and MOFs, analyzed and discussed in the article, (b) summary of methodology used for CBMC simulations, (c) detailed derivations of the lattice models for mixture adsorption equilibrium, (d) details of Ideal Adsorbed Solution Theory (IAST) calculations for mixture adsorption equilibria, and (e) input data on isotherm fits used in the lattice, and IAST model calculations.

We start our discussions by considering mixture separations in zeolites and MOFs having one-dimensional (1D) channel structures.

2. Entropy effects in frameworks with 1D channels

2.1. Adsorption of propane/n-hexane on Co-FA

Consider the adsorption of propane (C3), and n-hexane (nC6) in cobalt formate (Co-FA) framework [44]. The Co-FA structure consists of 1D zig-zag channels; see the pore landscapes in Fig. 3(a). The network exhibits diamondoid connectivity and the overall framework gives rise to zig-zag channels along the b axis. The effective pore size of these one-dimensional channels is 5–6 Å; one unit cell of Co-FA comprises a total of four distinct channel "segments"; each channel segment forms part of the repeat zig-zag structure. The length of each channel segment is commensurate with that of one propane (C3) molecule, and n-hexane (nC6) must straddle two channel segments. CBMC simulations of the unary adsorption isotherms are presented in Fig. 3(b). The saturation capacity of C3 is 4 per uc (uc = unit cell; see Fig. 3(b)), corresponding to one molecule per channel segment; the saturation capacity of nC6 is 2 per uc, corresponding to one molecule per 2 channel segments. From the pure component adsorption isotherms in Fig. 3(b) we also note that at fugacities below 1 kPa, the binding constant of C3 is nearly the same as that of nC6, $b_k \approx b_l$.

CBMC simulations of the component loadings for C3/nC6 mixture with equal partial fluid phase fugacities in the bulk fluid phase, are shown in Fig. 3(c). When operating at total mixture fugacities $f_t > 1$ MPa, corresponding to conditions in which the bulk fluid mixture is in the liquid state (as determined by use of the Peng-Robinson

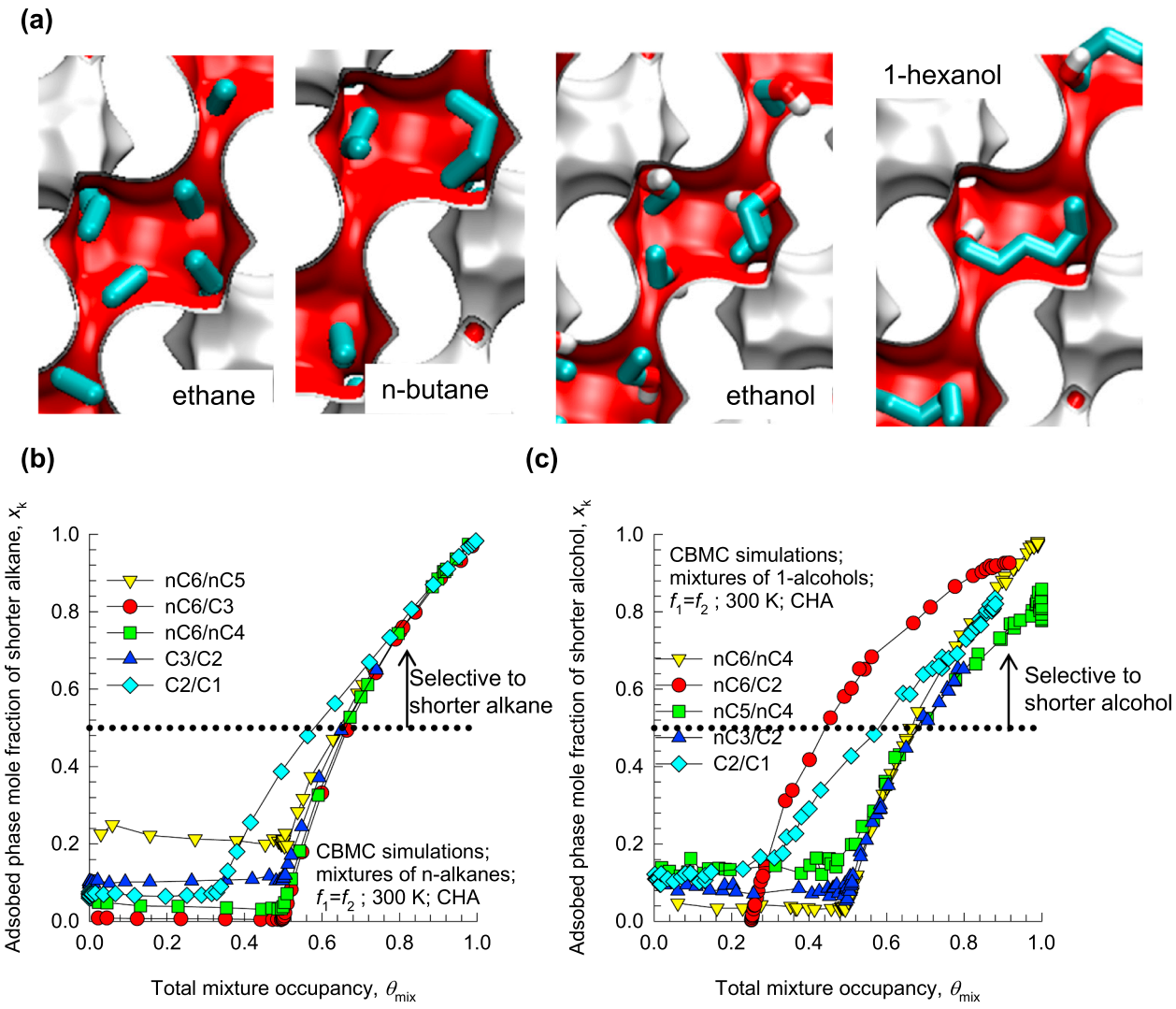

Fig. 1. (a) Pore landscape of CHA zeolite, showing snapshots of ethane, n-butane, ethanol, and 1-hexanol within cages at pore saturation. (b) CBMC simulations [34] of adsorption of binary C1/C2, C2/C3, C3/nC6, nC4/nC6, and nC5/nC6 mixtures of n-alkanes in CHA zeolite at 300 K; the plots show the mole fraction in the adsorbed phase of the shorter alkane as a function of the cage occupancy of the mixture, θ_{mix}. (c) CBMC simulations [35] of the adsorption of binary C1/C2, C2/C3, nC4/nC5, C2/nC6, and nC4/nC6 mixtures of 1-alcohols in CHA zeolite at 300 K; the plots show the mole fraction in the adsorbed phase of the shorter alcohol as a function of the cage occupancy of the mixture, θ_{mix}. In the CBMC simulations the partial fugacities in the bulk phase are equal to each other, i.e. $f_1 = f_2$.

equation of state), we note that the adsorbed phase contains practically no nC6 and almost exclusively loaded with C3. The adsorbed phase mole fraction of the propane, x_k, determined from the CBMC simulations of the component loadings are plotted in Fig. 3(d) as function of the occupancy of the adsorbed mixture, θ_{mix}. Fig. 3(d) shows that the adsorbed phase becomes increasingly richer in the shorter alkane as the occupancy of the adsorbed mixture, θ_{mix}, within the channels increases. At $\theta_{mix} \approx 1$, we note that the adsorbed phase contains practically no nC6 and almost exclusively loaded with C3; these characteristics are precisely analogous to those observed in Fig. 1(b, c) for adsorption of linear molecules in CHA.

2.2. 1D lattice model for mixture adsorption

To elucidate the unusual characteristics noted in Fig. 3(c, d), we use the model of Dávila et al. [45] for adsorption of a binary mixture of rigid k-mers and rigid l-mers on one-dimensional (1D) lattice; see schematic in Fig. 4(a). The adsorbent surface is modeled by a 1D lattice of M sites ($M \to \infty$). The k-mers (l-mers) are assumed to be composed by k (l) identical units in a linear array with constant bond length equal to the lattice dimension. The k-mers (l-mers) can only adsorb flat on the surface occupying k (l) contiguous lattice sites. Also, there are no adsorbate-adsorbate interactions, i.e. no repulsive or attractive forces. Since different particles do not interact with each other, all configurations of N_k k-mers and N_l l-mers on M sites are equally probable. Dávila et al. [45] derive the following expression for the number of "arrangements" of N_k k-mers and N_l l-mers on M sites:

$$W = \frac{(M-(k-1)N_k-(l-1)N_l)!}{(M-kN_k-lN_l)!N_k!N_l!} \tag{1}$$

The entropy for binary mixture adsorption, quantified by the Boltzmann expression, $S = k_B \ln(W)$, can be calculated using the Stirling's approximation $\ln(M!) = M\ln M - M$; the expression for the dimensionless entropy per site can be derived:

$$\frac{S}{k_B M} = \ln\left[\frac{\left(1-\frac{(k-1)}{k}\theta_k-\frac{(l-1)}{l}\theta_l\right)^{\left(1-\frac{(k-1)}{k}\theta_k-\frac{(l-1)}{l}\theta_l\right)}}{(1-\theta_k-\theta_l)^{(1-\theta_k-\theta_l)}\left(\frac{\theta_k}{k}\right)^{\frac{\theta_k}{k}}\left(\frac{\theta_l}{l}\right)^{\frac{\theta_l}{l}}}\right] \tag{2}$$

where the fractional occupancies are defined as $\theta_k = \frac{kN_k}{M}$; $\theta_l = \frac{lN_l}{M}$. By defining the mole fraction of k in the adsorbed phase, $x_k = \frac{N_k}{N_k+N_l} = \frac{\theta_k/k}{\theta_{mix}}$

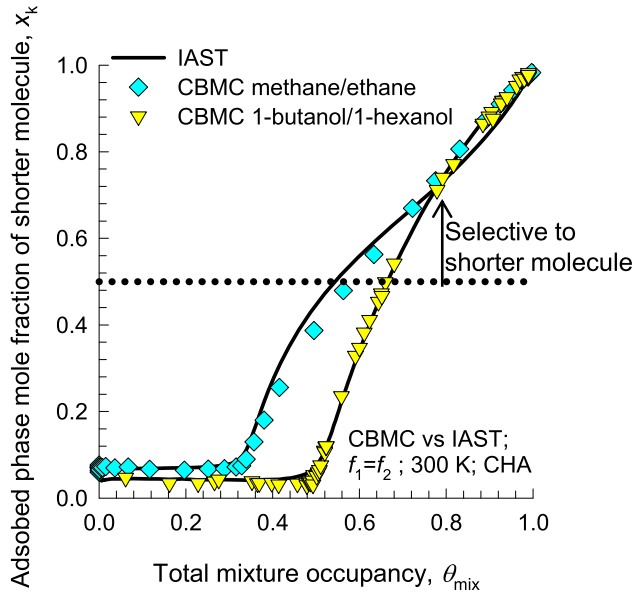

Fig. 2. Comparison of CBMC simulations [34,35] of adsorption of binary methane/ethane, and 1-butanol/1-hexanol mixture adsorption with IAST calculations of the mole fraction in the adsorbed phase of the shorter molecule as a function of the cage occupancy of the mixture, θ_{mix}. The IAST calculations are based on dual-Langmuir-Freundlich isotherm fits of the unary isotherms; further details are provided in Chapter 12 of Supporting Material.

and noting that $N_l = \theta_l/l = (1-x_k)\theta_{mix}$ we can express the dimensionless entropy per site, as a function of the two variables x_k, and $\theta_{mix} = \frac{\theta_k}{k} + \frac{\theta_l}{l} = \frac{N_k+N_l}{M}$:

$$\frac{S}{k_B M} = \ln\left[\frac{(1-(k-1)x_k\theta_{mix}-(l-1)(1-x_k)\theta_{mix})^{(1-(k-1)x_k\theta_{mix}-(l-1)(1-x_k)\theta_{mix})}}{(1-kx_k\theta_{mix}-l(1-x_k)\theta_{mix})^{(1-kx_k\theta_{mix}-l(1-x_k)\theta_{mix})}(x_k\theta_{mix})^{(x_k\theta_{mix})}((1-x_k)\theta_{mix})^{((1-x_k)\theta_{mix})}}\right] \tag{3}$$

At any chosen value of total mixture occupancy, θ_{mix}, by setting $\frac{\partial}{\partial x_k}\left(\frac{S}{k_B M}\right) = 0$, we can determine the adsorbed phase mole fraction x_k, that yields a maximum in the $\frac{S}{k_B M}$. The solution thus obtained is in the form of the implicit expression

$$x_k = \frac{1}{1+\frac{1}{\Omega}}; \quad x_l = 1 - x_k \tag{4}$$

where an "entropy factor" Ω is defined as

$$\Omega = \frac{\left(1-\frac{(k-1)}{k}\theta_k - \frac{(l-1)}{l}\theta_l\right)^{(l-k)}}{(1-\theta_k-\theta_l)^{(l-k)}} = \frac{(1-(k-1)x_k\theta_{mix}-(l-1)(1-x_k)\theta_{mix})^{(l-k)}}{(1-kx_k\theta_{mix}-l(1-x_k)\theta_{mix})^{(l-k)}} \tag{5}$$

Eqs. (4), and (5) need to be solved, simultaneously, using a suitable root-finder in order to determine the adsorbed phase composition for a specified value of the mixture occupancy θ_{mix}. It is important to note that the "entropy factor" Ω is a function of the occupancies of *both* components.

It is easy to check that for $k = l$, the adsorbed phase composition $x_k = 0.5$, irrespective of the mixture occupancy; this implies there is no entropic preference for either component. For $k < l$, in the limit of vanishingly low occupancies, we have $\theta_{mix} \to 0$; $\Omega \to 1$; $x_k \to 0.5$, and there is no entropic preference for either of the constituent species, because there is no competition for adsorption sites at vanishingly low occupancies. For $k < l$, the adsorbed phase composition x_k increases with increasing θ_{mix}, reaching the limit $\theta_{mix} \to 1$; $\Omega \to \infty$; $x_k \to 1$.

Since C3 (species k) adsorbs commensurately with one channel segment, we take $k = 1$, $M = 4$/uc, and $\frac{M}{k} = N_{k,sat} = 4$/uc. The linear hexane nC6 (species l) adsorbs commensurately with two channel segments, and so we take $l = 2$, and $\frac{M}{l} = N_{l,sat} = 2$/uc. The continuous solid line in Fig. 3(d), represents the numerical solution to Eqs. (4), and (5); this "maximum entropy line" is in reasonably good agreement with the CBMC simulation data on the adsorbed phase mole fraction of propane, x_k. The important conclusion to be drawn is that the C3/nC6 mixture separation in Co-FA is predominantly driven by entropy considerations. Put another way, there are many more ways to "arrange" the shorter C3 molecule on the 1D lattice, as compared to nC6.

The free energy for mixture adsorption is obtained by adding the contribution of the binding energies to entropic contribution, $-ST$; see Dávila et al. [45]. Differentiation of the resulting expression for the free energy, allows calculation of the chemical potentials of k-mers and l-mers. Equating the chemical potential of each of the adsorbed species to the component chemical potentials in the bulk fluid phase mixture, results in the set of two coupled equations describing mixture adsorption equilibrium

$$b_k f_k = \frac{\frac{\theta_k}{k}\left(1-\frac{(k-1)}{k}\theta_k - \frac{(l-1)}{l}\theta_l\right)^{(k-1)}}{(1-\theta_k-\theta_l)^k}; \quad b_l f_l = \frac{\frac{\theta_l}{l}\left(1-\frac{(k-1)}{k}\theta_k - \frac{(l-1)}{l}\theta_l\right)^{(l-1)}}{(1-\theta_k-\theta_l)^l} \tag{6}$$

where b_k and b_l are the binding constants for the two adsorbates; f_k and f_l are the partial fugacities in the bulk fluid phase in equilibrium with the adsorbates. The interpretation of the binding constants b_k and b_l in terms of statistical thermodynamics and partition functions is provided by Dávila et al. [45]. It is to be noted that since the Eq. (6) are not explicit in terms of the occupancies, $\theta_k = \frac{kN_k}{M}$; $\theta_l = \frac{lN_l}{M}$, the set of two equations need to be solved numerically; no analytic solution is possible expect for the degenerate scenario: $k = 1$, $l = 1$.

From Eq. (6), we can derive the following expression for the mole fraction of k in the adsorbed phase x_k is expressed in implicit form as

$$x_k = \frac{1}{1+\frac{b_l f_l}{b_k f_k}\frac{1}{\Omega}} = 1 - x_l \tag{7}$$

in which the Ω has the same definition as in Eq. (5). The solutions to Eqs. (5), and (7) yield the mole fractions corresponding to "minimization of free energy". For C3/nC6 adsorption in Co-FA, we have the special scenario in which $\frac{b_l f_l}{b_k f_k} = 1$ and therefore, the calculations of the adsorbed phase composition x_k also corresponds to that of "maximum entropy".

It is also easy to check that for $k = 1$, $l = 1$, Eq. (6) degenerate to the mixed-gas Langmuir model

$$b_k f_k = \frac{\theta_k}{(1-\theta_k-\theta_l)}; \quad b_l f_l = \frac{\theta_k}{(1-\theta_k-\theta_l)} \tag{8}$$

Eq. (8) can be solved explicitly to obtain the occupancies, and loadings. In Eq. (6), when either $k \neq 1$, or $l \neq 1$, no explicit determination of the occupancies, and loadings, is possible.

The corresponding *unary isotherms* can be derived as limiting scenarios for Eq. (6), by setting one of the partial fugacities equal to zero:

$$b_k f_k = \frac{\left(1-\frac{(k-1)}{k}\theta_k\right)^{(k-1)}\frac{\theta_k}{k}}{(1-\theta_k)^k}; \quad b_l f_l = \frac{\left(1-\frac{(l-1)}{l}\theta_l\right)^{(l-1)}\frac{\theta_l}{l}}{(1-\theta_l)^l} \tag{9}$$

The unary isotherms in Fig. 3(b) were fitted using Eq. (9). A fair, but not perfect, match between the 1D lattice model and CBMC simulations of the unary isotherms is obtained with the fitted binding constants are $b_k = b_l = 2.4 \times 10^{-4}\,\text{Pa}^{-1}$; see continuous solid lines in Fig. 3(b). With these fitted values of the binding constants, Eq. (6) may be solved simultaneously to obtain the component occupancies, and loadings; the results are presented as the continuous solid lines in Fig. 3(c). The 1D

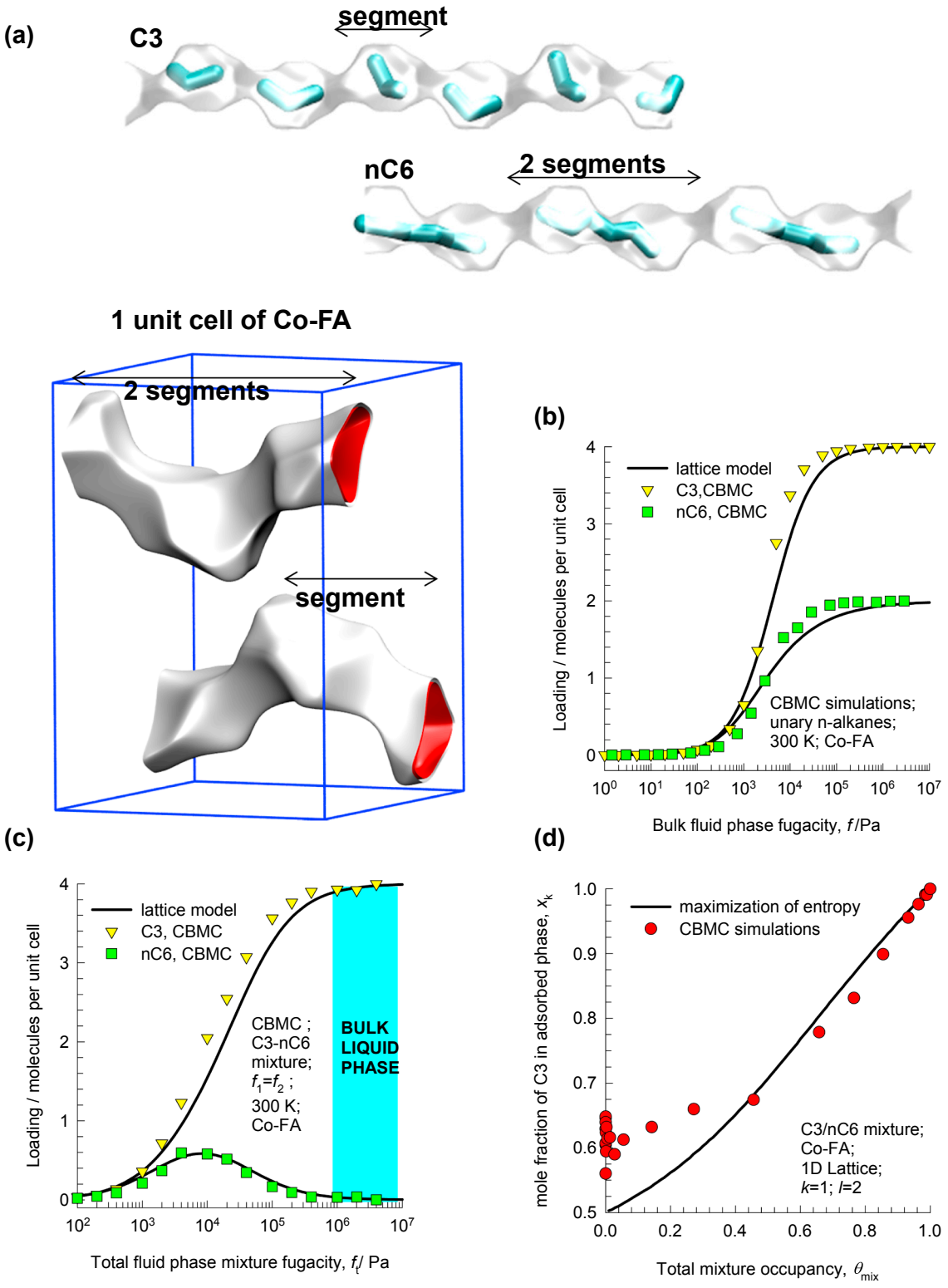

Fig. 3. (a) Computational snapshots of propane (C3) and n-hexane (nC6) in the 1D zig-zag channels of Co-FA. (b) CBMC simulations of unary isotherms for C3 and nC6 in Co-FA at 300 K. (c) CBMC simulations (shown by symbols) for C3/nC6 mixture adsorption in Co-FA at 300 K; in the CBMC simulations the partial fugacities in the bulk phase are equal to each other, i.e. $f_1 = f_2$. The continuous solid lines are the estimations of the 1D lattice model. (c) CBMC simulation data for the mole fraction of C3 in the adsorbed phase, x_k, as function of the mixture occupancy, θ_{mix}. The continuous solid line in (d) represents the solutions to Eqs. (4), and (5), corresponding to maximization of entropy.

lattice model affords a quantitative description of mixture adsorption and selectivity reversal. The departures between the CBMC simulations and the predictions of the 1D lattice model at mixture occupancies $\theta_{mix} < 0.4$ is entirely ascribable to the fact that Eq. (9) does not provide an adequately good fit of the unary isotherms at low occupancies. Put another way, the equality of binding constants, $b_k = b_l$, as assumed in the isotherm fits is not an entirely accurate one. However, for mixture occupancies $\theta_{mix} > 0.6$, the mixture adsorption is entirely dominated by

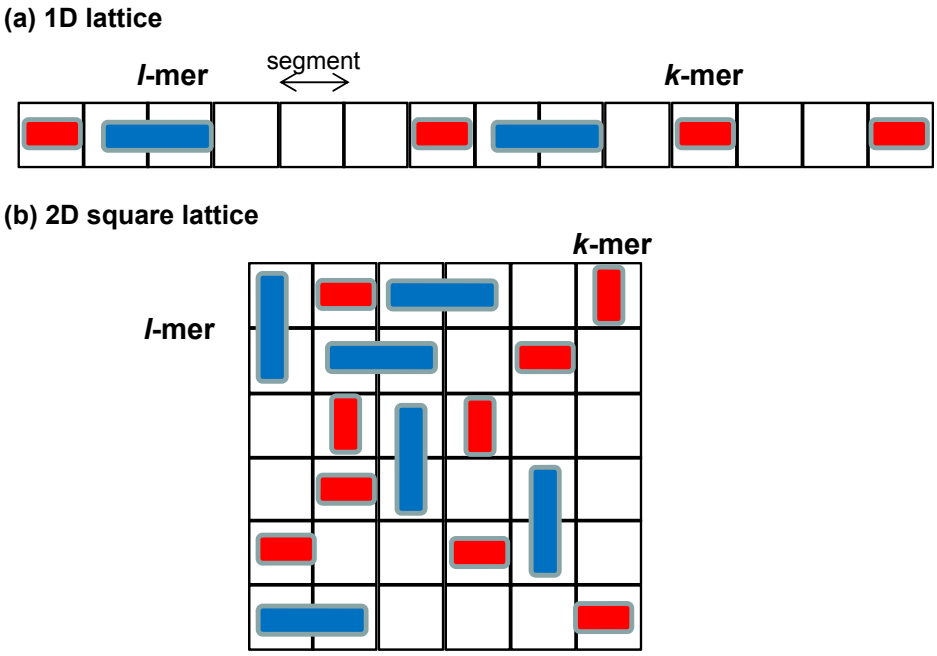

Fig. 4. (a) Schematic of the 1D lattice model of Dávila et al.[45] for adsorption of a mixture of *k*-mers and *l*-mers on 1D lattice. (b) Schematic of 2D square lattice model.

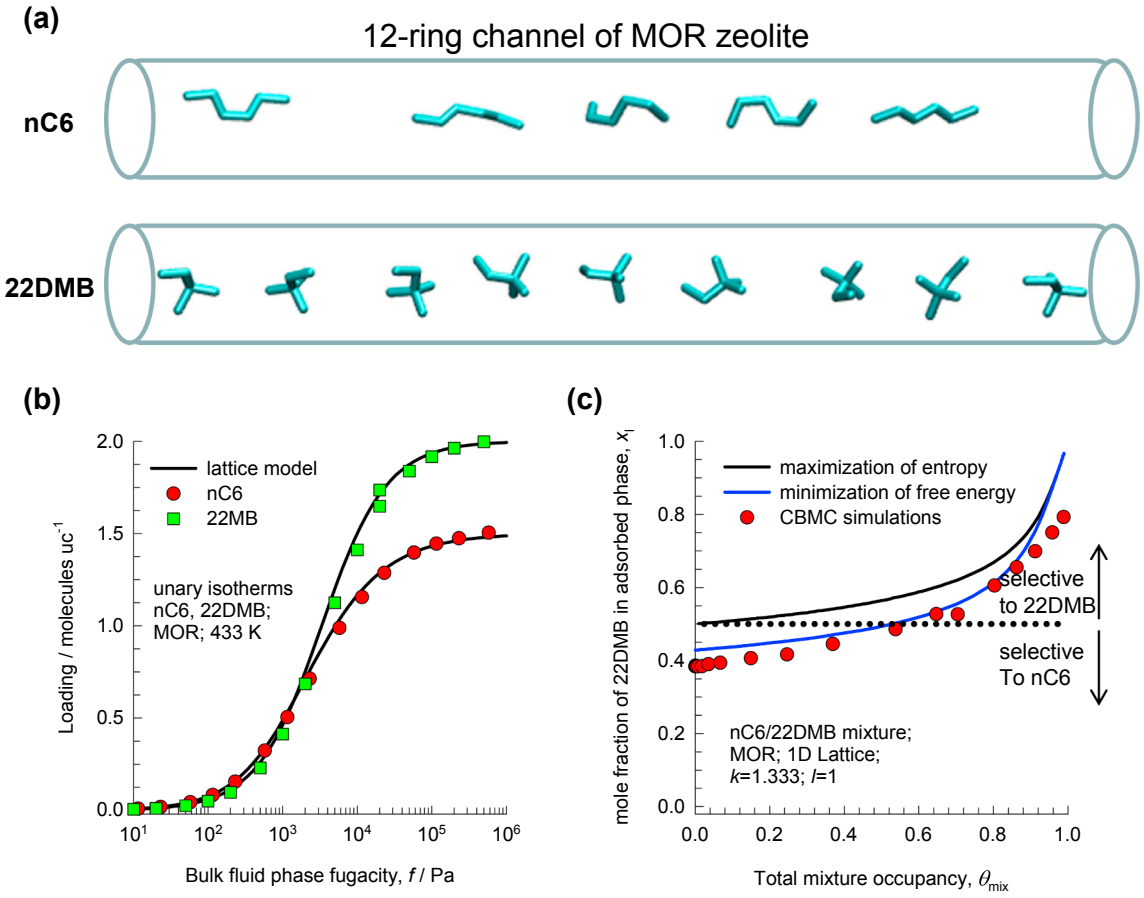

Fig. 5. (a) Snapshots of the conformation and siting of siting of nC6, and 22DMB along 1D 12-ring channel, 8 unit cells long at total fugacity f_t = 1 MPa. (b) CBMC data for unary isotherms of nC6 and 22DMB in MOR zeolite, compared with the fits of the 1D lattice model. (c) CBMC simulations of the values of the adsorbed phase mole fractions of 22DMB, $x_l = 1 - x_k$, as a function of the occupancy, θ_{mix}. The continuous solid lines are the calculations of the lattice model corresponding to the maximum entropy (by equations Eqs. (4), and (5)), and minimum free energy (blue line, Eqs. (5), and (7)). (For interpretation of the references to colour in this figure legend, the reader is referred to the web version of this article.)

entropy effects and the choice of the binding constants for unary isotherm fits is of little consequence.

We have also checked for a wide range of problems, that the solutions to Eq. (6) are identical to those obtained from use of the IAST, provided that the unary isotherm model used in the IAST correspond to those described by Eq. (9).

An important limitation of the lattice model is that its applicability rests on the accuracy with which Eq. (9) can be used to describe the experimental or CBMC data on unary isotherms. The IAST, on the other hand, can be applied to any isotherm model; see the detailed discussions in Chapters 8, 9, 10, 11, and 12 of the Supporting Material. Furthermore, the use of the lattice model requires the mixture adsorption to be described in terms of distinct and well-defined adsorption sites; such a description is not always possible.

2.3. Adsorption of n-hexane/2,2 dimethylbutane in MOR zeolite

MOR zeolite (Mordenite) consists of 12-ring (7.0 Å × 6.5 Å) 1D channels, connected to 8-ring (5.7 Å × 2.6 Å) pockets. Some representative snapshots [46] showing the siting and conformation of hexane isomers, n-hexane (nC6) and 2,2 dimethylbutane (22DMB) along one of the 12-ring channels, 8 unit cells long, for a total bulk fluid phase fugacity $f_t = 1$ MPa are presented in Fig. 5(a). Within the same channel length we find five nC6 molecules, and nine 22DMB molecules. The higher loading of 22DMB is due to increased degree of compactness of the di-branched isomer, i.e. smaller footprint. These data also explain why the saturation capacity for 22DMB is higher (=2 molecules per unit cell), compared to that of nC6 (=1.5 molecules per unit cell); see CBMC simulations of the unary isotherms in Fig. 5(b). The unary isotherms can be described quantitatively by Eq. (9). For nC6 (species k), we take $k = 1.333$, $M = 2$/uc, and $\frac{M}{k} = N_{k,sat} = 1.5$/uc. For 22DMB, we take $l = 1$, and $\frac{M}{l} = N_{l,sat} = 2$/uc. A good match between the 1D lattice model and CBMC simulations of the unary isotherms is obtained with the fitted binding constants are $b_k = 4 \times 10^{-4}\,\mathrm{Pa}^{-1}$, and $b_l = 3 \times 10^{-4}\,\mathrm{Pa}^{-1}$; see continuous solid lines in Fig. 5(b).

The symbols in Fig. 5(c) are the CBMC simulated data on the adsorbed phase mole fractions of 22DMB, $x_l = 1 - x_k$, plotted as function of the total occupancy, θ_{mix}. For $\theta_{mix} > 0.6$, the adsorbed phase is richer in 22DMB that packs the channels more efficiently. The CBMC simulation data for $x_l = 1 - x_k$ fall slightly below the "maximum entropy" line, described by the solutions to Eqs. (4), and (5), because of the slightly stronger binding strength of nC6. The entropy effects are able to override the binding energy contributions for $\theta_{mix} > 0.6$. The continuous blue line represents the calculations using Eqs. (5), and (7), that are based on the minimization of free energy concept, that is in quantitative agreement with the CBMC simulations, as is to be expected. The conclusion to be drawn from the information presented in Fig. 5(c) is that entropy effects are the prime drivers for selective adsorption of 22DMB in MOR at high channel occupancies, and at pore saturation we should expect the adsorbed phase to be predominantly richer in 22DMB, the di-branched isomer.

2.4. Separation of mixtures of aromatics

The separation of p-xylene from mixtures containing o, m, p-xylene, along with ethylbenzene is currently carried out in Simulated Moving Bed (SMB) adsorption devices that operate in the liquid phase. In current industrial practice BaX zeolite is used as adsorbent, but there is considerable commercial incentive for developing and synthesizing MOF structures that can offer significant improvements over BaX, that preferentially adsorbs p-xylene. To meet this objective we need to have a clearer appreciation of molecular dimensions of the guest molecules. The height and width of the C8 aromatic molecules are: o-xylene: 8 Å × 7.4 Å; m-xylene: 8.9 Å × 7.4 Å; p-xylene: 9.3 Å × 6.7 Å; ethylbenzene: 9.5 Å × 6.7 Å; styrene: 9.3 Å × 7 Å; see dimensions provided in Fig. 6. A further point to note is that xylene isomers are flat; these isomers can align themselves parallel to the channel walls, affording better van der Waals interactions with the framework atoms. Ethylbenzene is not a flat molecule; the ethyl branch is not in the same plane as the benzene ring. Due to the differences in the molecular dimensions of the xylene isomers, the efficiencies with which the xylene isomers stack within the channels of different dimensions are different. We can deliberately choose a material with a specified channel dimension in order to allow the optimum stacking of one or other of the xylene isomers.

Consider the separation of xylenes using AFI zeolite, that has 1D channels of approximately 7.3 Å; see structural details and pore landscape in Fig. 7(a). For m-xylene, and p-xylene, either the "height" or "width" is too large to allow vertical alignment; the orientation of these isomers occurs at an inclination. The molecular dimensions of o-xylene allow the molecules to be stacked vertically within the 8.4 Å "grooves" of AFI zeolite; this face-to-face is akin to the packing of potato crisps in cylindrical tubes as marketed by Pringles. An important consequence of the differences in the orientation of isomers is that the "footprints" of o-xylene molecules is significantly shorter than the footprints of m-xylene, and p-xylene molecules. Consequently, we should expect the saturation capacity of the ortho isomer to be significantly higher than that of its isomers. This expectation is fulfilled by CBMC simulations of the unary isotherms of C8 aromatics as presented in Fig. 7(b). Differences in packing efficiencies can be exploited to adsorb the ortho isomer preferentially from a mixture of xylenes. CBMC simulations of the adsorption of 4-component o-xylene/m-xylene/p-xylene/ethylbenzene mixtures in AFI zeolite at 433 K are shown in Fig. 7(c). For mixture occupancies $\theta_{mix} > 0.6$ entropy effects cause the adsorbed phase to be predominatly occupied by o-xylene. Indeed, at pore saturation conditions, $\theta_{mix} \approx 1$, the adsorbed phase is almostly exclusively occupied by o-xylene. Hu et al. [47,48] report transient breakthrough experiments to demonstrate that the breakthrough of o-xylene occurs significantly later than that of either m-xylene or p-xylene, confirming the selectivity of AFI to o-xylene. It is also noteworthy that $AlPO_4$-5 zeolite (with AFI topology) has been patented by Exxon Research & Engineering for o-xylene selective separation of aromatic mixtures [49].

Experimental data [50–52] for MIL-47 and MIL-53 with 1D rhombohedric channels of 8.5 Å show that these MOFs are selective to adsorption of o-xylene when operating at conditions close to pore

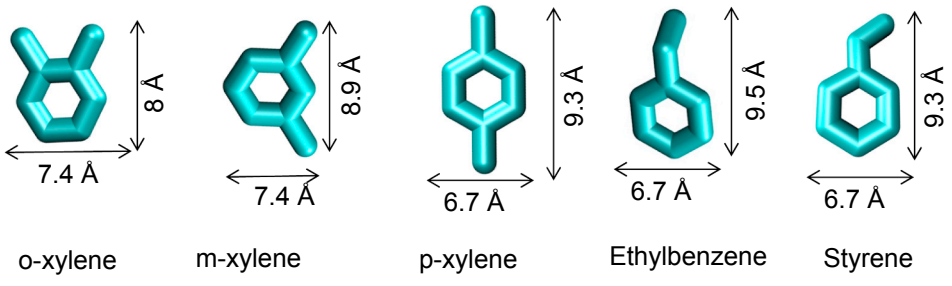

Fig. 6. The molecular dimensions of xylene isomers, ethylbenzene and styrene culled from Torres-Knoop et al. [26].

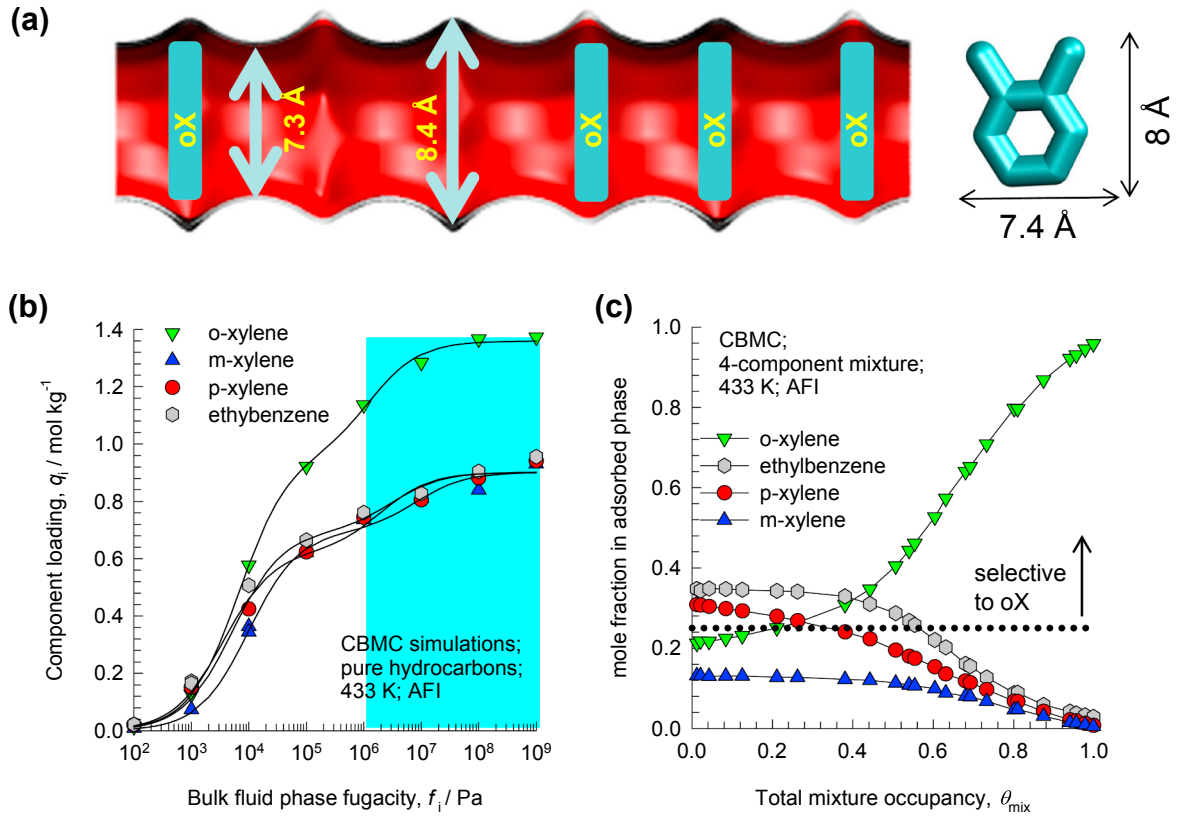

Fig. 7. (a) Pore landscape of AFI zeolite, with schematic of face-to-face stacking of o-xylene along the 1D channel. (b) CBMC simulations [55] of the unary isomers for C8 aromatics in AFI zeolite at 433 K.(c) CBMC simulations of the adsorption of 4-component o-xylene/m-xylene/p-xylene/ethylbenzene mixtures in AFI zeolite at 433 K; the partial fugacities in the bulk fluid phase, f_i, are equal to one another. The component mole fractions in the adsorbed phase are plotted as a function of the total occupancy of the mixture, θ_{mix}.

saturation. Fig. 8(a), schematized on the basis of CBMC simulated snapshots [26], indicate the commensurate stacking of o-xylene within 8.5 Å channels of MIL-47.

For selective adsorption of p-xylene, as desired in industrial practice, we need to select, or synthesize a MOF, with channel dimensions large enough to allow vertical stacking of the para isomer. Within the one-dimensional 10 Å channels of MAF-X8, we have commensurate stacking of p-xylene [26]; see Fig. 8(b). Fig. 8(c) presents snapshots of stacking of p-xylene within the 1D zig-zag shaped channels of Co-CUK-1; the synthesis of this MOF is described by Yoon et al. [27]. The p-xylene molecules can stack vertically, and this results in a higher saturation capacity for the para-isomer, as demonstrated by the experimental data on unary isotherms [27]. IAST calculations of mixture adsorption, along with transient breakthrough simulations, show that the recovery of pure p-xylene using MAF-X8 and Co-CUK-1 are significantly superior to that of BaX zeolite, the adsorbent that is currently used in industrial practice [2].

Maes et al. [53] and Remy et al. [54] have demonstrated that MIL-47 (V) and MIL-53 (Al) also have the potential for separation of mixtures of styrene and ethylbenzene. Styrene is a flat molecule; by contrast, ethylbenzene is not a flat molecule; the ethyl branch is not in the same plane as the benzene ring. Being flat, styrene molecules stack more efficiently within the 1D channels of MIL-47 (V) and MIL-53 (Al); see Fig. 9(a). Due to its higher packing efficiency of styrene, the mixture adsorption is strongly in favor of styrene; see CBMC simulations data for mixture adsorption in Fig. 9(b). At pore saturation conditions, the pores are almost exclusively filled with styrene.

Torres-Knoop et al. [55,56] have also provided other examples in which optimum face-to-face stacking of aromatic molecules can lead to uncommonly effective separations. Within triangular channels of a structure such as $Fe_2(BDP)_3$ [31], 1,3,5 tri-chlorobenzene (TCB) can be selectively separated from the 1,2,3 and 1,2,4 TCB isomers; the preferential adsorption of the 1,3,5 isomer is due to optimum face-to-face stacking; see Fig. 10(a). Fig. 10(b) shows CBMC simulations for adsorption of equimolar mixtures of the three isomers: 1,2,3 tri-chlorobenzene (TCB), 1,2,4 TCB, and 1,3,5 TCB in modified $Fe_2(BDP)_3$ at 433 K. At pore saturation, the adsorbed phase is practically devoid of the 1,2,3 and 1,2,4 isomers due to entropy effects that favor of 1,3,5 TCB, the component with the smallest footprint.

3. Entropy effects in cage-type zeolite structures

3.1. Separation of 1-butanol/1-hexanol mixtures in CHA zeolite

We use the 2D square lattice model of Azizian and Bashiri [57] for modeling the adsorption of linear alcohols in CHA zeolite; see schematic of the square array in Fig. 4(b). The equations describing unary and mixture adsorption are formally equivalent to that of Dávila et al. [45], and Eqs. (1)–(9) apply here as well; further details are provided in Chapter 6 of Supplementary Material.

As illustration, Fig. 11(a) presents the CBMC simulations of the unary isotherms of 1-butanol and 1-hexanol in CHA at 300 K; the saturation capacities of 1-butanol and 1-hexanol are, respectively, 2 molecule per cage, and 1 molecule per cage. Therefore, we take $k = 1$, $M = 2$/cage, and $\frac{M}{k} = N_{k,sat} = 2$/cage, and $l = 2$, and $\frac{M}{l} = N_{l,sat} = 1$/cage. The CBMC simulations of the unary isotherms can be fitted reasonably with Eq. (9) taking $b_k = 4 \times 10^{-1}\,\mathrm{Pa}^{-1}$, $b_l = 20\,\mathrm{Pa}^{-1}$, and $b_l/b_k = 50$. For binary 1-butanol/1-hexanol adsorption, Fig. 11(b) presents CBMC simulation data on the mole fractions of 1-butanol in the adsorbed phase as a function the occupancy, θ_{mix}. The

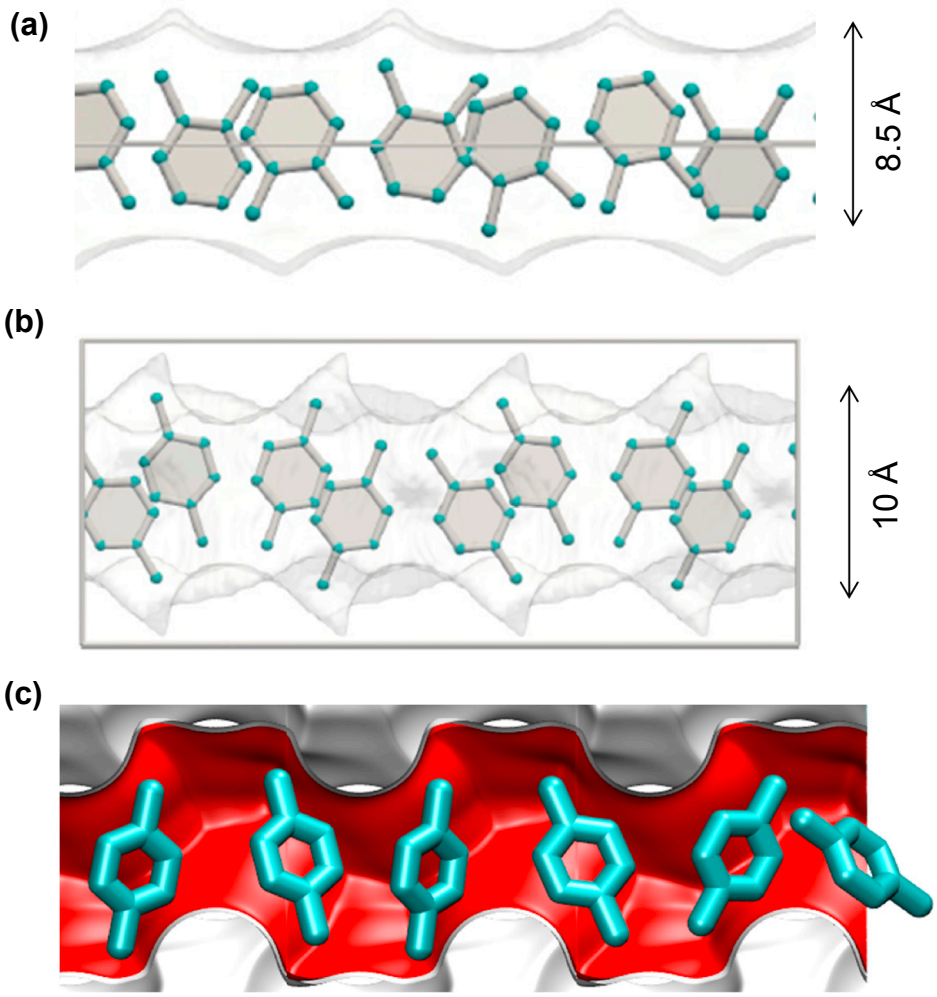

Fig. 8. (a) Schematic showing the stacking of o-xylene within 8.5 Å channels of MIL-47 [26]. (b) Schematic showing the stacking of *p*-xylene within 10 Å channels of MAF-X8 [26]. (c) Computational snapshot showing the stacking of *p*-xylene within the 1D zig-zag shaped channels of Co-CUK-1 [27].

plot clearly shows that entropy effects come into play at occupancies $\theta_{mix} > 0.6$. When the cages of CHA are saturated, i.e. $\theta_{mix} \approx 1$, the adsorbed phase mole fraction of 1-butanol $x_k \to 1$ and 1-hexanol is excluded from the cages. The CBMC data are in quantitative agreement with the lattice model calculations of x_k using Eqs. (5), and (7), corresponding to the minimization of free energy. Also plotted are the calculations corresponding to the maximum entropy (using Eqs. (4), and (5)). The selectivity reversal in favor of 1-butanol is due to the entropic term of the free energy that favors the adsorption of 1-butanol from maximum entropy considerations. An analogous interpretation holds for all ten mixtures considered in Fig. 1; see Chapter 12 of Supplementary Material.

Fig. 11(b) also portrays the generic characteristics of separations of binary mixtures with different saturation capacities. At low occupancies, $\theta_{mix} < 0.4$ in this specific instance, the separations are dictated by differences in binding constants, b_k, b_l. For all mixture separations, entropy effects come into play for $\theta_{mix} > 0.5$. A testimony to the manifestation of entropy effects is that the adsorbed phase becomes increasingly richer in the component with the higher saturation capacity. As a consequence, at a certain occupancy level, $\theta_{mix} = 0.65$ in this specific instance, selectivity reversal takes place. The selectivity reversal occurs at higher occupancies $\theta_{mix} > 0.65$ when (a) the ratio of saturation capacities $q_{k,sat}/q_{l,sat}$ is lower that 2 as in this case, and/or (b) if ratio of binding constants $b_l/b_k > 50$. On the other hand, selectivity reversal occurs at occupancies lower than 0.65 when (a) the ratio of saturation capacities $q_{k,sat}/q_{l,sat}$ is higher that 2 as the case for 1-butanol/1-hexanol, and/or (b) if ratio of binding strengths b_l/b_k is lower than 50. In the special case of $b_l/b_k = 1$, the separations are entirely entropy driven as is the case for C3/nC6/Co-FA witnessed in Fig. 3(d).

3.2. Separation of mixtures of linear alkanes in TSC zeolite

For separation of chain molecules with carbon numbers higher than say 20, as is required in the petroleum industry in lube oil processing, we need microporous host structures with sufficiently large cages. Of particular importance in this context is all-silica TSC zeolite, with a Tschörtnerite framework, that has the largest cage volume of any known zeolite [58]. Each unit cell of TSC has four "LTA type cages" of 743 Å^3, and four "TSC supercages" of 2553 Å^3; the cages are separated by two types of windows: 4.02 Å × 4.17 Å, and 3.1 Å × 5.41 Å. For structural details and pore landscapes see Chapter 13 of Supplementary Material.

Fig. 12(a) presents CBMC simulations [35] of pure component isotherms for n-alkanes nC21, nC22, nC23, nC24, and nC25 in TSC at 500 K. The loadings are expressed as molecules per TSC supercage, because the LTA-type cages are too small to accommodate these long chain alkanes. Entropy effects will be expected to come into play for separations of mixtures of n-alkanes with different saturation capacities. This expectation is fulfilled in the CBMC simulation data for binary nC21/nC24, and nC22/nC25 mixture adsorption. In Fig. 12(b) the mole fractions of the shorter alkane in the adsorbed phase is plotted as a function the mixture occupancy, θ_{mix}. For both mixtures, the

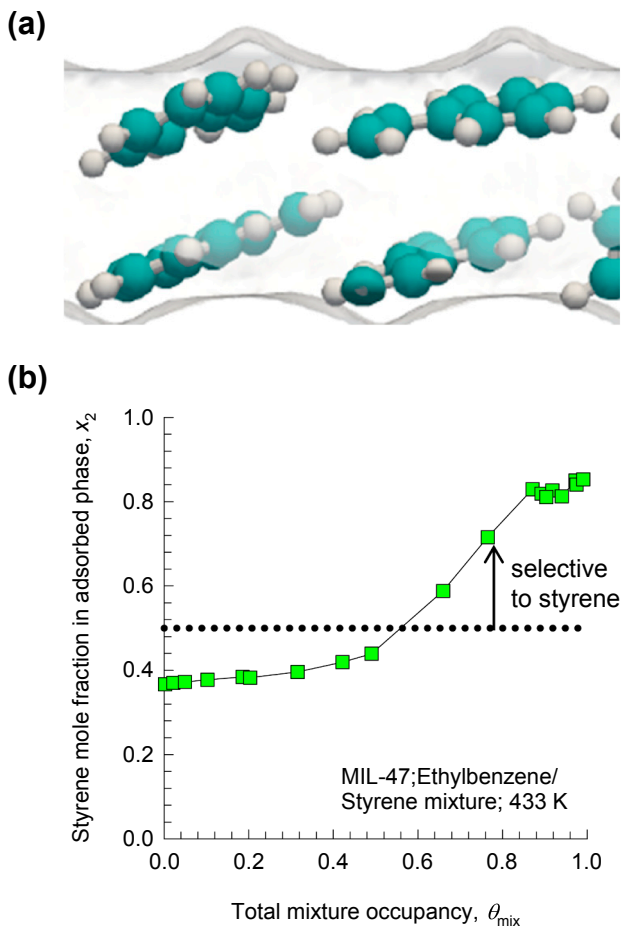

Fig. 9. (a) Snapshot showing commensurate stacking of styrene in MIL-47. (b) CBMC simulations [29] for adsorption of binary ethylbenzene/styrene mixtures in MIL-47 at 433 K; the mole fraction of styrene in the adsorbed phase is plotted as a function of the total occupancy of the mixture, θ_{mix}.

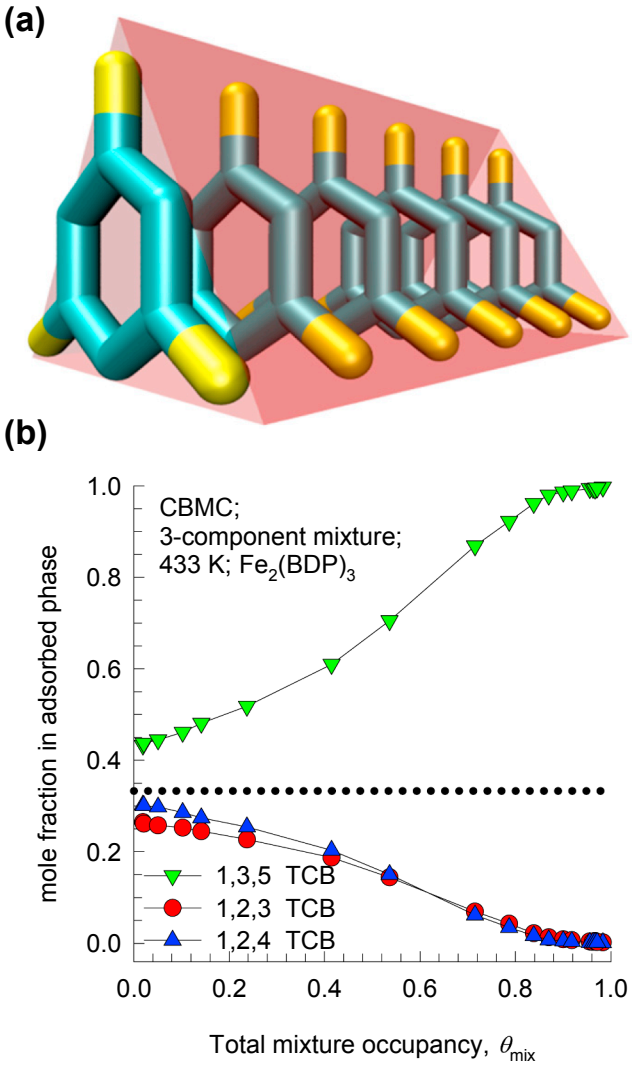

Fig. 10. (a) Schematic showing face-to-face stacking of 1,3,5 tri-chlorobenzene (TCB) within the triangular channels of modified $Fe_2(BDP)_3$; adapted from Torres-Knoop et al. [55] (b) CBMC simulations [55] of the adsorbed phase mole fractions for adsorption of equimolar ternary TCB mixtures in modified $Fe_2(BDP)_3$ at 433 K.

selectivity reversals occur at cage occupancies $\theta_{mix} > 0.7$. Also plotted are the calculations of x_k using the lattice model corresponding to the maximum entropy (using Eqs. (4), and (5)) that clearly indicate that selectivity reversals are entropy driven.

4. Configurational entropy effects in MFI zeolite

MFI zeolite (also called silicalite-1) has a topology consisting of a set of intersecting straight channels, and zig-zag (or sinusoidal) channels of approximately 5.5 Å size. A linear molecule such as n-hexane (nC6) can locate anywhere along the straight and zig-zig channels; see Fig. 13(a). The saturation capacity of nC6 in MFI, as evidenced by the CBMC simulations of unary isotherms (see Fig. 13(b)) is 8 molecules per unit cell. Branched alkanes such as 2-methylpentane (2MP) prefer to locate at the channel intersections because of the extra "leg room" that is available here; see snapshot in Fig. 13(a). Per unit cell of MFI, there are only 4 intersection sites, and therefore the saturation capacity of 2MP is limited to 4 molecules per unit cell. We now demonstrate with the aid of 2D square lattice model of Azizian and Bashiri [57], that the differences in the saturation capacities, due to differences in molecular configurations, can be exploited to separate nC6/2MP mixtures with MFI zeolite.

The unary isotherms can be described quantitatively by Eq. (9). For nC6 (species k), we take $k = 1$, $M = 8$/uc, and $\frac{M}{k} = N_{k,sat} = 8$/uc. For 22DMB, we take $l = 2$, $M = 8$/uc, and $\frac{M}{l} = N_{l,sat} = 4$/uc. A reasonably good match between Eq. (9) and the CBMC simulations of the unary isotherms is obtained with the choice $b_k = 1\,\text{Pa}^{-1}$, and $b_l = 1.5\,\text{Pa}^{-1}$; see Fig. 13(b). It is noteworthy that the binding constant of 2MP is slightly higher than that of nC6.

The CBMC simulations of nC6/2MP mixture adsorption at 300 K are presented in Fig. 13(c); these show that for bulk fluid phase fugacities $f_t > 1$ Pa, the adsorbed phase mixture gets increasingly richer in nC6, and the branched isomer 2MP is progressively excluded from the zeolite. Experimental data of Titze et al. [59], obtained by Infra-Red Microscopy (IRM) (also plotted in Fig. 13(c) as open symbols) provide direct confirmation of the exclusion of 2MP due to configurational entropy effects. Fig. 13(d) plots the CBMC simulated data on the mole fraction of nC6 in the adsorbed phase, x_k, is plotted as function of the total occupancy, θ_{mix}. As the occupancies increase beyond 0.5, the adsorbed phase becomes increasingly richer in nC6, and as $\theta_{mix} \to 1$; $x_k \to 1$; the adsorbed phase is practically devoid of 2MP. Also plotted are the calculations of x_k using the lattice model corresponding to the maximum entropy (using Eqs. (4), and (5)) that clearly indicate the exclusion of 2MP from the channels is entropy driven.

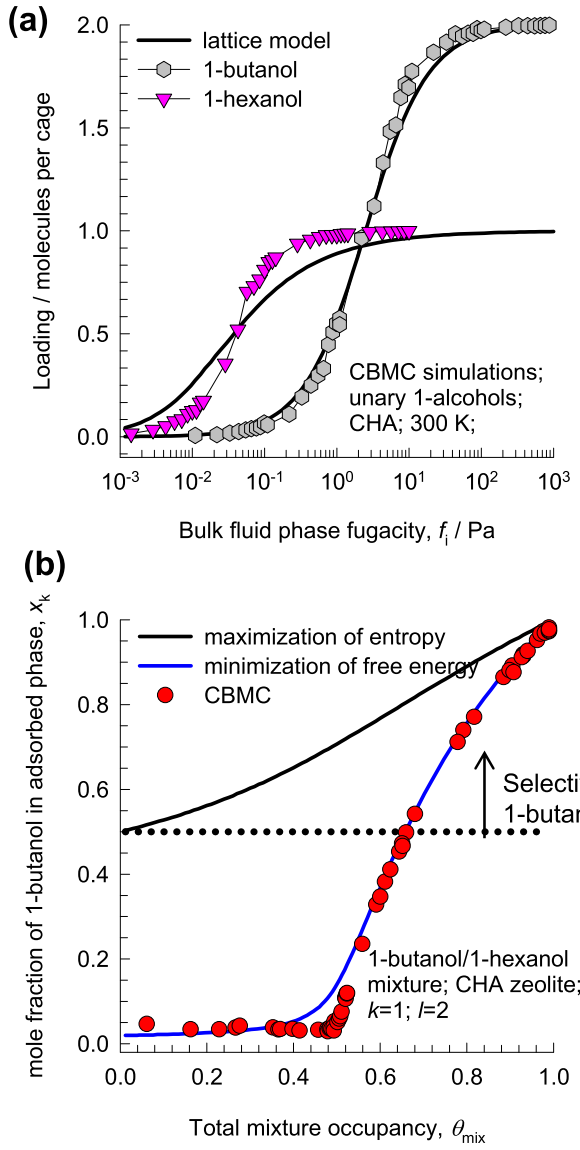

Fig. 11. (a) CBMC simulations of the unary isotherms of 1-butanol and 1-hexanol in CHA at 300 K. (b) CBMC simulations (symbols) of the mole fractions of 1-butanol in the adsorbed phase as a function the occupancy, θ_{mix}. Also plotted are the lattice model calculations of x_k corresponding to the maximum entropy (using Eqs. (4), and (5)), and minimum free energy (blue line, Eqs. (5), and (7)). (For interpretation of the references to colour in this figure legend, the reader is referred to the web version of this article.)

5. Entropy effects described by the explicit model of vas Assche

An important point to note is that calculations of the component loadings, by either the lattice models discussed above, or the IAST, are not explicit in terms of the binding strengths and the partial fugacities in the bulk fluid phase; robust numerical procedures are required in the calculations. For that reason, an explicit calculation procedure for the component loadings has been suggested by van Assche et al. [43], that, purportedly, has its basis in statistical thermodynamics. For a mixture of species 1 and 2, the following expressions for the component loadings are derived for the scenario in which species 1 has the higher saturation capacity

$$q_1 = \frac{q_{1sat} b_1 f_1 (1 + b_1 f_1)^{\frac{q_{1sat}}{q_{2sat}} - 1}}{(1 + b_1 f_1)^{\frac{q_{1sat}}{q_{2sat}}} + b_2 f_2}; \quad q_2 = \frac{q_{2sat} b_2 f_2}{(1 + b_1 f_1)^{\frac{q_{1sat}}{q_{2sat}}} + b_2 f_2} \tag{10}$$

From Eq. (10), the mole fraction of the component in the adsorbed phase x_1 that has the *higher* saturation capacity, is:

$$x_1 = \frac{1}{1 + \frac{b_2 f_2}{b_1 f_1} \frac{1}{\Omega}}; \quad \Omega = \frac{q_{1sat}}{q_{2sat}} (1 + b_1 f_1)^{\frac{q_{1sat}}{q_{2sat}} - 1} \tag{11}$$

From Eq. (11), we note that the entropy factor Ω varies only with the occupancy of component 1, and ignores the contribution of the occupancy of component 2 to the Boltzmann re-arrangement statistics, that characterizes entropy effects. This is in sharp contrast to the entropy factor described by Eq. (5), wherein Ω is seen to depend on the occupancies of both components in the mixture. The very essence of

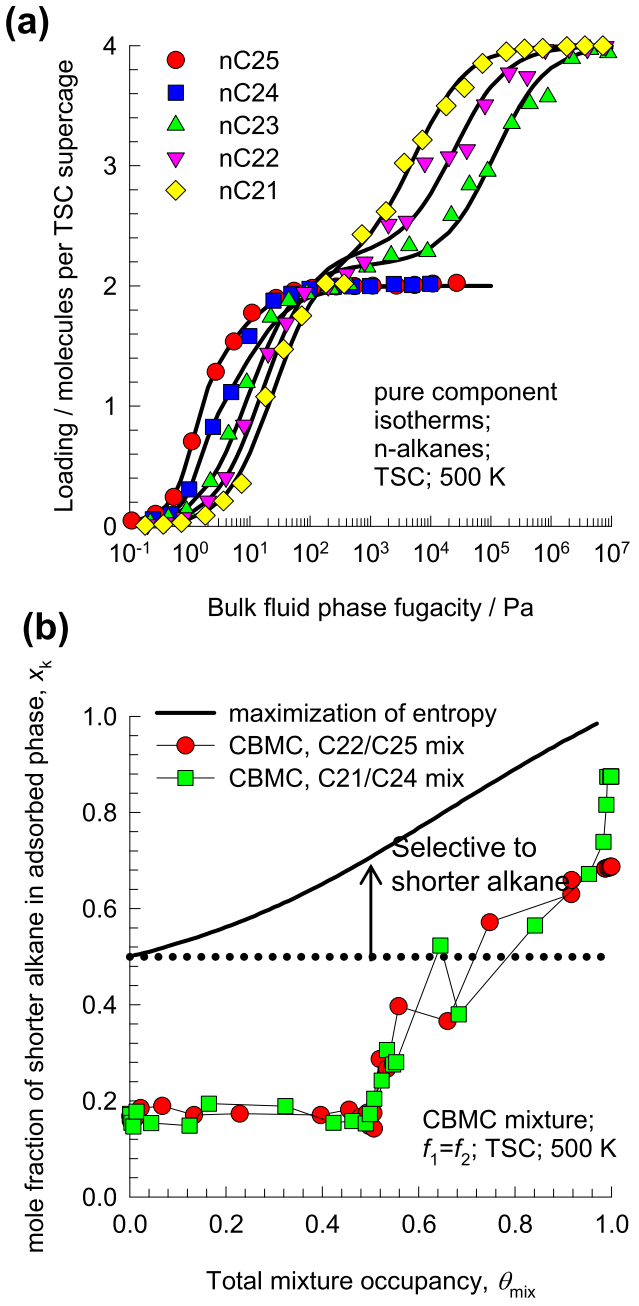

Fig. 12. (a) CBMC simulations of pure component adsorption isotherms for n-alkanes in TSC at 500 K. (b) CBMC simulations of binary nC21/nC24, and nC22/nC25 mixture adsorption in TSC at 500 K. The partial fugacities in the bulk fluid phase, $f_1 = f_2$. The mole fractions of the shorter alkane in the adsorbed phase plotted as a function the mixture occupancy, θ_{mix}. Also plotted are the calculations of x_k using the lattice model corresponding to the maximum entropy (using Eqs. (4), and (5)).

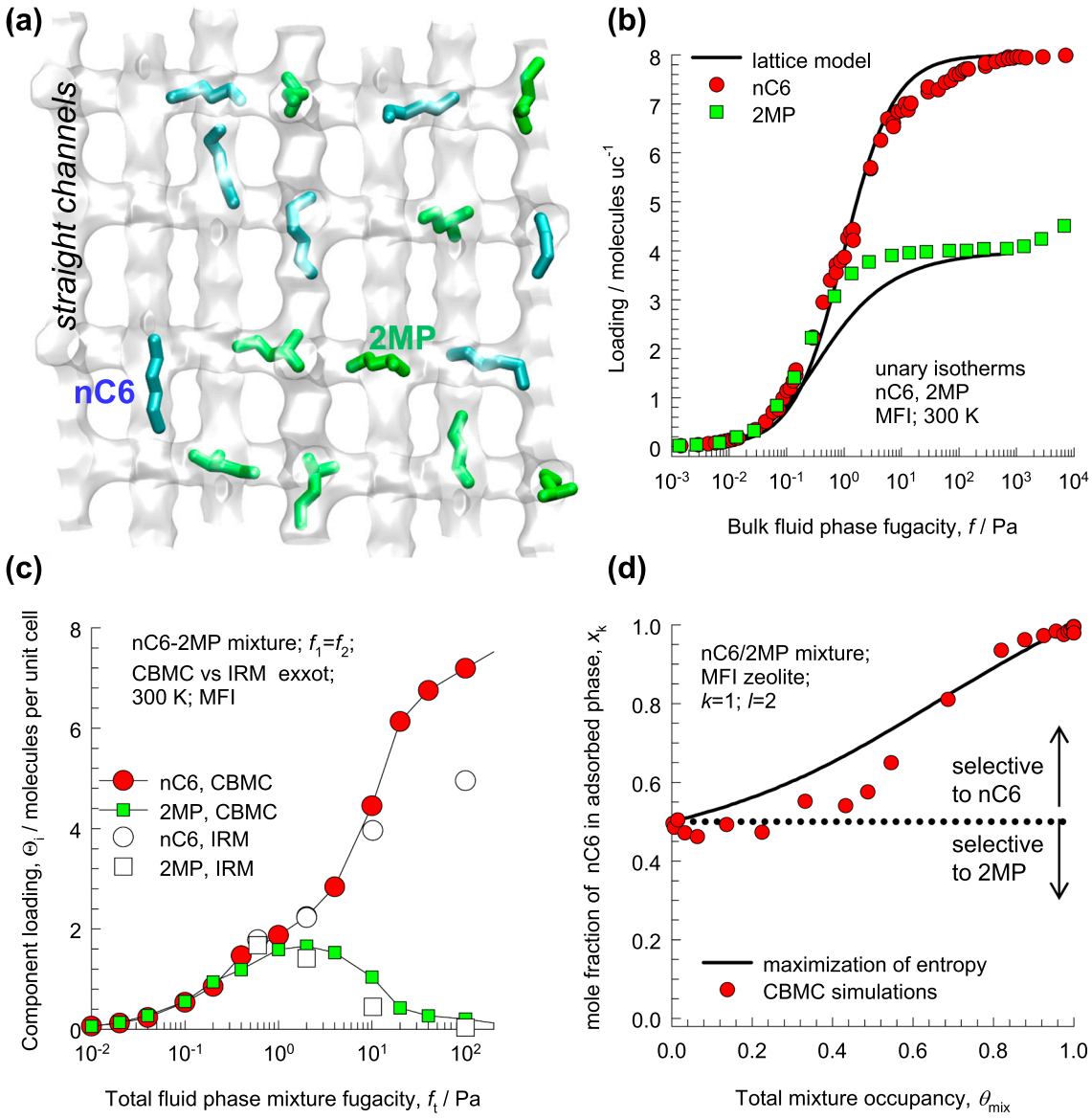

Fig. 13. (a) Snapshots showing the location of nC6 and 2MP within the intersecting channels of MFI zeolite. (b) CBMC data for unary isotherms of nC6 and 2MP in MFI zeolite at 300 K, compared with the fits of the lattice model, described by Eq. (6). (c) CBMC simulated values of adsorbed phase component loadings of nC6, and 2MP, plotted as a function of the total bulk mixture fugacity, f_t, compared to the IRM experimental data of Titze et al. [59], (c) CBMC simulated values of adsorbed phase mole fraction of nC6, x_k, plotted as a function of the mixture occupancy, θ_{mix}. The continuous solid line represents calculations of x_k using the lattice model corresponding to the maximum entropy (using Eqs. (4), and (5)).

entropy effects is that they involve *re-arrangement* of the adsorbed phase mole fractions attendant with increasing pore occupancies; such re-arrangements must accurately reflect the loadings of each of the guest molecules, and not just one of them, as implied in Eqs. (10) and (11).

For a mixture of species 1 and 2, in which each species follows 1-site Langmuir adsorption characteristics, the following expressions for the component loadings are also derived by van Assche et al. [43], for the scenario in which species 2 has the higher saturation capacity

$$q_1 = \frac{q_{1sat} b_1 f_1}{(1 + b_2 f_2)^{\frac{q_{2sat}}{q_{1sat}}} + b_1 f_1}; \quad q_2 = \frac{q_{2sat} b_2 f_2 (1 + b_2 f_2)^{\frac{q_{2sat}}{q_{1sat}} - 1}}{(1 + b_2 f_2)^{\frac{q_{2sat}}{q_{1sat}}} + b_1 f_1} \tag{12}$$

The mole fraction of the component in the adsorbed phase that has the *lower* saturation capacity, can be derived:

$$x_1 = \frac{1}{1 + \frac{b_2 f_2}{b_1 f_1} \frac{1}{\Omega}} = 1 - x_2; \quad \Omega = \frac{q_{1sat}}{q_{2sat}} \frac{1}{(1 + b_2 f_2)^{\frac{q_{2sat}}{q_{1sat}} - 1}} \tag{13}$$

From Eq. (13), we note that the entropy factor Ω varies only with the occupancy of component 2, and ignores the contribution of the occupancy of component 1 to the Boltzmann re-arrangement statistics. Eqs. (10) and (12) are both inherently asymmetric in nature, and the species numbering cannot be inter-changed, as also stressed by van Assche et al. [43].

As illustration of the limitations of the explicit model of van Assche et al. [43], we consider binary ethanol(1)/1-hexanol(2) mixture adsorption in CHA zeolite at 300 K, and total fugacity $f_t = f_1 + f_2 = 100$ kPa, and varying mole fraction of ethanol (1) in the bulk fluid phase, y_1. On the basis of the CBMC simulations [35], the saturation capacities of ethanol (1), and 1-hexanol (2) are respectively 4 molecules per cage, and 1 molecule per cage, respectively; i.e. $q_{1sat} = 4$/cage, $q_{2sat} = 1$/cage; $\frac{q_{1sat}}{q_{2sat}} = 4$. The CBMC simulated unary isotherms could be fitted with 1-site Langmuir model with binding constants $b_1 = 3 \times 10^{-4}\,\text{Pa}^{-1}$, $b_2 = 30\,\text{Pa}^{-1}$. Fig. 14(a) presents comparison of the calculations of the mole fraction of ethanol in the

adsorbed phase x_1 as function of y_1, the mole fraction of ethanol in the bulk fluid phase mixture. We compare the estimations of Eq. (11), that is appropriate for $q_{1sat} > q_{2sat}$, with the corresponding IAST estimates. The estimations of the explicit model of van Assche et al.[43] are extremely poor in the range $0 < y_1 < 0.5$. The reason for this is that Eqs. (10), and (11) do not have the proper limiting behaviors for the component loadings, q_1 for $y_1 \to 0$, and q_2 for $y_2 \to 0$. Witness the comparisons in the component loadings for ethanol, and 1-hexanol as estimated by the IAST and van Assche models in Fig. 14(b, c). Fig. 14(d) shows that the entropy factor Ω calculated from Eq. (11) is about 4 orders of magnitude lower than the corresponding IAST estimates for vanishingly small fraction of ethanol in the bulk fluid phase $y_1 \to 0$.

The "solution" that is offered by van Assche et al. [43] to address the issue of incorrect limiting behaviors is to suggest that the component loadings be calculated by taking the arithmetic average of those determined by Eqs. (10) and (12). Essentially, the van Assche approach is to postulate that the arithmetic average of two flawed formulae will yield the correct numerical answer. Their suggested approach lacks any theoretical foundation and cannot be recommended for use in practice.

Entropy effects in mixture adsorption involve re-arrangements of the adsorbed phase compositions with increasing mixture occupancies, θ_{mix}; such re-arrangements cannot be captured by explicit analytic formulae. Rather, implicit iterative procedures such as the IAST, or the multi-site occupancy model of Nitta et al. [60] (see Chapter 5 of Supplementary material for details) are needed to adequately model entropy effects.

6. Conclusions

The following major conclusions emerge from our analysis of binary (k, l) mixture adsorption in microporous crystalline materials.

(1) At pore occupancies $\theta_{mix} > 0.5$, mixture separations are significantly influenced by differences in saturation capacities of the guest species.
(2) Differences in saturation capacities in 1D channel structures arise due to a variety of reasons: (a) molecular lengths of linear alkanes, alkenes, and alcohols, (b) differences in the molecular "footprints"

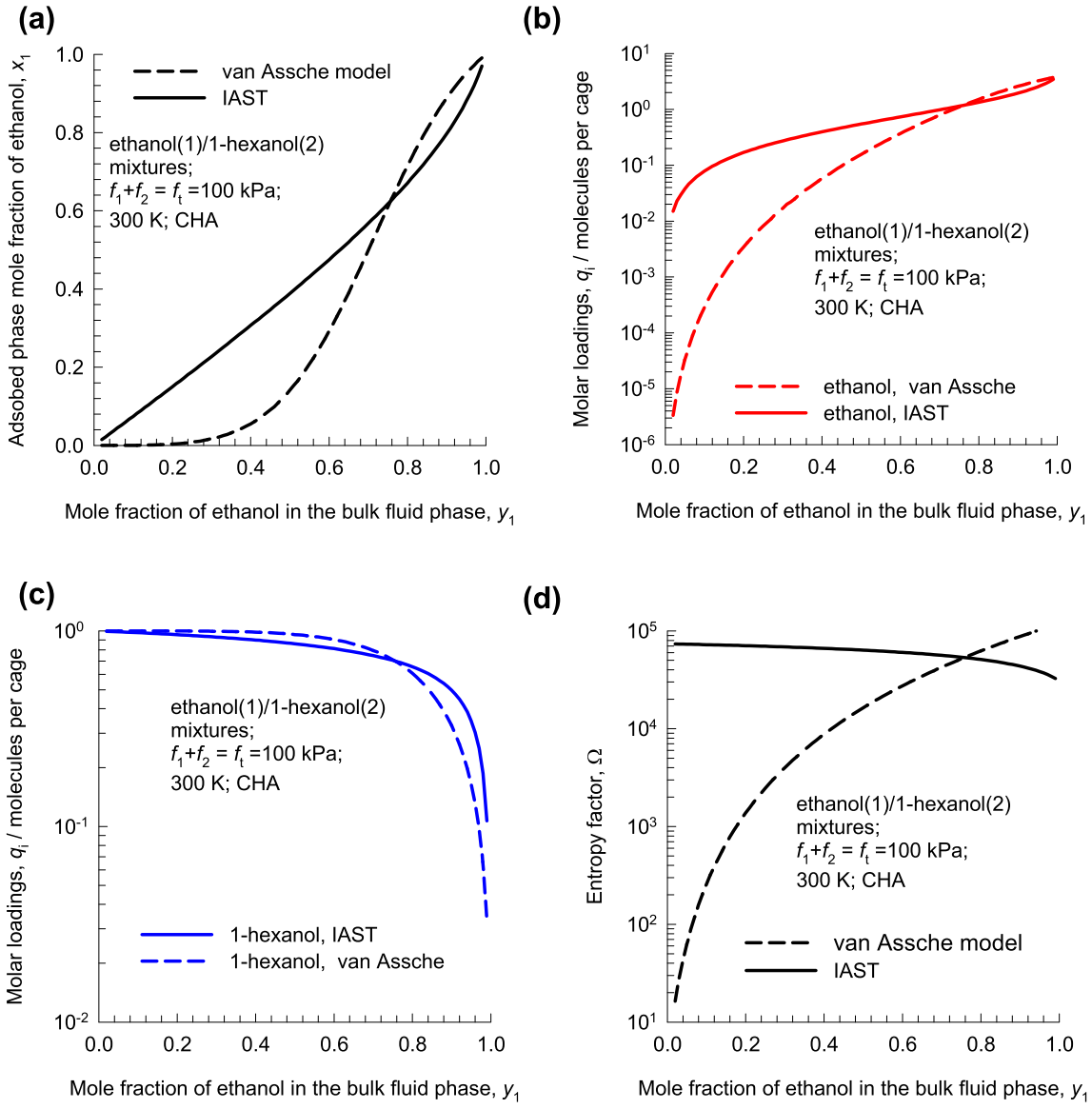

Fig. 14. Calculations for binary ethanol(1)/1-hexanol(2) mixture adsorption in CHA at 300 K and total fugacity $f_t = f_1 + f_2 = 100$ kPa, and varying mole fraction of ethanol (1) in the bulk fluid phase composition, y_1. (a) Mole fraction of ethanol in the adsorbed phase plotted as function of the bulk fluid phase composition, y_1. (b, c) The component molar loadings for (a) ethanol, and (b) 1-propanol. (d) Calculations of the entropy factor Ω. Two sets of calculations are presented: IAST (continuous solid line), and the explicit model of van Assche et al. [43] (dashed line).

reflecting the compactness of the molecular conformations of the hydrocarbon isomer, and (c) differences in molecular "footprints" arising out of commensurate/incommensurate stacking. Differences in saturation capacities in cage-type structures arise due to limitations in the cage size, and the ability to accommodate a molecule of a given length (or size). Differences in saturation capacities in the intersecting channels of MFI, is because the branched alkane demands extra "leg room", and can be located only at the intersection sites, whose number is limited.

(3) For all guest/host combinations, the plots of the mole fraction of the adsorbed phase, x_k, as function of the occupancy, θ_{mix}, show three common characteristics: (a) selectivity reversals in favor of the component with the higher saturation capacity usually occur at $\theta_{mix} > 0.5$, (b) as $\theta_{mix} \to 1$; $x_k \to 1$; the adsorbed phase is practically devoid of the component with the lower saturation capacity, even if that component has the much stronger binding, and (c) for mixtures in which the components have equal binding strengths, $b_k \approx b_l$, the separations are entirely driven by entropic considerations.

(4) Entropy effects can be simply, and elegantly, elucidated using simple 1D and 2D lattice model descriptions of mixture adsorption, along with the Boltzmann relation, $S = k_B \ln(W)$. The underlying physical reasoning is that there are many more molecular "arrangements", W, realizable if the adsorbed phase is predominantly richer in the component that is smaller in size, shorter in length, has the smaller footprint, or is not demanding of extra "leg room" space.

(5) Appreciation of the significant importance of entropic contributions, allows us to choose, or develop, materials or channel topologies that would facilitate the packing of the component that needs to be selectively adsorbed. This concept is of particular significance in separations of aromatic molecules.

(6) Though statistical thermodynamics, and lattice models, assist in gaining physical insights, the use of the IAST is required in process design of adsorbers and membrane devices. In this context, it has been established that use of the simpler, explicit, approach of van Assche et al. [43] is not to be recommended, in general, because of the wrong limiting behaviors at either end of the composition extremes of the bulk phase fluid mixture.

Appendix A. Supplementary material

Supplementary data to this article can be found online at https://doi.org/10.1016/j.seppur.2019.01.014.

References

[1] J.A. Mason, K. Sumida, Z.R. Herm, R. Krishna, J.R. Long, Evaluating metal-organic frameworks for post-combustion carbon dioxide capture via temperature swing adsorption, Energy Environ. Sci. 4 (2011) 3030–3040.

[2] R. Krishna, Methodologies for screening and selection of crystalline microporous materials in mixture separations, Sep. Purif. Technol. 194 (2018) 281–300, https://doi.org/10.1016/j.seppur.2017.11.056.

[3] S. Mukherjee, M. Das, A. Manna, R. Krishna, S. Das, Newly designed 1,2,3-triazole functionalized covalent triazine frameworks with exceptionally high uptake capacity of both CO_2 and H_2, J. Mater. Chem. A (2019), https://doi.org/10.1039/C8TA08185A.

[4] J. Yang, B. Du, J. Liu, R. Krishna, F. Zhang, W. Zhou, Y. Wang, J. Li, B. Chen, MIL-100Cr with open Cr sites for a record N_2O capture, Chem. Commun. 54 (2018) 14061–14064, https://doi.org/10.1039/C8CC07679K.

[5] Z.R. Herm, J.A. Swisher, B. Smit, R. Krishna, J.R. Long, Metal-organic frameworks as adsorbents for hydrogen purification and pre-combustion carbon dioxide capture, J. Am. Chem. Soc. 133 (2011) 5664–5667.

[6] H. Wu, K. Yao, Y. Zhu, B. Li, Z. Shi, R. Krishna, J. Li, Cu-TDPAT, an *rht*-type dual-functional metal-organic framework offering significant potential for use in H_2 and natural gas purification processes operating at high pressures, J. Phys. Chem. C 116 (2012) 16609–16618.

[7] S.C. Xiang, Y. He, Z. Zhang, H. Wu, W. Zhou, R. Krishna, B. Chen, Microporous metal-organic framework with potential for carbon dioxide capture at ambient conditions, Nat. Commun. 3 (2012) 954, https://doi.org/10.1038/ncomms1956.

[8] R. Krishna, Methodologies for evaluation of metal-organic frameworks in separation applications, RSC Adv. 5 (2015) 52269–52295.

[9] F. Luo, C. Yan, L. Dang, R. Krishna, W. Zhou, H. Wu, X. Dong, Y. Han, T.-L. Hu, M. O'Keeffe, L. Wang, M. Luo, R.-B. Lin, B. Chen, UTSA-74: A MOF-74 isomer with two accessible binding sites per metal center for highly selective gas separation, J. Am. Chem. Soc. 138 (2016) 5678–5684.

[10] D. Banerjee, A.J. Cairns, J. Liu, R. Krishna, P.K. Thallapally, D.M. Strachan, Potential of metal-organic frameworks for capture of noble gases, Acc. Chem. Res. 48 (2015) 211–219.

[11] X. Cui, K. Chen, H. Xing, Q. Yang, R. Krishna, Z. Bao, H. Wu, W. Zhou, X. Dong, Y. Han, B. Li, Q. Ren, M.J. Zaworotko, B. Chen, Pore chemistry and size control in hybrid porous materials for acetylene capture from ethylene, Science 353 (2016) 141–144.

[12] H.-H. Wang, C.-Y. Liu, L. Li, R. Krishna, Y.-L. Wang, X.-W. Peng, C.-T. He, R.-B. Lin, B. Chen, Nickel-4′-(3,5-dicarboxyphenyl)-2,2′,6′,2″-terpyridine framework: efficient separation of ethylene from acetylene/ethylene mixtures with a high productivity, Inorg. Chem. 57 (2018) 9489–9494, https://doi.org/10.1021/acs.inorgchem.8b01479.

[13] Y. He, R. Krishna, B. Chen, Metal-organic frameworks with potential for energy-efficient adsorptive separation of light hydrocarbons, Energy Environ. Sci. 5 (2012) 9107–9120.

[14] Z. Bao, G. Chang, H. Xing, R. Krishna, Q. Ren, B. Chen, Potential of microporous metal-organic frameworks for separation of hydrocarbon mixtures, Energy Environ. Sci. 9 (2016) 3612–3641.

[15] L. Li, R.-B. Lin, R. Krishna, H. Li, S. Xiang, H. Wu, J. Li, W. Zhou, B. Chen, Ethane/ethylene separation in a metal-organic framework with iron-peroxo sites, Science 362 (2018) 443–446, https://doi.org/10.1126/science.aat0586.

[16] R.-B. Lin, L. Li, H.-L. Zhou, H. Wu, C. He, S. Li, R. Krishna, J. Li, W. Zhou, B. Chen, Molecular sieving of ethylene from ethane using a rigid metal-organic framework, Nature Mater. 17 (2018) 1128–1133, https://doi.org/10.1038/s41563-018-0206-2.

[17] Z. Bao, J. Wang, Z. Zhang, H. Xing, Q. Yang, Y. Yang, H. Wu, R. Krishna, W. Zhou, B. Chen, Q. Ren, Molecular sieving of ethane from ethylene through the molecular cross-section size differentiation in gallate-based metal-organic frameworks, Angew. Chem. Int. Ed. 57 (2018) 16020–16025, https://doi.org/10.1002/anie.201808716.

[18] L. Li, R. Krishna, Y. Wang, J. Yang, X. Wang, J. Li, Exploiting the gate opening effect in a flexible MOF for selective adsorption of propyne from C1/C2/C3 hydrocarbons, J. Mater. Chem. A 4 (2016) 751–755.

[19] E.D. Bloch, W.L. Queen, R. Krishna, J.M. Zadrozny, C.M. Brown, J.R. Long, Hydrocarbon separations in a metal-organic framework with open iron(II) coordination sites, Science 335 (2012) 1606–1610.

[20] L. Li, H.-M. Wen, C. He, R.-B. Lin, R. Krishna, H. Wu, W. Zhou, J. Li, B. Li, B. Chen, A metal-organic framework with suitable pore size and specific functional site for removal of trace propyne from propylene, Angew. Chem. Int. Ed. 57 (2018) 15183–15188, https://doi.org/10.1002/anie.201809869.

[21] W. Zhang, D. Banerjee, J. Liu, H.T. Schaef, J.V. Crum, C.A. Fernandez, R.K. Kukkadapu, Z. Nie, S.K. Nune, R.K. Motkuri, K.W. Chapman, M.H. Engelhard, J.C. Hayes, K.L. Silvers, R. Krishna, B.P. McGrail, J. Liu, P.K. Thallapally, Redox-active metal-organic composites for highly selective oxygen separation applications, Adv. Mater. 28 (2016) 3572–3577.

[22] R. Krishna, A Maxwell-Stefan-Glueckauf description of transient mixture uptake in microporous adsorbents, Sep. Purif. Technol. 191 (2018) 392–399, https://doi.org/10.1016/j.seppur.2017.09.057.

[23] S.J. Bhadra, S. Farooq, Separation of methanenitrogen mixture by pressure swing adsorption for natural gas upgrading, Ind. Eng. Chem. Res. 50 (2011) 14030–14045.

[24] R. Krishna, Diffusing uphill with James Clerk Maxwell and Josef Stefan, Chem. Eng. Sci. 195 (2019) 851–880, https://doi.org/10.1016/j.ces.2018.10.032.

[25] R. Krishna, Separating mixtures by exploiting molecular packing effects in microporous materials, Phys. Chem. Chem. Phys. 17 (2015) 39–59.

[26] A. Torres-Knoop, R. Krishna, D. Dubbeldam, Separating xylene isomers by commensurate stacking of p-xylene within channels of MAF-X8, Angew. Chem. Int. Ed. 53 (2014) 7774–7778.

[27] J.W. Yoon, J.S. Lee, G.W. Piburn, K.H. Cho, K. Jeon, H.-K. Lim, H. Kim, C.-H. Jun, S.M. Humphrey, R. Krishna, J.-S. Chang, Highly selective adsorption of p-Xylene over other C8 aromatic hydrocarbons by Co-CUK-1: a combined experimental and theoretical assessment, Dalton Trans. 46 (2017) 16096–16101, https://doi.org/10.1039/C7DT03304D.

[28] S. Mukherjee, B. Joarder, A.V. Desai, B. Manna, R. Krishna, S.K. Ghosh, Exploiting framework flexibility of a metal-organic framework for selective adsorption of styrene over ethylbenzene, Inorg. Chem. 54 (2015) 4403–4408.

[29] A. Torres-Knoop, J. Heinen, R. Krishna, D. Dubbeldam, Entropic separation of styrene/ethylbenzene mixtures by exploitation of subtle differences in molecular configurations in ordered crystalline nanoporous adsorbents, Langmuir 31 (2015) 3771–3778.

[30] D. Dubbeldam, R. Krishna, S. Calero, A.Ö. Yazaydın, Computer-assisted screening of ordered crystalline nanoporous adsorbents for separation of alkane isomers, Angew. Chem. Int. Ed. 51 (2012) 11867–11871.

[31] Z.R. Herm, B.M. Wiers, J.M. Van Baten, M.R. Hudson, P. Zajdel, C.M. Brown, N. Maschiocchi, R. Krishna, J.R. Long, Separation of hexane isomers in a metal-organic framework with triangular channels, Science 340 (2013) 960–964.

[32] R. Krishna, B. Smit, S. Calero, Entropy effects during sorption of alkanes in zeolites, Chem. Soc. Rev. 31 (2002) 185–194.

[33] R.K. Motkuri, P.K. Thallapally, H.V.R. Annapureddy, L. Dang, R. Krishna, S.K. Nune, C.A. Fernandes, J. Liu, B.P. McGrail, Separation of polar compounds using a flexible metal-organic framework, Chem. Commun. 51 (2015) 8421–8424.

[34] R. Krishna, J.M. van Baten, Separating n-alkane mixtures by exploiting differences

in the adsorption capacity within cages of CHA, AFX and ERI zeolites, Sep. Purif. Technol. 60 (2008) 315–320.
[35] R. Krishna, J.M. van Baten, Entropy-based separation of linear chain molecules by exploiting differences in the saturation capacities in cage-type zeolites, Sep. Purif. Technol. 76 (2011) 325–330.
[36] T. Remy, J.C. Saint-Remi, R. Singh, P.A. Webley, G.V. Baron, J.F.M. Denayer, Adsorption and separation of C1–C8 alcohols on SAPO-34, J. Phys. Chem. C 115 (2011) 8117–8125.
[37] A.L. Myers, J.M. Prausnitz, Thermodynamics of mixed gas adsorption, A.I.Ch.E.J. 11 (1965) 121–130.
[38] K.S. Walton, D.S. Sholl, predicting multicomponent adsorption: 50 years of the ideal adsorbed solution theory, A.I.Ch.E.J. 61 (2015) 2757–2762.
[39] R. Krishna, J.M. van Baten, R. Baur, Highlighting the origins and consequences of thermodynamic nonidealities in mixture separations using zeolites and metal-organic frameworks, Microporous Mesoporous Mater. 267 (2018) 274–292, https://doi.org/10.1016/j.micromeso.2018.03.013.
[40] R. Krishna, J.M. Van Baten, Investigating the non-idealities in adsorption of CO_2-bearing mixtures in cation-exchanged zeolites, Sep. Purif. Technol. 206 (2018) 208–217, https://doi.org/10.1016/j.seppur.2018.06.009.
[41] R. Krishna, The Maxwell-Stefan description of mixture diffusion in nanoporous crystalline materials, Microporous Mesoporous Mater. 185 (2014) 30–50.
[42] R. Krishna, Tracing the origins of transient overshoots for binary mixture diffusion in microporous crystalline materials, Phys. Chem. Chem. Phys. 18 (2016) 15482–15495.
[43] T.R.C. Van Assche, G.V. Baron, J.F.M. Denayer, An explicit multicomponent adsorption isotherm model: accounting for the size-effect for components with langmuir adsorption behavior, Adsorption 24 (2018) 517–530, https://doi.org/10.1007/s10450-018-9962-1.
[44] R. Krishna, J.M. van Baten, A molecular simulation study of commensurate – incommensurate adsorption of n-alkanes in cobalt formate frameworks, Molecular Simulation 35 (2009) 1098–1104.
[45] M. Dávila, J.L. Riccardo, A.J. Ramirez-Pastor, Exact statistical thermodynamics of alkane binary mixtures in zeolites: new interpretation of the adsorption preference reversal phenomenon from multisite-occupancy theory, Chem. Phys. Lett. 477 (2009) 402–405.
[46] J.M. van Baten, R. Krishna, Entropy effects in adsorption and diffusion of alkane isomers in mordenite: an investigation using CBMC and MD simulations, Microporous Mesoporous Mater. 84 (2005) 179–191.
[47] E. Hu, A.T. Derebe, A. Almansoori, K. Wang, Xylene separation on plate-like SAPO-5 zeolite molecular sieves, Int. Journal. Materials Sci. Eng. 2 (2014) 10–14.
[48] E. Hu, Z. Lai, K. Wang, Adsorption properties of the SAPO-5 molecular sieve, J. Chem. Eng. Data 55 (2010) 3286–3289.
[49] D.D. Rosenfeld, D.M. Barthomeuf, Separation of ortho aromatic isomers by selective adsorption with an aluminophosphate, Exxon Research & Engineering Co., Florham Park, N.J., U.S. Pat., US 4482776, 1984.
[50] R. El Osta, A. Carlin-Sinclair, N. Guillou, R.I. Walton, F. Vermoortele, M. Maes, D. De Vos, F. Millange, Liquid-phase adsorption and separation of xylene isomers by the flexible porous metal – organic framework MIL-53(Fe), Chem. Mater. 24 (2012) 2781–2791.
[51] V. Finsy, H. Verelst, L. Alaerts, D. De Vos, P.A. Jacobs, G.V. Baron, J.F.M. Denayer, Pore-filling-dependent selectivity effects in the vapor-phase separation of xylene isomers on the metal-organic framework MIL-47, J. Am. Chem. Soc. 130 (2008) 7110–7118.
[52] T. Remy, G.V. Baron, J.F.M. Denayer, Modeling the effect of structural changes during dynamic separation processes on MOFs, Langmuir 27 (2011) 13064–13071.
[53] M. Maes, F. Vermoortele, L. Alaerts, S. Couck, C.E.A. Kirschhock, J.F.M. Denayer, D.E. De Vos, Separation of styrene and ethylbenzene on metal-organic frameworks: analogous structures with different adsorption mechanisms, J. Am. Chem. Soc. 132 (2010) 15277–15285.
[54] T. Remy, L. Ma, M. Maes, D.E. De Vos, G.V. Baron, J.F.M. Denayer, Vapor-phase adsorption and separation of ethylbenzene and styrene on the metal – organic frameworks MIL-47 and MIL-53(Al), Ind. Eng. Chem. Res. 51 (2012) 14824–14833.
[55] A. Torres-Knoop, S.R.G. Balestra, R. Krishna, S. Calero, D. Dubbeldam, Entropic separations of mixtures of aromatics by selective face-to-face molecular stacking in one-dimensional channels of metal-organic frameworks and zeolites, ChemPhysChem 16 (2015) 532–535.
[56] A. Torres-Knoop, D. Dubbeldam, Exploiting large-pore metal-organic frameworks for separations through entropic molecular mechanisms, ChemPhysChem 16 (2015) 2046–2067.
[57] S. Azizian, H. Bashiri, A new isotherm for multisite occupancy adsorption of binary gaseous mixtures, Langmuir 25 (2009) 2309–2312.
[58] M.D. Foster, I. Rivin, M.M.J. Treacy, O.D. Friedrichs, A geometric solution to the largest-free-sphere problem in zeolite frameworks, Microporous Mesoporous Mater. 90 (2006) 32–38.
[59] T. Titze, C. Chmelik, J. Kärger, J.M. van Baten, R. Krishna, Uncommon synergy between adsorption and diffusion of hexane isomer mixtures in MFI zeolite induced by configurational entropy effects, J. Phys. Chem. C 118 (2014) 2660–2665.
[60] T. Nitta, T. Shigetomi, M. Kuro-Oka, T. Katayama, An adsorption isotherm of multi-site occupancy model for homogeneous surface, J. Chem. Eng. Japan. 17 (1984) 39–45.

Supplementary Material

Elucidation and Characterization of Entropy Effects in Mixture Separations with Microporous Crystalline Adsorbents

Rajamani Krishna

Van 't Hoff Institute for Molecular Sciences

University of Amsterdam

Science Park 904

1098 XH Amsterdam, The Netherlands

email: r.krishna@contact.uva.nl

Table of Contents

1 Preamble

This Supplementary Material accompanying our article *Elucidation and Characterization of Entropy Effects in Mixture Separations with Microporous Crystalline Adsorbents* provides (a) detailed structural information on all of the zeolites, and MOFs, analyzed and discussed in the article, (b) summary of methodology used for CBMC simulations, (c) detailed derivations of the lattice models for mixture adsorption equilibrium, (d) details of Ideal Adsorbed Solution Theory (IAST) calculations for mixture adsorption equilibria, and (e) input data on isotherm fits used in the lattice, and IAST model calculations.

For ease of reading, this Supplementary Material is written as a stand-alone document; as a consequence, there is some overlap of material with the main manuscript.

2 Structural details of microporous crystalline materials

A wide variety of ordered crystalline microporous materials is used in several applications in separation applications.[1-4] These include zeolites (crystalline aluminosilicates), and metal-organic frameworks (MOFs). The characteristic pore dimensions of these structures are in the *micro*-porous range: $d_p < 2$ nm.

A number of different channel topologies and connectivities are encountered in zeolites, and MOFs; these can be divided into five broad classes;

1. One-dimensional (1D) channels (e.g. AFI, LTL, TON, MTW, Co-BDP, $Fe_2(BDP)_3$, MgMOF-74, NiMOF-74, Zn-MOF-74, MIL-47, MIL-53(Cr), BTP-COF); see Figure 2-1.
2. 1D channels with side pockets (e.g. MOR, FER); see Figure 2-2.
3. Intersecting channels (e.g. MFI, ISV, BEA, Zn(bdc)dabco, Co(bdc)dabco); see Figure 2-3
4. Cages separated by narrow windows (e.g. LTA (all-silica), CHA, DDR, ERI, TSC); see Figure 2-4.
5. Cavities with large windows (e.g. FAU (all-silica), IRMOF-1, CuBTC, MOF-177); see Figure 2-5.

The crystallographic data are available on the zeolite atlas website of the International Zeolite Association (IZA).[5, 6] Further details on the structure, landscape, pore dimensions of a very wide variety of micro-porous materials are available in the published literature.[7-14] Table 6-1, Table 2-2, Table 2-3, and Table 2-4 provide some salient structural information on various zeolites and MOFs of interest.

2.1 List of Tables for Structural details of microporous crystalline materials

Table 2-1. Salient structural information on zeolites.

Structure	Topology	Fractional pore volume, ϕ	Pore volume/ cm^3/g	Framework density/ kg/m^3
AFI	12-ring 1D channels of 7.3 Å size	0.274	0.159	1730
BEA	Intersecting channels of two sizes: 12-ring of 6.1 Å - 6.8 Å and 10-ring of 5.6 Å – 6.7 Å	0.408	0.271	1509
CHA	316 $Å^3$ cages separated by 3.77 Å × 4.23 Å size windows	0.382	0.264	1444
DDR	277.8 $Å^3$ cages separated by 3.65 Å × 4.37 Å size windows	0.245	0.139	1760
ERI	408 $Å^3$ cages separated by 3.8 Å – 4.9 Å size windows	0.363	0.228	1595
FAU (all silica)	790 $Å^3$ cages separated by 7.4 Å size windows	0.439	0.328	1338
FER	10-ring 1D main channels of 4.2 Å -5.4 Å size, connected with 8-ring side pockets of 3.5 Å -4.8 Å size	0.283	0.160	1772
ISV	Intersecting channels of two sizes: 12-ring of 6.1 Å -6.5 Å and 12-ring of 5.9 Å - 6.6 Å	0.426	0.278	1533
LTL	12-ring 1D channels of 7.1 Å size	0.277	0.170	1627
LTA (all silica)	743 $Å^3$ cages separated by 4.11 Å × 4.47 Å size windows	0.399	0.310	1285
MFI	10-ring intersecting channels of 5.4 Å – 5.5 Å and 5.4 Å – 5.6 Å size	0.297	0.165	1796
MOR	12-ring 1D main channels of 6.5 Å -7 Å size, connected with 8-ring side pockets of 2.6 Å -5.7 Å size	0.285	0.166	1715
MTW	12-ring 1D channels of 5.6 Å -6 Å size	0.215	0.111	1935
TON	10-ring 1D channels of 4.6 Å -5.7 Å size	0.190	0.097	1969

Table 2-2. Pore volumes, surface areas, and characteristic (Delaunary) dimenions for zeolites

Structure	**Pore volume** / $cm^3\ g^{-1}$	**Surface area** / $m^2\ g^{-1}$	**Delaunay diameter**/ Å
MFI	0.165	487.2	5.16
ISV	0.278	911.4	5.96
BEA	0.271	922.7	5.87
LTL	0.170	520.6	7.26
MOR	0.166	416.7	7.47
FER	0.160	402.5	6.44
FAU (all silica)	0.328	1086	4.65
LTA (all silica)	0.310	896	7.37
TSC	0.344	829	
CHA	0.264	757.5	3.98
ERI	0.228	635.3	4.10
DDR	0.139	350	4.02
AFX	0.246	674.5	3.77

Table 2-3. Salient structural information on MOFs, ZIFs, and COFs.

Structure	Topology	Fractional pore volume, ϕ	Pore volume/ cm^3/g	Framework density/ kg/m^3
CuBTC	Large cages are inter-connected by 9 Å windows of square cross-section. The large cages are also connected to tetrahedral-shaped pockets of ca. 6 Å size through triangular-shaped windows of 4.6 Å size	0.759	0.863	879
IRMOF-1	Two alternating, inter-connected, cavities of 10.9 Å and 14.3 Å with window size of 8 Å.	0.812	1.369	593
Zn(bdc)dabco	There exist two types of intersecting channels of about 7.5 Å × 7.5 Å along the x-axis and channels of 3.8 Å × 4.7 Å along y and z axes.	0.662	0.801	826
Co(bdc)dabco	There exist two types of intersecting channels of about 7.6 Å × 7.6 Å along the x-axis and channels of 3.7 Å × 5.1 Å along y and z axes.	0.648	0.796	814
MOF-177	Six diamond-shaped channels (upper) with diameter of 10.8 Å surround a pore containing eclipsed BTB^{3-} moieties.	0.840	1.968	427
Co(BDP)	1D square-shaped channels of 10 Å	0.67	0.927	721
MgMOF-74	1D hexagonal-shaped channels of 11 Å	0.708	0.782	905
NiMOF-74	1D hexagonal-shaped channels of 11 Å	0.695	0.582	1193
CoMOF-74	1D hexagonal-shaped channels of 11 Å	0.707	0.599	1180
ZnMOF-74	1D hexagonal-shaped channels of 11 Å	0.709	0.582	1219
FeMOF-74	1D hexagonal-shaped channels of 11 Å	0.705	0.626	1126
MIL-47	1D diamond-shaped channels of 8.5 Å	0.608	0.606	1004
MIL-53 (Cr)-lp	1D lozenge-shaped channels of 8.5 Å	0.539	0.518	1041

Table 2-4. Pore volumes, surface areas, and characteristic (Delaunary) dimensions for MOFs, ZIFs.

Structure	**Pore volume** / $cm^3\ g^{-1}$	**Surface area** / $m^2\ g^{-1}$	**Delaunay diameter**/ Å
IRMOF1	1.369	3522.2	7.38
CuBTC	0.848	2097.0	6.23
MIL47	0.606	1472.8	8.03
MIL53(Cr)-lp	0.518	1280.5	7.40
CoFA	0.139		3.41
MnFA	0.190		3.66
Zn(tbip)	0.118		3.96
Zn(BDC)dabco	0.801	2022.5	8.32
Co(BDC)dabco	0.796		8.35
ZIF-68	0.439	1066.0	7.52
MOF-177	1.968	4781.0	10.1
ZnMOF-74	0.582	1176.0	9.49
MgMOF-74	0.782	1640.0	10.66
NiMOF-74	0.582	1239.0	9.80
CoMOF-74	0.599	1274.0	9.52
FeMOF-74	0.626	1277.3	11.1
Co(BDP)	0.927	2148.8	10
BeBTB	1.908	4706	
CuBTT (blocked)	0.709	1564.6	9.99
$Fe_2(BDP)_3$		1230	

2.2 List of Figures for Structural details of microporous crystalline materials

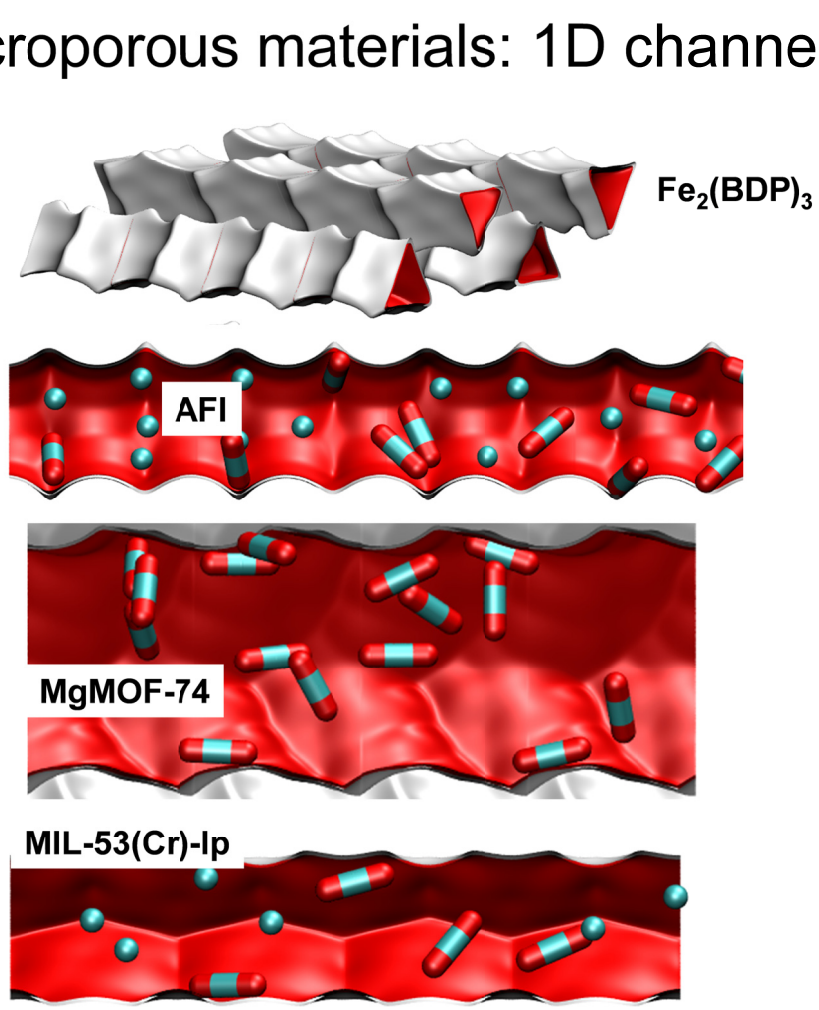

Figure 2-1. Examples of one-dimensional (1D) channel structures: AFI, MgMOF-74, and MIL-53(Cr)-lp, BTP-COF, and $Fe_2(BDP)_3$.

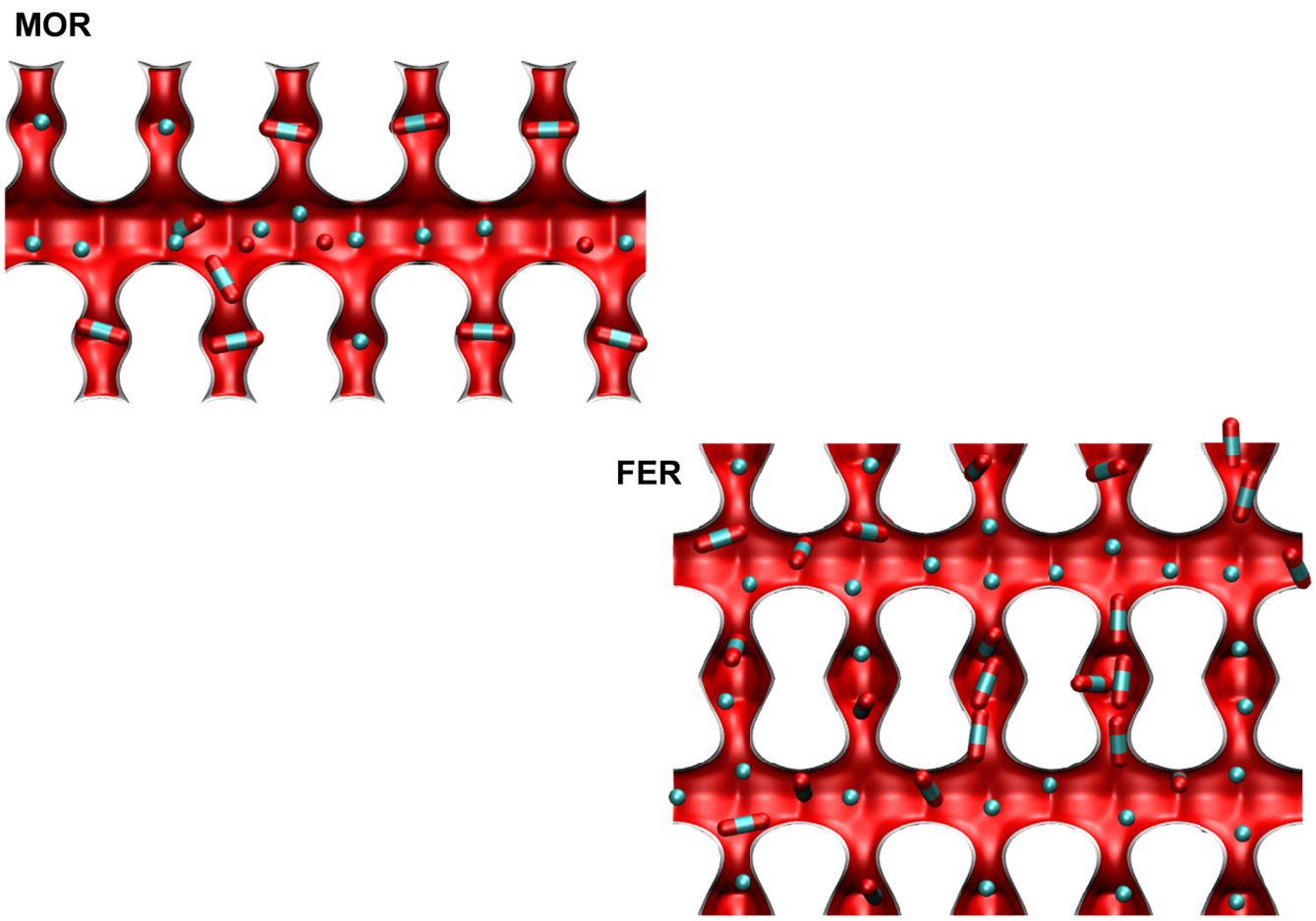

Figure 2-2. Examples of 1D channel structures with side pockets: MOR and FER.

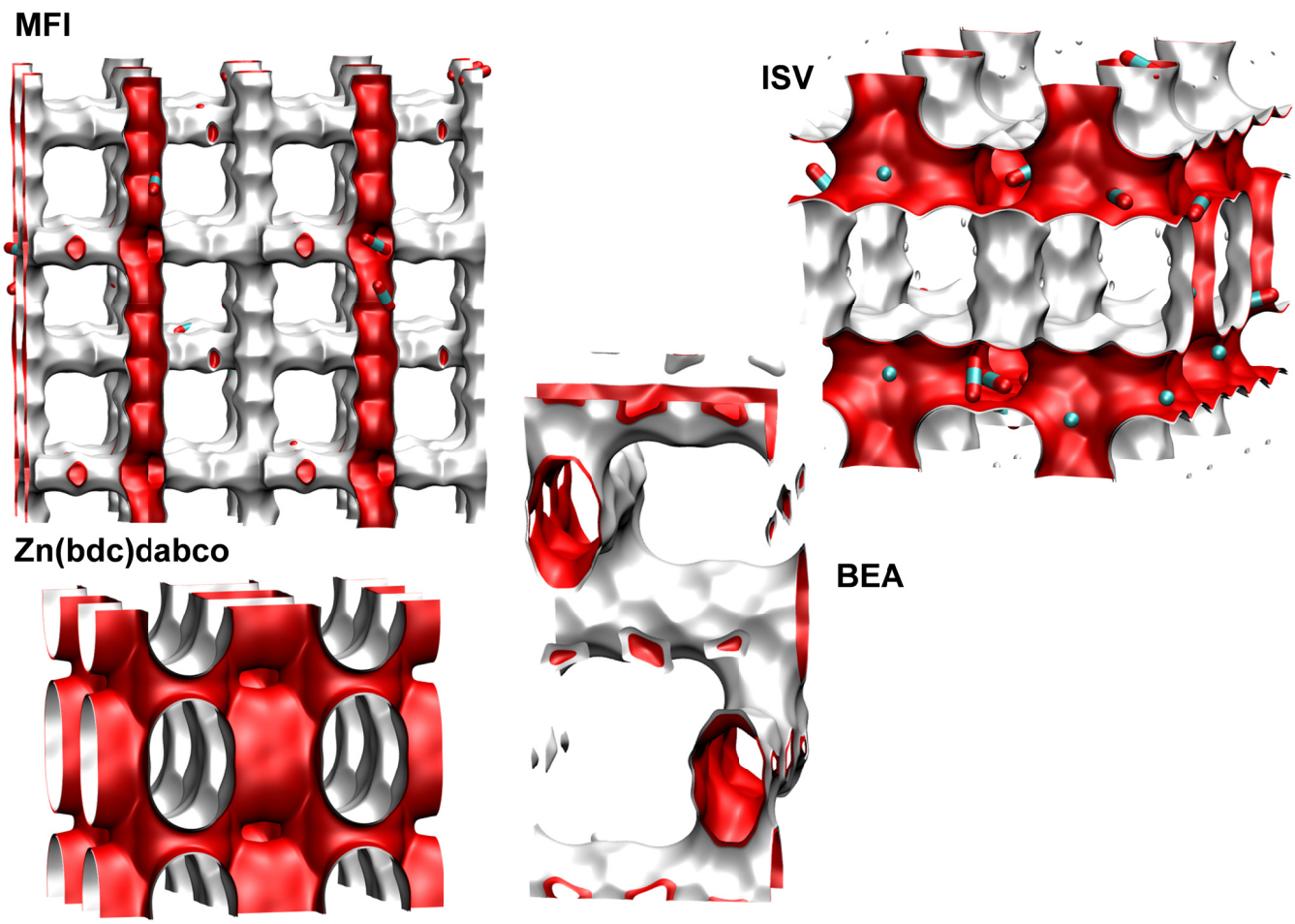

Figure 2-3. Examples of structures consisting of intersecting channels: MFI, ISV, BEA, and Zn(bdc)dabco.

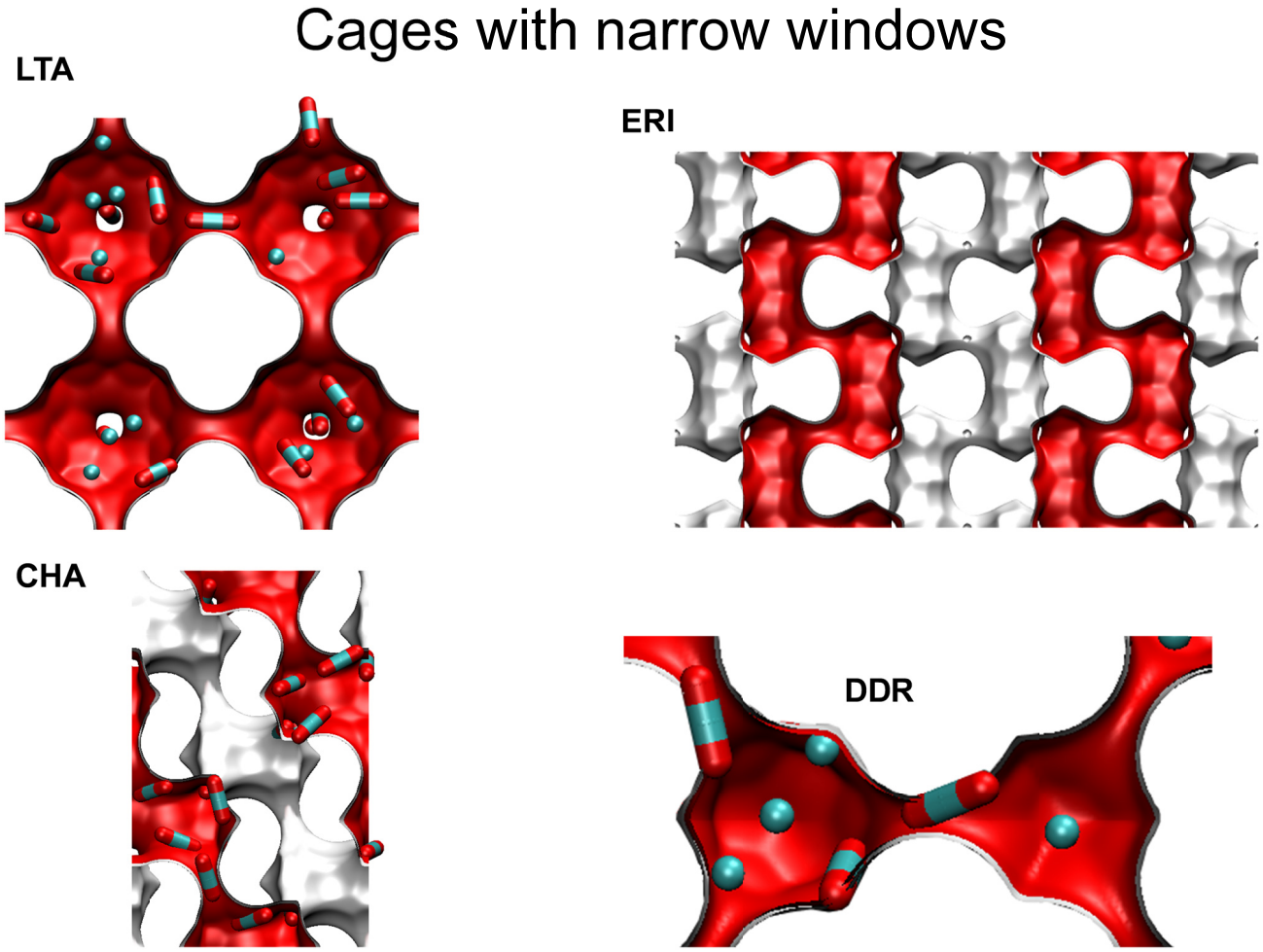

Figure 2-4. Structures consisting of cages separated by narrow windows: LTA, CHA, DDR, and ERI.

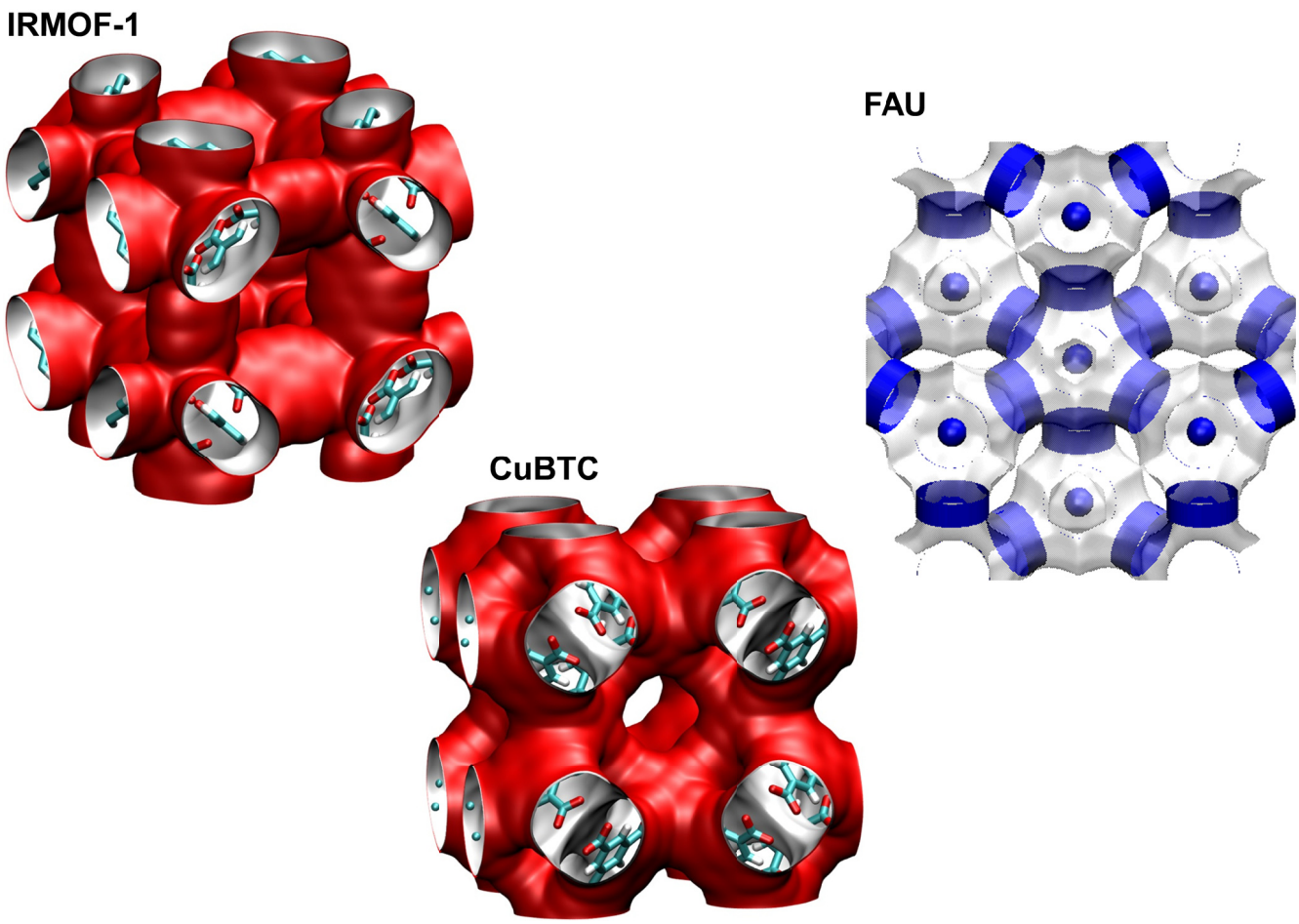

Figure 2-5. "Open" structures that consist of cages separated by large windows: IRMOF-1, CuBTC, and FAU.

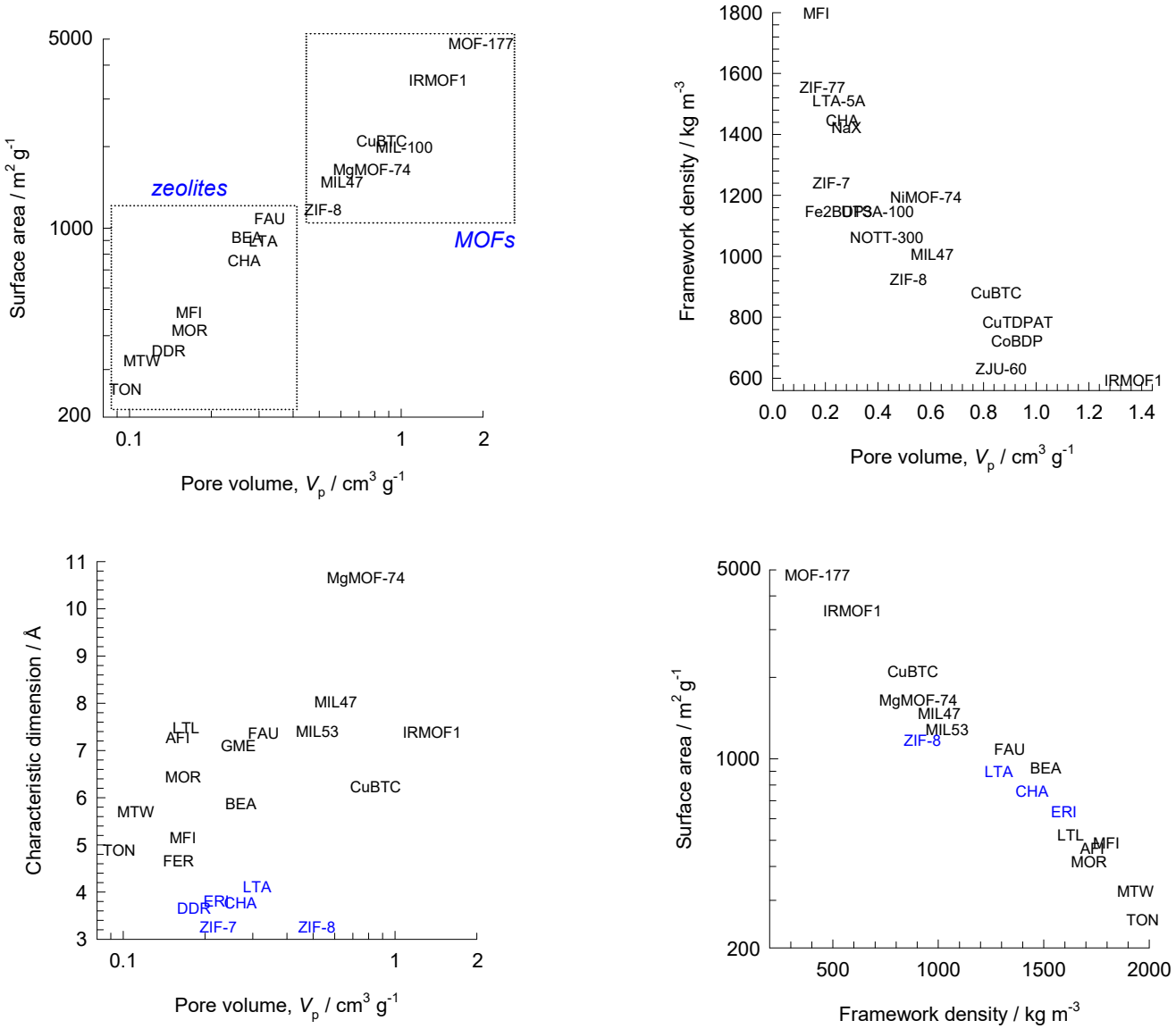

Figure 2-6. Comparison of surface area, pore volumes, framework densities, fractional pore volumes, and characteristic dimensions of some representative zeolites, MOFs and ZIFs.

3 Configurational-Bias Monte Carlo Simulation Methodology

The simulation methodologies and the force field information used are the same as detailed in the Supplementary Materials accompanying our earlier publications.[2, 3, 7, 9, 13, 15, 16] A short summary is provided hereunder.

3.1 Zeolites (all silica)

CH_4 molecules are described with a united atom model, in which each molecule is treated as a single interaction center.[17]The interaction between adsorbed molecules is described with Lennard-Jones terms. The Lennard-Jones parameters for CH_4-zeolite interactions are taken from Dubbeldam et al.[18]. The force fields for Ne and Ar are taken from the paper by Skoulidas and Sholl[19]. The force field for Kr is from Talu and Myers.[20] The Lennard-Jones parameters for CO_2-zeolite are essentially those of Makrodimitris et al.[21]; see also García-Pérez et al.[22] For simulations with linear alkanes with two or more C atoms, the beads in the chain are connected by harmonic bonding potentials. A harmonic cosine bending potential models the bond bending between three neighboring beads, a Ryckaert-Bellemans potential controls the torsion angle. The beads in a chain separated by more than three bonds interact with each other through a Lennard-Jones potential; see schematic in The force fields of Dubbeldam et al.[18] was used for the variety of potentials. The Lennard-Jones potentials are shifted and cut at 12 Å.

The zeolite frameworks were considered to be rigid in all the simulation results reported in the article.

In the CBMC simulations both Lennard-Jones and Coulombic interactions are taken into consideration; see schematic sketch in Figure 3-2.

3.2 MOFs

The structural information for CuBTC (= $Cu_3(BTC)_2$ with BTC = 1,3,5-benzenetricarboxylate) have been taken from Chui et al.[23] and Yang and Zhong.[24] The crystal structure of Chui et al. [23] includes axial oxygen atoms weakly bonded to the Cu atoms, which correspond to water ligands. Our simulations have been performed on the dry CuBTC with these oxygen atoms removed.

MIL-47 structural data was taken from Alaerts et al.,[25] Finsy et al., [26] and Barthelet et al.[27]

The structural data for MIL-53 (Cr) = $Cr(OH)(O_2C\text{-}C_6H_4\text{-}CO_2)$ was taken from Coombes et al. [28] (the simulations were carried out with the large-pore (-lp) structure).

The metal organic framework structures were considered to be rigid in the simulations. For the atoms in the host metal organic framework, the generic UFF[29] and DREIDING[30] force fields were used. The Lorentz-Berthelot mixing rules were applied for calculating σ and ε/k_B for guest-host interactions.

The adsorbate-adsorbate interactions are the same as those used for zeolites, discussed in the foregoing section.

3.3 Pore volume

The pore volume is determined using a simulation of a single helium molecule at the reference temperature T [31-33]

$$V_{pore} = \frac{1}{m} \int_0^{V_{pore}} \exp\left(-\frac{U(\mathbf{r})}{k_B T} \right) d\mathbf{r} \tag{3-1}$$

where U is the interaction energy between a single helium atom and the framework, and m is the mass of the framework. The pore volume can be readily computed from Monte Carlo sampling using Widom particle insertion.[34] Basically, the average Boltzmann factor associated with the random insertion of a probe molecule is computed. This value is averaged over all generated trial positions. In equation (3-1) the integration is over the entire mass of the sample and yields the value of the accessible pore volume per unit mass of the framework; the units of V_{pore} are m^3/kg, or in more commonly used units mL/(g framework). The volume fraction, ϕ, is then given by V_{pore}/V_{total} where V_{total} is the total volume of the unit cell. Usually, a reference temperature of 298.15 K is chosen in experiment for determination of the helium void volume; this value is also used in the simulations.

The force field for He-He interactions are taken from Table 1 of Talu and Myers.[35] For zeolites the He-O interaction parameters were also taken from this Table 1. We should mention here that the force field for He of Talu and Myers [35] is not the same as that in Skoulidas and Sholl;[19] in particular there are

significant differences in the energy parameter ε/k_B. We had earlier used the Skoulidas force field to simulate diffusion of He in a variety of zeolites.[13] For determination of the pore volume fraction we have switched to the Talu and Myers force field parameters that has been tuned to represent experimental data on pore volumes in MFI.

For MOFs, the interaction between He and the atoms of the MOF structures were then determined using the Lorentz-Berthelot mixing rules. For determination of the pore volumes the Lennard-Jones parameters for interactions of the He probe atoms with cations are also considered

For determination of the accessible pore volumes of FAU, NaX, NaY, TSC, ITQ-29, LTA, LTA-5A and LTA-4A the sodalite cages were blocked and no He probe atoms could enter these cages. Only the supercage volumes are determined for these structures.

3.4 Surface areas

The surface area of various structures were determined using the method described by Düren et al.[36].

3.5 Characteristic dimensions (Delaunay diameters)

In many cases, the characteristic size of the channels or windows of microporous structures are referred to in the article. These data are obtained following the method of Delaunay triangulation, described in the work by Foster et al.[37] These values represent the maximum hard-sphere diameter that can pass through the structure. The values quoted are obtained by substracting the Lennard-Jones sigma parameter of the framework atom.

3.6 CBMC software used and simulation times

The CBMC simulations were carried out using BIGMAC, a code originally developed by T.J.H. Vlugt, Delft. This code was further updated and modified.

Typical simulation times for CBMC simulations are about 1-10 h for determination of the adsorbed phase equilibrium loadings for specified bulk fluid phase compositions.

3.7 List of Figures for Configurational-Bias Monte Carlo Simulation Methodology

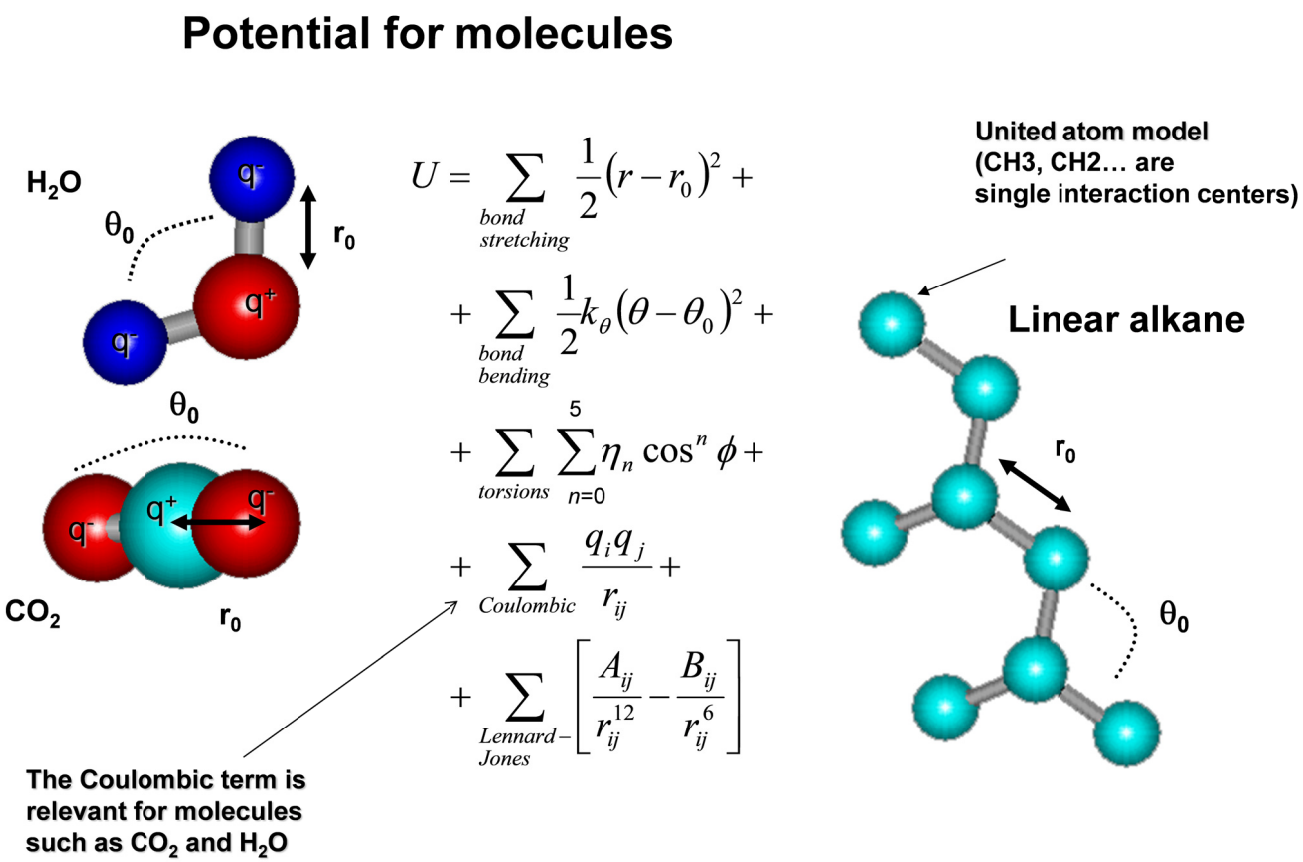

Figure 3-1. Potential for molecules.

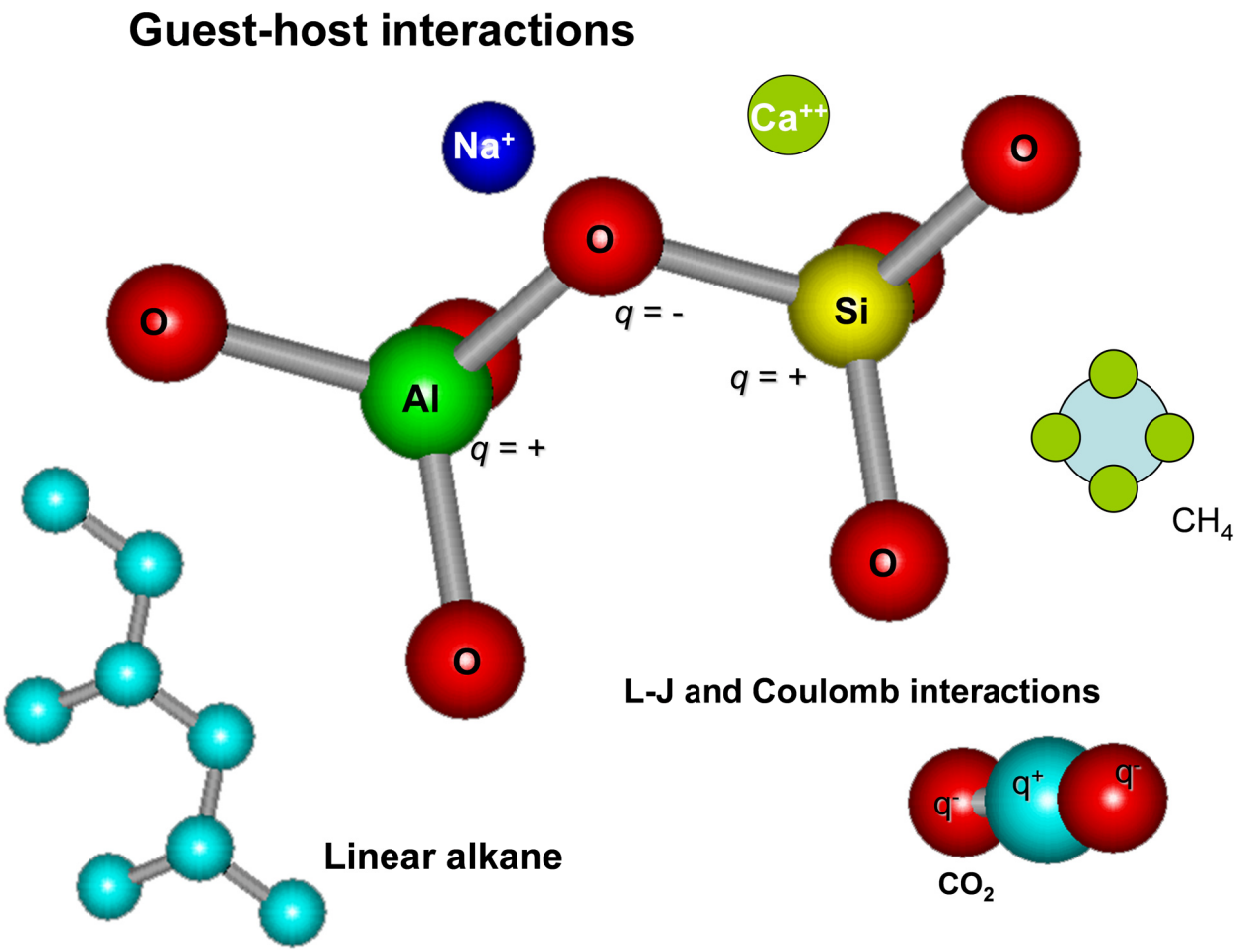

Figure 3-2. Guest-host interactions.

4 The Ideal Adsorbed Solution Theory (IAST)

A brief summary of the IAST theory is provided in order to facilitate comparisons with the statistical thermodynamics based models to be discussed later in this document.

4.1 Brief outline of theory

Within microporous crystalline materials, the guest molecules exist in the adsorbed phase. The Gibbs adsorption equation[38] in differential form is

$$Ad\pi = \sum_{i=1}^{n} q_i d\mu_i \tag{4-1}$$

The quantity A is the surface area per kg of framework, with units of m^2 per kg of the framework of the crystalline material; q_i is the molar loading of component i in the adsorbed phase with units moles per kg of framework; μ_i is the molar chemical potential of component i. The spreading pressure π has the same units as surface tension, i.e. N m^{-1}.

The chemical potential of any component in the adsorbed phase, μ_i, equals that in the bulk fluid phase. If the partial fugacities in the bulk fluid phase are f_i, we have

$$d\mu_i = RTd \ln f_i \tag{4-2}$$

where R is the gas constant (= 8.314 J mol^{-1} K^{-1}).

Briefly, the basic equation of Ideal Adsorbed Solution Theory (IAST) theory of Myers and Prausnitz[39] is the analogue of Raoult's law for vapor-liquid equilibrium, i.e.

$$f_i = P_i^0 x_i; \quad i = 1,2,...n \tag{4-3}$$

where x_i is the mole fraction in the adsorbed phase

$$x_i = \frac{q_i}{q_1 + q_2 + ...q_n} \tag{4-4}$$

and P_i^0 is the pressure for sorption of every component *i*, which yields the same spreading pressure, π for each of the pure components, as that for the mixture:

$$\frac{\pi A}{RT} = \int_0^{P_1^0} \frac{q_1^0(f)}{f} df = \int_0^{P_2^0} \frac{q_2^0(f)}{f} df = \int_0^{P_3^0} \frac{q_3^0(f)}{f} df = ... \tag{4-5}$$

where $q_i^0(f)$ is the *pure* component adsorption isotherm. The units of $\frac{\pi A}{RT}$, also called the adsorption potential,[40] are mol kg^{-1}.

The unary isotherm may be described by say the 1-site Langmuir isotherm

$$q^0(f) = q_{sat} \frac{bf}{1+bf}; \quad \theta = \frac{bf}{1+bf} \tag{4-6}$$

where we define the fractional *occupancy* of the adsorbate molecules, $\theta = q^0(f)/q_{sat}$. The superscript 0 is used to emphasize that $q^0(f)$ relates the *pure component* loading to the bulk fluid fugacity. More generally, the unary isotherms may need to be described by, say, the dual-Langmuir-Freundlich model

$$q^0(f) = q_{A,sat} \frac{b_A f^{\nu A}}{1+b_A f^{\nu A}} + q_{B,sat} \frac{b_B f^{\nu B}}{1+b_B f^{\nu B}} \tag{4-7}$$

or the 3-site Langmuir-Freundlich model:

$$q^0 = q_{A,sat} \frac{b_A f^{\nu_A}}{1+b_A f^{\nu_A}} + q_{B,sat} \frac{b_B f^{\nu_B}}{1+b_B f^{\nu_B}} + q_{C,sat} \frac{b_C f^{\nu_C}}{1+b_C f^{\nu_C}} \tag{4-8}$$

Each of the integrals in Equation (4-5) can be evaluated analytically. For the 3-site Langmuir-Freundlich isotherm, for example, the integration yields for component *i*,

$$\begin{aligned} \int_{f=0}^{P_i^0} \frac{q^0(f)}{f} df &= \frac{q_{A,sat}}{\nu_A} \ln\left(1+b_A\left(P_i^0\right)^{\nu_A}\right) + \frac{q_{B,sat}}{\nu_B} \ln\left(1+b_B\left(P_i^0\right)^{\nu_B}\right) + \frac{q_{C,sat}}{\nu_C} \ln\left(1+b_C\left(P_i^0\right)^{\nu_C}\right) \\ \int_{f=0}^{P_i^0} \frac{q^0(f)}{f} df &= \frac{q_{A,sat}}{\nu_A} \ln\left(1+b_A\left(\frac{f_i}{x_i}\right)^{\nu_A}\right) + \frac{q_{B,sat}}{\nu_B} \ln\left(1+b_B\left(\frac{f_i}{x_i}\right)^{\nu_B}\right) + \frac{q_{C,sat}}{\nu_C} \ln\left(1+b_C\left(\frac{f_i}{x_i}\right)^{\nu_C}\right) \end{aligned} \tag{4-9}$$

The right hand side of equation (4-9) is a function of P_i^0. For multicomponent mixture adsorption, each of the equalities on the right hand side of Equation (4-5) must be satisfied. These constraints may

be solved using a suitable equation solver, to yield the set of values of P_1^0, P_2^0, P_3^0,.. P_n^0, all of which satisfy Equation (4-5). The corresponding values of the integrals using these as upper limits of integration must yield the same value of $\frac{\pi A}{RT}$ for each component; this ensures that the obtained solution is the correct one.

The adsorbed phase mole fractions x_i are then determined from

$$x_i = \frac{f_i}{P_i^0}; \quad i = 1,2,...n \tag{4-10}$$

A key assumption of the IAST is that the enthalpies and surface areas of the adsorbed molecules do not change upon mixing. If the total mixture loading is q_t, the area covered by the adsorbed mixture is $\frac{A}{q_t}$ with units of m^2 (mol mixture)$^{-1}$. Therefore, the assumption of no surface area change due to mixture adsorption translates as $\frac{A}{q_t} = \frac{Ax_1}{q_1^0\left(P_1^0\right)} + \frac{Ax_2}{q_2^0\left(P_2^0\right)} + \cdots \frac{Ax_n}{q_n^0\left(P_n^0\right)}$; the total mixture loading is q_t is calculated from

$$q_t = q_1 + q_2 ... + q_n = \frac{1}{\frac{x_1}{q_1^0(P_1^0)} + \frac{x_2}{q_2^0(P_2^0)} + ... + \frac{x_n}{q_n^0(P_n^0)}} \tag{4-11}$$

in which $q_1^0(P_1^0)$, $q_2^0(P_2^0)$,… $q_n^0(P_n^0)$ are determined from the unary isotherm fits, using the sorption pressures for each component P_1^0, P_2^0, P_3^0,.. P_n^0 that are available from the solutions to equations Equations (4-5), and (4-9).

The entire set of equations (4-3) to (4-11) need to be solved numerically to obtain the loadings, q_i of the individual components in the mixture. In all of the calculations presented in this article, the set of equations were solved using the Given-Find solve block of MathCad 15.[41]

4.2 IAST model: 1-site Langmuir isotherms

The IAST procedure for will be explained in a step-by-step manner for binary mixture adsorption in which the unary isotherms are described by the 1-site Langmuir model. The objective is to determine the molar loadings, q_1, and q_2, in the adsorbed phase.

Performing the integration of Equation (4-5) results in an expression relating the sorption pressures P_i^0 of the two species

$$\begin{aligned}&\frac{\pi A}{RT} = q_{1,sat}\ln\left(1+b_1P_1^0\right) = q_{2,sat}\ln\left(1+b_2P_2^0\right)\\ &b_1P_1^0 = \exp\left(\frac{\pi A}{q_{1,sat}RT}\right)-1;\quad b_2P_2^0 = \exp\left(\frac{\pi A}{q_{2,sat}RT}\right)-1\end{aligned} \tag{4-12}$$

The adsorbed phase mole fractions of component 1, and component 2 are given by equation (4-10)

$$x_1 = \frac{f_1}{P_1^0};\quad x_2 = 1-x_1 = \frac{f_2}{P_2^0} \tag{4-13}$$

Since the mole fractions add to unity, we may combine equations (4-12), and (4-13) to obtain a relation in just *one* unknown, x_1:

$$\frac{\pi A}{RT} = q_{1,sat}\ln\left(1+b_1\frac{f_1}{x_1}\right) = q_{2,sat}\ln\left(1+b_2\frac{f_2}{1-x_1}\right) \tag{4-14}$$

Equation (4-14) is a non-linear equation

$$q_{1,sat}\ln\left(1+b_1\frac{f_1}{x_1}\right) - q_{2,sat}\ln\left(1+b_2\frac{f_2}{1-x_1}\right) = 0 \tag{4-15}$$

The partial fugacities of the two components in the bulk gas phase are known, and equation (4-15) needs to be solved using a root finder to solve for the unknown, x_1. Once x_1, and $x_2 = 1-x_1$ are determined, the sorption pressures can be calculated:

$$P_1^0 = \frac{f_1}{x_1};\quad P_2^0 = \frac{f_2}{x_2} = \frac{f_2}{1-x_1} \tag{4-16}$$

The total amount adsorbed, $q_t = q_1 + q_2$ can be calculated from

$$q_t = q_1 + q_2 = \frac{1}{\dfrac{x_1}{q_1^0(P_1^0)} + \dfrac{x_2}{q_2^0(P_2^0)}} \tag{4-17}$$

in which $q_1^0(P_1^0)$, and $q_2^0(P_2^0)$ are determined from the Langmuir parameters along with the sorption pressures, determined from equation (4-16). The component loadings, q_1, and q_2 are then determined from $q_1 = q_t x_1; \quad q_2 = q_t(1 - x_1)$.

4.3 IAST model: Langmuir isotherms with equal saturation capacities

For the special case of binary mixture adsorption with equal saturation capacities, $q_{1,sat} = q_{2,sat} = q_{sat}$, the component loadings can be determined explicitly. Equation (4-15) can be solved explicitly to obtain the adsorbed phase mole fractions

$$\frac{x_1}{x_2} = \frac{q_1}{q_2} = \frac{b_1 f_1}{b_2 f_2}; \quad x_1 = \frac{q_1}{q_t} = \frac{b_1 f_1}{b_1 f_1 + b_2 f_2}; \quad x_2 = \frac{q_2}{q_t} = \frac{b_2 f_2}{b_1 f_1 + b_2 f_2} \tag{4-18}$$

Equation (4-12) simplifies to yield

$$\begin{aligned} &\frac{\pi A}{RT} = q_{sat} \ln\left(1 + b_1 P_1^0\right) = q_{sat} \ln\left(1 + b_2 P_2^0\right) \\ &b_1 P_1^0 = b_2 P_2^0 = \exp\left(\frac{\pi A}{q_{sat} RT}\right) - 1 = \exp\left(\frac{\pi A}{q_{sat} RT}\right) - 1 \end{aligned} \tag{4-19}$$

From equation (4-16) we get

$$\begin{aligned} &b_i P_1^0 = \frac{b_1 f_1}{x_1} = b_2 P_2^0 = \frac{b_2 f_2}{x_2} = b_1 f_1 + b_2 f_2 \\ &1 + b_i P_1^0 = 1 + b_2 P_2^0 = 1 + b_1 f_1 + b_2 f_2 \end{aligned} \tag{4-20}$$

Equations (4-17), (4-18), (4-19), and (4-20) yield

$$\begin{aligned} &\frac{q_{sat}}{q_t} = \frac{x_1}{b_1 P_1^0}\left(1 + b_1 P_1^0\right) + \frac{x_2}{b_2 P_2^0}\left(1 + b_2 P_2^0\right) = \frac{1 + b_1 f_1 + b_2 f_2}{b_1 f_1 + b_2 f_2} \\ &q_t = q_{sat} \frac{b_1 f_1 + b_2 f_2}{1 + b_1 f_1 + b_2 f_{22}} \end{aligned} \tag{4-21}$$

Combining equations (4-18), and (4-21) we obtain the following explicit expressions for the component loadings, and fractional occupancies

$$\theta_1 = \frac{q_1}{q_{sat}} = \frac{b_1 f_1}{1 + b_1 f_1 + b_2 f_2}; \quad \theta_2 = \frac{q_2}{q_{sat}} = \frac{b_2 f_2}{1 + b_1 f_1 + b_2 f_2} \tag{4-22}$$

Equation (4-22) is commonly referred to as the mixed-gas Langmuir model, or extended Langmuir model. Rao and Sircar[42] show that the mixed-gas Langmuir model described by Equation (4-22) passes the thermodynamic consistency test only when the saturation capacities equal each other, i.e. $q_{1,sat} = q_{2,sat}$.

From Equation (4-22), it also follows that the adsorbed phase mole fraction is

$$x_1 = \frac{1}{1 + \frac{b_2 f_2}{b_1 f_1}} \tag{4-23}$$

5 Multi-site Occupancy Model of Nitta et al. (1984)

Nitta et al.[43] developed an extension of the Langmuir model for multi-site occupancy. For unary adsorption of a species that occupies *k* sites, out of a total of *M* sites per unit cell:

$$bf = \frac{\theta}{(1-\theta)^k}; \quad \theta = \frac{q}{q_{sat}}; \quad q_{sat} = \frac{M}{k} \tag{5-1}$$

In equation (5-1), *f* is the bulk fluid phase fugacity with units of Pa, and the binding constant *b* has the units of Pa^{-1}. It is to be noted that for $k \neq 1$, loadings are not explicitly calculable from the bulk fluid phase fugacity, *f*; the unary isotherms need to be calculated using a root finder. It is also to be noted that there is no requirement that k be an integer quantity.

For adsorption of a binary (*k*, *l*) mixture of species that occupy, *k* sites and *l* sites, respectively:

$$\begin{aligned} b_k f_k &= \frac{q_k}{q_{k,sat}} = \frac{\theta_k}{(1-\theta_k-\theta_l)^k}; \quad q_{k,sat} = \frac{M}{k} \\ b_l f_l &= \frac{q_l}{q_{l,sat}} = \frac{\theta_l}{(1-\theta_k-\theta_l)^l}; \quad q_{l,sat} = \frac{M}{l} \end{aligned} \tag{5-2}$$

In equation (5-2), f_k and f_l are the partial fluid phase fugacities in the bulk fluid phase, with units of Pa, and the binding constant b_k and b_l have the units of Pa^{-1}. An equation solver is required to determine the component loadings q_k, q_l for specified f_k and f_l are in the bulk fluid phase. If *k* = l = 1, we recover Equation (4-22). Equation (5-2) is thermodynamically consistent, because the saturation capacities of the two components are not independent:

$$kq_{k,sat} = lq_{l,sat} = M \tag{5-3}$$

For unary isotherms described by equation (5-1), the IAST model gives numerical results that are identical to those determined by solving the set of equations (5-2) with the Given-Find solve block of MathCad 15.[41] Indeed, there is no computational benefit to using the Nitta model over the IAST model. Both approaches require solution to a set of implicit simultaneous equations.

The extension of the Nitta model to multi-region adsorption is developed by Bai et al.[44]

6 Statistical thermodynamics and lattice models

6.1 1D Lattice model for binary mixture adsorption

The adsorption of a binary mixture of rigid *k*-mers and rigid *l*-mers on one-dimensional (1D) lattices is described by Dávila et al.[45] The adsorbent surface is modeled by a 1D lattice of M sites ($M \to \infty$); see schematic in Figure 6-1. The *k*-mers are assumed to be composed by k identical units in a linear array with constant bond length equal to the lattice dimension. The *k*-mers can only adsorb flat on the surface occupying k contiguous lattice sites. Analogously, the *l*-mers are assumed to be composed by l identical units in a linear array with constant bond length equal to the lattice constant a. The *l*-mers can only adsorb flat on the surface occupying l contiguous lattice sites. For adsorption of methane/ethane mixtures, for example, k = 1, l =2. Furthermore, double site occupancy is not disallowed and only mono-layer adsorption is considered. Also, there are no adsorbate-adsorbate interactions. Since different particles do not interact with each other, all configurations of N_k *k*-mers and N_l *l*-mers on M sites are equally probable.

Dávila et al.[45] derive the following expression for the number of arrangements of N_k *k*-mers and N_l *l*-mers on M sites:

$$W = \frac{\left(M-(k-1)N_k-(l-1)N_l\right)!}{\left(M-kN_k-lN_l\right)!\,N_k!\,N_l!} \tag{6-1}$$

Of particular interest is the calculation of the entropy contribution to binary mixture adsorption $S = k_B \ln(W)$; this can be calculated using the Stirling's approximation $\ln(M!) = M\ln M - M$. The expression for the dimensionless entropy per site for a 1D lattice is

$$\begin{aligned}\frac{S}{k_B M} &= \left(1-\frac{(k-1)}{k}\frac{kN_k}{M}-\frac{(l-1)}{l}\frac{lN_l}{M}\right)\ln\left(1-\frac{(k-1)}{k}\frac{kN_k}{M}-\frac{(l-1)}{l}\frac{lN_l}{M}\right)\\ &-\left(1-\frac{kN_k}{M}-\frac{lN_l}{M}\right)\ln\left(1-\frac{kN_k}{M}-\frac{lN_l}{M}\right)-\frac{N_k}{M}\ln\frac{N_k}{M}-\frac{N_l}{M}\ln\frac{N_l}{M}\end{aligned} \tag{6-2}$$

Defining, the fractional occupancies $\theta_k = \frac{kN_k}{M}; \theta_l = \frac{lN_l}{M}$, we obtain the following expression for the dimensionless entropy per site

$$\begin{aligned}
&\frac{S}{k_B M} = \left(1-\frac{(k-1)}{k}\theta_k - \frac{(l-1)}{l}\theta_l\right)\ln\left(1-\frac{(k-1)}{k}\theta_k - \frac{(l-1)}{l}\theta_l\right) \\
&-\left(1-\theta_k-\theta_l\right)\ln\left(1-\theta_k-\theta_l\right) - \frac{\theta_k}{k}\ln\frac{\theta_k}{k} - \frac{\theta_l}{l}\ln\frac{\theta_l}{l} \\
&\frac{S}{k_B M} = \ln\left[\frac{\left(1-\frac{(k-1)}{k}\theta_k - \frac{(l-1)}{l}\theta_l\right)^{\left(1-\frac{(k-1)}{k}\theta_k - \frac{(l-1)}{l}\theta_l\right)}}{\left(1-\theta_k-\theta_l\right)^{(1-\theta_k-\theta_l)}\left(\frac{\theta_k}{k}\right)^{\frac{\theta_k}{k}}\left(\frac{\theta_l}{l}\right)^{\frac{\theta_l}{l}}}\right]
\end{aligned} \tag{6-3}$$

By defining the mole fraction of k in the adsorbed phase, $x_k = \frac{N_k}{N_k + N_l} = \frac{\theta_k/k}{\theta_{mix}}$ and noting that $N_l = \theta_l/l = (1-x_k)\theta_{mix}$ we can express the dimensionless entropy per site, as a function of the two variables x_k, and $\theta_{mix} = \frac{\theta_k}{k} + \frac{\theta_l}{l} = \frac{N_k + N_l}{M}$:

$$\begin{aligned}
&\frac{S}{k_B M} = \left(1-(k-1)x_k\theta_{mix} - (l-1)(1-x_k)\theta_{mix}\right)\ln\left(1-(k-1)x_k\theta_{mix} - (l-1)(1-x_k)\theta_{mix}\right) \\
&-\left(1-kx_k\theta_{mix} - l(1-x_k)\theta_{mix}\right)\ln\left(1-kx_k\theta_{mix} - l(1-x_k)\theta_{mix}\right) \\
&-\left(x_k\theta_{mix}\right)\ln\left(x_k\theta_{mix}\right) - \left((1-x_k)\theta_{mix}\right)\ln\left((1-x_k)\theta_{mix}\right) \\
&\frac{S}{k_B M} = \ln\left[\frac{\left(1-(k-1)x_k\theta_{mix} - (l-1)(1-x_k)\theta_{mix}\right)^{\left(1-(k-1)x_k\theta_{mix} - (l-1)(1-x_k)\theta_{mix}\right)}}{\left(1-kx_k\theta_{mix} - l(1-x_k)\theta_{mix}\right)^{\left(1-kx_k\theta_{mix} - l(1-x_k)\theta_{mix}\right)}\left(x_k\theta_{mix}\right)^{\left(x_k\theta_{mix}\right)}\left((1-x_k)\theta_{mix}\right)^{\left((1-x_k)\theta_{mix}\right)}}\right]
\end{aligned} \tag{6-4}$$

At any chosen value of total mixture occupancy, θ_{mix}, by setting $\frac{\partial}{\partial x_k}\left(\frac{S}{k_B M}\right) = 0$, we can determine the adsorbed phase mole fraction x_k, that yields a maximum in the $\frac{S}{k_B M}$. The solution thus obtained is in the form of the implicit expression

$$x_k = \frac{1}{1+\frac{1}{\Omega}}; \quad x_l = 1 - x_k \tag{6-5}$$

where an "entropy factor" Ω is defined as

$$\Omega = \frac{\left(1-\frac{(k-1)}{k}\theta_k - \frac{(l-1)}{l}\theta_l\right)^{(l-k)}}{\left(1-\theta_k-\theta_l\right)^{(l-k)}} = \frac{\left(1-(k-1)x_k\theta_{mix} - (l-1)(1-x_k)\theta_{mix}\right)^{(l-k)}}{\left(1-kx_k\theta_{mix} - l(1-x_k)\theta_{mix}\right)^{(l-k)}} \tag{6-6}$$

Equations (6-5) and (6-6) need to be solved simultaneously using a suitable root-finder in order to determine the adsorbed phase composition for a specified value of the mixture occupancy θ_{mix}. It is important to note that the "entropy factor" Ω is a function of the occupancies of *both* components.

It is easy to check that for $k = l$, the adsorbed phase composition $x_k = 0.5$, irrespective of the mixture occupancy; this implies there is no entropic preference for either component. For $k < l$, in the limit of vanishingly low occupancies, we have $\theta_{mix} \to 0; \quad \Omega \to 1; \quad x_k \to 0.5$, and there is no entropic preference for either of the constituent species, because there is not competition for adsorption sites at vanishingly low occupancies. For $k < l$, the adsorbed phase composition x_k increases with increasing θ_{mix}, reaching the limit $\theta_{mix} \to 1; \quad \Omega \to \infty; \quad x_k \to 1$.

The mixture adsorption equilibrium for a 1D lattice is described by a set of two, coupled, equations:

$$\begin{aligned}
&(k-1)\ln\left(1-\frac{(k-1)}{k}\theta_k - \frac{(l-1)}{l}\theta_l\right) + \ln\frac{\theta_k}{k} - k\ln\left(1-\theta_k-\theta_l\right) = \ln\left(b_k f_k\right) \\
&(l-1)\ln\left(1-\frac{(k-1)}{k}\theta_k - \frac{(l-1)}{l}\theta_l\right) + \ln\frac{\theta_l}{l} - l\ln\left(1-\theta_k-\theta_l\right) = \ln\left(b_l f_l\right)
\end{aligned} \tag{6-7}$$

where b_k and b_l are the binding constants for the two adsorbates; f_k and f_l are the partial fugacities in the bulk fluid phase in equilibrium with the adsorbates. It is to be noted that since the equations (6-7) are not explicit in terms of the occupancies, $\theta_k = \frac{kN_k}{M}; \theta_l = \frac{lN_l}{M}$, the set of two equations need to be solved numerically. All the calculations presented in this article were performed using the Given-Find solve

block of MathCad 15.[41] The solutions to Equations (6-7) implicitly satisfy the requirements of the minimum Helmholtz free energy for mixture adsorption.

The corresponding *unary isotherms* can be derived as limiting scenarios for equations (6-7):

$$\begin{aligned}
&(k-1)\ln\left(1-\frac{(k-1)}{k}\theta_k\right)+\ln\frac{\theta_k}{k}-k\ln(1-\theta_k)=\ln(b_k f)\\
&(l-1)\ln\left(1-\frac{(l-1)}{l}\theta_l\right)+\ln\frac{\theta_l}{l}-l\ln(1-\theta_l)=\ln(b_l f)\\
&b_k f=\frac{\left(1-\frac{(k-1)}{k}\theta_k\right)^{(k-1)}\frac{\theta_k}{k}}{(1-\theta_k)^k};\quad b_l f=\frac{\left(1-\frac{(l-1)}{l}\theta_l\right)^{(l-1)}\frac{\theta_l}{l}}{(1-\theta_l)^l}
\end{aligned} \tag{6-8}$$

The binding constants b_k and b_l can be fitted to match the unary isotherm data. For $k\neq 1;\quad l\neq 1$, the binding constants $b_k;\quad b_l$ do *not* correspond to the unary Langmuir model fits. It is also noteworthy that for $k\neq 1;\quad l\neq 1$, the occupancies and loadings are not explicitly relatable to the bulk fluid fugacities, f, and a numerical solution is required.

In applying the 1D lattice model to match unary isotherm data in zeolites and MOFs, we interpret the parameters k and l to be representative of the inverse saturation capacities of the unary isotherms. For this purpose, we may identify M as the total number of sites in one unit cell. So, if N_k and N_l are the loadings in the units of molecules per unit cell, and their saturation capacities are, respectively, $N_{k,sat}$ and $N_{l,sat}$: $\frac{M}{k}=N_{k,sat};\quad \frac{M}{l}=N_{l,sat};\quad \frac{l}{k}=\frac{N_{k,sat}}{N_{l,sat}}$. There is no strict requirement to restrict k and l to have integer values. The molar loadings, expressed in molecules uc^{-1}, are $N_k=\frac{M}{k}\theta_k=N_{l,sat}\theta_k;\quad N_l=\frac{M}{l}\theta_l=N_{l,sat}\theta_l$. It is also to be noted that the quantities N_k and N_l have the same significance as the molar loadings q_i, introduced in the earlier Chapter on the IAST on page 22.

Let us re-write equations (6-7) as

$$\frac{\frac{\theta_k}{k}\left(1-\frac{(k-1)}{k}\theta_k-\frac{(l-1)}{l}\theta_l\right)^{(k-1)}}{\left(1-\theta_k-\theta_l\right)^k}=b_k f_k;\quad \frac{\frac{\theta_l}{l}\left(1-\frac{(k-1)}{k}\theta_k-\frac{(l-1)}{l}\theta_l\right)^{(l-1)}}{\left(1-\theta_k-\theta_l\right)^l}=b_l f_l \tag{6-9}$$

Let the mole fraction of component k in the bulk fluid phase be y_k; $y_l=1-y_k$; so, $f_k=f_t y_k$; $f_l=f_t y_l=f_t\left(1-y_k\right)$ where f_t is the total mixture fugacity of the bulk fluid phase, $f_k+f_l=f_t$. The adsorption selectivity, $S_{//k}=\frac{N_l/N_k}{f_l/f_k}=\frac{N_l/N_k}{y_l/y_k}=\frac{\left(\frac{\theta_l}{l}\right)\Big/\left(\frac{\theta_k}{k}\right)}{y_l/y_k}$, defined for l (the longer molecule) with respect to k (the shorter molecule), can be expressed as follows

$$S_{l/k}=\frac{N_l/N_k}{y_l/y_k}=\frac{\left(\frac{\theta_l}{l}\right)\Big/\left(\frac{\theta_k}{k}\right)}{y_l/y_k}=\frac{b_l/b_k}{\Omega} \tag{6-10}$$

where Ω has the same definition as in equation (6-6). For $l\geq k$, the factor $\Omega\geq 1$, and favors the adsorption of the shorter molecule. The factor Ω increases with increasing total occupancies $\frac{N_k+N_l}{M}=\frac{\theta_k}{k}+\frac{\theta_l}{l}=\theta_{mix}$. Generally speaking the longer molecule will have the higher binding constant, i.e. $b_l/b_k\geq 1$; consequently, the factor Ω has the effect of reducing the magnitude of $S_{k/l}$. The corresponding adsorption selectivity $S_{k/l}$ defined for k (the shorter molecule) with respect to l (the longer molecule), can be expressed as follows

$$S_{k/l}=\frac{N_k/N_l}{y_k/y_l}=\frac{\left(\frac{\theta_k}{k}\right)\Big/\left(\frac{\theta_l}{l}\right)}{y_k/y_l}=\left(b_k/b_l\right)\Omega \tag{6-11}$$

The mole fraction of k in the adsorbed is expressed in implicit form as

$$x_k=\frac{N_k}{N_k+N_l}=\frac{1}{1+\left(N_l/N_k\right)}=\frac{1}{1+\frac{b_l f_l}{b_k f_k}\frac{1}{\Omega}}=1-x_l \tag{6-12}$$

Equation (6-12) needs to be solved using a suitable root-finder in order to determine the adsorbed phase composition for specified values of the mixture occupancy θ_{mix}, and $\frac{b_k f_k}{b_l f_l}$. We have checked for a wide range of problems, that the solutions to Equation (6-12) are identical to those obtained from use of the IAST provided that the unary isotherm model used in the IAST estimations correspond to those described by equation (6-8). It is also noteworthy that for $k \neq 1; \quad l \neq 1$, the occupancies and loadings are not explicitly relatable to the bulk fluid fugacities, *f*, and a numerical integrations in Equations (4-5) are required for determination of the spreading pressures, adsorption potential, and sorption pressures. For all of the numerical calculations presented in this article, we have checked that the lattice model and the IAST yield identical results for the component loadings, and adsorbed phase mole fractions.

If the ratio of binding constants $b_k / b_l = 1$, and the partial fugacities in the bulk phase are equal, i.e. $f_k = f_l$, the separation selectivity $S_{k/l} \geq 1$, and will be driven entirely by entropic considerations, and the mole fraction of k in the adsorbed phase will be

$$x_k = \frac{1}{1+\frac{1}{\Omega}} = 1 - x_l; \quad b_k = b_l; \quad f_k = f_l \tag{6-13}$$

Equation (6-13) is the same as equation (6-5) that was derived to achieve maximum entropy $\frac{S}{k_B M}$. Put another was, if the ratio of binding constants $b_k / b_l = 1$, the separation is solely on the basis of entropic considerations, favoring the shorter molecule.

Table 6-1 provides a summary of key relations for the lattice models for adsorption of N_k *k*-mers and N_l *l*-mers on *M* sites of 1D lattice.

It is easy to check from equations (6-8) that for $k = l = 1$, we recover the unary Langmuir isotherms $b_k f = \frac{\theta_k}{(1-\theta_k)}; \quad b_l f = \frac{\theta_l}{(1-\theta_l)^l}$ for both guest molecules. Also, for k=1, l=1, equations (6-9), describing binary mixture adsorption, reduce to the mixed-gas Langmuir model

$$\frac{\theta_k}{\left(1-\theta_k-\theta_l\right)} = b_k f_k; \quad \frac{\theta_k}{\left(1-\theta_k-\theta_l\right)} = b_l f_l \tag{6-14}$$

6.2 2D lattice model of Matoz-Fernandez for mixture adsorption

Matoz-Fernandez and Ramirez-Pastor[46] present the generalization of the foregoing analysis to two-dimensional (2D) square lattices, by introduction of a coordination number Z; for a square lattice $Z = 4$.

Matoz-Fernandez and Ramirez-Pastor[46] derive the following expression for the number of arrangements of N_k k-mers and N_l l-mers on M sites on a square lattice:

$$W = \frac{M!}{\left(M - kN_k - lN_l\right)!}\left[\frac{\left(M-\left(k-1\right)\frac{Z}{2}N_k-\left(l-1\right)\frac{Z}{2}N_l\right)!}{M!N_k!N_l!}\right]^{\frac{Z}{2}} \tag{6-15}$$

The mixture adsorption equilibrium for a 2D lattice is described by a set of two, coupled, equations:

$$\begin{aligned}
&\left(k-1\right)\ln\left(\frac{Z}{2}-\frac{\left(k-1\right)}{k}\theta_k-\frac{\left(l-1\right)}{l}\theta_l\right)+\ln\frac{\theta_k}{k}-k\ln\left(1-\theta_k-\theta_l\right)-k\ln\left(\frac{Z}{2}\right)=\ln\left(b_k f_k\right)\\
&\left(l-1\right)\ln\left(\frac{Z}{2}-\frac{\left(k-1\right)}{k}\theta_k-\frac{\left(l-1\right)}{l}\theta_l\right)+\ln\frac{\theta_l}{l}-l\ln\left(1-\theta_k-\theta_l\right)-l\ln\left(\frac{Z}{2}\right)=\ln\left(b_l f_l\right)
\end{aligned} \tag{6-16}$$

where b_k and b_l are the binding constants for the two adsorbates; f_k and f_l are the partial fugacities in the bulk fluid phase in equilibrium with the adsorbates. It is to be noted that since the equations (6-7) are not explicit in terms of the occupancies, $\theta_k = \frac{kN_k}{M}; \theta_l = \frac{lN_l}{M}$, the set of two equations need to be solved numerically. All the calculations presented in this article were performed using the Given-Find solve block of MathCad 15.[41]

The corresponding *unary isotherms* can be derived as limiting scenarios for equations (6-16):

$$\begin{aligned}(k-1)\ln\left(\frac{Z}{2}-\frac{(k-1)}{k}\theta_k\right)+\ln\frac{\theta_k}{k}-k\ln(1-\theta_k)-k\ln\left(\frac{Z}{2}\right)&=\ln(b_k f)\\(l-1)\ln\left(\frac{Z}{2}-\frac{(l-1)}{l}\theta_l\right)+\ln\frac{\theta_l}{l}-l\ln(1-\theta_l)-l\ln\left(\frac{Z}{2}\right)&=\ln(b_l f)\end{aligned} \tag{6-17}$$

The generalization of equation (6-6) to 2D square lattice is

$$\Omega=\frac{\left(\frac{Z}{2}-\frac{(k-1)}{k}\theta_k-\frac{(l-1)}{l}\theta_l\right)^{(l-k)}}{(1-\theta_k-\theta_l)^{(l-k)}\left(\frac{Z}{2}\right)^{l-k}}=\frac{\left(\frac{Z}{2}-(k-1)x_k\theta_{mix}-(l-1)(1-x_k)\theta_{mix}\right)^{(l-k)}}{\left(1-kx_k\theta_{mix}-l(1-x_k)\theta_{mix}\right)^{(l-k)}\left(\frac{Z}{2}\right)^{l-k}} \tag{6-18}$$

The mole fraction of k in the adsorbed is

$$x_k=\frac{N_k}{N_k+N_l}=\frac{1}{1+(N_l/N_k)}=\frac{1}{1+\frac{b_l f_l}{b_k f_k}\frac{1}{\Omega}}=1-x_l \tag{6-19}$$

which equation is identical in a formal sense to equation (6-12) derived for 1D lattice.

The binding constants b_k and b_l can be fitted to match the unary isotherm data. In applying the 2D lattice model to match unary isotherm data in zeolites and MOFs, we interpret the parameters k and l to be representative of the inverse saturation capacities of the unary isotherms. For this purpose we may identify M as the total number of sites in one unit cell. So, if N_k and N_l are the loadings in the units of molecules per unit cell, and their saturation capacities are, respectively, $N_{k,sat}$ and $N_{l,sat}$: $\frac{M}{k}=N_{k,sat}$; $\frac{M}{l}=N_{l,sat}$; $\frac{l}{k}=\frac{N_{k,sat}}{N_{l,sat}}$. There is no strict requirement to restrict k and l to have integer values. The molar loadings, expressed in molecules uc^{-1}, are $N_k=\frac{M}{k}\theta_k=N_{l,sat}\theta_k$; $N_l=\frac{M}{l}\theta_l=N_{l,sat}\theta_l$. It is also to be noted that the quantities N_k and N_l have the same significance as the molar loadings q_i, introduced in the earlier Chapter on the IAST on page 22. If the ratio of binding constants $b_k/b_l=1$, and the partial fugacities in the bulk phase are equal, i.e. $f_k=f_l$, the separation selectivity $S_{k/l}\geq 1$, and will be driven entirely by entropic considerations, and the mole fraction of k in the adsorbed phase will be

$$x_k = \frac{1}{1+\frac{1}{\Omega}}; \quad b_k = b_l; \quad f_k = f_l \tag{6-20}$$

Table 6-2 provides a summary of key relations for the lattice models for adsorption of N_k k-mers and N_l l-mers on M lattice sites with coordination number, Z. Taking $Z = 2$, will result in the same equations as presented in the previous section for a 1D lattice.

There is however an important drawback of the square lattice model of Matoz-Fernandez and Ramirez-Pastor;[46] equations (6-17) do not degenerate to the Langmuir isotherm for the special case, k=1, l=1. For this reason, we do not use the 2D square lattice model of Matoz-Fernandez and Ramirez-Pastor[46] in the calculations presented in this article.

6.3 2D lattice model of Azizian and Bashir for mixture adsorption

Azizian and Bashiri[47] consider a two-dimensional lattice of M sites for binary adsorption of A and B molecules. N_k and N_l molecules of A and B are adsorbed on the surface, respectively, in such a way that each A molecule occupies k lattice sites and each B molecule occupies l lattice sites. It is assumed that there are no adsorbate-adsorbate interactions, consistent with the assumptions in the classical Langmuir model. The number of configurations that are possible for arrangement of N_k and N_l molecules on M sites of the 2D lattice is given by equation (1) of Azizian and Bashiri:[47]

$$W = \frac{\left(M-(k-1)N_k-(l-1)N_l\right)!}{\left(M-kN_k-lN_l\right)!\,N_k!\,N_l!} \tag{6-21}$$

Using the Stirling approximation, the following expression can be derived for the entropy per site

$$\begin{aligned}\frac{S}{k_B M} &= \left(1-\frac{(k-1)}{k}\frac{kN_k}{M}-\frac{(l-1)}{l}\frac{lN_l}{M}\right)\ln\left(1-\frac{(k-1)}{k}\frac{kN_k}{M}-\frac{(l-1)}{l}\frac{lN_l}{M}\right)\\ &-\left(1-\frac{kN_k}{M}-\frac{lN_l}{M}\right)\ln\left(1-\frac{kN_k}{M}-\frac{lN_l}{M}\right)-\frac{N_k}{M}\ln\frac{N_k}{M}-\frac{N_l}{M}\ln\frac{N_l}{M}\end{aligned} \tag{6-22}$$

Defining, the fractional coverages of A and B molecules, $\theta_k = \frac{kN_k}{M}; \theta_l = \frac{lN_l}{M}$, we obtain the following expression for the dimensionless entropy per site

$$\frac{S}{k_B M} = \left(1-\frac{(k-1)}{k}\theta_k - \frac{(l-1)}{l}\theta_l\right)\ln\left(1-\frac{(k-1)}{k}\theta_k - \frac{(l-1)}{l}\theta_l\right)$$
$$-(1-\theta_k-\theta_l)\ln(1-\theta_k-\theta_l) - \frac{\theta_k}{k}\ln\frac{\theta_k}{k} - \frac{\theta_l}{l}\ln\frac{\theta_l}{l} \qquad (6\text{-}23)$$

Formally, equation (6-23) is identical to the corresponding expression (6-3) derived by Dávila et al.[45] for adsorption of N_k k-mers and N_l l-mers on M sites on a 1D lattice. The mixture adsorption equilibrium for a 2D lattice is described by a set of two, coupled, equations:

$$\frac{\frac{\theta_k}{k}\left(1-\frac{(k-1)}{k}\theta_k - \frac{(l-1)}{l}\theta_l\right)^{(k-1)}}{(1-\theta_k-\theta_l)^k} = b_k f_k; \quad \frac{\frac{\theta_l}{l}\left(1-\frac{(k-1)}{k}\theta_k - \frac{(l-1)}{l}\theta_l\right)^{(l-1)}}{(1-\theta_k-\theta_l)^l} = b_l f_l \qquad (6\text{-}24)$$

where b_k and b_l are the binding constants for the two adsorbates; f_k and f_l are the partial fugacities in the bulk fluid phase in equilibrium with the adsorbates. Equations (6-24) is formally identical to the equations (6-7) for the 1D lattice model. It is to be noted that since the Equations (6-24) are not explicit in terms of the occupancies, $\theta_k = \frac{kN_k}{M}; \theta_l = \frac{lN_l}{M}$, the set of two equations need to be solved numerically. All the calculations presented in this article were performed using the Given-Find solve block of MathCad 15.[41]

The corresponding *unary isotherms* are described by the limiting cases of Equations (6-24)

$$b_k f = \frac{\left(1-\frac{(k-1)}{k}\theta_k\right)^{(k-1)}\frac{\theta_k}{k}}{(1-\theta_k)^k}; \quad b_l f = \frac{\left(1-\frac{(l-1)}{l}\theta_l\right)^{(l-1)}\frac{\theta_l}{l}}{(1-\theta_l)^l} \qquad (6\text{-}25)$$

The binding constants b_k and b_l can be fitted to match the unary isotherm data. In applying the 1D lattice model to rationalize the selectivity reversal phenomena observed for binary mixture adsorption in zeolites and MOFs, we interpret the parameters k and l to be representative of the inverse saturation capacities of the unary isotherms, taking $\frac{M}{k} = N_{k,sat}; \quad \frac{M}{l} = N_{l,sat}$. For example, we may also arbitrarily

set k=1, and take $l = \frac{N_{k,sat}}{N_{l,sat}}$. Alternatively, we set l=1, and take $k = \frac{N_{l,sat}}{N_{k,sat}}$. There is no strict requirement to restrict k and l to have integer values.

The expressions for the adsorbed phase compositions and selectivity are the same as those for the 1D lattice model of Dávila et al.,[45] conveniently summarized in Table 6-1.

For the special case, k=1, l=1, equations (6-25) reduce to the unary Langmuir isotherms

$$\frac{\theta_k}{(1-\theta_k)} = b_k f; \quad \frac{\theta_l}{(1-\theta_l)} = b_l f \tag{6-26}$$

Furthermore, for k=1, l=1, equations (6-24) reduce to

$$\frac{\theta_k}{(1-\theta_k-\theta_l)} = b_k f_k; \quad \frac{\theta_k}{(1-\theta_k-\theta_l)} = b_l f_l \tag{6-27}$$

Equation (6-27) is precisely equivalent to Equation (4-22), the mixed-gas Langmuir model.

Equation (6-23), the dimensionless entropy per site, for k=1, l=1, simplifies to

$$\frac{S}{k_B M} = -(1-\theta_k-\theta_l)\ln(1-\theta_k-\theta_l) - \theta_k \ln\theta_k - \theta_l \ln\theta_l \tag{6-28}$$

Equation (6-28) should be compared to the entropy of mixing for binary *fluid* mixtures $\frac{S}{k_B} = -x_k \ln x_k - x_l \ln x_l$ where x_k and x_l are the mole fractions.

6.4 List of Tables for Statistical thermodynamics and lattice models

Table 6-1. Summary of key relations for the lattice models for adsorption of N_k k-mers and N_l l-mers on M sites of 1D lattice.

	Species k	Species l	Total mixture
Number of adsorbed molecules on lattice of M sites	N_k	N_l	$N_k + N_l$
Saturation capacity	$q_{k,sat} = \frac{M}{k}$	$q_{l,sat} = \frac{M}{l}$	M
Fractional occupancy	$\theta_k = \frac{kN_k}{M} = \frac{N_k}{N_{k,sat}}$	$\theta_l = \frac{lN_l}{M} = \frac{N_l}{N_{l,sat}}$	$\frac{N_k + N_l}{M} = \frac{\theta_k}{k} + \frac{\theta_l}{l} = \theta_{mix}$
Component loadings	$N_k = \frac{M}{k}\theta_k = N_{k,sat}\theta_k$	$N_l = \frac{M}{l}\theta_l = N_{l,sat}\theta_l$	$N_k + N_l = M\theta_{mix}$
Entropic factor Ω	$\Omega = \frac{\left(1 - \frac{(k-1)}{k}\theta_k - \frac{(l-1)}{l}\theta_l\right)^{(l-k)}}{\left(1-\theta_k-\theta_l\right)^{(l-k)}} \frac{\left(1-(k-1)x_k\theta_{mix} - (l-1)(1-x_k)\theta_{mix}\right)^{(l-k)}}{\left(1-kx_k\theta_{mix} - l(1-x_k)\theta_{mix}\right)^{(l-k)}}$		
Mole fraction in the adsorbed phase is given by the implicit expression:	$x_k = \frac{N_k}{N_k+N_l} = \frac{1}{1+(N_l/N_k)} = \frac{1}{1+\frac{b_l f_l}{b_k f_k}\frac{1}{\Omega}} = 1 - x_l$		$x_k + x_l = 1$
Adsorption selectivity	$S_{l/k} = \frac{N_l/N_k}{y_l/y_k} = \frac{\left(\frac{\theta_l}{l}\right)\Big/\left(\frac{\theta_k}{k}\right)}{y_l/y_k} = \frac{b_l/b_k}{\Omega}$; $S_{k/l} = \frac{N_k/N_l}{y_k/y_l} = \frac{\left(\frac{\theta_k}{k}\right)\Big/\left(\frac{\theta_l}{l}\right)}{y_k/y_l} = (b_k/b_l)\Omega$		

Table 6-2. Summary of key relations for the lattice models for adsorption of N_k k-mers and N_l l-mers on M lattice sites. For 1D lattice, the coordination number $Z = 2$; for 2D lattice, $Z = 4$.

	Species k	Species l	Total mixture
Number of adsorbed molecules on lattice of M sites	N_k	N_l	$N_k + N_l$
Saturation capacity	$q_{k,sat} = \frac{M}{k}$	$q_{l,sat} = \frac{M}{l}$	M
Fractional occupancy	$\theta_k = \frac{kN_k}{M} = \frac{N_k}{N_{k,sat}}$	$\theta_l = \frac{lN_l}{M} = \frac{N_l}{N_{l,sat}}$	$\frac{N_k + N_l}{M} = \frac{\theta_k}{k} + \frac{\theta_l}{l} = \theta_{mix}$
Component loadings	$N_k = \frac{M}{k}\theta_k = N_{k,sat}\theta_k$	$N_l = \frac{M}{l}\theta_l = N_{l,sat}\theta_l$	$N_k + N_l = M\theta_{mix}$
Entropic factor Ω	$\Omega = \frac{\left(\frac{Z}{2} - \frac{(k-1)}{k}\theta_k - \frac{(l-1)}{l}\theta_l\right)^{(l-k)}}{\left(1-\theta_k-\theta_l\right)^{(l-k)}\left(\frac{Z}{2}\right)^{l-k}} = \frac{\left(\frac{Z}{2} - (k-1)x_k\theta_{mix} - (l-1)(1-x_k)\theta_{mix}\right)^{(l-k)}}{\left(1-kx_k\theta_{mix} - l(1-x_k)\theta_{mix}\right)^{(l-k)}\left(\frac{Z}{2}\right)^{l-k}}$		
Mole fraction in the adsorbed phase is given by the implicit expression:	$x_k = \frac{N_k}{N_k + N_l} = \frac{1}{1+(N_l/N_k)} = \frac{1}{1+\frac{b_l f_l}{b_k f_k}\frac{1}{\Omega}} = 1 - x_l$		$x_k + x_l = 1$
Adsorption selectivity	$S_{l/k} = \frac{N_l/N_k}{y_l/y_k} = \frac{\left(\frac{\theta_l}{l}\right)\Big/\left(\frac{\theta_k}{k}\right)}{y_l/y_k} = \frac{b_l/b_k}{\Omega}$; $S_{k/l} = \frac{N_k/N_l}{y_k/y_l} = \frac{\left(\frac{\theta_k}{k}\right)\Big/\left(\frac{\theta_l}{l}\right)}{y_k/y_l} = (b_k/b_l)\Omega$		

6.5 List of Figures for Statistical thermodynamics and lattice models

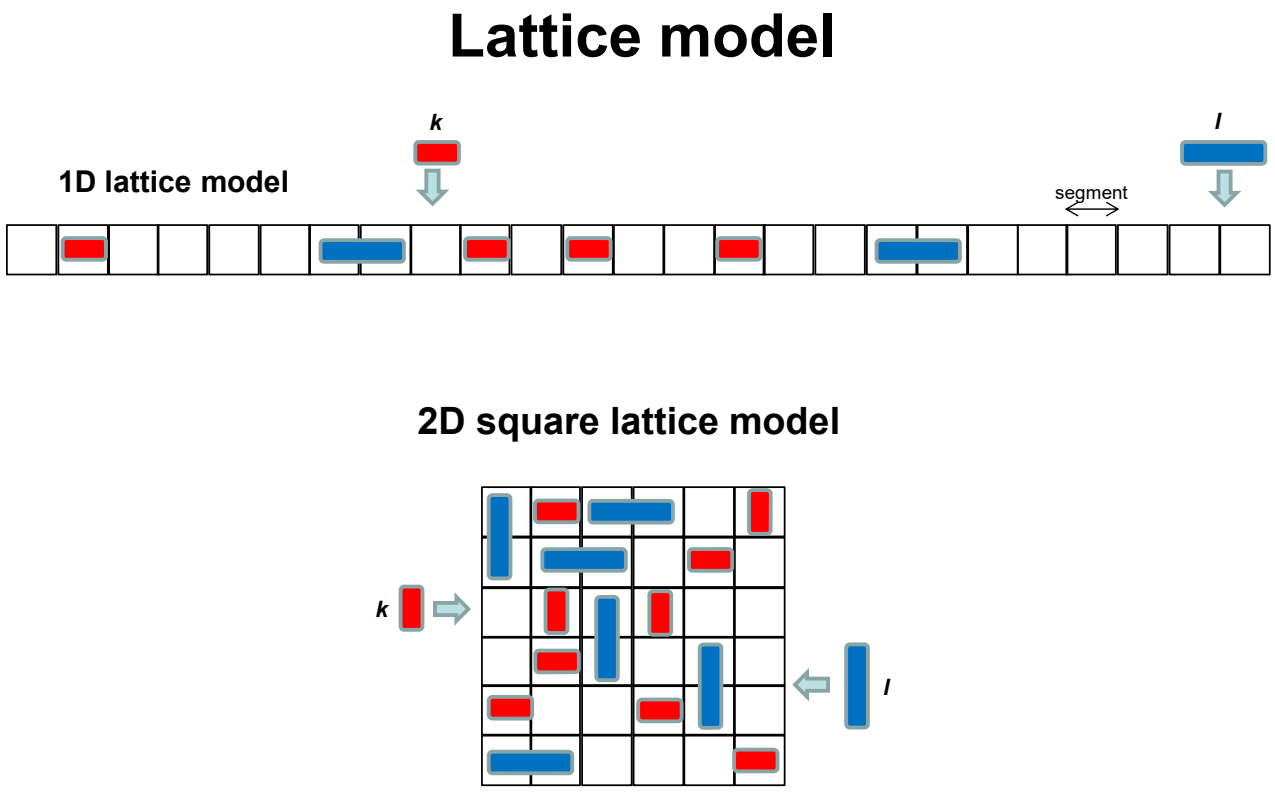

Figure 6-1. Schematic showing the adsorption of binary mixture of *k*-mers (*k*=1), and *l*-mers (*l*=2) on 1D and 2D (square) lattices.

7 Explicit Mixture Adsorption Model of van Assche

In a recent paper, van Assche et al.[48] derive a model to describe mixture adsorption, that purportedly has its basis in statistical thermodynamics. For a mixture of species 1 and 2, in which each species follows 1-site Langmuir adsorption characteristics, the following expressions for the component loadings are derived for the scenario in which species 2 has the higher saturation capacity

$$q_1 = \frac{q_{1sat} b_1 f_1}{\left(1+b_2 f_2\right)^{\frac{q2sat}{q1sat}} + b_1 f_1}; \quad q_2 = \frac{q_{2sat} b_2 f_2 \left(1+b_2 f_2\right)^{\frac{q2sat}{q1sat}-1}}{\left(1+b_2 f_2\right)^{\frac{q2sat}{q1sat}} + b_1 f_1} \tag{7-1}$$

The mole fraction of the component in the adsorbed phase that has the *lower* saturation capacity (1), can be derived:

$$x_1 = \frac{1}{1+\frac{b_2 f_2}{b_1 f_1}\frac{1}{\Omega}} = 1 - x_2; \quad \Omega = \frac{q_{1sat}}{q_{2sat}} \frac{1}{\left(1+b_2 f_2\right)^{\frac{q2sat}{q1sat}-1}} \tag{7-2}$$

In sharp contrast with the corresponding expression derived from the model of Dávila et al.,[45] the adsorbed phase mole fractions, x_1, x_2 can be determined explicitly in terms of the binding constants, saturation capacities, and partial bulk fluid phase fugacities. However, as stressed by van Assche et al.,[48] the important disadvantage of equations (7-1), and (7-2) is that they are *not* symmetric. Another important factor to note is that the entropic factor Ω only varies with the occupancy of component 2. This is in sharp contrast to the entropy factor described by equation (6-6) model of Dávila et al.,[45] wherein the Ω is seen to depend on the occupancies of both of the components in the mixture.

For the scenario in which scenario in which species 1 has the higher saturation capacity, the corresponding expressions are

$$q_1 = \frac{q_{1sat} b_1 f_1 \left(1+b_1 f_1\right)^{\frac{q1sat}{q2sat}-1}}{\left(1+b_1 f_1\right)^{\frac{q1sat}{q2sat}} + b_2 f_2}; \quad q_2 = \frac{q_{2sat} b_2 f_2}{\left(1+b_1 f_1\right)^{\frac{q1sat}{q2sat}} + b_2 f_2} \tag{7-3}$$

The mole fraction of the component in the adsorbed phase x_1 that has the *higher* saturation capacity (component 1), is:

Explicit Mixture Adsorption Model of van Assche

$$x_1 = \frac{1}{1+\frac{b_2 f_2}{b_1 f_1}\frac{1}{\Omega}}; \quad \Omega = \frac{q_{1sat}}{q_{2sat}}\left(1+b_1 f_1\right)^{\frac{q1sat}{q2sat}-1} \tag{7-4}$$

From equation (7-4), we note that the entropic factor Ω only varies with the occupancy of component 1. This is in sharp contrast to the entropy factor described by equation (6-6) model of Dávila et al.,[45] wherein the Ω is seen to depend on the occupancies of both of the components in the mixture.

We have tested the accuracy of Equations (7-1), (7-2), (7-3), and (7-4) and found these to be of poor accuracy when the ratio of saturation capacities exceeds 2. As illustration of the limitations of the explicit model of van Assche et al.,[48] we consider binary ethanol(1)/1-hexanol(2) mixture adsorption in CHA zeolite at 300 K, wherein the partial fugacities in the bulk phase are equal to each other, i.e. $f_1 = f_2$. On the basis of the Configurational-Bias Monte Carlo (CBMC) simulations reported by Krishna and van Baten,[49] the saturation capacities of ethanol (1), and 1-hexanol (2) are respectively 4 molecules cage^{-1}, and 1 molecule cage^{-1}, respectively; i.e. q_{1sat} = 4 cage^{-1}, q_{2sat} = 1 cage^{-1}; $\frac{q_{1sat}}{q_{2sat}} = 4$. The unary isotherms could be fitted with 1-site Langmuir model with binding constants $b_1 = 3\times10^{-4}$ Pa^{-1}, $b_2 = 30$ Pa^{-1}. In Figure 7-1(a) the calculations of the mole fraction in the adsorbed phase using Equation (7-4) (shown by the dashed line) are compared with the corresponding IAST calculations (indicated by the continuous solid line). Also shown for comparison are the CBMC simulations of mixture adsorption (indicated by symbols). We note that the accuracy of Equation (7-4) for estimation of the mole fraction of ethanol in the adsorbed phase x_1 shows large deviations from the IAST for bulk fugacities in the range 10 kPa < $f_t = f_1 + f_2$ < 200 kPa, in which selectivity reversal takes place. The phenomenon of selectivity reversal has been confirmed in the experiments reported by Remy et al.[50] for transient breakthroughs in a fixed bed adsorber packed with SAPO-34 (that has the same structural topology as CHA) and operating under conditions with bulk liquid phase mixtures; see Figure 12-11(a,b). The component that is eluted first from the adsorber is the alcohol with the longer chain length.

The reason for the poor agreement between the van Assche model and IAST estimates is primarily due to the fact that the entropic factor Ω calculated from equation (7-4) does not account for the influence of the occupancy contribution of component 2 to the Boltzmann re-arrangement statistics. In order to underscore this point, Figure 7-1(b) compares the calculations of the entropy factor Ω from equation (7-4) with the corresponding calculations from IAST, using:

$$\Omega = \frac{b_2 f_2}{b_1 f_1} \frac{1}{\left(\frac{1}{x_1} - 1\right)} \tag{7-5}$$

In which the adsorbed phase mole fraction of component 1, $\Omega = \frac{b_2 f_2}{b_1 f_1} \frac{1}{\left(\frac{1}{x_1} - 1\right)}$, is determined from equation (4-10). For total bulk fluid phase fugacities $f_t = f_1 + f_2 < 200$ kPa, the entropy factor Ω calculated from equation (7-4) is about 1 – 4 orders of magnitude lower than the corresponding IAST estimates using equation (7-5).

Also, the accuracy of Equations (7-1), (7-2), (7-3), and (7-4) is poor for mixture adsorption calculations in which the bulk fluid phase compositions are not held constant at y_1=0.5 but varied. As illustration, Figure 7-2(a) presents calculations using Equation (7-4) for the adsorbed phase mode adsorbed phase mole fraction of ethanol(1) for binary ethanol(1)/1-hexanol(2) mixture adsorption in CHA at 300 K and total fugacity $f_t = f_1 + f_2 = 100$ kPa, and varying mole fraction of ethanol (1) in the bulk fluid phase, y_1. The estimations of the explicit model of van Assche et al.[48] are extremely poor in the range $0 < y_1 < 0.5$. The reason for this is that Equations (7-1), (7-2), (7-3), and (7-4) do not have the proper limiting behaviors for the component loadings, q_1 for $y_1 \to 0$, and q_2 for $y_2 \to 0$. Witness the comparisons in the component loadings for ethanol, and 1-hexanol as estimated by the IAST and van Assche models in Figure 7-2(b,c). Figure 7-2(d) shows that the entropy factor Ω calculated from equation (7-4) is about 4 orders of magnitude lower than the corresponding IAST estimates using equation (7-5) when $y_1 \to 0$.

The accuracy of the use of the Equations (7-1), (7-2), (7-3), and (7-4) improves, albeit slightly, when the saturation capacities are closer together. As illustration, Figure 7-3(a) presents calculations of the adsorbed phase mode adsorbed phase mole fraction of 1-butanol(1) for binary 1-butanol(1)/1-hexanol(2) mixture adsorption in CHA at 300 K and total fugacity $f_t = f_1 + f_2 = 100$ Pa, and varying mole fraction of 1-butanol (1) in the bulk fluid phase, y_1. The saturation capacity of 1-butanol as determined in the CBMC simulations of Krishna and van Baten,[49] $q_{1sat} = 2$ cage^{-1}; the corresponding Langmuir binding constant, $b_1 = 0.45$ Pa^{-1}. For this mixture, for which $\frac{q_{1sat}}{q_{2sat}} = 2$, the deviations of the estimations using Equation (7-4) from the IAST are smaller than that witnessed in Figure 7-2(a), but the van Assche model remain of unacceptable accuracy for estimation of the molar loadings for the scenarios: q_1 for $y_1 \to 0$, and q_2 for $y_2 \to 0$; see Figure 7-3(b,c). Specifically, the estimations of the explicit model of van Assche et al.[48] are extremely poor in the range $0 < y_1 < 0.4$. Figure 7-3(d) shows that the entropy factor Ω calculated from equation (7-4) is about one order of magnitude lower than the corresponding IAST estimates using equation (7-5) when $y_1 \to 0$.

In order to address the problem of the improper limiting behaviors, van Assche et al.[48] have suggested the loading be determined by averaging the results of equations (7-1) and (7-3); this approach appears to be arbitrary and there is no theoretical justification for this.

7.1 List of Figures for Explicit Mixture Adsorption Model of van Assche

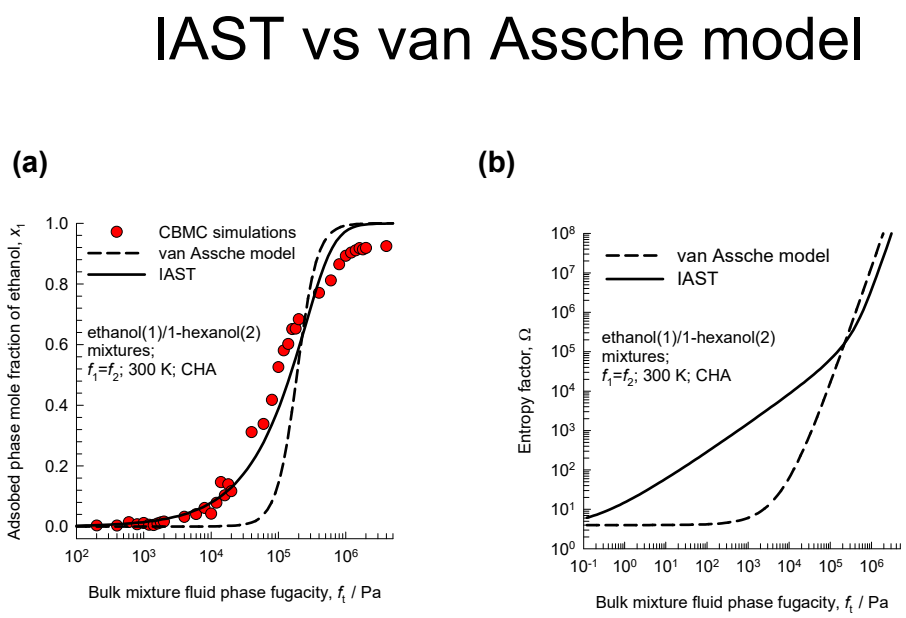

Figure 7-1. (a) CBMC simulations (indicated by symbols) for the adsorbed phase mole fraction of ethanol(1) for binary ethanol(1)/1-hexanol(2) mixture adsorption in CHA at 300 K; in these simulations the partial fugacities in the bulk phase are equal to each other, i.e. $f_1 = f_2$. The x-axis the bulk fluid phase fugacity of the mixture, $f_t = f_1 + f_2$. Also shown are the estimates using the IAST (continuous solid line), and the explicit model of van Assche et al.[48] (dashed line). (b) Calculations of the entropic factor Ω using equation (7-4) with the corresponding IAST calculations.

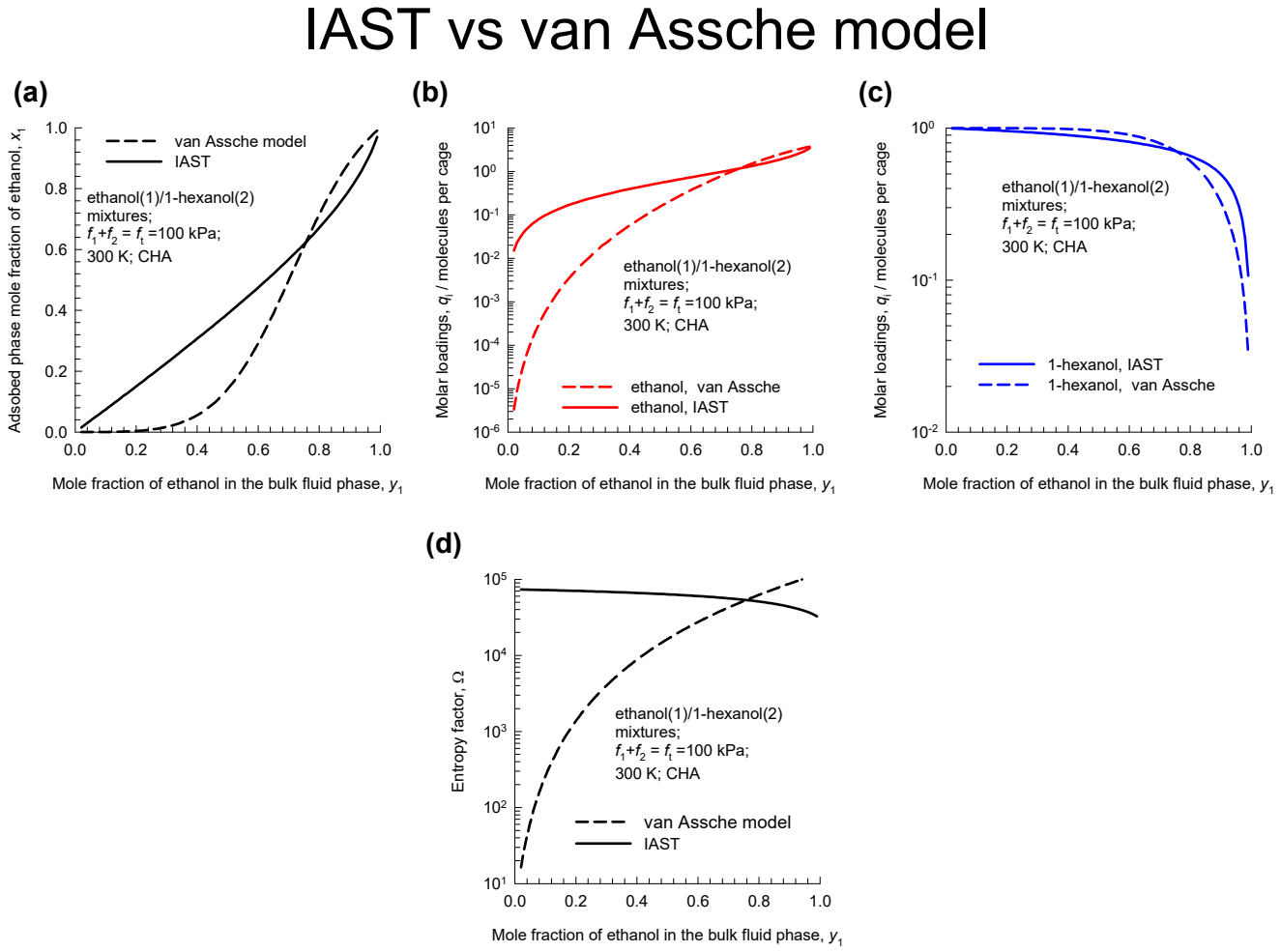

Figure 7-2. (a) The adsorbed phase mode adsorbed phase mole fraction of ethanol(1), and (b, c) the component molar loadings for binary ethanol(1)/1-hexanol(2) mixture adsorption in CHA at 300 K and total fugacity $f_t = f_1 + f_2 = 100$ kPa, and varying mole fraction of ethanol (1) in the bulk fluid phase, y_1. Two sets of calculations are presented: IAST (continuous solid line), and the explicit model of van Assche et al.[48] (dashed line). (d) Calculations of the entropic factor Ω using equation (7-4) with the corresponding IAST calculations.

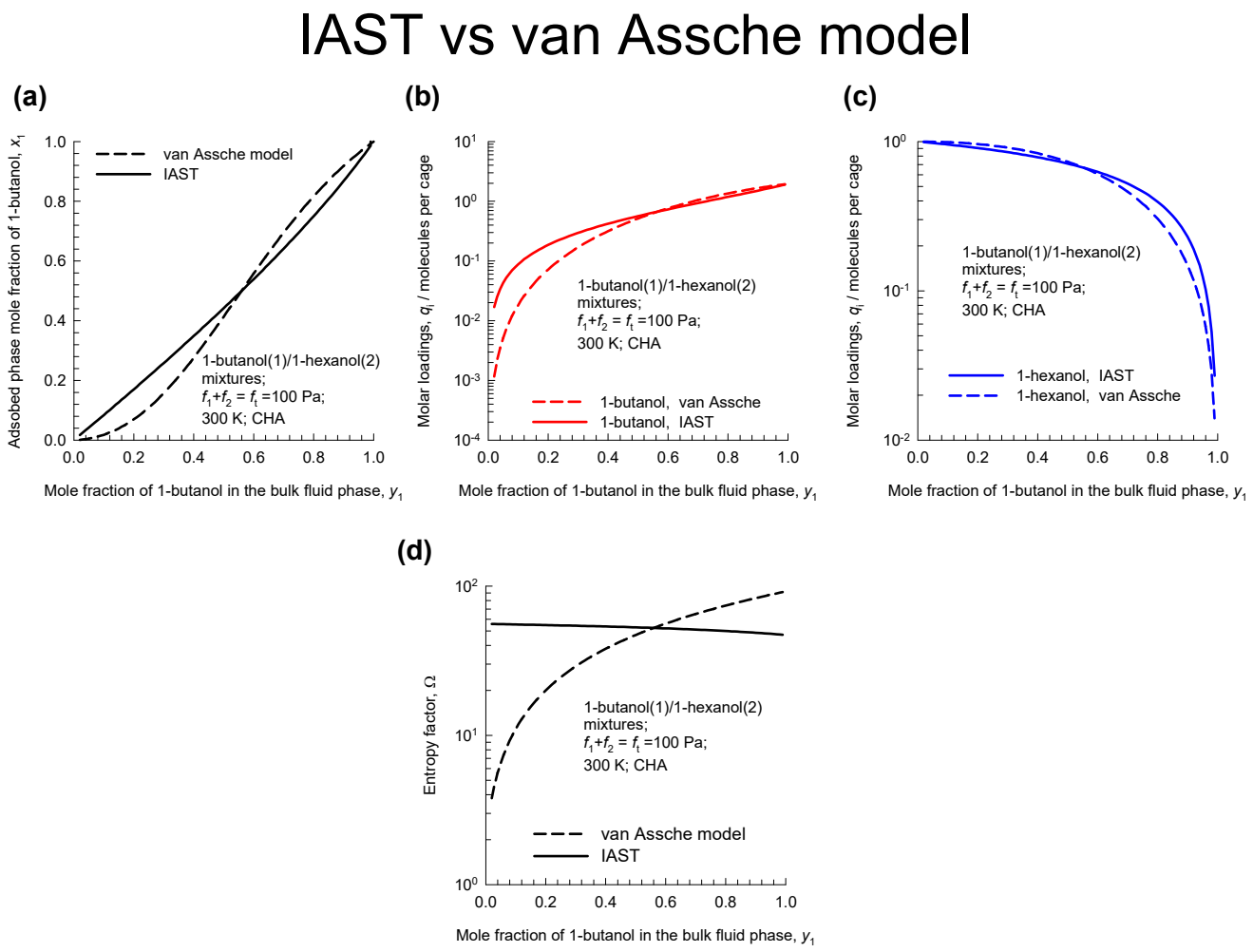

Figure 7-3. (a) The adsorbed phase mode adsorbed phase mole fraction of 1-butanol(1), and (b, c) the component molar loadings for binary 1-butanol(1)/1-hexanol(2) mixture adsorption in CHA at 300 K and total fugacity $f_t = f_1 + f_2 = 100$ Pa, and varying mole fraction of 1-butanol (1) in the bulk fluid phase, y_1. Two sets of calculations are presented: IAST (continuous solid line), and the explicit model of van Assche et al.[48] (dashed line). (d) Calculations of the entropic factor Ω using equation (7-4) with the corresponding IAST calculations.

8 Adsorption of n-alkanes in Manganese Formate (Mn-FA)

We consider adsorption of linear alkanes in manganese formate (Mn-FA) framework.[51] The Mn-FA structure consists of 1D zig-zag channels; see the pore landscapes in Figure 8-1. Figure 8-2 presents computational snapshots showing the location and conformation of propane (C3) and n-hexane (nC6) molecules within the zig-zag 1D channel segments of Mn-FA; one unit cell of Mn-FA contains four channel segments.

8.1 Adsorption of C3/nC6 mixtures in Mn-FA

Configurational-Bias Monte Carlo (CBMC) simulations [51] of the unary adsorption isotherms of C3 and nC6 are presented in Figure 8-3(a). The saturation capacity for C3 is 4 molecules per unit cell (uc), corresponding to one molecule per channel segment; the length of each channel segment is commensurate with that of the propane molecule. Longer alkane molecules such as nC6 must straddle two channel segments; the length of the nC6 molecule is commensurate with the length of two channel segments. The saturation capacities of nC6 is restricted to 2 molecules uc^{-1}. The unary isotherms can be described quantitatively by equations (6-8) of the 1D lattice model of Dávila et al.[45] Since C3 (species *k*) adsorbs commensurately with one channel segment, we take *k*=1, *M* = 4/uc, and $\frac{M}{k} = N_{k,sat} = 4/\text{uc}$. The linear hexane nC6 (species *l*) adsorbs commensurately with two channel segments, and so we take *l*=2, *M* = 4/uc, and $\frac{M}{l} = N_{l,sat} = 2/\text{uc}$. A good match between the 1D lattice model and CBMC simulations of the unary isotherms is obtained with the fitted binding constants are $b_k = 8\times10^{-4}$ Pa^{-1}, and $b_l = 4\times10^{-2}$ Pa^{-1}; see continuous solid lines in Figure 8-3(a). This implies that the unary isotherm is described by the Langmuir model $\frac{\theta_k}{(1-\theta_k)} = b_k f; \quad \theta_k = \frac{kN_k}{M}$. The isotherm for nC6 is described by the

model $\frac{\left(1-\frac{\theta_l}{2}\right)\frac{\theta_l}{2}}{\left(1-\theta_l\right)^2}=b_l f;\quad \theta_l=\frac{lN_l}{M}$; this model can be expressed as a quadratic equation in θ_l, and an explicit expression of θ_l as a function of $b_l f$ is derivable.

Consider adsorption of C3(1)/nC6(2) mixtures. CBMC simulations of the component loadings for a mixture with equal partial fluid phase fugacities, $f_1 = f_2$, are shown in Figure 8-3(b). When operating at total fugacities $f_t = f_1 + f_2 > 100$ kPa, we note that the adsorbed phase composition is richer in the shorter alkane. Increase in f_t beyond 100 kPa causes a progressive increase in the component loading of propane, with a concomitant decrease in the loading of nC6. For total fugacities $f_t = f_1 + f_2 > 1$ MPa, the bulk mixture exists in the liquid phase (this has been determined by use of the Peng-Robinson equation of state). Operations at $f_t = f_1 + f_2 > 1$ MPa, result in almost total exclusion of nC6 from the 1D channels.

To elucidate, and quantify, the reasons behind the selectivity reversal that occurs at $f_t \approx 100$ kPa, and also the total exclusion of nC6 for $f_t = f_1 + f_2 > 1$ MPa, we apply equations (6-7) of the 1D lattice model of Dávila et al.[45] The component loading of C3, in molecules per unit cell, is given by $N_k = \theta_k \frac{M}{k}$. The component loading of nC6, in molecules per unit cell, is given by $N_l = \theta_l \frac{M}{l}$. The calculations of the component loadings are indicated by the continuous solid lines in Figure 8-3(b). The lattice model is able to quantitatively capture the selectivity reversal phenomenon. It was also verified that use of the IAST, along with the unary isotherms, $\frac{\theta_k}{\left(1-\theta_k\right)}=b_k f;\quad \theta_k=\frac{kN_k}{M}$, and $\frac{\left(1-\frac{\theta_l}{2}\right)\frac{\theta_l}{2}}{\left(1-\theta_l\right)^2}=b_l f;\quad \theta_l=\frac{lN_l}{M}$ for C3, and nC6, respectively, results in numerical results that are identical to the 1D lattice model of Dávila et al.[45]

Figure 8-3(c) presents calculations of the dimensionless entropy per site $\frac{S}{k_B M}$, using equation (6-4), for a binary mixture of C3 (k=1), and nC6 (l=2) in 1D lattice as a function of the mole fraction of

propane in the adsorbed phase, $x_k = \frac{N_k}{N_k + N_l} = \frac{\frac{\theta_k}{k}}{\frac{\theta_k}{k} + \frac{\theta_l}{l}}$, for three different values of total occupancies, $\frac{N_k + N_l}{M} = \frac{\theta_k}{k} + \frac{\theta_l}{l} = \theta_{mix}$ = 0.1, 0.3, and 0.5. At the lowest occupancy, θ_{mix} = 0.1, the maximum in the $\frac{S}{k_B M}$ occurs at the adsorbed composition $x_k \approx 0.5$. With increasing total occupancies, θ_{mix}, the maximum in the $\frac{S}{k_B M}$ occurs at values the adsorbed composition x_k, that are significantly richer in propane, the shorter alkane. This is because the vacancies are more efficiently filled up by molecules with the shorter chain length. The precise composition of the adsorbed phase, corresponding to the maximum entropy can be determined by setting $\frac{\partial}{\partial x_k}\left(\frac{S}{k_B M}\right) = 0$, and is described by equations (6-5), and (6-6). The continuous solid black line in Figure 8-3(d) presents a plot of the values of x_k corresponding to the maximum entropy as a function of the total occupancy, θ_{mix}. The corresponding calculations using equation (6-12) is shown by the continuous solid blue line; this line is in excellent agreement with the CBMC simulated values of x_k. Entropy effects become increasingly significant for $\theta_{mix} > 0.5$, causing total exclusion of the longer nC6 molecule as $\theta_{mix} \to 1$.

For entropy effects to be fully exploited and nC6 to be totally rejected, the operations must be under conditions such that pore saturation prevails; adsorption from mixtures in the liquid phase usually ensures prevalence of pore saturation conditions.

8.2 Adsorption of nC4/nC5 mixtures in Mn-FA

Configurational-Bias Monte Carlo (CBMC) simulations[51] of the unary adsorption isotherms of nC4, and nC5 and nC6 in Mn-FA at 300 K are shown in Figure 8-4(a). The saturation capacities of nC4, and nC5 are, respectively, 4, and 2.67 molecules/uc. The unary isotherms can be described quantitatively by equations (6-8) of the 1D lattice model of Dávila et al.[45] For nC4 (species *k*) adsorbs commensurately

with one channel segment, we take k=1, M = 4/uc, and $\frac{M}{k} = N_{k,sat} = 4/\text{uc}$. For the linear pentane nC5 we take l=1.5, M = 4/uc, and $\frac{M}{l} = N_{l,sat} = 2.6667/\text{uc}$. A good match between the 1D lattice model and CBMC simulations of the unary isotherms is obtained with the fitted binding constants are $b_k = 1.5\times10^{-3}$ Pa^{-1}, and $b_l = 1.5\times10^{-3}$ Pa^{-1}; see continuous solid lines in Figure 8-4(a). It is noteworthy that the binding constants of the two molecules are equal to each other.

For adsorption of nC4/nC5 mixtures, CBMC simulations[51] show that the longer alkane is virtually excluded from the channels at pore saturation conditions; see Figure 8-4(b). For a quantitative description we apply equations (6-7) of the 1D lattice model of Dávila et al;[45] the numerical solution to the set of these two equations is represented by the solid lines in Figure 8-4(b). The 1D lattice model is able to provide near-quantitative description of the exclusion of the longer alkane at pore saturation.

The symbols in Figure 8-4(c) are the CBMC simulated data on the adsorbed phase mole fractions x_k plotted as function of the total occupancy, θ_{mix}. For $\theta_{mix} > 0.7$ these data are in excellent agreement with the calculations using equations (6-5), and (6-6), that are based on the maximization of entropy concept; this confirms that the separation is driven by entropic effects as pore saturation is approached.

8.3 List of Figures for Adsorption of n-alkanes in Manganese Formate (Mn-FA)

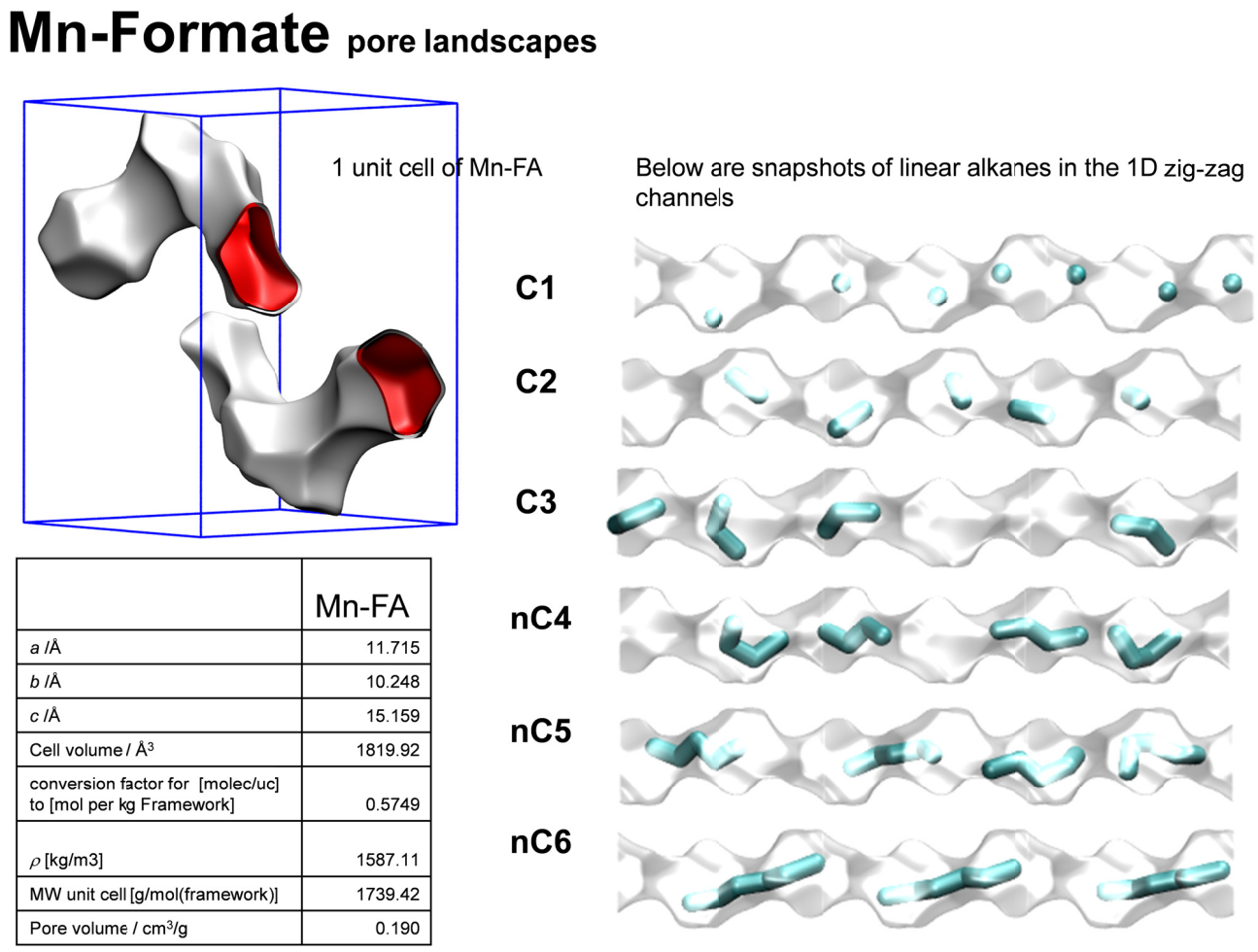

	Mn-FA
a /Å	11.715
b /Å	10.248
c /Å	15.159
Cell volume / Å^3	1819.92
conversion factor for [molec/uc] to [mol per kg Framework]	0.5749
ρ [kg/m3]	1587.11
MW unit cell [g/mol(framework)]	1739.42
Pore volume / cm^3/g	0.190

Figure 8-1. Pore landscape, and structural details of Mn-Formate. Also shown are computational snapshots of the location of n-alkanes in the 1D zig-zag channels.

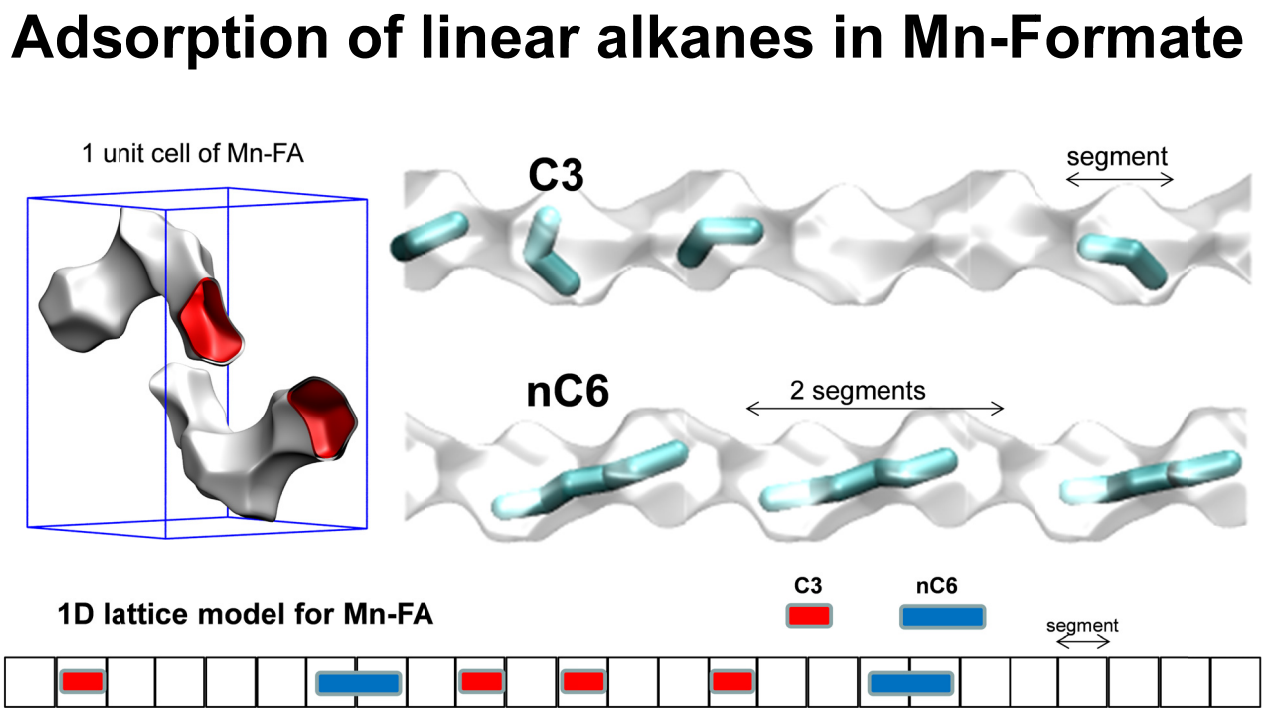

Figure 8-2. Snapshots showing the location of propane (C3) and n-hexane (nC6) molecules within the zig-zag 1D channel segments of Mn-FA.

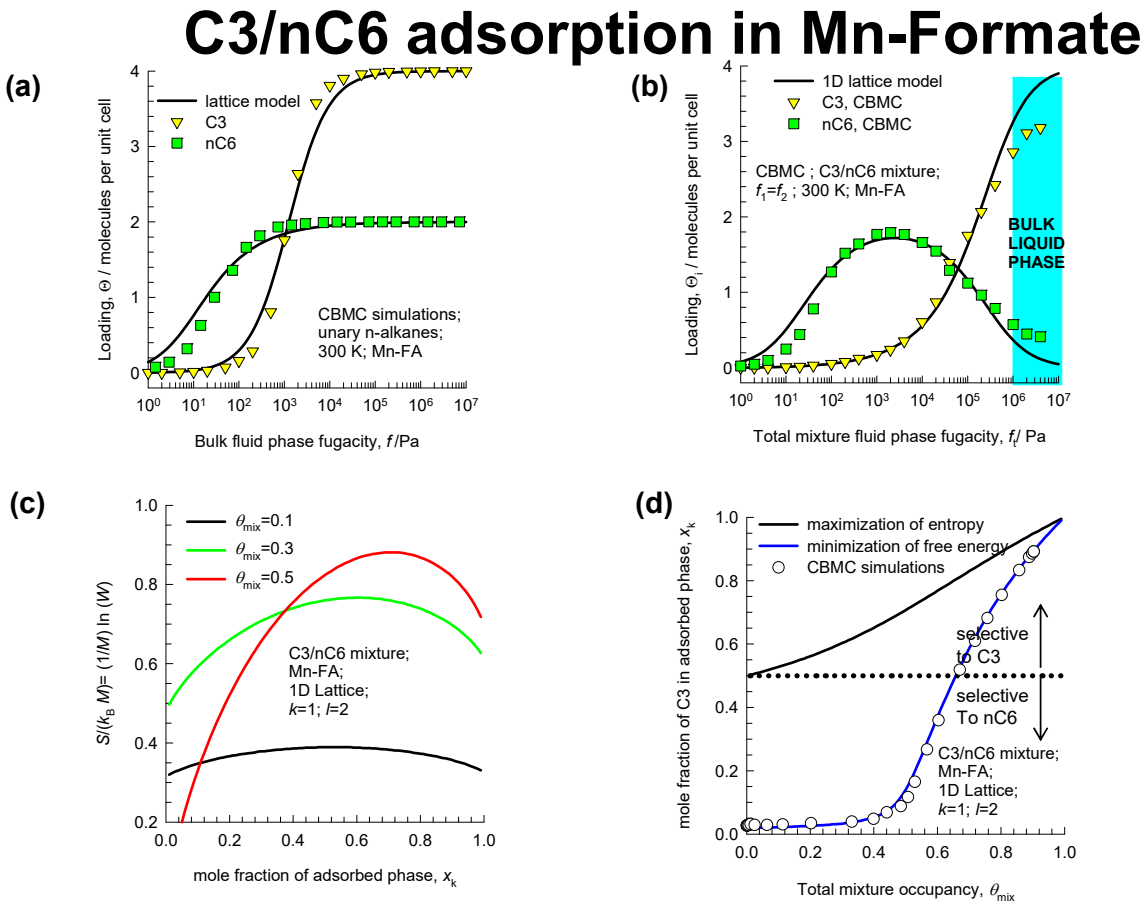

Figure 8-3. (a) CBMC data[51] (symbols) for unary isotherms of C3 and nC6 in Mn-FA at 300 K, compared with the fits of the 1D lattice model. (b) Comparison of the CBMC simulations for C3/nC6 mixture adsorption with the estimations of the 1D lattice model. (c) Calculations of the dimensionless entropy per site $\frac{S}{k_B M}$, as a function of the mole fraction of propane in the adsorbed phase, x_k, for three different values of total occupancies, θ_{mix} = 0.1, 0.3, and 0.5. (d) Plot of the values of mole fraction of C3 in the adsorbed phase, x_k, corresponding to the maximum entropy (by equations (6-5), and (6-6)), and minimum free energy (blue line, equation (6-12)), as a function of the occupancy, θ_{mix}. Also shown by the symbols in (d) are the CBMC simulated values of x_k.

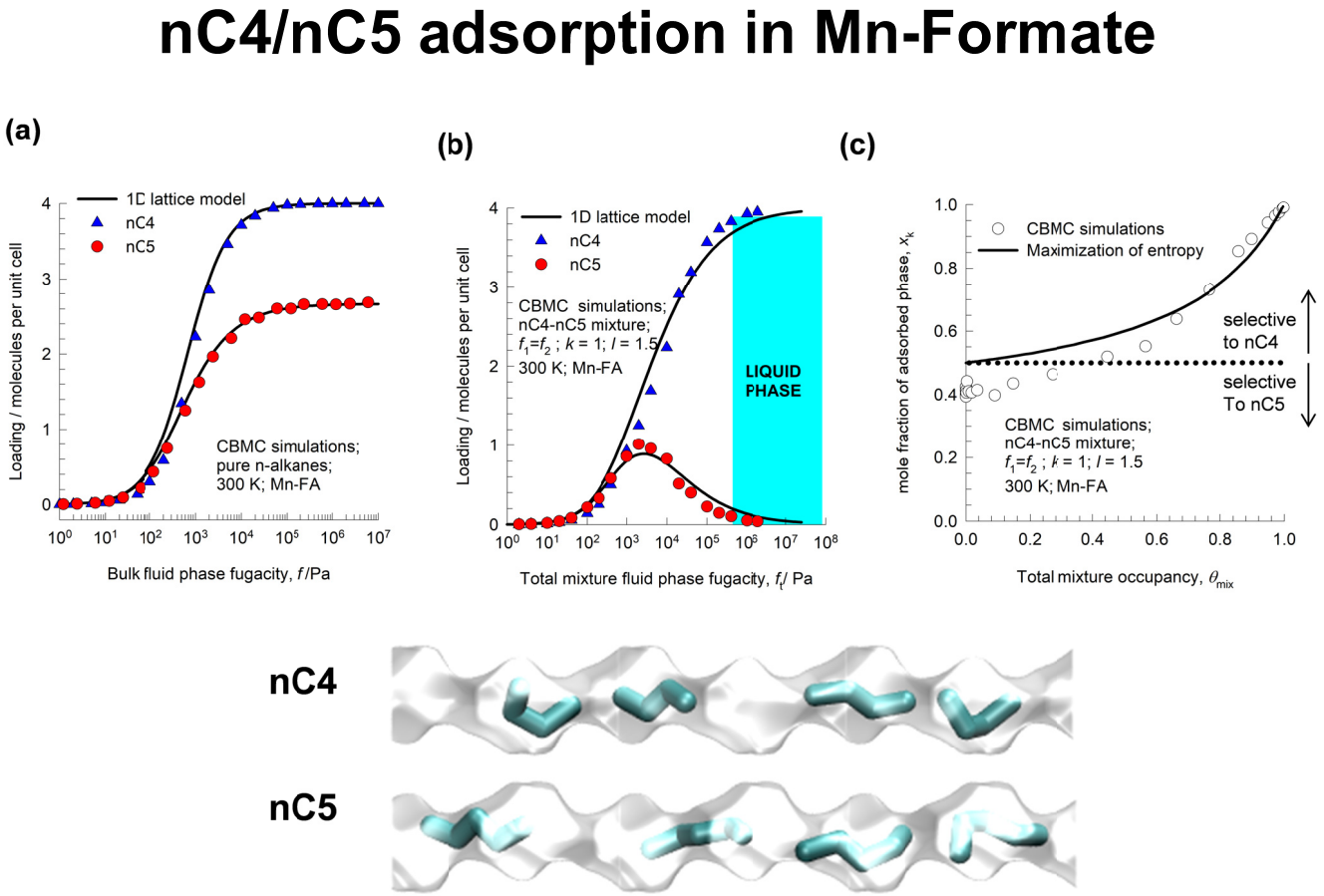

Figure 8-4. (a) CBMC data[51] (symbols) for unary isotherms of nC4 and nC5 in Mn-FA at 300 K, compared with the fits of the 1D lattice model. (b) Comparison of the CBMC simulations (shown by symbols) for nC4/nC5 mixture adsorption with the estimations of the 1D lattice model (shown by continuous solid lines). The range of liquid phase operation is indicated by the shaded region; the transition between vapor and liquid bulk phase is determined using the Peng-Robinson equation of state. (c) Plot of the values of the composition of n-butane in the adsorbed phase, x_k, corresponding to the maximum entropy (by equations (6-5), and (6-6)), as a function of the occupancy, θ_{mix}. Also shown by the symbols in (c) are the CBMC simulated values of x_k. Also shown are computational snapshots of the location of n-alkanes in the 1D zig-zag channels.

9 Adsorption of n-alkanes in Cobalt Formate (Co-FA)

Consider the adsorption of n-alkanes, with C numbers ranging from 1 to 7, in cobalt formate (Co-FA) framework.[51] The Co-FA structure consists of 1D zig-zag channels; see the pore landscapes in Figure 9-1. The network exhibits diamondoid connectivity and the overall framework gives rise to zig-zag channels along the *b* axis. The effective pore size of these one-dimensional channels is 5 – 6 Å; one unit cell of Co-FA comprises a total of four distinct channel "segments"; each channel segment forms part of the repeat zig-zag structure. The pore topology of Co-FA is analogous to that of Mn-FA. Figure 9-2 presents computational snapshots of the conformations of adsorbed n-alkanes molecules within the zig-zag 1D channel segments of Co-FA. One unit cell of Co-FA contains four channel segments.

Configurational-Bias Monte Carlo (CBMC) simulations of the unary adsorption isotherms of C1, C2, C3, nC4, nC5, nC6, and nC7 alkanes are presented in Figure 9-3(a). The hierarchy of adsorption strengths for C1, C2 and C3 is as expected; increasing chain length results in higher adsorption strength. The saturation capacity for C1, C2, and C3 are found to be 4 molecules per unit cell (uc), corresponding to one molecule per channel segment. However, with increasing chain lengths beyond C3 we note an unusual adsorption hierarchy: C3 > nC4 > nC5; the length of each channel segment is commensurate with that of the propane molecule and longer molecules such as n-pentane (nC5), and n-hexane (nC6) must straddle two channel segments. The length of the nC6 molecule is commensurate with the length of two channel segments, and further increase in chain length, results in the expected hierarchy, i.e. nC7 > nC6 > nC5. The saturation capacities of nC5, nC6, and nC7 are restricted to 2 molecules uc^{-1}.

Due to commensurate-incommensurate adsorption, the hierarchy of adsorption strengths displays non-monotonic characteristics in the plot of Henry coefficient vs C chain length; see Figure 9-3(b). The non-monotonous adsorption characteristics, along with differences in saturation capacities can be exploited to achieve unusual separation possibilities.

9.1 Adsorption of C3/nC6 mixtures in Co-FA

From the pure component adsorption isotherms in Figure 9-4(a) we note that at low pressures the adsorption strengths of C3 is nearly the same as that of nC6; this is evidenced also in Figure 9-3(b) wherein the Henry constants for C3 and nC6 are nearly equal to each other. However, the saturation capacity of C3 is twice that of nC6. We can devise a strategy for separating C3 from nC6 by exploiting the differences in the saturation capacities. CBMC simulations of the component loadings for a C3/nC6 mixture with equal partial fluid phase fugacities, $f_1 = f_2$, are shown in Figure 9-4(b). When operating at fugacities $f_t = f_1 + f_2 > 1$ MPa, we note that the adsorbed phase contains practically no nC6 and predominantly loaded with C3. The preferential adsorption of C3 is due to entropy effects that favor the molecule with the higher saturation capacity, i.e. higher "packing efficiency".

To elucidate the reasons behind the exclusion of nC6 at fugacities $f_t > 1$ MPa, we use the model of Dávila et al.[45] for a 1D lattice. Since C3 (species *k*) adsorbs commensurately with one channel segment, we take *k*=1.The linear hexane (species *l*) adsorbs commensurately with two channel segments, and so we take *l*=2. To determine the component loadings in the units of molecules per unit cell, we take *M* = 4. The component loading of C3, in molecules per unit cell, is given by $N_k = \theta_k \frac{M}{k}$. The component loading of nC6, in molecules per unit cell, is given by $N_l = \theta_l \frac{M}{l}$.

The unary isotherms can be described quantitatively by equations (6-8) of the 1D lattice model of Dávila et al.[45] Since C3 (species *k*) adsorbs commensurately with one channel segment, we take *k*=1, *M* = 4/uc, and $\frac{M}{k} = N_{k,sat} = 4/\text{uc}$. The linear hexane nC6 (species *l*) adsorbs commensurately with two channel segments, and so we take *l*=2, *M* = 4/uc, and $\frac{M}{l} = N_{l,sat} = 2/\text{uc}$. A good match between the 1D lattice model and CBMC simulations of the unary isotherms is obtained with the fitted binding constants are $b_k = 2.4\times10^{-4}$ Pa^{-1}, and $b_l = 2.4\times10^{-4}$ Pa^{-1}; see continuous solid lines Figure 9-4(a). This implies that

the unary isotherm is described by the Langmuir model $\frac{\theta_k}{(1-\theta_k)} = b_k f; \quad \theta_k = \frac{kN_k}{M}$. The isotherm for nC6 is described by the model $\frac{\left(1-\frac{\theta_l}{2}\right)\frac{\theta_l}{2}}{(1-\theta_l)^2} = b_l f; \quad \theta_l = \frac{lN_l}{M}$; this model can be expressed as a quadratic equation in θ_l, and an explicit expression of θ_l as a function of $b_l f$ is derivable.

To elucidate, and quantify, the reasons behind the total exclusion of nC6 for $f_t = f_1 + f_2 > 1$ MPa, we apply equations (6-7) of the 1D lattice model of Dávila et al.[45] The component loading of C3, in molecules per unit cell, is given by $N_k = \theta_k \frac{M}{k}$. The component loading of nC6, in molecules per unit cell, is given by $N_l = \theta_l \frac{M}{l}$. The calculations of the component loadings are indicated by the continuous solid lines in Figure 9-4(b). The lattice model is able to phenomena of entropic exclusion of nC6. It was also verified that use of the IAST, along with the unary isotherms, $\frac{\theta_k}{(1-\theta_k)} = b_k f; \quad \theta_k = \frac{q_k}{q_{k,sat}} = \frac{kN_k}{M}$ $\frac{\left(1-\frac{\theta_l}{2}\right)\frac{\theta_l}{2}}{(1-\theta_l)^2} = b_l f; \quad \theta_l = \frac{lN_l}{M}$ for C3, and nC6, respectively, results in numerical results that are identical to the 1D lattice model of Dávila et al.[45]

Figure 9-4(c) presents calculations of the dimensionless entropy per site $\frac{S}{k_B M}$, using equation (6-4), for a binary mixture of C3 (k=1), and nC6 (l=2) in 1D lattice as a function of the mole fraction of propane in the adsorbed phase, $x_k = \frac{N_k}{N_k + N_l} = \frac{\frac{\theta_k}{k}}{\frac{\theta_k}{k} + \frac{\theta_l}{l}}$, for three different values of total occupancies, $\frac{N_k + N_l}{M} = \frac{\theta_k}{k} + \frac{\theta_l}{l} = \theta_{mix}$ = 0.1, 0.3, and 0.5. At the lowest occupancy, θ_{mix} = 0.1, the maximum in the $\frac{S}{k_B M}$ occurs at the adsorbed composition $x_k \approx 0.5$. With increasing total occupancies, θ_{mix}, the

maximum in the $\frac{S}{k_B M}$ occurs at values the adsorbed composition x_k, that are significantly richer in propane, the shorter alkane. This is because the vacancies are more efficiently filled up by molecules with the shorter chain length.

The symbols in Figure 9-4(d) are the CBMC simulated data on the adsorbed phase mole fractions x_k plotted as function of the total occupancy, θ_{mix}. Also plotted in Figure 9-4(d) are the calculations using equations (6-5), and (6-6), that are based on the maximization of entropy concept. For $\theta_{mix} > 0.5$ the CBMC data are in excellent agreement with the calculations using equations (6-5), and (6-6), that are based on the maximization of entropy concept; this confirms that the separation is driven by entropic effects as pore saturation is approached.

It is important to stress that the lattice model can only be applied if the unary isotherms are fitted using $\frac{\theta_k}{(1-\theta_k)} = b_k f; \quad \theta_k = \frac{q_k}{q_{k,sat}} = \frac{kN_k}{M}$ $\frac{\left(1-\frac{\theta_l}{2}\right)\frac{\theta_l}{2}}{(1-\theta_l)^2} = b_l f; \quad \theta_l = \frac{lN_l}{M}$ for C3, and nC6, respectively. The IAST can be applied to the unary isotherms fitted in any manner, and are not restricted to the foregoing forms. For example, if the unary isotherms for both C3 and nC6 are fitted with the 1-site Langmuir isotherm models: for C3 with $b_{C3} = 3\times10^{-4}$ Pa^{-1}; $\Theta_{C3,sat} = 4$ uc^{-1}; for nC6, the Langmuir binding constant, $b_{nC6} = 2.65\times10^{-4}$ Pa^{-1}, $\Theta_{nC6,sat} = 2$ uc^{-1}. The IAST calculations with these isotherm fits are compared with the CBMC simulations in Figure 9-5.

9.2 List of Figures for Adsorption of n-alkanes in Cobalt Formate (Co-FA)

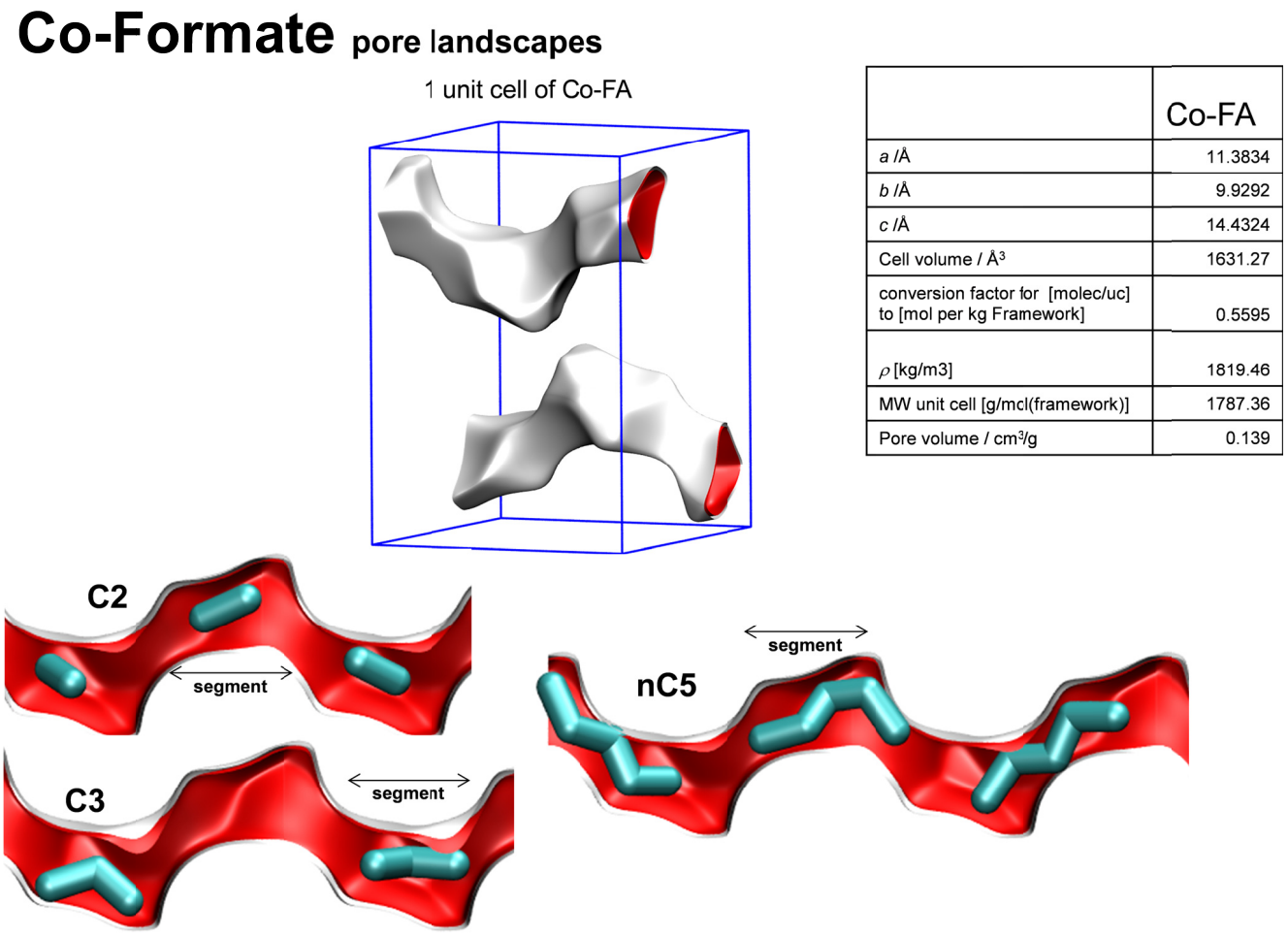

	Co-FA
a /Å	11.3834
b /Å	9.9292
c /Å	14.4324
Cell volume / Å^3	1631.27
conversion factor for [molec/uc] to [mol per kg Framework]	0.5595
ρ [kg/m3]	1819.46
MW unit cell [g/mcl(framework)]	1787.36
Pore volume / cm^3/g	0.139

Figure 9-1. Pore landscape, and structural details of Co-Formate. Also shown are computational snapshots of the location of n-alkanes in the 1D zig-zag channels.

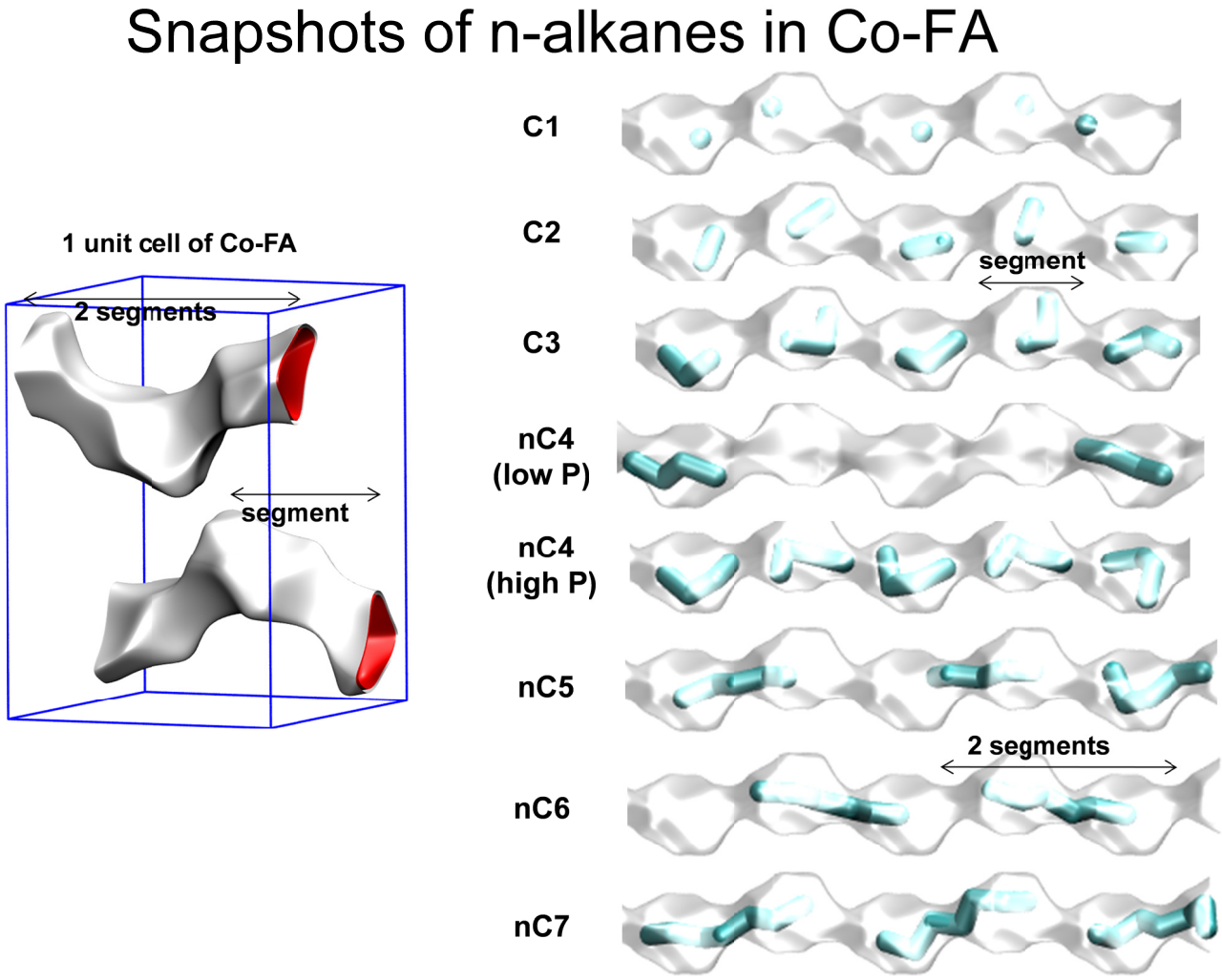

Figure 9-2. Snapshots showing the location of linear alkanes within the zig-zag 1D channel segments of Co-FA.

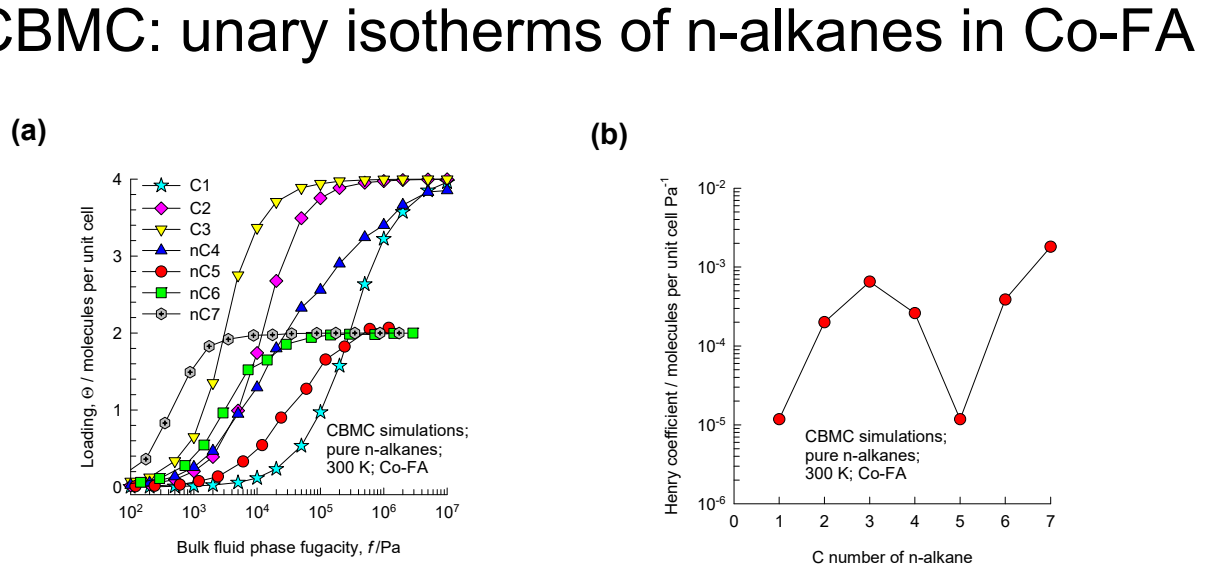

Figure 9-3. (a) CBMC simulations of adsorption isotherms for C1, C2, C3, nC4, nC5, nC6 and nC7 in Co-FA at 300 K. (b) Henry coefficients for n-alkanes in Co-FA as a function of C number.

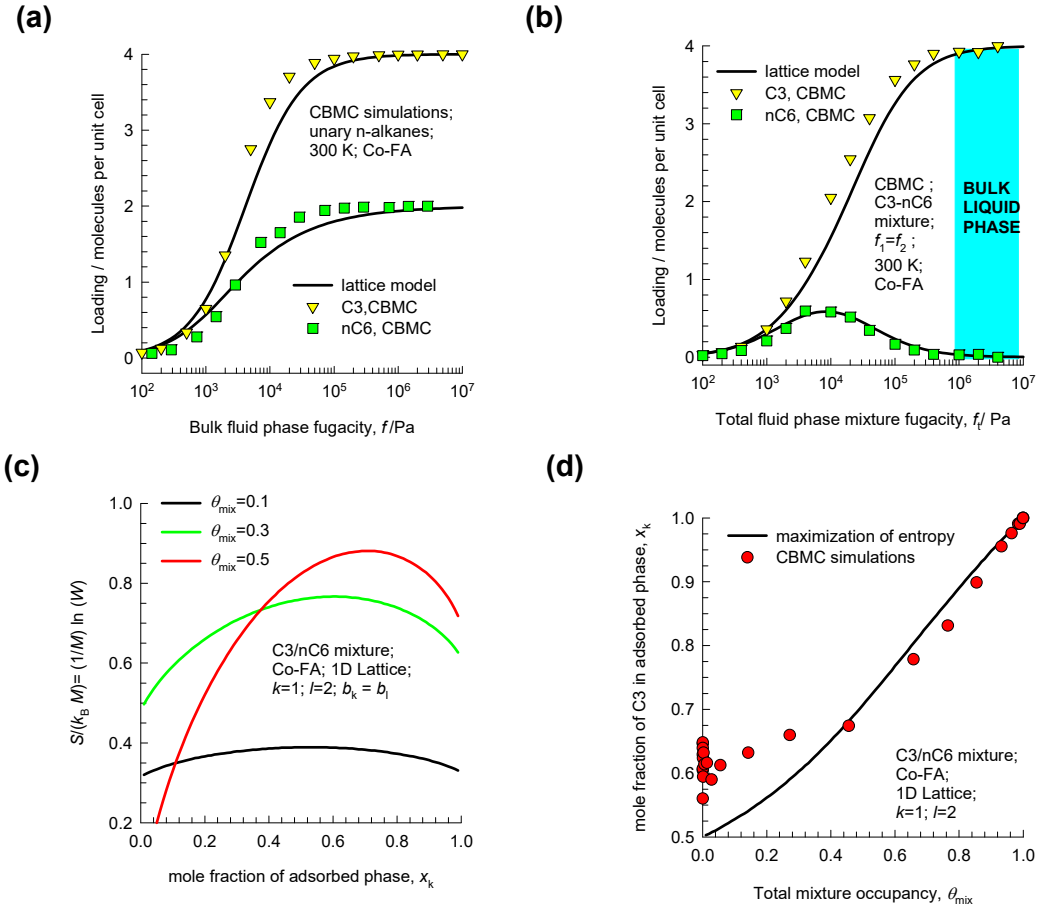

Figure 9-4. (a) CBMC data[51] (symbols) for unary isotherms of C3 and nC6 in Co-FA at 300 K, compared with the fits of the 1D lattice model. (b) CBMC simulations for C3/nC6 mixture adsorption in Co-FA at 300 K with the estimations of the 1D lattice model. (c) Calculations of the dimensionless entropy per site $\frac{S}{k_B M}$, as a function of the mole fraction of propane in the adsorbed phase, x_k, for three different values of total occupancies, θ_{mix} = 0.1, 0.3, and 0.5. (d) Plot of the mole fraction of C3 in the adsorbed phase, x_k, corresponding to the maximum entropy (by equations (6-5), and (6-6)), as function of the mixture occupancy, θ_{mix}. Also shown by the symbols in (d) are the CBMC simulated values of x_k

IAST vs CBMC for C3/nC6/CoFA

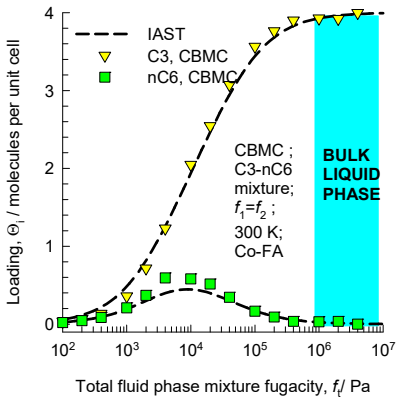

Figure 9-5. CBMC simulations for C3/nC6 mixture adsorption in Co-FA at 300 K compared with the estimations of the IAST. In the IAST calculations, the unary isotherms for both C3 and nC6 are fitted with the 1-site Langmuir model.

10 Separating hexane isomers with MOR zeolite

MOR zeolite (Mordenite) consists of 12-ring (7.0 Å × 6.5 Å) 1D channels, connected to 8-ring (5.7 Å × 2.6 Å) pockets; the pore landscapes and structural details are provided in Figure 10-1, and Figure 10-2.

Some representative snapshots [52] showing the siting and conformation of hexane isomers along one of the 12-ring channels, 8 unit cells long, are presented in Figure 10-2 for a total bulk fluid phase fugacity f_t = 1 MPa. Within the same channel length we find five nC6 molecules, seven 2MP molecules and nine 22DMB molecules. The higher loading with increased degree of branching is due to increased degree of compactness of the molecules, i.e. smaller footprint. The more compact the molecule, the higher the packing efficiency within the one-dimensional channels. This point is emphasized further by determining the projected lengths of the molecules of the hexane isomers on the *z*-axis for f_t = 1 MPa; the data on the distribution of molecular lengths are shown in Figure 10-3(a) The projected lengths are obtained by monitoring the positions of each of the pseudo-atoms in the alkane molecules and determining the maximum span of the molecule by projecting the positions of the pseudo-atoms along the direction of the 12-ring channels. The mean lengths of the hexane isomers are 5.2 Å, 4.3 Å and 3 Å for nC6, 2MP and 22DMB respectively. This data also explains why the saturation capacity for 22DMB is significantly higher (Θ_{sat} = 2 molecules uc^{-1}), compared to that for 2MP (= 1.7 molecules uc^{-1}) and nC6 (= 1.5 molecules uc^{-1}); see CBMC simulations of the unary adsorption isotherms in Figure 10-3(b).

CBMC simulations for nC6/22DMB mixture adsorption shows that for total fugacities, $f_t = f_2 + f_2 >$ 100 kPa, the selectivity is heavily in favor of the di-branched isomer and the linear isomer is virtually excluded from the 1D channels of MOR; see Figure 10-3(c,d).

10.1 1D Lattice model for nC6/22DMB mixture adsorption in MOR zeolite

To elucidate the reasons for the selectivity reversal at bulk fluid fugacities f_t > 50 kPa, we use the model of Dávila et al.[45] for a 1D lattice. The ratio of the "effective lengths" of nC6 (species *k*) and 22DMB (species *l*) is taken to be inversely proportional to the saturation capacities, i.e. 2:1.5. We take *k*=1.333, and *l*=1. To determine the component loadings in the units of molecules per unit cell, we take M = 2. The component loading of nC6, in molecules per unit cell, is given by $N_k = \theta_k \frac{M}{k}$. The component loading of 22DMB, in molecules per unit cell, is given by $N_l = \theta_l \frac{M}{l}$.

The unary isotherms can be described quantitatively by equations (6-8) of the 1D lattice model of Dávila et al.[45] For nC6 (species *k*), we take *k*=1.333, M = 2/uc, and $\frac{M}{k} = N_{k,sat} = 1.5/\text{uc}$. For 22DMB, we take *l*=1, M = 2/uc, and $\frac{M}{l} = N_{l,sat} = 2/\text{uc}$. A good match between the 1D lattice model and CBMC simulations of the unary isotherms is obtained with the fitted binding constants are $b_k = 4\times10^{-4}$ Pa^{-1}, and $b_l = 3\times10^{-4}$ Pa^{-1}; see continuous solid lines in Figure 10-4(a).

To elucidate, and quantify, the reasons behind the selectivity reversal for $f_t = f_2 + f_2 > 50$ kPa, we apply equations (6-7) of the 1D lattice model of Dávila et al.[45] The calculations of the component loadings are indicated by the continuous solid lines in Figure 10-4(b). The lattice model is able to capture the selectivity reversal in favor of 22DMB in a quantitative manner. We also verified, that the IAST calculations with the unary isotherms described by equations (6-8), yields precisely the same component loadings as the Dávila model; this is to be expected.

The symbols in Figure 10-4(c) are the CBMC simulated data on the adsorbed phase mole fractions of 22DMB, $x_l = 1 - x_k$, plotted as function of the total occupancy, θ_{mix}; these data are in reasonably good agreement with the calculations using equation (6-12), shown by the continuous solid blue line. Also shown by the continuous solid black line are the calculations using equations (6-5), and (6-6), that are based on the maximization of entropy concept. The CBMC simulations for the adsorbed phase mole

fraction of 22DMB fall slightly below the solid black line because of the slightly stronger binding constant for nC6.

The important advantage of the IAST over the lattice model is that the unary isotherms can be fitted to any model, and are not restricted to equations (6-8) used in the foregoing lattice model calculations. Figure 10-5 presents a comparison of the CBMC simulations (shown by symbols) for nC6/22DMB mixture adsorption with IAST estimations using the unary isotherms for nC6 and 22DMB that are both fitted with 1-site Langmuir parameters, as listed in Table 10-1. As expected, the IAST model captures the selectivity reversal quantitatively.

10.2 Nitta multi-site model for nC6/22DMB mixture adsorption in MOR zeolite

We now examine the applicability of the multi-site Langmuir model Nitta et al.[43] to described nC6 (component *k*)/22DMB (component *l*) mixture adsorption in MOR zeolite. The first step is the fitting of the unary isotherm data with equation (5-1). For nC6 (species *k*), we take *k*=1.333, *M* = 2/uc, and $q_{k,sat} = 1.5/\text{uc}$. For 22DMB, we take *l*=1, *M* = 2/uc, and $q_{l,sat} = 2/\text{uc}$. The values of the fitting binding constants are $b_k = 6\times10^{-4}$ Pa^{-1}, and $b_l = 3\times10^{-4}$ Pa^{-1}; see Figure 10-6(a).

A numerical solution of the set of equations (5-2) using the Given-Find solve block of MathCad 15[41] yields component loadings that are in good agreement with the CBMC simulated data; see Figure 10-6(b). We also verified that the IAST model gives numerical results that are identical to the Nitta model, provided the unary isotherms are described by equation (5-1), In this case, the IAST calculations are more time intensive because the unary isotherm for nC6 are not explicit in the component loading.

10.3 List of Tables for Separating hexane isomers with MOR zeolite

Table 10-1. 1-site Langmuir parameters for hexane isomers in MOR at 433 K. The fits correspond to CBMC simulations. Note that the saturation capacities are specified in molecules per unit cell. Multiply these by 0.34673 to obtain the loading values in mol per kg framework.

$\Theta = \frac{\Theta_{sat} bf}{1 + bf}$	Θ_{sat}/molecules uc^{-1}	b/Pa^{-1}
nC_6	1.5	4×10^{-4}
2MP	1.7	4×10^{-4}
2DMB	2	3×10^{-4}

10.4 List of Figures for Separating hexane isomers with MOR zeolite

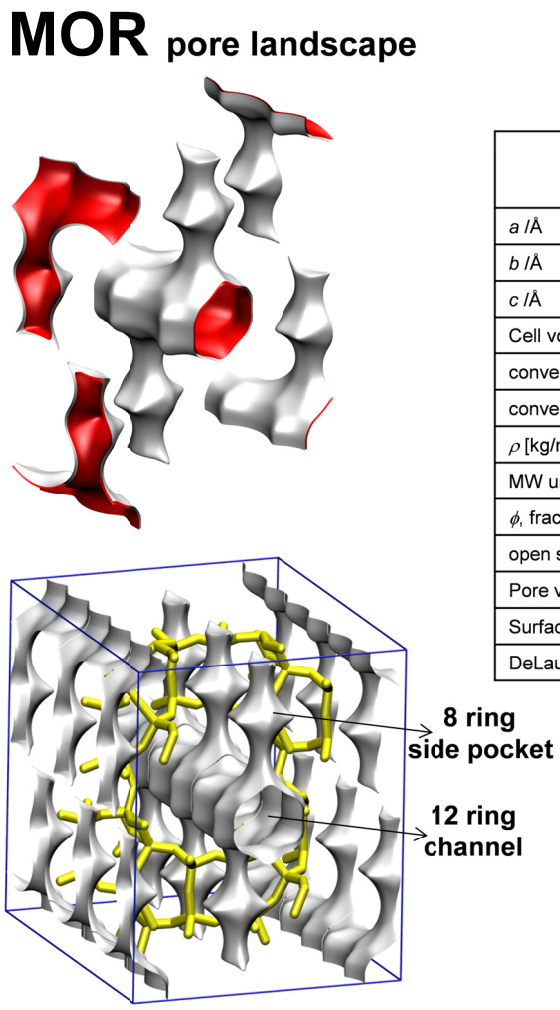

	MOR
a /Å	18.094
b /Å	20.516
c /Å	7.524
Cell volume / Å^3	2793.033
conversion factor for [molec/uc] to [mol per kg Framework]	0.3467
conversion factor for [molec/uc] to [kmol/m^3]	2.0877
ρ [kg/m3]	1714.691
MW unit cell [g/mol(framework)]	2884.07
ϕ, fractional pore volume	0.285
open space / Å^3/uc	795.4
Pore volume / cm^3/g	0.166
Surface area /m^2/g	417.0
DeLaunay diameter /Å	6.44

Figure 10-1. Structural details for MOR zeolite.

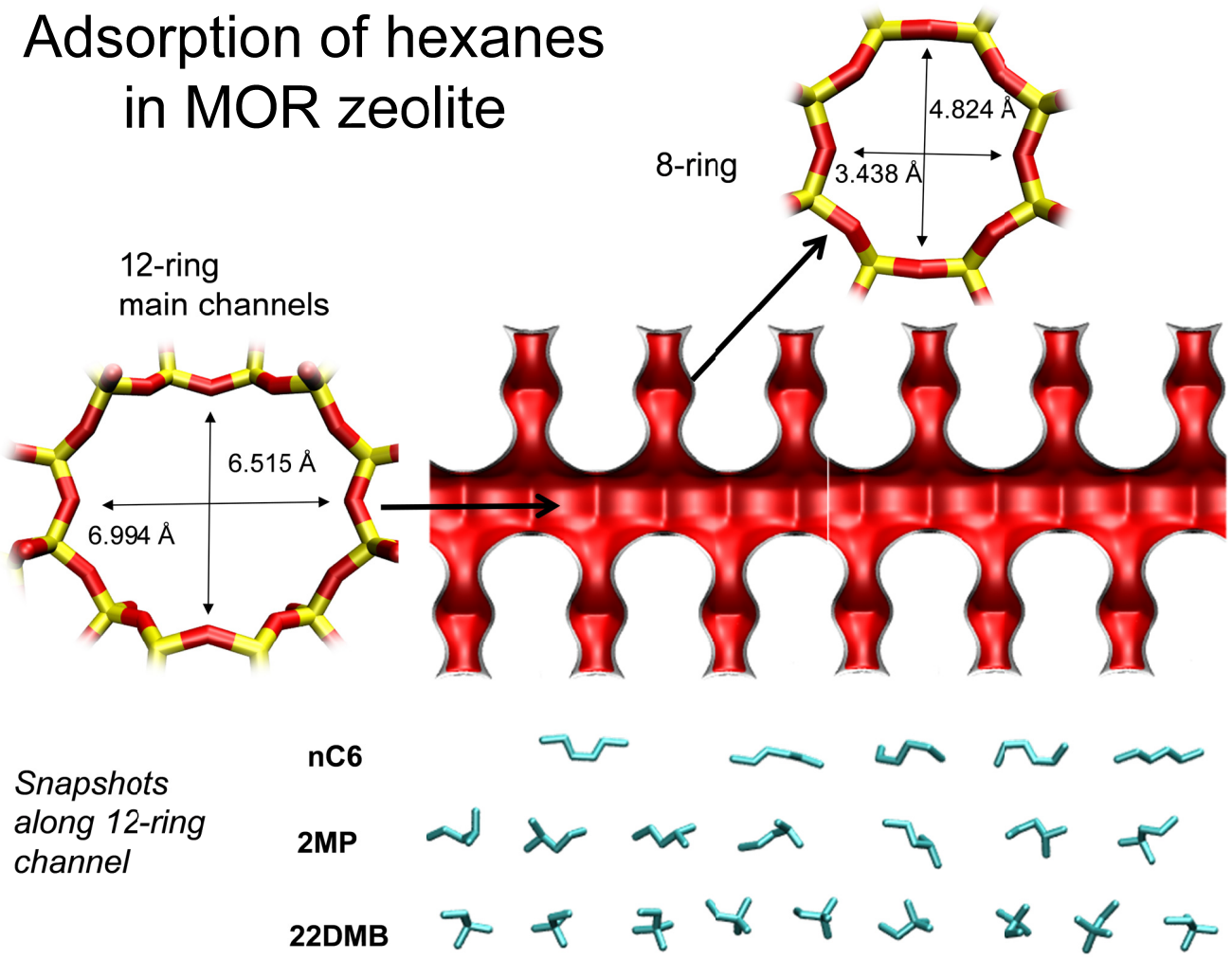

Figure 10-2. Pore landscape of MOR zeolite.[52] Snapshots of the conformation and siting of siting of nC6, 2MP, and 22DMB along 1D 12-ring channel, 8 unit cells long.

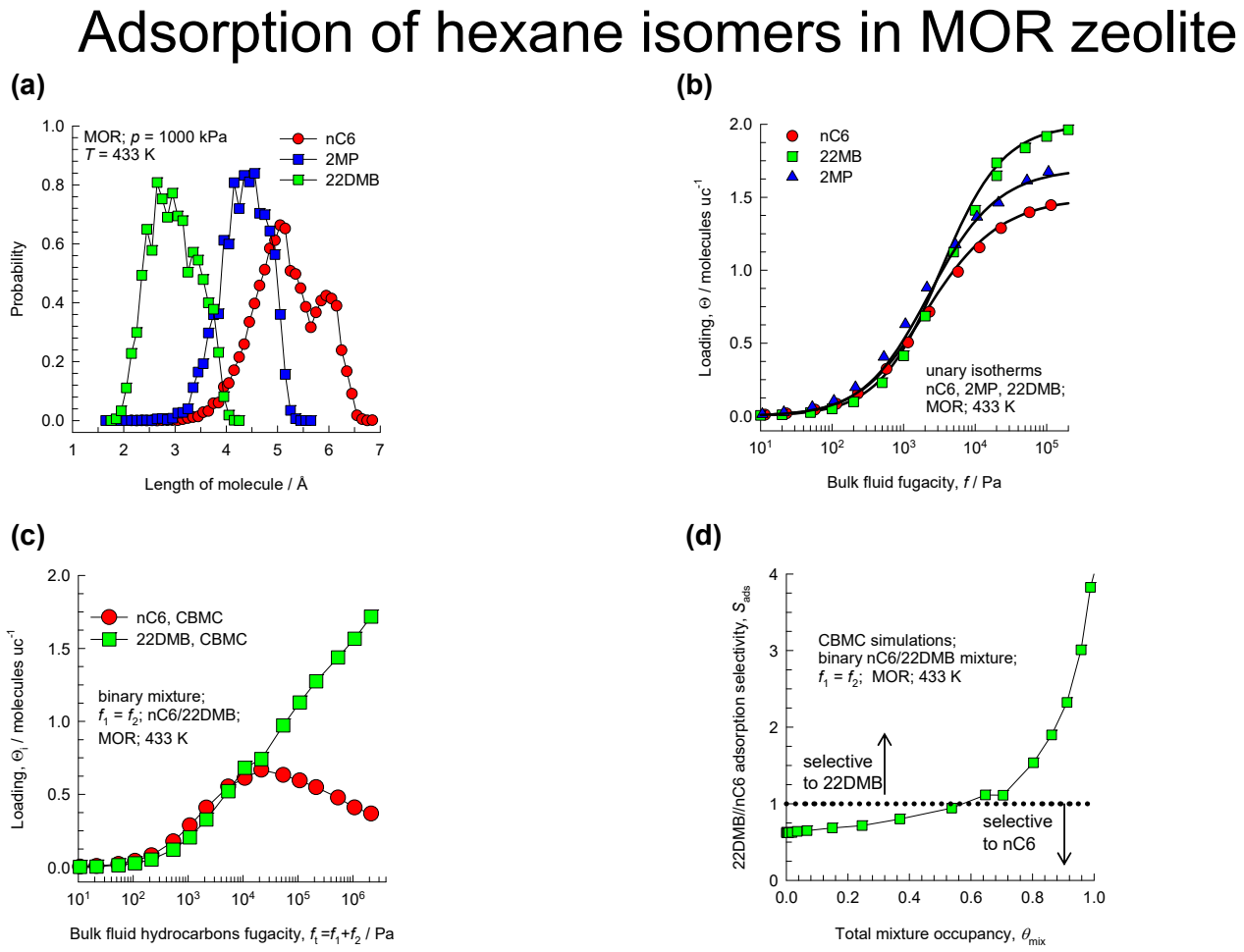

Figure 10-3. (a) Distribution of lengths of hexane isomers (f_t = 1000 kPa, T = 433 K) along the z-direction of MOR obtained from CBMC simulations. (b) CBMC simulations [52] of the unary sorption isotherms for pure hexane isomers nC6, 2MP, 22DMB in MOR at 433 K. (c) CBMC simulations[52] for equimolar binary mixture nC6/22DMB in MOR at T = 433 K. (d) Plot of 22DMB/nC6 adsorption selectivity as a function of the total mixture occupancy, θ_{mix}.

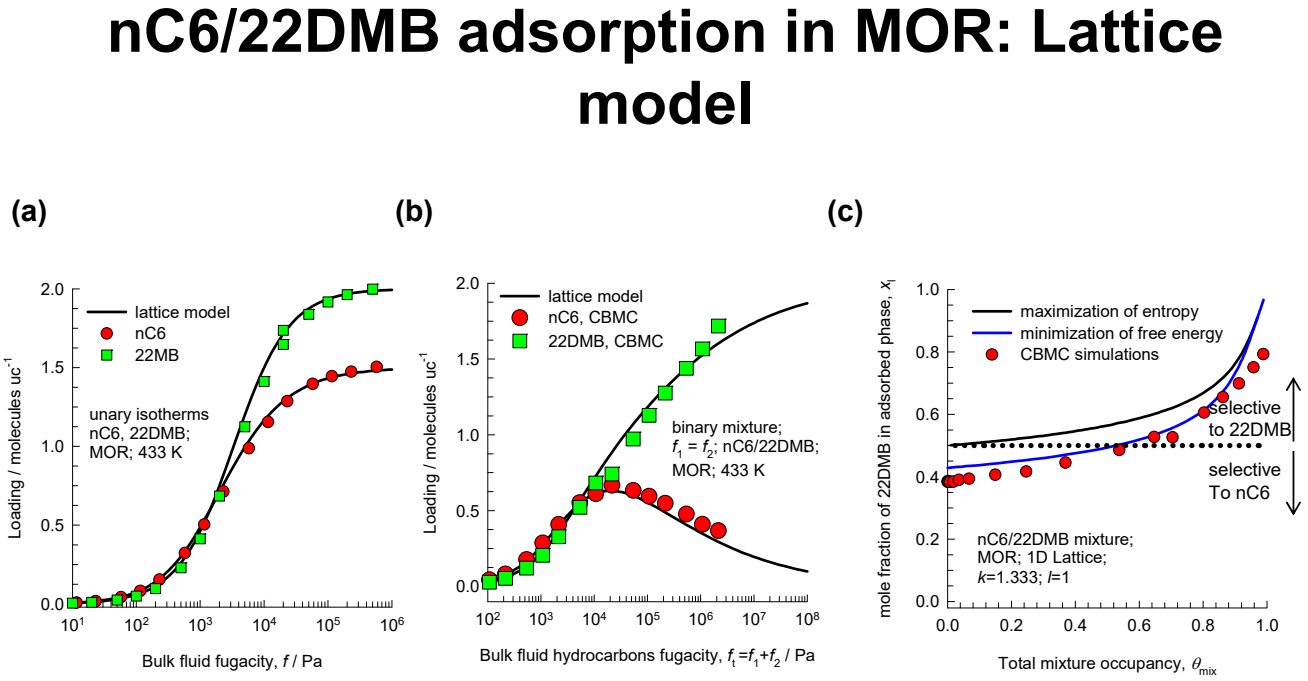

Figure 10-4. (a) CBMC data for unary isotherms of nC6 and 22DMB in MOR zeolite, compared with the fits of the 1D lattice model. (b) Comparison of the CBMC simulations (shown by symbols) for nC6/22DMB mixture adsorption with the estimations of the 1D lattice model (shown by continuous solid lines). (c) Plot of the values of the adsorbed phase mole fractions of 22DMB $x_l = 1 - x_k$ corresponding to the maximum entropy (by equations (6-5), and (6-6)), and minimum free energy (blue line, equation (6-12)), as a function of the occupancy, θ_{mix}. Also shown by the symbols in (c) are the CBMC simulated values of $x_l = 1 - x_k$.

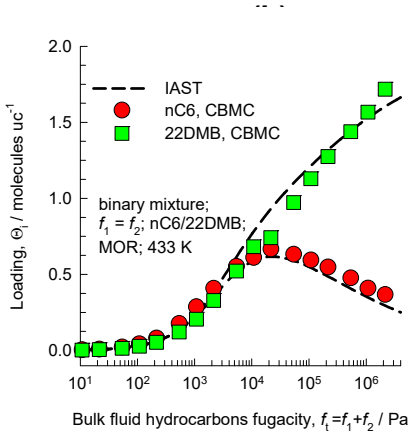

Figure 10-5. Comparison of the CBMC simulations (shown by symbols) for nC6/22DMB mixture adsorption with IAST estimations. For the IAST calculations, the unary isotherms for nC6 and 22DMB are both fitted with 1-site Langmuir parameters, as listed in Table 10-1.

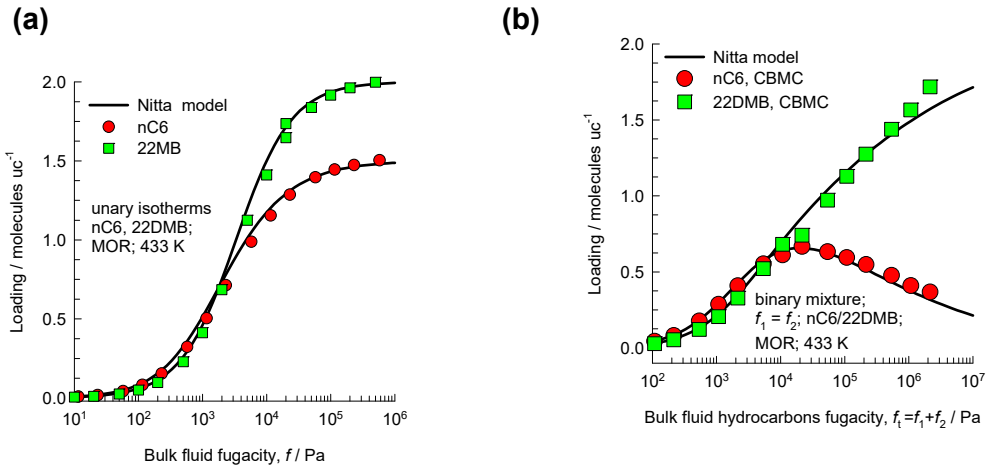

Figure 10-6. (a) CBMC data for unary isotherms of nC6 and 22DMB in MOR zeolite at 433 K, compared with the fits of the Nitta model. (b) Comparison of the CBMC simulations (shown by symbols) for nC6/22DMB mixture adsorption in MOR at 433 K with the estimations of the Nitta model (shown by continuous solid lines).

11 Entropy effects for mixture adsorption in MFI zeolite

11.1 Adsorption of alkanes in MFI

MFI zeolite (also called silicalite-1) has a topology consisting of a set of intersecting straight channels, and zig-zag (or sinusoidal) channels of approximately 5.5 Å size. The pore landscapes and structural details are provided in Figure 11-1, and Figure 11-2. Snapshots showing the location and conformations of n-butane (nC4) and n-hexane (nC6) are shown in Figure 11-3(a,b); the length of an n-hexane molecule is commensurate with the distance between intersections of MFI zeolite. CBMC simulations of the unary adsorption isotherms of C1, C2, C3, nC4, nC5, and nC6 alkanes at 300 K are shown in Figure 11-3(c). The saturation capacities of the linear alkanes decrease progressively with increasing chain length. Due to commensurate adsorption of nC6, the saturation capacity of nC6 is precisely 8 molecules uc^{-1}. Figure 11-3(d) presents CBMC simulation data for the adsorption selectivity of C1/C2 and C1/C3 mixtures. For both these mixtures, there is a range of bulk fluid phase mixture fugacities, $f_t = f_1 + f_2$, for which the adsorption selectivity $S_{l/k} = \frac{N_l/N_k}{f_k/f_l}$ is constant; in this regime the separation selectivity is dictated by the ratio of binding constants. However, as pore saturation is approached, there is a tendency for a reduction in $S_{l/k} = \frac{N_l/N_k}{f_k/f_l}$ in favor of the guest alkane with the shorter chain length, a clear manifestion of entropy effects.

Due to configurational considerations, branched alkanes prefer to locate at the channel intersections because of the extra “leg room” that is available here. This is evident in Figure 11-4(a,b), showing snapshots of the location of iso-butane (iC4), and 2-methylpentane (2MP) within the intersecting channels of MFI. An extra “push” is required to locate these molecules within the channel interiors. This extra push results in an inflection in the pure component isotherms at a loading of 4 molecules per unit

cell.[53-56] See CBMC simulation data for iso-butane (iC4), 2-methylpentane (2MP), and 2,2dimethylbutane (22DMB) in Figure 11-4(c). Cyclic hydrocarbons, such as cyclohexane, Benzene (Bz), and ethylbenzene (EthBz) also prefer to locate at the intersections; the unary isotherm for benzene also exhibits a strong inflection at a loading, $\Theta = 4$ molecules per unit cell.

11.2 Adsorption of n-hexane/2-methylpentane mixtures in MFI zeolite

Separations of hexane isomers with MFI are based on the exploitation of the differences in molecular configurations; we underscore the significance of configurational entropy effects in adsorption of nC6/2MP mixtures at 300 K. CBMC simulation data for the unary adsorption isotherms are presented in Figure 11-5(a). We use the square lattice model of Azizian and Bashiri,[47] that is formally equivalent to the 1D lattice model of Dávila et al.[45] The unary isotherms can be described quantitatively by equations (6-8). For nC6 (species k), we take k=1, M = 8/uc, and $\frac{M}{k} = N_{k,sat} = 8/\text{uc}$. For 22DMB, we take l=2, M = 8/uc, and $\frac{M}{l} = N_{l,sat} = 4/\text{uc}$. A reasonably good match between equations (6-8) and the CBMC simulations of the unary isotherms is obtained with the choice $b_k = 1$ Pa^{-1}, and $b_l = 1.5$ Pa^{-1}; see Figure 11-5(a). It is noteworthy that the binding constant of 2MP is slightly higher than that of nC6.

The CBMC simulations of nC6/2MP mixture adsorption at 300 K are shown by the symbols in Figure 11-5(b). Up to total hydrocarbons fugacities $f_t = f_1 + f_2 = 2$ Pa, the component loadings increase in an expected manner; increasing f_t leads to a corresponding increase in the component loading. At $f_t = 2$ Pa, the total loading $\Theta_t = 4$/uc, signifying that all the intersection sites are fully occupied. To further adsorb 2MP we need to provide an extra “push”. Energetically, it is more efficient to obtain higher mixture loadings by "replacing" the 2MP with nC6; this *configurational entropy* effect is the reason behind the curious maxima in the 2MP loading in the mixture. The CBMC mixture simulations are in good agreement with the experimental of Titze et al.[57] determined by Infra-Red Microscopy (IRM). The IRM experiments offer direct experimental verification of the configurational entropy effects in mixture adsorption for nC6/2MP that was first observed on the basis of CBMC mixture simulations.[54, 58]

To elucidate, and quantify, the reasons behind the selectivity reversal for $f_t = f_2 + f_2 > 2$ Pa, we apply equations (6-7) of Dávila et al.[45] The calculations of the component loadings are indicated by the continuous solid lines in Figure 11-5(b). The lattice model is able to capture the selectivity reversal in favor of nC6 in a quantitative manner.

The symbols in Figure 11-5(c) are the CBMC simulated data on the adsorbed phase mole fractions of nC6, x_k, plotted as function of the total occupancy, θ_{mix}; these data are in reasonably good agreement with the calculations using equation (6-12), shown by the continuous solid blue line. Also shown by the continuous solid black line are the calculations using equations (6-5), and (6-6), that are based on the maximization of entropy concept. The CBMC simulations for the adsorbed phase mole fraction of nC6 fall slightly below the solid black line because of the slightly stronger binding constant for 2MP.

MFI (silicalite) appears in the list of materials patented by Universal Oil Products (UOP) for separation of hexane isomers:[59-61] "The adsorbent may be silicalite, ferrierite, zeolite Beta, MAPO-31, SAPO-31, SAPO-11, zeolite X ion exchanged with alkaline cations, alkaline earth cations, or a mixture thereof, and zeolite Y ion exchanged with alkaline cations…." Even though a vast number of zeolites are named in the patent, a careful examination of the separation performance of all zeolites[8, 55, 62] reveals the pulse chromatographic separation data, as presented in the UOP patents, and reproduced in Figure 11-6, is obtained with MFI zeolite. This chromatographic pulse data clearly shows the potential of MFI zeolite to separate a mixture of hexane isomers into three different fractions consisting of linear, mono-branched, and di-branched isomers. The separation relies essentially on configurational entropy effects; mono-branched and di-branched isomers prefer to locate at the intersections of MFI, because these are too bulky to locate within the channels.[3]

11.3 Nitta multi-site model for nC6/2MP mixture adsorption in MFI zeolite

We now examine the applicability of the multi-site Langmuir model Nitta et al.[43] to described nC6 (component *k*)/2MP (component *l*) mixture adsorption in MFI zeolite. The first step is the fitting of the unary isotherm data with equation (5-1). For nC6 (species *k*), we take *k*=1, *M* = 8/uc, and $q_{k,sat} = 8$/uc.

For 2MP, we take l=2, M = 8/uc, and $q_{l,sat} = 4/\text{uc}$. The values of the fitting binding constants are b_k = 1 Pa^{-1}, and b_l = 4 Pa^{-1}; see Figure 11-7(a).

A numerical solution of the set of equations (5-2) using the Given-Find solve block of MathCad 15[41] yields component loadings that are in good agreement with the CBMC simulated data; see Figure 11-7(b). We also verified that the IAST model gives numerical results that are identical to the Nitta model, provided the unary isotherms are described by equation (5-1),

11.4 Explicit model of Bai-Yang for nC6/2MP mixture adsorption in MFI

A cursory examination of the article by Bai and Yang titled "Thermodynamically Consistent Langmuir Model for Mixed Gas Adsorption" would lead the uninitiated reader to conclude that this model is suitable to describe nC6/2MP mixture adsorption in MFI zeolite. We shall demonstrate that the Bai-Yang does not capture the entropy effects in mixture adsorption.

For application of the Bai-Yang model, we consider the MFI zeolite to be made up of a total of 8 adsorption sites per unit cell: (a) 4 interesection sites, and (b) 4 channel sites; see Figure 11-8(a). The linear nC6 can inhabit any of the intersection and channel sites, and has a saturation capacity of 8 molecules per uc. The branched 2MP can only occupy the 4 intersection sites, and its saturation capacity is restricted ot 4 molecules per unit cell. The CBMC simulation data for unary isotherms can be adequately described by the Langmuir model, taking b_{nC6} = 1 Pa^{-1} for nC6 and b_{2MP} = 3 Pa^{-1} for 2MP, respectively; see Figure 11-8(b).

According to the Bai-Yang model, the competition for mixture adsorption manifests only at the intereresection site because both nC6 and 2MP can adsorb at these sites. The component loadings of nC6 and 2MP at the intersection sites for adsorption of mixtures with partial fugacities, f_1, and f_2 in the bulk fluid phase are:

$$q_{nC6,\text{intersection}} = \frac{4b_{nC6}f_1}{1+b_{nC6}f_1+b_{2MP}f_2}; \quad q_{2MP,\text{intersection}} = \frac{4b_{2MP}f_2}{1+b_{nC6}f_1+b_{2MP}f_2} \tag{11-1}$$

The branched 2MP cannot locate at the channel sites, and these sites are inhabited only by nC6; the component loading for adsorption of mixtures with partial fugacities, f_1, and f_2 in the bulk fluid phase are:

$$q_{nC6,channel} = \frac{4b_{nC6}f_1}{1+b_{nC6}f_1}; \quad q_{2MP,chanel} = 0 \tag{11-2}$$

Figure 11-8(c) compares the CBMC simulated data on the component loadings for mixture adsorption with the component loadings obtained by summing the contributions at the intersection sites, and channel sites, from equations (11-1), and (11-2); these calculations are shown by the continuous solid lines in Figure 11-8(c). The entropic exclusion of 2MP is not catered for by the Bai-Yang model.

For completeness, Figure 11-8(d) compares the IAST estimates of the component loadings for nC6 and 2MP with CBMC simulated data; the IAST captures the entropic exclusion effects quantitatively and correctly.

We conclude that explicit calculations of mixture adsorption do not capture the entropic re-arrangement of mixture compositions of the adsorbed phase that signifies entropy effects.

11.5 List of Figures for Entropy effects for mixture adsorption in MFI zeolite

MFI pore landscape

	MFI
a /Å	20.022
b /Å	19.899
c /Å	13.383
Cell volume / Å^3	5332.025
conversion factor for [molec/uc] to [mol per kg Framework]	0.1734
conversion factor for [molec/uc] to [kmol/m^3]	1.0477
ρ [kg/m3]	1796.386
MW unit cell [g/mol(framework)]	5768.141
ϕ, fractional pore volume	0.297
open space / Å^3/uc	1584.9
Pore volume / cm^3/g	0.165
Surface area /m^2/g	487.0
DeLaunay diameter /Å	5.16

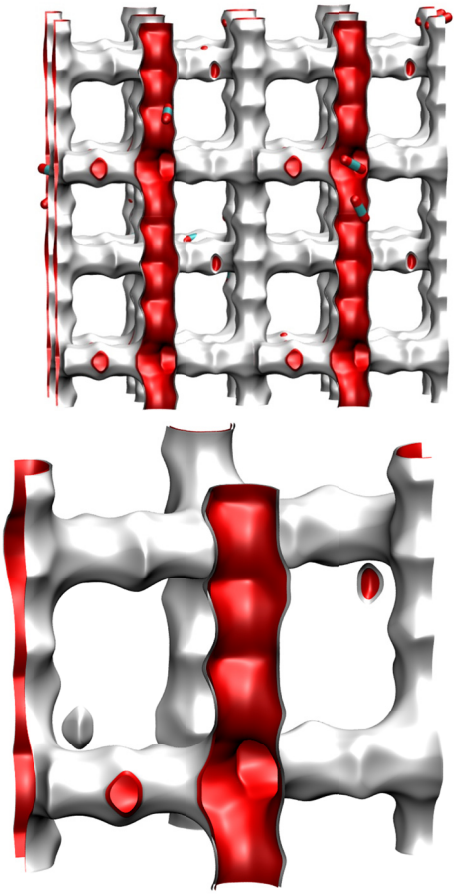

Figure 11-1. Structural details and pore landscape for MFI zeolite.

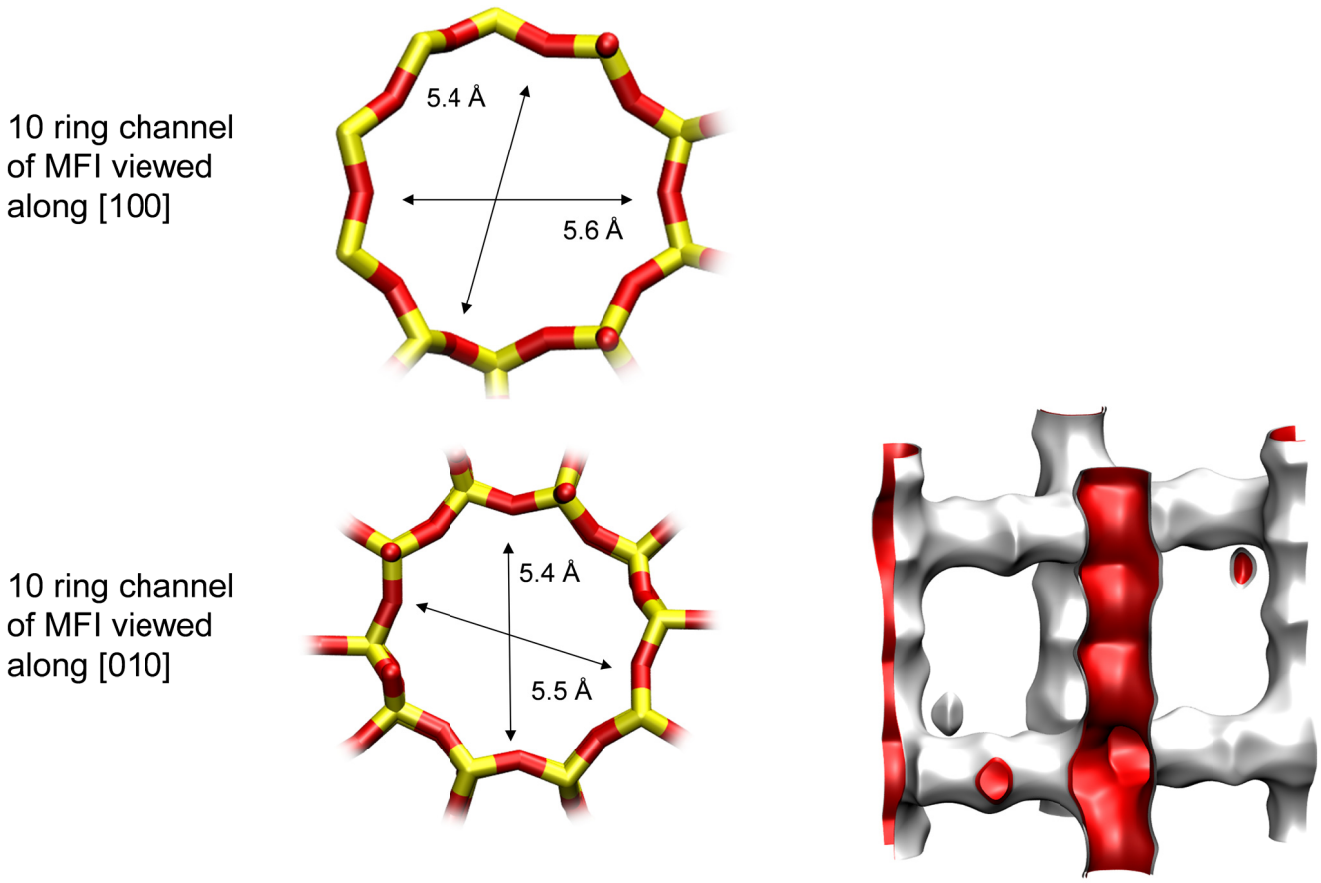

Figure 11-2. Structural details and pore landscape for MFI zeolite.

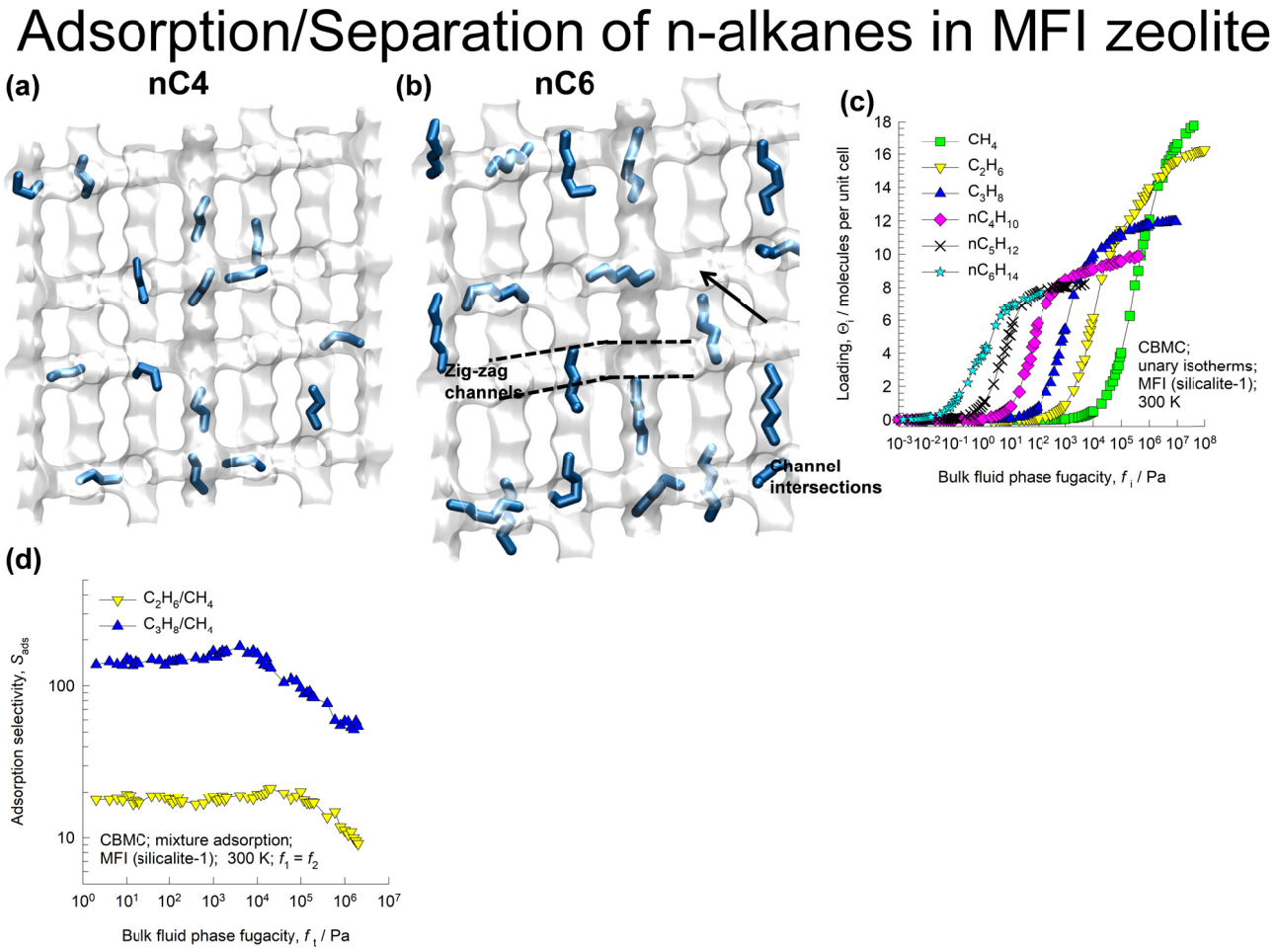

Figure 11-3 (a, b) Snapshots showing the locations of (a) nC4, and (b) nC6 within the intersecting channels of MFI zeolite. (c) CBMC simulations of adsorption isotherms for C1, C2, C3, nC4, nC5, nC6 and nC7 in MFI at 300 K. (d) CBMC simulations for C1/C2 and C1/C3 mixtures in MFI zeolite; in these simulations, the partial fugacities in the bulk fluid phase equal each other, i.e. f_1=f_2. The CBMC data are culled from the papers of Krishna and van Baten.[8, 13, 14, 63]

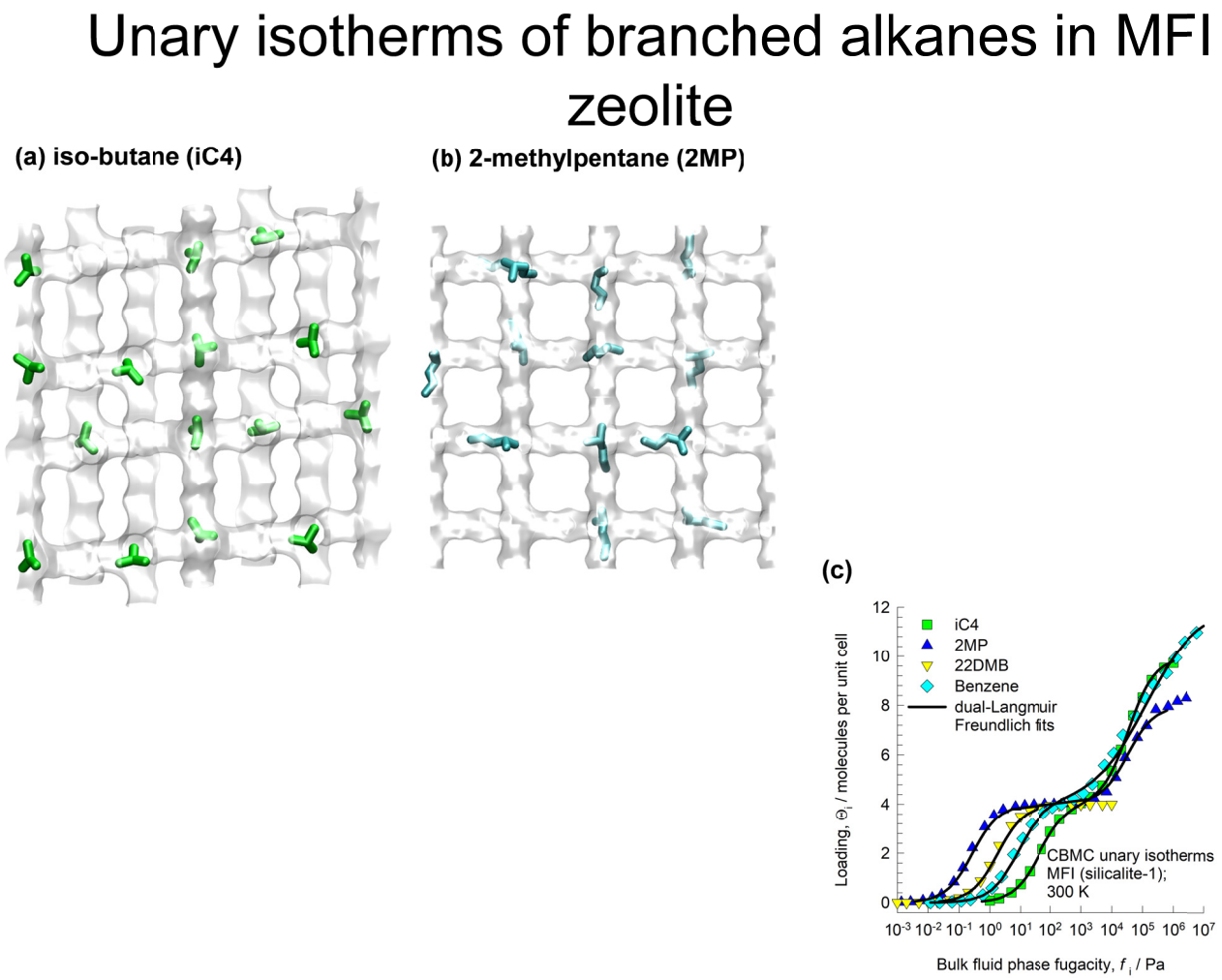

Figure 11-4 (a, b) Snapshots showing the locations of (a) iso-butane, and (b) 2-methylpentane (2MP) within the intersecting channels of MFI zeolite. (c) CBMC simulations of adsorption isotherms for iC4, 2MP, 22DMB, and benzene in MFI at 300 K.

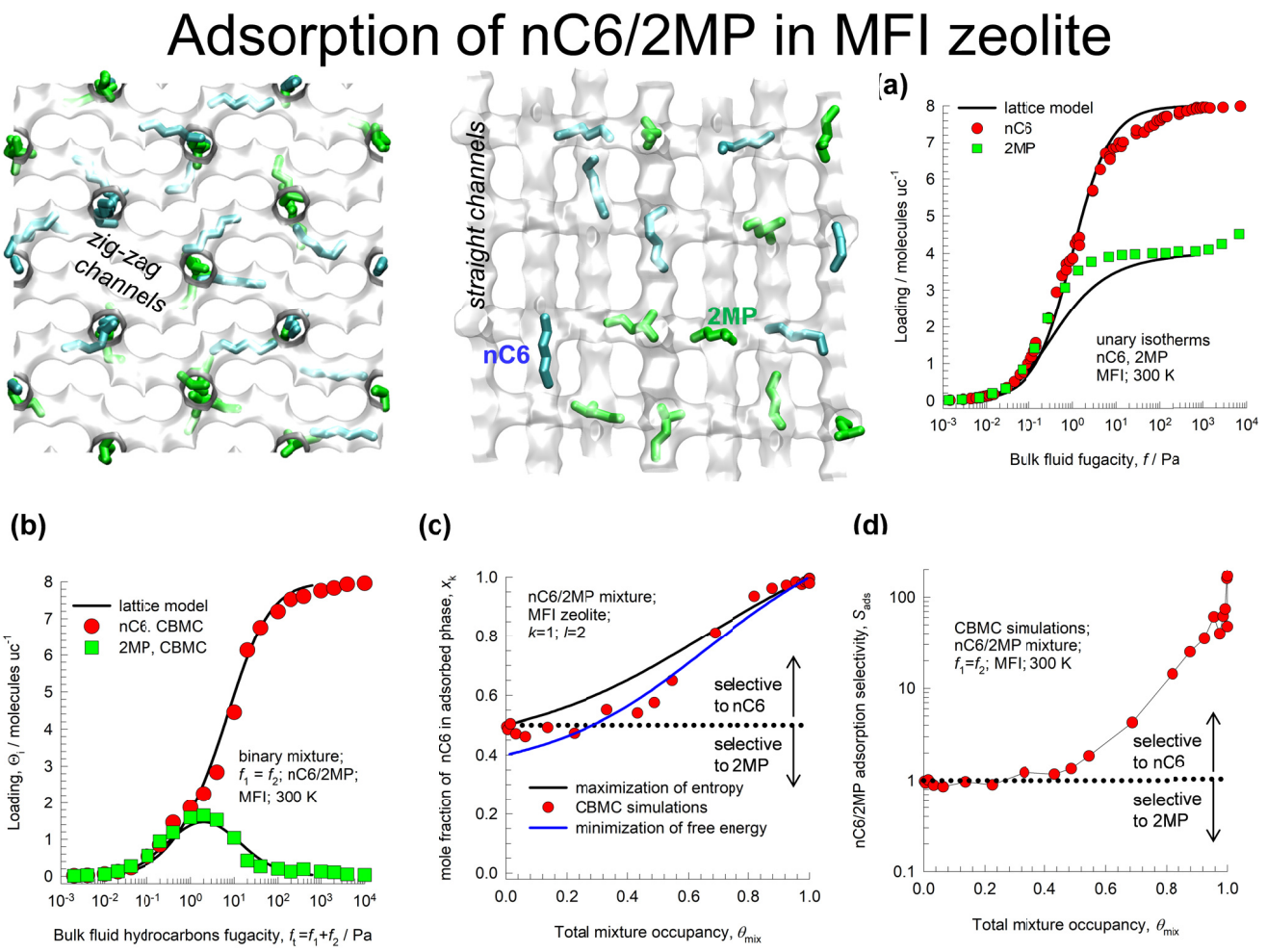

Figure 11-5. (a) CBMC data for unary isotherms of nC6 and 2MP in MFI zeolite at 300 K, compared with the fits of the lattice model, described by equations (6-8). (b) Comparison of the CBMC simulations (shown by symbols) for nC6/2MP mixture adsorption with the estimations of the lattice model (shown by continuous solid lines), described by equations (6-7). (c) Plot of the values of the adsorbed phase mole fracions of nC6, x_k corresponding to the maximum entropy (using equations (6-5), and (6-6)), as a function of the mixture occupancy, θ_{mix}. The continuous solid blue line represents calculations using equation (6-12). Also shown by the symbols in (c) are the CBMC simulated values of x_k. (d) Plot of the 22DMB/nC6 adsorption selectivity as a function of the mixture occupancy, θ_{mix}.

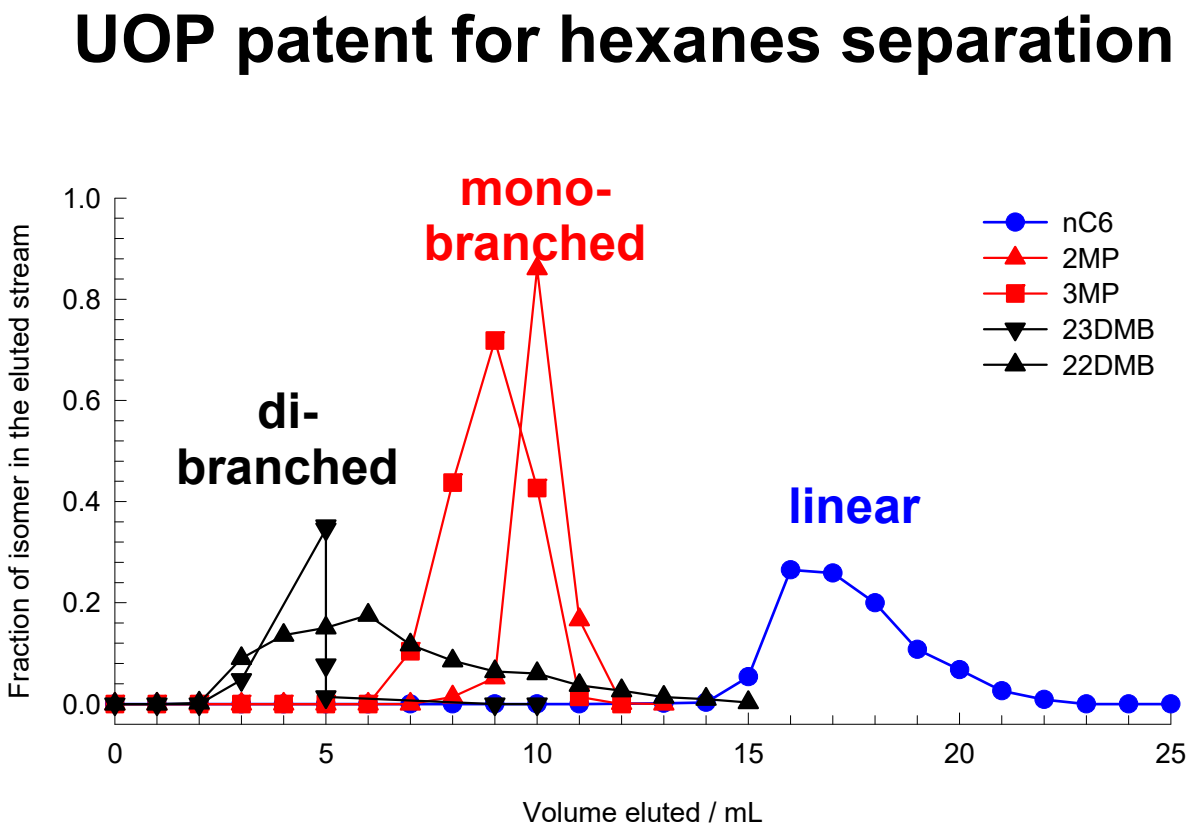

Figure 11-6 Pulsed chromatographic separation of hexane isomers as reported in the patents assigned to Universal Oil Products (UOP).[59-61]

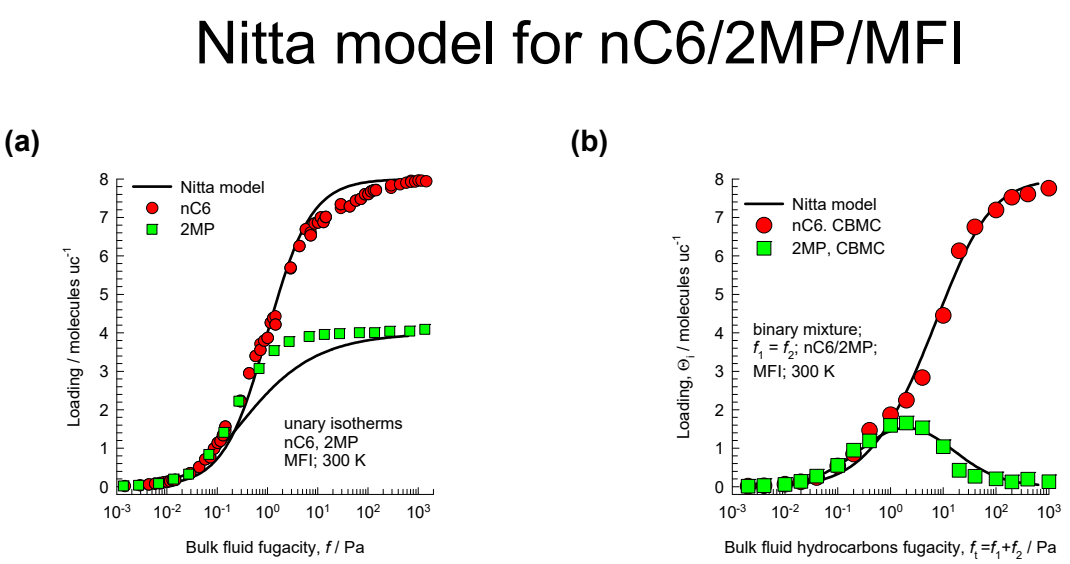

Figure 11-7. (a) CBMC data for unary isotherms of nC6 and 2MP in MFI zeolite at 300 K, compared with the fits of the Nitta model. (b) Comparison of the CBMC simulations (shown by symbols) for nC6/2MP mixture adsorption in MFI at 300 K with the estimations of the Nitta model (shown by continuous solid lines).

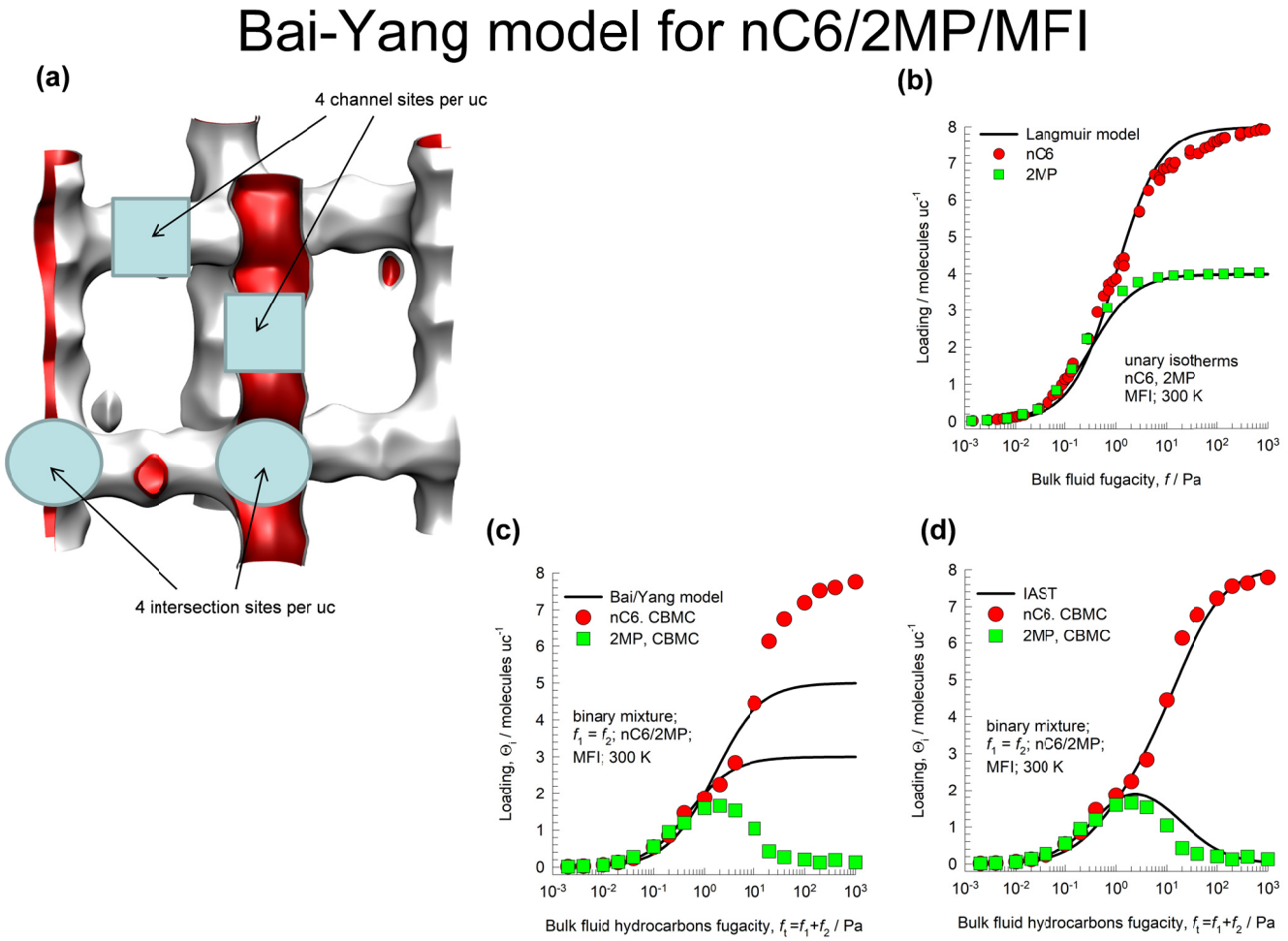

Figure 11-8. (a) The MFI zeolite is made up of intersection sites and channel sites. (b) CBMC data for unary isotherms of nC6 and 2MP in MFI zeolite at 300 K, compared with the Langmuir fits. (c) Comparison of the CBMC simulations (shown by symbols) for nC6/2MP mixture adsorption with the estimations of the Bai-Yang model (solid lines), described by equations (6-7). (d) Comparison of the CBMC simulations (shown by symbols) for nC6/2MP mixture adsorption with the estimations using the IAST.

12 Entropy effects for mixture adsorption in CHA zeolite

12.1 Adsorption of linear alkanes in CHA

Let us examine the adsorption of n-alkanes in CHA zeolite, which is a cage type zeolite that consists of cages of volume 316 Å^3, separated by 3.8 Å × 4.2 Å 8-ring windows. The pore landscapes and structural details are provided in Figure 12-1 and Figure 12-2.

Figure 12-3 presents snapshots of the location, and conformation, of the n-alkanes within the cages of CHA at saturation conditions. We note that in all cases there appears to be no n-alkane molecules at the window between two cages and, therefore, the cage capacity at saturation must be an integral number. Figure 12-4(a) presents CBMC simulation data[64] on the unary isotherms for linear alkanes in CHA at 300 K.The saturation capacity of methane is 6 molecules per cage. For ethane, the saturation capacity remains 4 cage^{-1} up to a fugacity of 10^{12} Pa, and increases to 5/cage on further increase of fugacity to 10^{15} Pa. For propane, the saturation capacity remains 2/cage up to a fugacity of 10^{12} Pa, and increases to 4 cage^{-1} on further increase of fugacity to 10^{15} Pa. For nC4, and nC5, the saturation capacities are 2 cage^{-1}. For nC6, nC7, and nC8, the saturation capacities are 1 cage^{-1}. These saturation capacities, determined from CBMC simulations, are in good agreement with the experimental data of Daems et al.[65]

Figure 12-4(b) presents CBMC simulation data[64] of the adsorption selectivities for binary C1/C2, C2/C3, C3/nC6, nC4/nC6, and nC5/nC6 mixtures in CHA zeolite at 300 K; in these simulations the partial fugacities in the bulk phase are equal to each other, i.e. $f_1 = f_2$. For all five mixtures we observe two common characteristic features: (a) in the Henry regime of adsorption, the adsorption selectivities are practically constant, and independent of the total mixture fugacity $f_t = f_1 + f_2$; (b) with increasing bulk fugacity, f_t, the adsorption selectivity becomes increasingly in favor of the shorter alkane. The observed selectivity reversals are due to entropic effects that favor the shorter alkane; this has been confirmed by use of the 2D lattice model in earlier work.[66] The same set of data are plotted in Figure

12-4(c), with the total mixture occupancy θ_{mix} as the *x*-axis. We note that selectivity reversals at cage occupancies $\theta_{mix} > 0.6$; high cage occupancies are guaranteed when operating with the bulk phase in the liquid state. Figure 12-4(c) plots the CBMC mixture data using the mole fraction of the shorter alkane in the adsorbed phase as *y*-axis. Also plotted in Figure 12-4(c) are the calculations using the lattice model x_k corresponding to the maximum entropy (using equations (6-5), and (6-6)), as a function of the occupancy, θ_{mix}. In the lattice model calculations, two scenarios are chosen: k=1, l=2, and k=1, l=4. The conclusion to be drawn from Figure 12-4(c) is that the selectivity reversals are due to entropy effects that favors adsorption of the shorter alkane.

Entropy effects for all five binary mixtures are quantitatively captured by use of the IAST; see Figure 12-5.

12.2 Adsorption of linear alcohols in CHA

Figure 12-6(a) presents snapshots of the conformations of the 1-alcohols within the cages, at saturation conditions. CBMC simulations of unary 1-alcohols with C atoms in the 1 – 6 range in CHA at 300 K, as reported in the work of Krishna and van Baten,[49] are shown in Figure 12-6(b). The saturation capacities, decreases from 5.4 molecules cage^{-1} for methanol to 1 molecule cage^{-1} for 1-hexanol; see Figure 12-6(c). Except for methanol, the saturation cage capacity has an integer value because 1-alcohol molecules cannot locate at the window regions. For 1-butanol, the cage capacity is restricted to 2 molecules cage^{-1}; for 1-hexanol, the cage capacity is 1 molecule cage^{-1}.

This difference in the cage capacities can be exploited to separate binary mixtures of linear alcohols. The CBMC simulations for five different binary mixtures: (a) methanol/ethanol, (b) ethanol/1-propanol, (c) ethanol/1-hexanol, (d) 1-butanol/1-pentanol, (e) 1-butanol/1-hexanol, and (f) 1-pentanol/1-hexanol mixtures in CHA at 300 K are shown in Figure 12-7. The partial fugacities in the bulk fluid phase are taken to be equal, i.e. f_1=f_2. In all six cases, we note a tendency for selectivity to reverse in favor of the component with the higher saturation capacity. The shaded regions in Figure 12-7 indicate that the bulk fluid phase is in the liquid phase for the range of fugacities, f_t. Operations with bulk liquid phase

mixtures ensures that the shorter 1-alcohol will be preferentially adsorbed. The dashed lines represent calculations of the IAST using dual-Langmuir-Freundlich fits of pure component isotherms; Table 12-1 provides the pure component isotherm fit parameters. The IAST correctly, and quantitatively, anticipates selectivity reversals for all six mixtures.

In Figure 12-8 the focus is on ethanol/1-propanol mixture adsorption. The CBMC unary isotherms are shown in Figure 12-8(a). The CBMC mixture simulation data on the component loadings are compared with IAST estimates in Figure 12-8(b). In Figure 12-8(c,d) CBMC data on the adsorbed phase mole fraction of ethanol are compared with IAST estimates. The IAST is able to predict, quantitatively, the adsorbed phase mole fraction of ethanol as a function of the total bulk fluid fugacity, and the total mixture occupancy, θ_{mix}.

For adsorption of 1-butanol and 1-hexanol in CHA, we now demonstrate the applicability of the lattice model. We use the model of Azizian and Bashiri[47] for a 2D lattice consisting of cages, with each cage containing 2 sites; k=1, l=2, M = 2. The CBMC simulations of the unary isotherms can be fitted reasonably with the choice $b_k = 4\times10^{-1}$ Pa^{-1}, and $b_l = 20$ Pa^{-1}; see the continuous solid lines in Figure 12-9(a). With the fitted binding constants, the component loadings for mixture adsorption can be calculated using Equations (6-24). The lattice model calculations are shown by the continuous solid lines in Figure 12-9(b). The lattice model is able to quantitatively capture the phenomenon of 1-hexanol exclusion from CHA zeolite as the cages become increasingly occupied. Figure 12-9(c) plots the CBMC simulations (symbols) of the mole fractions of 1-butanol in the adsorbed phase as a function the occupancy, θ_{mix}. Also plotted are the calculations using the lattice model of x_k corresponding to the maximum entropy (using equations (6-5), and (6-6)), and minimum free energy (using equation (6-12)). The plot clearly shows that entropy effects come into play at occupancies $\theta_{mix} > 0.6$. When the cages of CHA are saturated, i.e. $\theta_{mix} \approx 1$, the adsorbed phase mole fraction of 1-butanol $x_k \to 1$ and 1-hexanol is excluded from the cages.

In Figure 12-10 the CBMC data on adsorption selectivities, and adsorbed phase mole fractions of the five different binary mixures are compared to one another. Figure 12-10(a) presents CBMC simulations of the adsorption selectivities for binary C1/C2, C2/C3, nC4/nC5, C2/nC6, and nC4/nC6 mixtures in CHA zeolite at 300 K.. For all five mixtures we observe two common characteristic features: (a) in the Henry regime of adsorption, the adsorption selectivities are practically constant, and independent of the total mixture fugacity $f_t = f_1 + f_2$; (b) with increasing bulk fugacity, f_t, the adsorption selectivity becomes increasingly in favor of the shorter 1-alcohol. The observed selectivity reversals are due to entropic effects that favor the shorter alkane; this has been confirmed by use of the 2D lattice model in earlier work.[66] The same set of data are plotted in Figure 12-10(b), with the total mixture occupancy θ_{mix} as the *x*-axis. We note that selectivity reversals at cage occupancies $\theta_{mix} > 0.6$; high cage occupancies are guaranteed when operating with the bulk phase in the liquid state. Figure 12-10(c) plots the CBMC mixture data using the mole fraction of the shorter alkane in the adsorbed phase as *y*-axis. Also plotted in Figure 12-10(c) are the calculations using the lattice model x_k corresponding to the maximum entropy (using equations (6-5), and (6-6)), as a function of the occupancy, θ_{mix}. In the lattice model calculations, two scenarios are chosen: k=1, l=2, and k=1, l=4. The conclusion to be drawn from Figure 12-10(c) is that the selectivity reversals are due to entropy effects that favors adsorption of the shorter alcohol.

Experimental confirmation of the selectivity reversal is observed in the experiments reported by Remy et al.[50] for transient breakthroughs of ethanol/propanol, and ethanol/1-hexanol feed mixtures, in the liquid state, in a fixed bed adsorber packed with SAPO-34, that has the same structural topology as CHA; see Figure 12-11(a,b). The component that is eluted first from the adsorber is the alcohol with the longer chain length. The rationalization of these experimental data can be traced to the entropy effects that favor the shorter alcohols under pore saturation conditions.

12.3 List of Tables for Entropy effects for mixture adsorption in CHA zeolite

Table 12-1. Dual-site Langmuir-Freundlich parameters for pure component water, and 1-alcohols in CHA at 300 K. The fit parameters are based on the CBMC simulations of pure component isotherms presented in earlier work.[49] Note that the saturation capacities are specified in molecules per cage; multiply these by 1.387 to obtain the values in mol per kg framework.

	Site A			Site B		
	$\Theta_{A,sat}$ Molecules cage^{-1}	b_A Pa$^{-\nu_A}$	ν_A dimensionless	$\Theta_{B,sat}$ molecules cage^{-1}	b_B Pa$^{-\nu_B}$	$\nu_{i,B}$ dimensionless
water	12	7.86×10^{-59}	17	9	8.32×10^{-6}	1
methanol	2.7	6.77×10^{-11}	3.3	2.7	4.45×10^{-4}	1
ethanol	2	7.93×10^{-5}	0.87	2	3.6×10^{-3}	1.14
1-propanol	1	1.28×10^{-2}	1.8	1	9.11×10^{-2}	1
1-butanol	1	0.231	1.46	1	0.5066	1
1-pentanol	0.5	19.26	1.72	0.5	6.91	1
1-hexanol	0.5	2561	2.4	0.5	24.8	1

12.4 List of Figures for Entropy effects for mixture adsorption in CHA zeolite

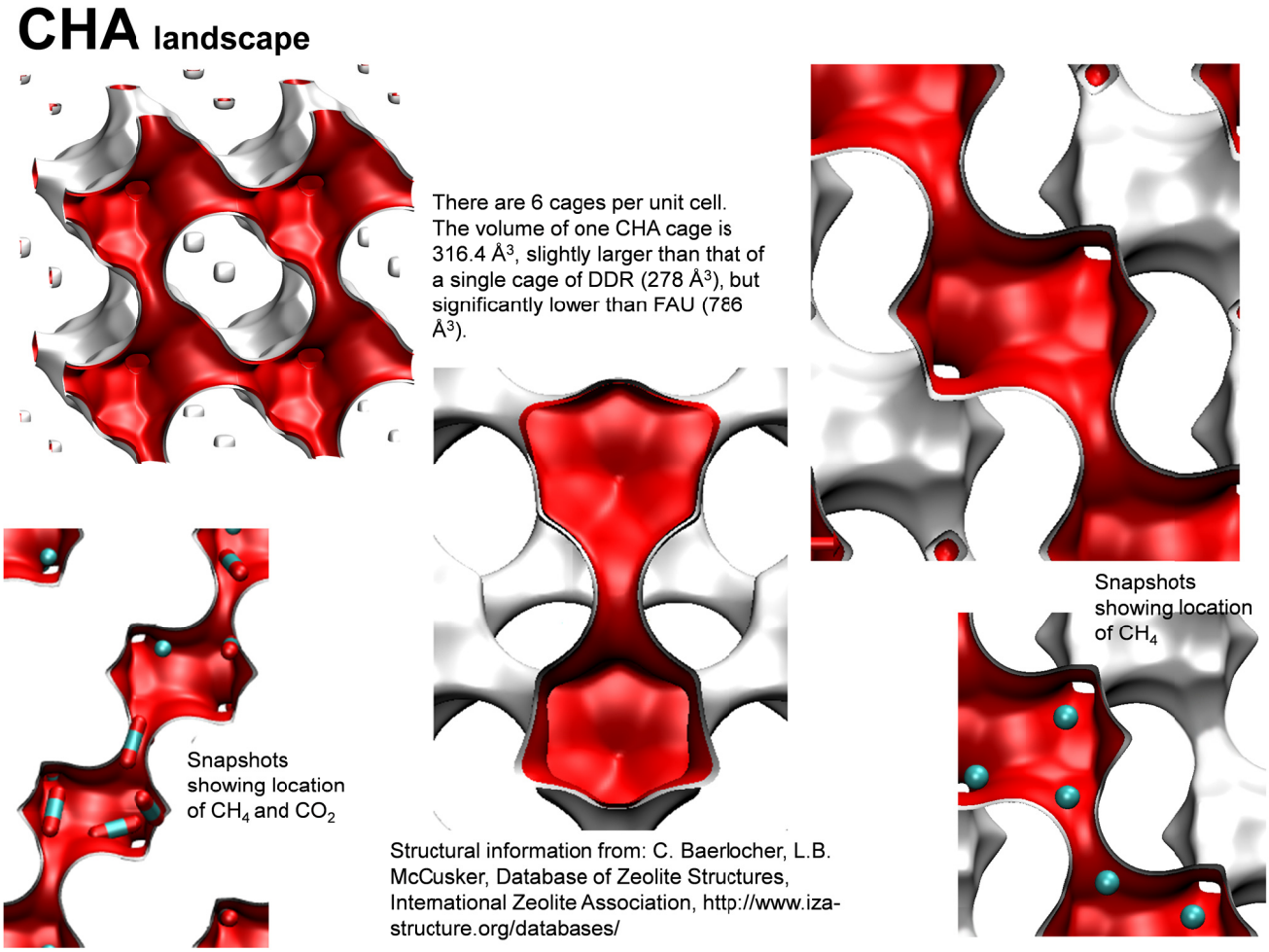

Figure 12-1. Pore landscapes and structural details for CHA zeolite.

CHA window and pore dimensions

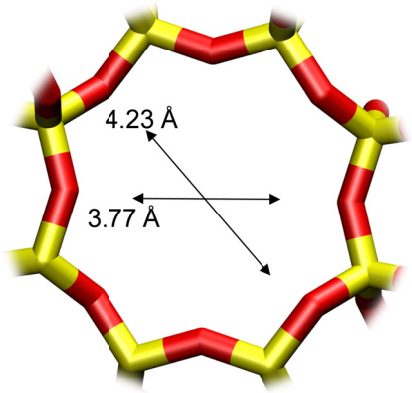

CHA

The window dimensions calculated using the van der Waals diameter of framework atoms = 2.7 Å are indicated above by the arrows.

	CHA
a /Å	15.075
b /Å	23.907
c /Å	13.803
Cell volume / Å^3	4974.574
conversion factor for [molec/uc] to [mol per kg Framework]	0.2312
conversion factor for [molec/uc] to [kmol/m^3]	0.8747
ρ [kg/m3]	1444.1
MW unit cell [g/mol(framework)]	4326.106
ψ, fractional pore volume	0.382
open space / Å^3/uc	1898.4
Pore volume / cm^3/g	0.264
Surface area /m^2/g	758.0
DeLaunay diameter /Å	3.77

Figure 12-2. Pore landscapes and structural details for CHA zeolite.

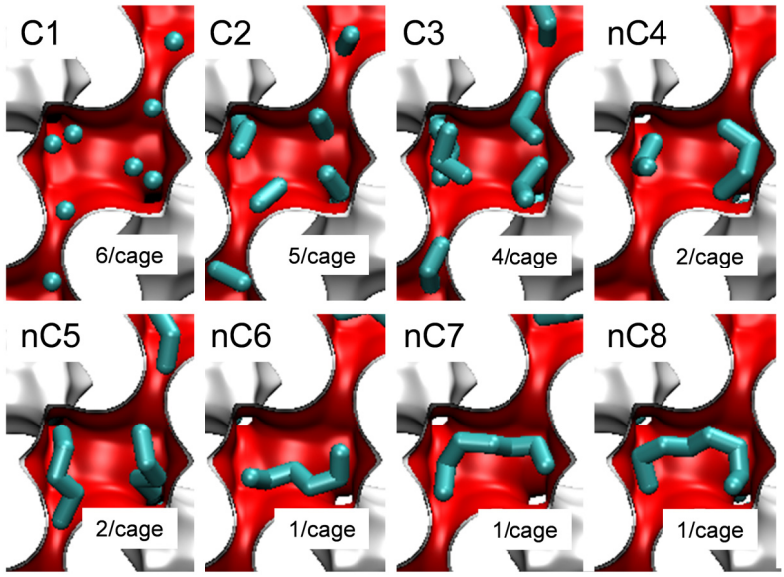

Figure 12-3. Snapshots showing the conformations of n-alkanes in CHA at saturation conditions.

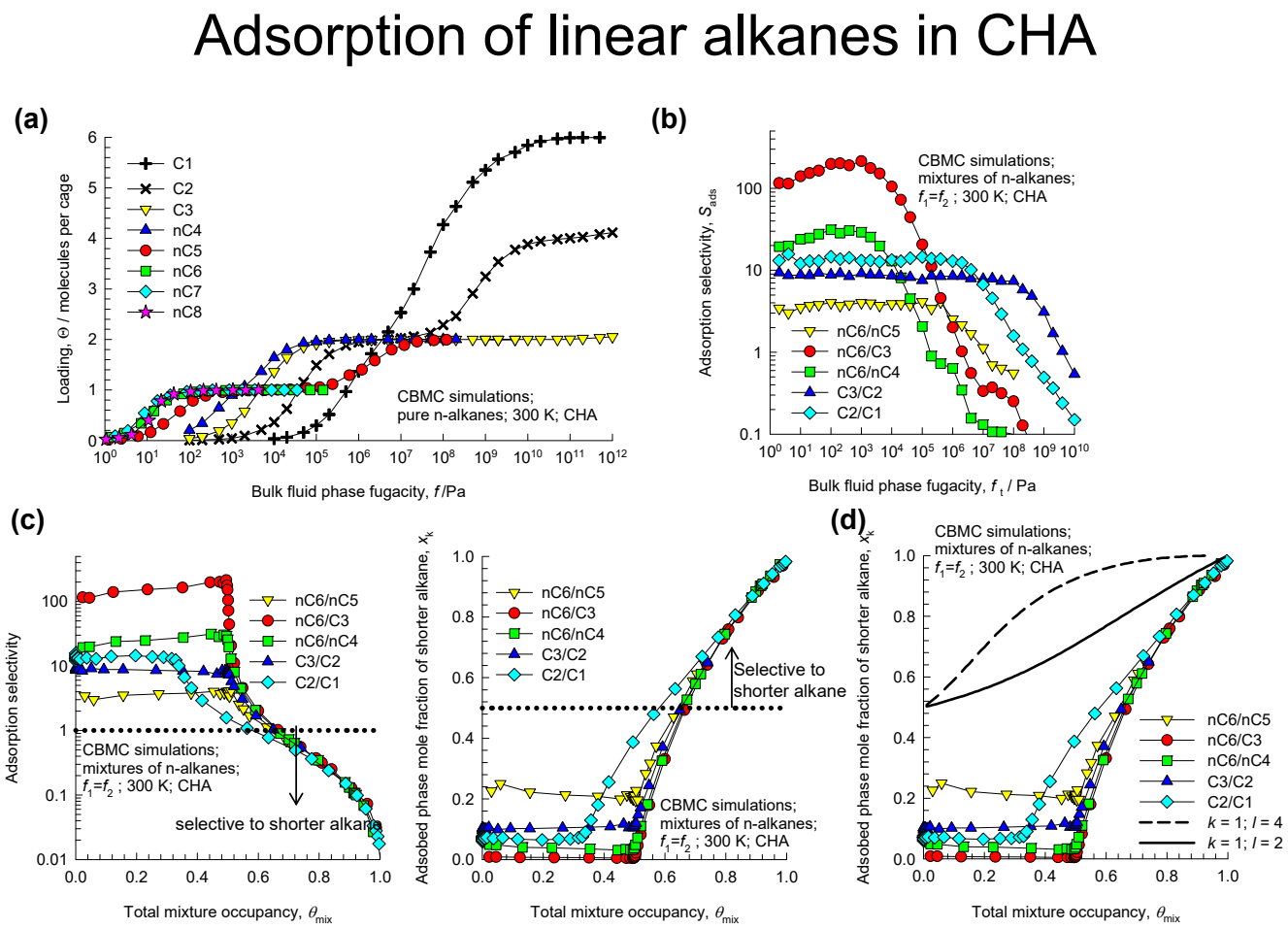

Figure 12-4. (a) CBMC simulations[64] of pure component adsorption isotherms for n-alkanes in CHA at 300 K. (b, c, d) CBMC simulations of the adsorption selectivities for binary C1/C2, C2/C3, C3/nC6, nC4/nC6, and nC5/nC6 mixtures of n-alkanes in CHA zeolite at 300 K; in these simulations the partial fugacities in the bulk phase are equal to each other, i.e. $f_1 = f_2$.

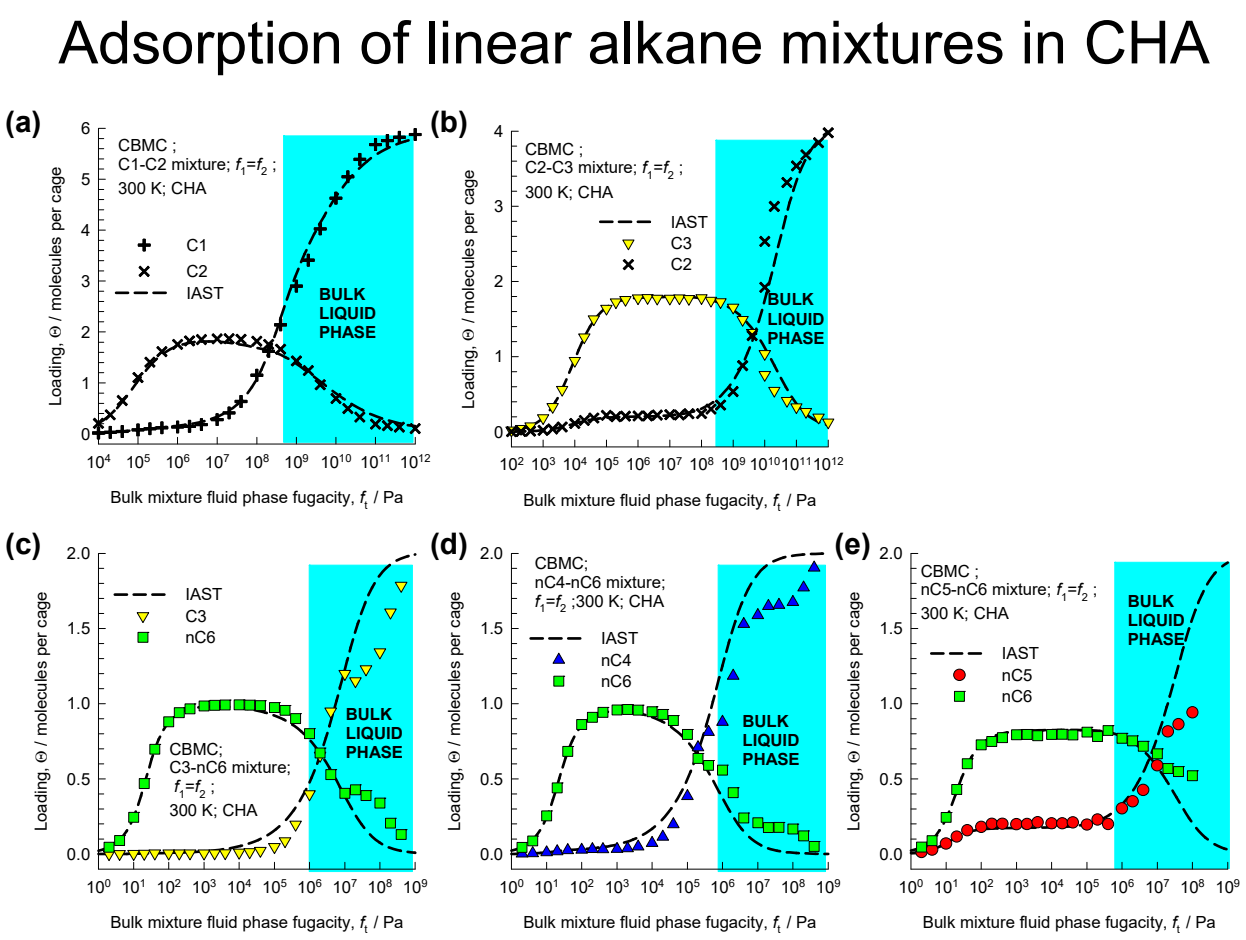

Figure 12-5. Comparison of CBMC mixture simulations[64] (symbols) for (a) C1/C2, (b) C2/C3, (c) C3/nC6, (d) nC4/nC6, and (e) nC4/nC6 in CHA at 300 K with the IAST predictions. The dashed lines represent calculations of the IAST,[39] using 3-site Langmuir fits of pure component isotherms. The region of liquid phase operation is indicated by the colored bar; the transition between vapor and liquid bulk phase is determined using the Peng-Robinson equation of state.

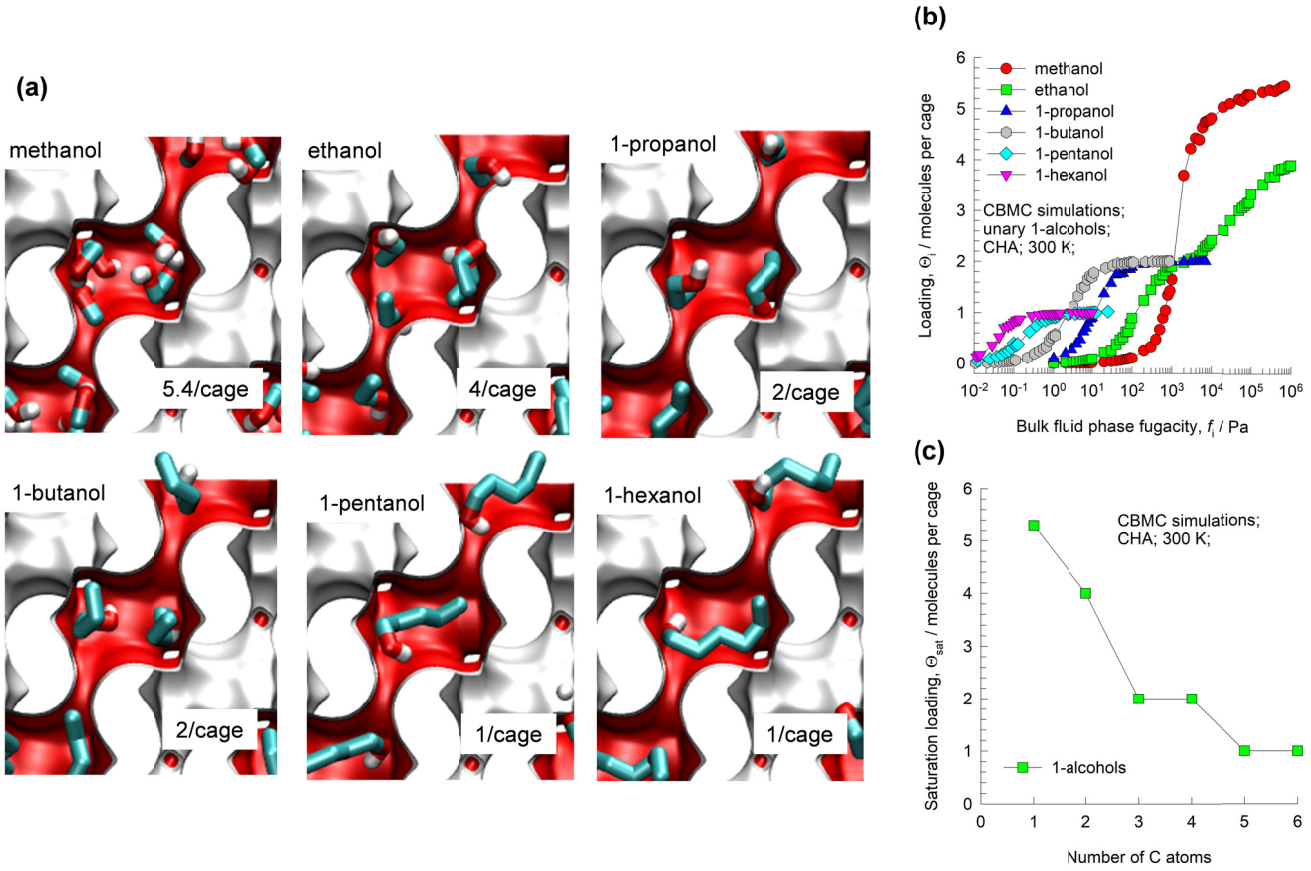

Figure 12-6. (a) Snapshots showing the conformations of 1-alcohols in CHA at saturation conditions. (b) CBMC simulations[49] of pure component adsorption isotherms for 1-alcohols in CHA at 300 K. (c) Saturation capacities for adsorption of 1-alcohols in CHA at 300 K.

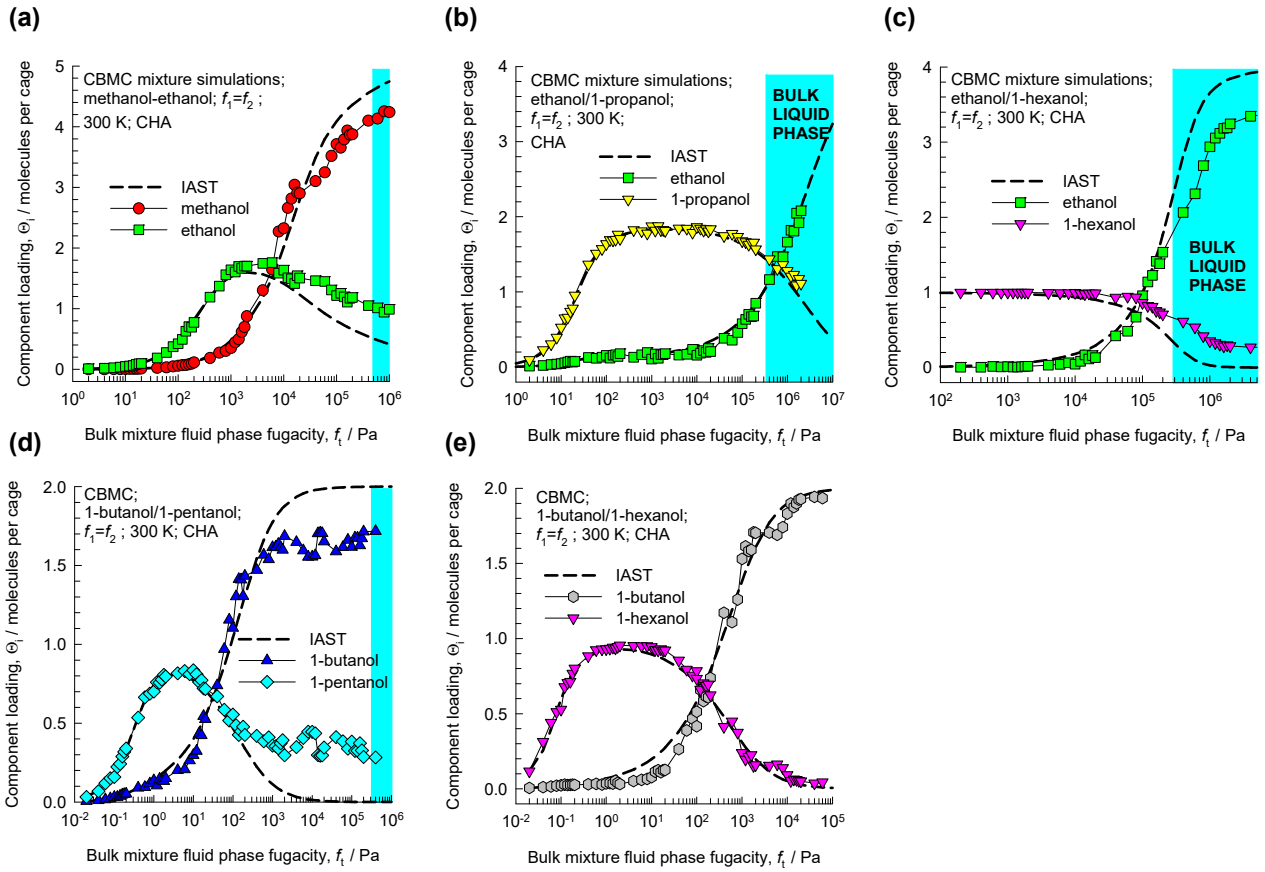

Figure 12-7. CBMC mixture simulations for (a) methanol/ethanol, (b) ethanol/1-propanol, (c) ethanol/1-hexanol, (d) 1-butanol/1-pentanol, and (e) 1-butanol/1-hexanol mixtures in CHA at 300 K. The partial fugacities in the bulk fluid phase are taken to be equal, i.e. $f_1=f_2$. The dashed lines represent IAST calculations using dual-site Langmuir-Freundlich fits of pure component isotherms. Table 12-1 provides the pure component isotherm fit parameters. The range of liquid phase operation is indicated by the shaded region; the transition between vapor and liquid bulk phase is determined using the Peng-Robinson equation of state.

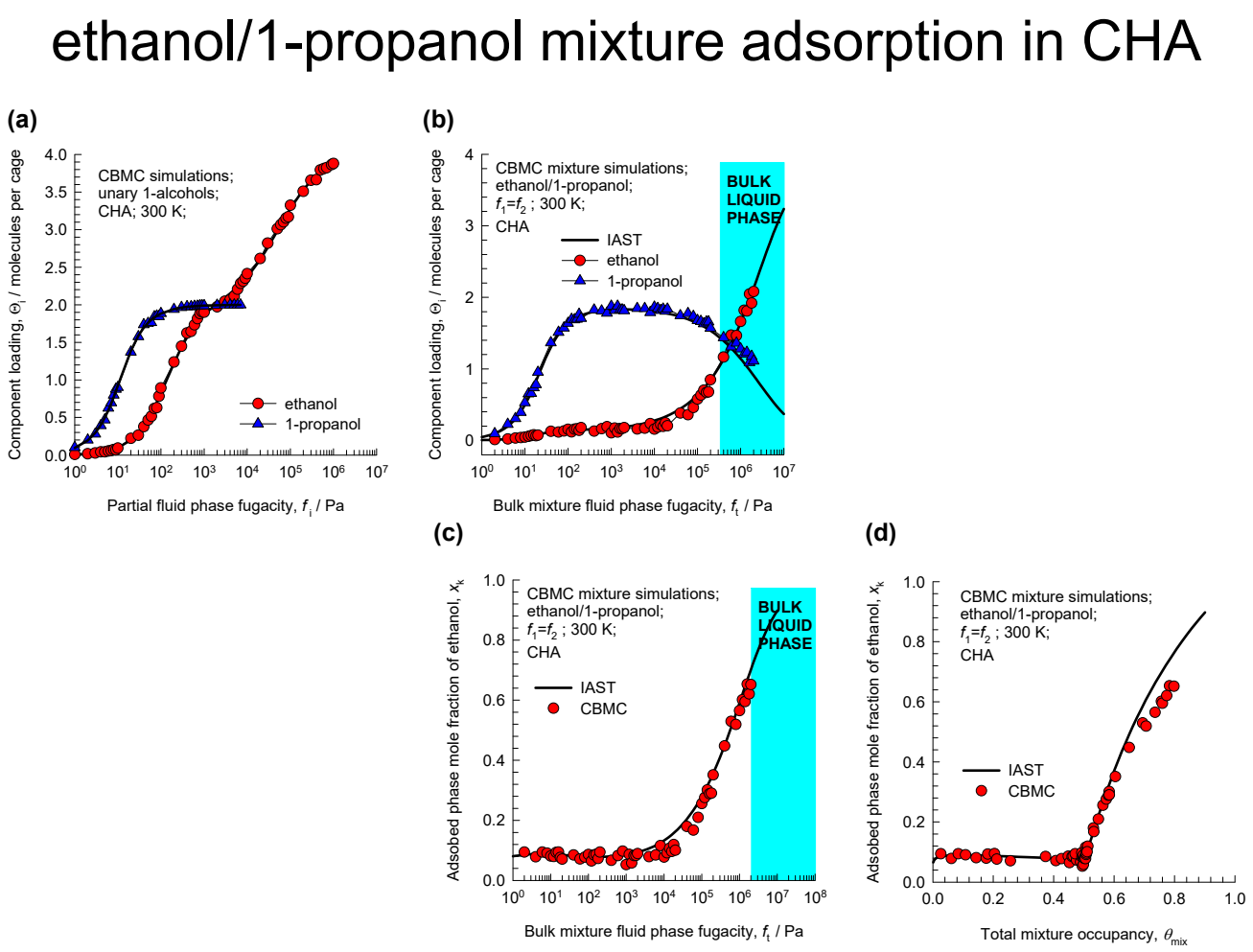

Figure 12-8. (a) CBMC simulations of the unary isotherms of ethanol and 1-propanol in CHA at 300 K. (b, c, d) CBMC simulations for adsorption of binary ethanol/1-propanol mixtures in CHA at 300 K. The partial fugacities in the bulk fluid phase are taken to be equal, i.e. f_1=f_2. The solid lines represent IAST calculations using dual-site Langmuir-Freundlich fits of pure component isotherms. Table 12-1 provides the pure component isotherm fit parameters. The range of liquid phase operation is indicated by the shaded region; the transition between vapor and liquid bulk phase is determined using the Peng-Robinson equation of state.

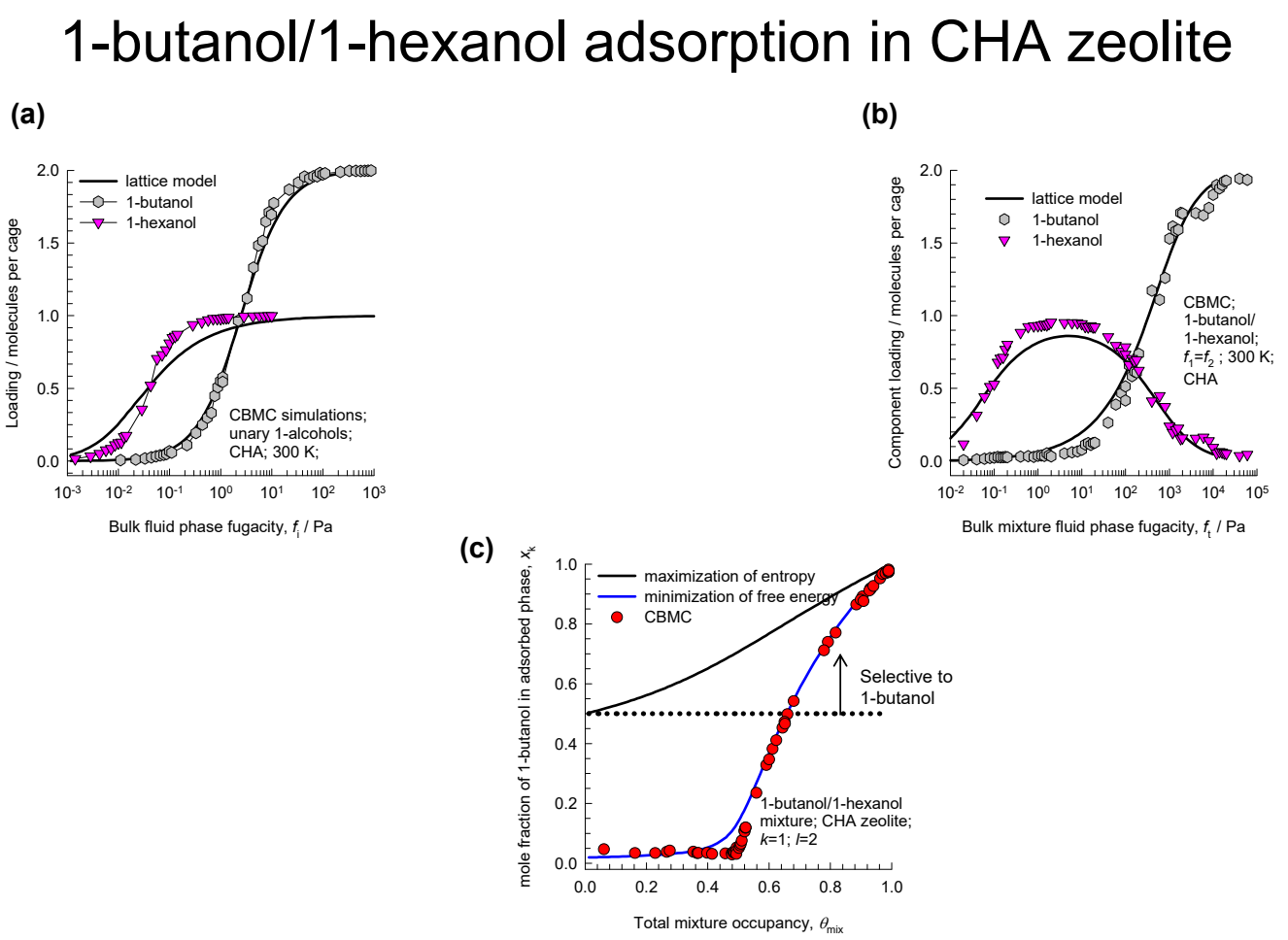

Figure 12-9. (a) CBMC simulations of the unary isotherms of 1-butanol and 1-hexanol in CHA at 300 K. (b) CBMC simulations of component loadings for adsorption of binary 1-butanol/1-hexanol mixtures in CHA at 300 K. The partial fugacities in the bulk fluid phase are taken to be equal, i.e. f_1=f_2. The solid lines represent the 2D square lattice model calculations. In the lattice model calculations, k=1, l=2. (c) CBMC simulations (symbols) of the mole fractions of 1-butanol in the adsorbed phase as a function the occupancy, θ_{mix}. Also plotted are the calculations using the lattice model of x_k corresponding to the maximum entropy (using equations (6-5), and (6-6)), and minimum free energy (using equation (6-12)).

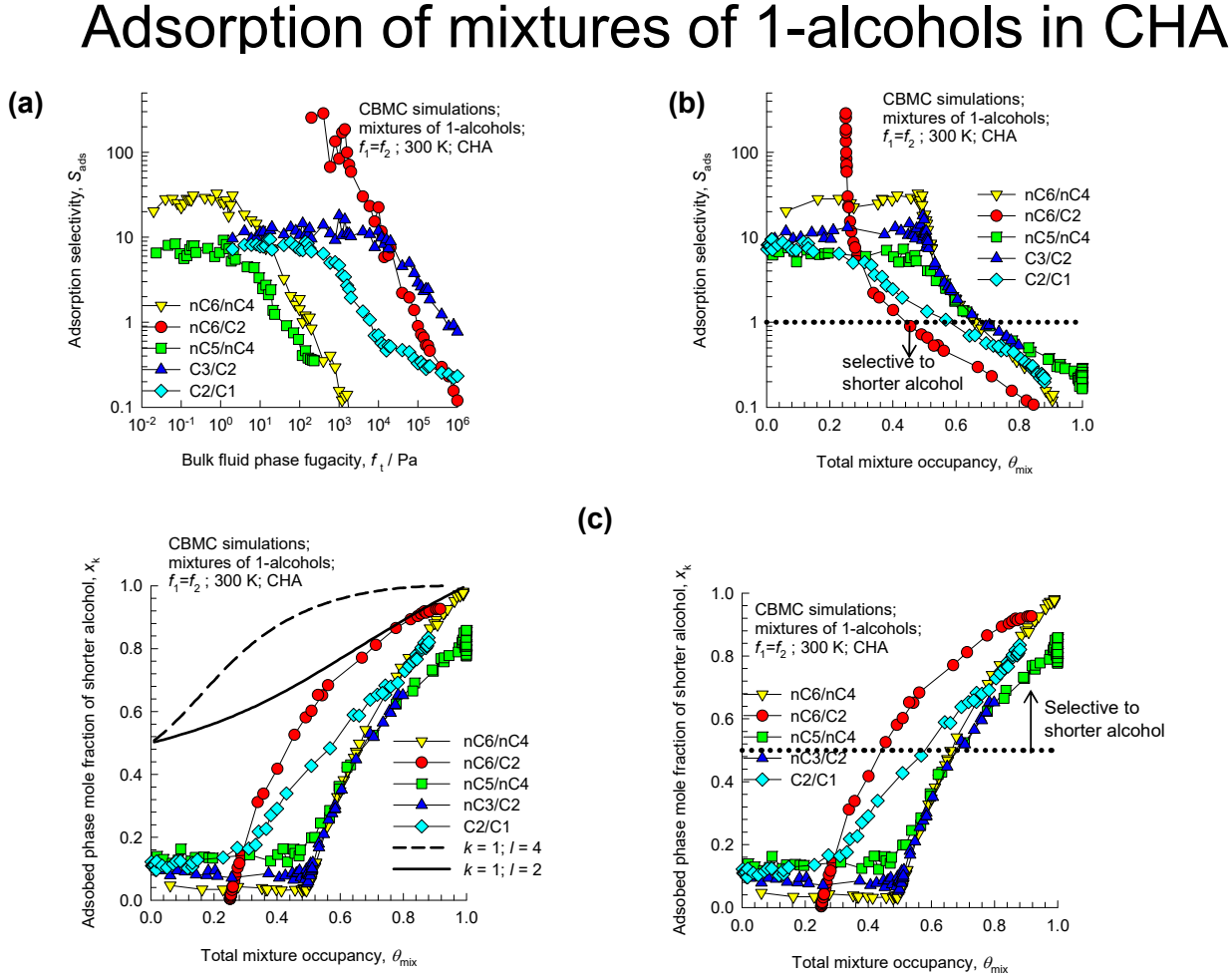

Figure 12-10. (a, b, c) CBMC simulations for adsorption of binary C1/C2, C2/C3, nC4/nC5, C2/nC6, and nC4/nC6 mixtures of 1-alcohols in CHA zeolite at 300 K; in these simulations the partial fugacities in the bulk phase are equal to each other, i.e. $f_1 = f_2$.

Selectivity reversals in experimental breakthroughs

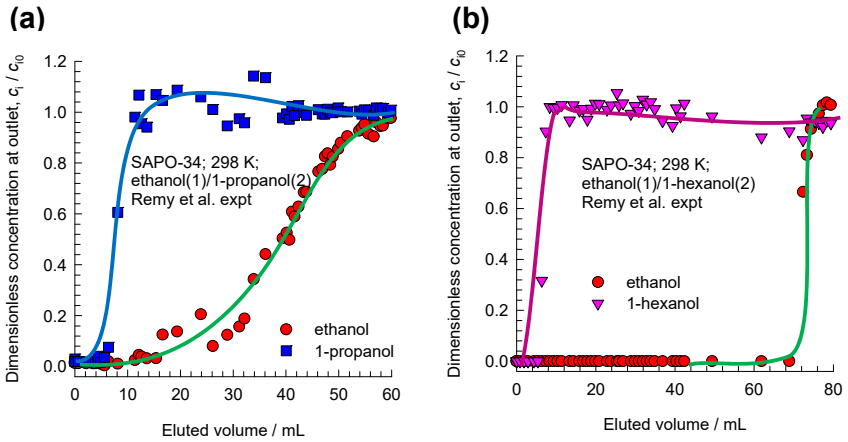

Figure 12-11. (a, b) Transient breakthrough experimental data of Remy et al.[50] for separation of (a) ethanol/1-propanol, and (b) ethanol/1-hexanol mixtures in a fixed bed adsorber packed with SAPO-34.

13 Separating linear alkanes using TSC zeolite

For separation of chain molecules with C numbers higher than say 20, as is required in the petroleum industry in lube oil processing, we need microporous host structures with sufficiently large cages. Of particular importance in this context is all-silica TSC zeolite, with a Tschörtnerite framework, that has the largest cage volume of any known zeolite;[37] the pore landscape and structural details are provided in Figure 13-1, Figure 13-2, and Figure 13-3. Each unit cell of TSC has four "LTA type cages" of 743 $Å^3$, and four "TSC supercages" of 2553 $Å^3$; the cages are separated by two types of windows: 4.02 Å × 4.17 Å, and 3.1 Å × 5.41 Å. Snapshots showing the conformations and location of nC21, nC22, nC23, nC24, and nC25 are shown in Figure 13-4, Figure 13-5, Figure 13-6, Figure 13-7, and Figure 13-8.

Figure 13-9(a) presents CBMC simulations of pure component isotherms for n-alkanes nC21, nC22, nC23, nC24, and nC25 in TSC at 500 K; these data are from our previous work.[49] The loadings are expressed as molecules per TSC supercage, because the LTA-type cages are too small to accommodate these long chain alkanes. Generally speaking, the adsorption separation selectivity for mixtures will be higher when the differences in the saturation capacities on the constituent species is larger.

Figure 13-9(b,c) present CBMC simulation data[49] for adsorption of binary nC1/nC25, and nC22/nC24 mixtures. For both mixtures, as anticipated, adsorption from a liquid phase will yield adsorbate compositions that are considerably richer in the shorter n-alkane. Figure 13-9(d) plots the nC25/nC21, and nC24/nC22 adsorption selectivities as a function of the mixture occupancy θ_{mix} in the cages. We note the selectivity reversals occur at cage occupancies $\theta_{mix} > 0.6$.

Figure 13-9(e) present the same set of data, using the mixture occupancy θ_{mix} as *x*-axis and the mole fraction of the shorter alkane in the adsorbed phase, x_k, as *y*-axis. We note that selectivity reversals at cage occupancies $\theta_{mix} > 0.6$; high cage occupancies are guaranteed when operating with the bulk phase in the liquid state. Also plotted in Figure 13-9(e) are the calculations using the lattice model, x_k

corresponding to the maximum entropy (using equations (6-5), and (6-6)), as a function of the occupancy, θ_{mix}. In the lattice model calculations, we tale k=1, l=2 as proper reflection of the differences in saturation cage capacities. The conclusion to be drawn from Figure 13-9(d ,e) is that the selectivity reversals are due to entropy effects that favors adsorption of the shorter alkane.

13.1 List of Figures for Separating linear alkanes using TSC zeolite

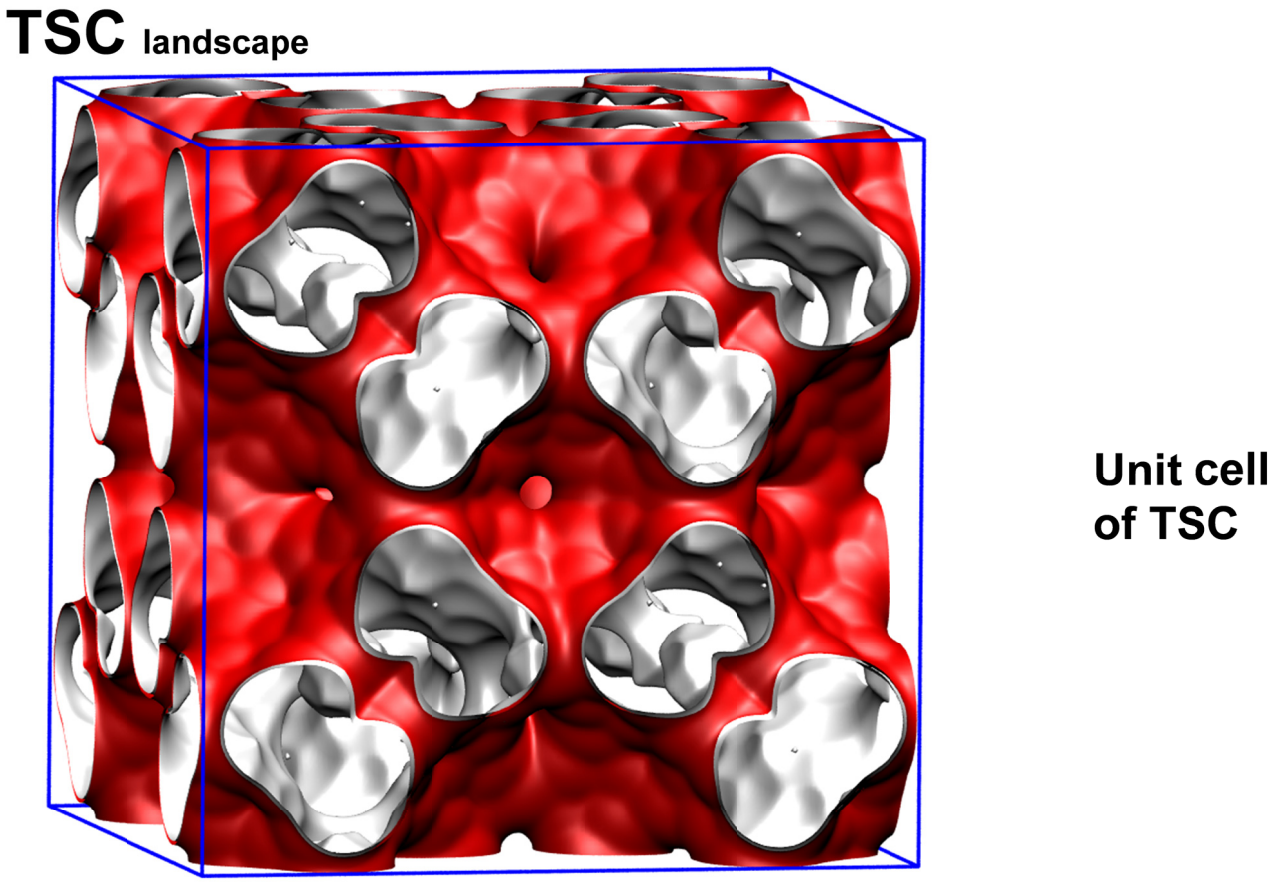

Structural information from: C. Baerlocher, L.B. McCusker, Database of Zeolite Structures, International Zeolite Association, http://www.iza-structure.org/databases/

Figure 13-1. Pore landscape of TSC zeolite.

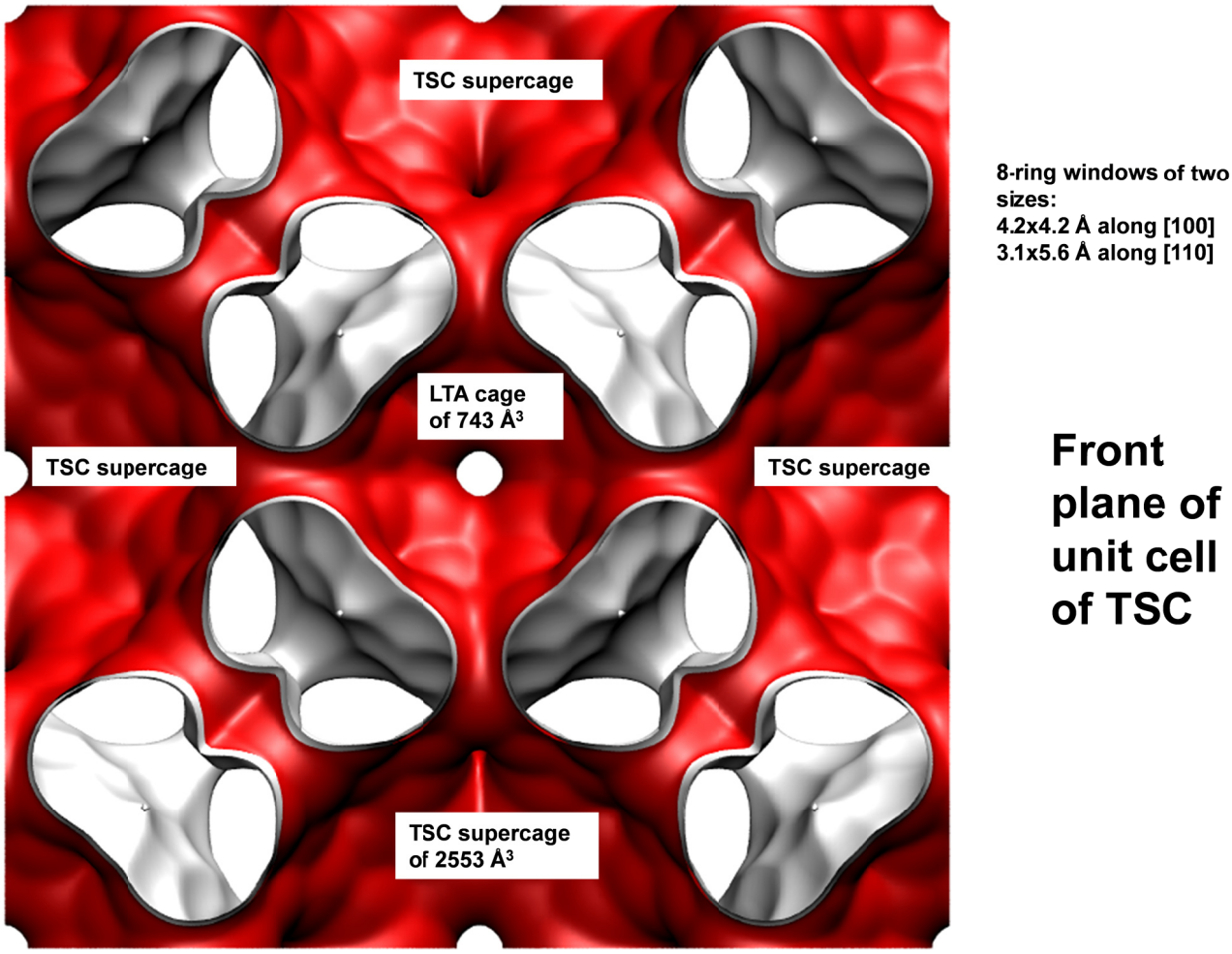

Figure 13-2. Pore landscape of TSC zeolite.

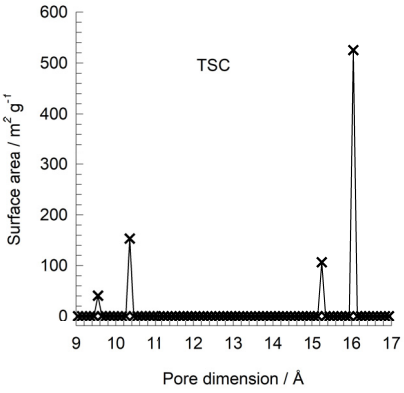

TSC window and pore dimensions

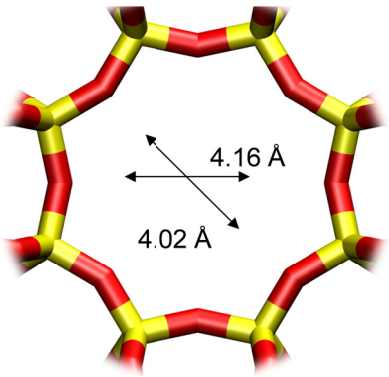

TSC
(supercage - cage)

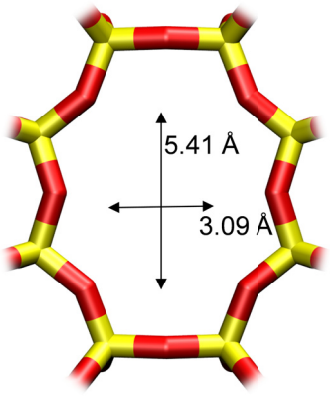

TSC
(supercage - pocket)

	TSC
a /Å	30.742
b /Å	30.742
c /Å	30.742
Cell volume / Å^3	29053.36
conversion factor for [molec/uc] to [mol per kg Framework]	0.0433
conversion factor for [molec/uc] to [kmol/m^3]	0.1260
ρ [kg/m3]	1318.729
MW unit cell [g/moliframework)]	23072.56
ϕ, fractional pore volume	0.454
open space / Å^3/uc	13182.6
Pore volume / cm^3/g	0.344
Surface area /m^2/g	829.0
DeLaunay diameter /Å	4.02

The window dimension calculated using the van der Waals diameter of framework atoms = 2.7 Å are indicated above by the arrows. It is likely that the pockets are inaccessible due to the narrow constriction of 3.092 Å. Another point to note is that the dimensions provided in the IZA website do not appear to be correct for the window on the left.

Figure 13-3. Structural details of TSC zeolite.

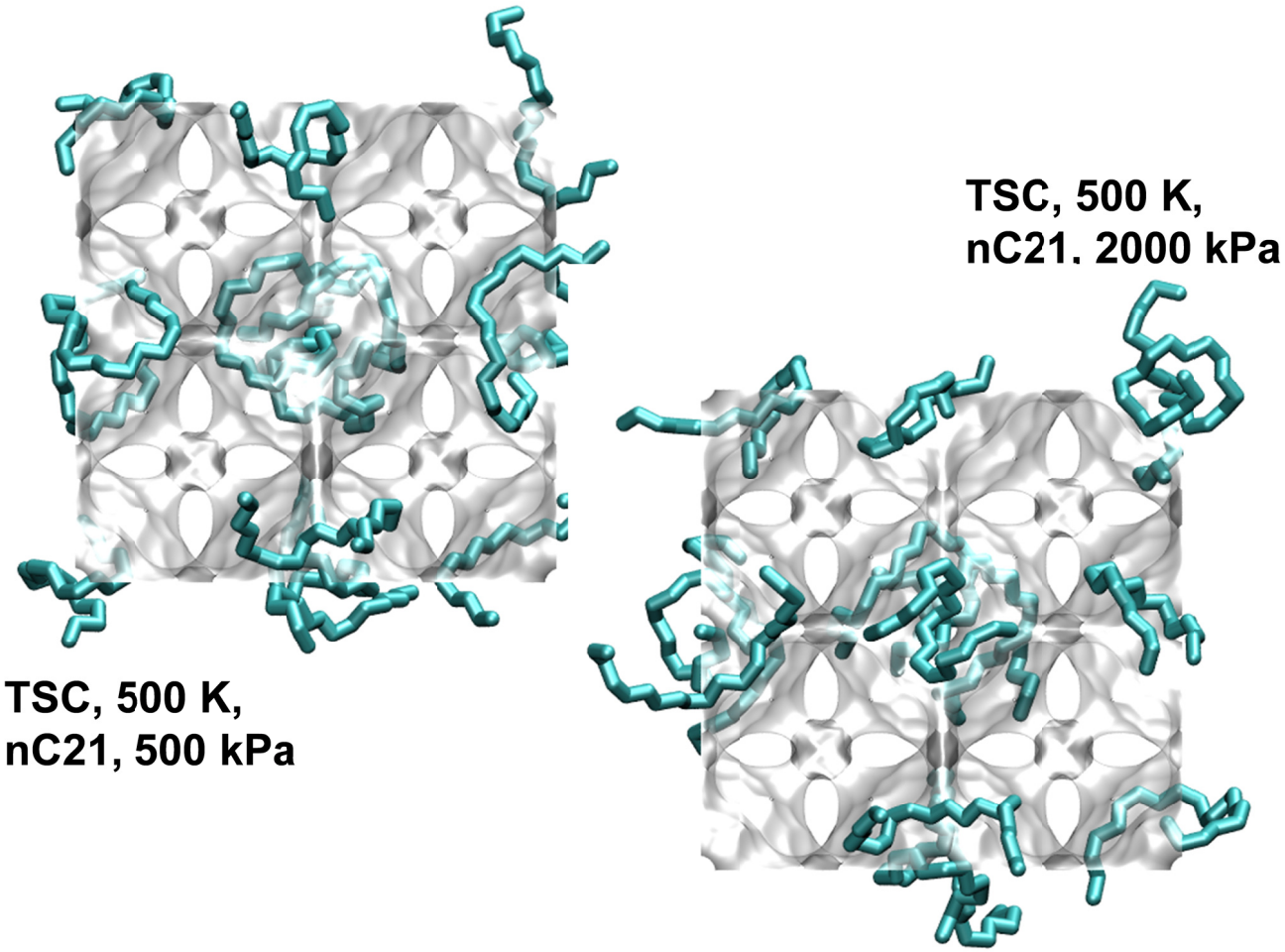

Figure 13-4. Snapshots showing the conformations and location of nC21 in TSC at 500 K.

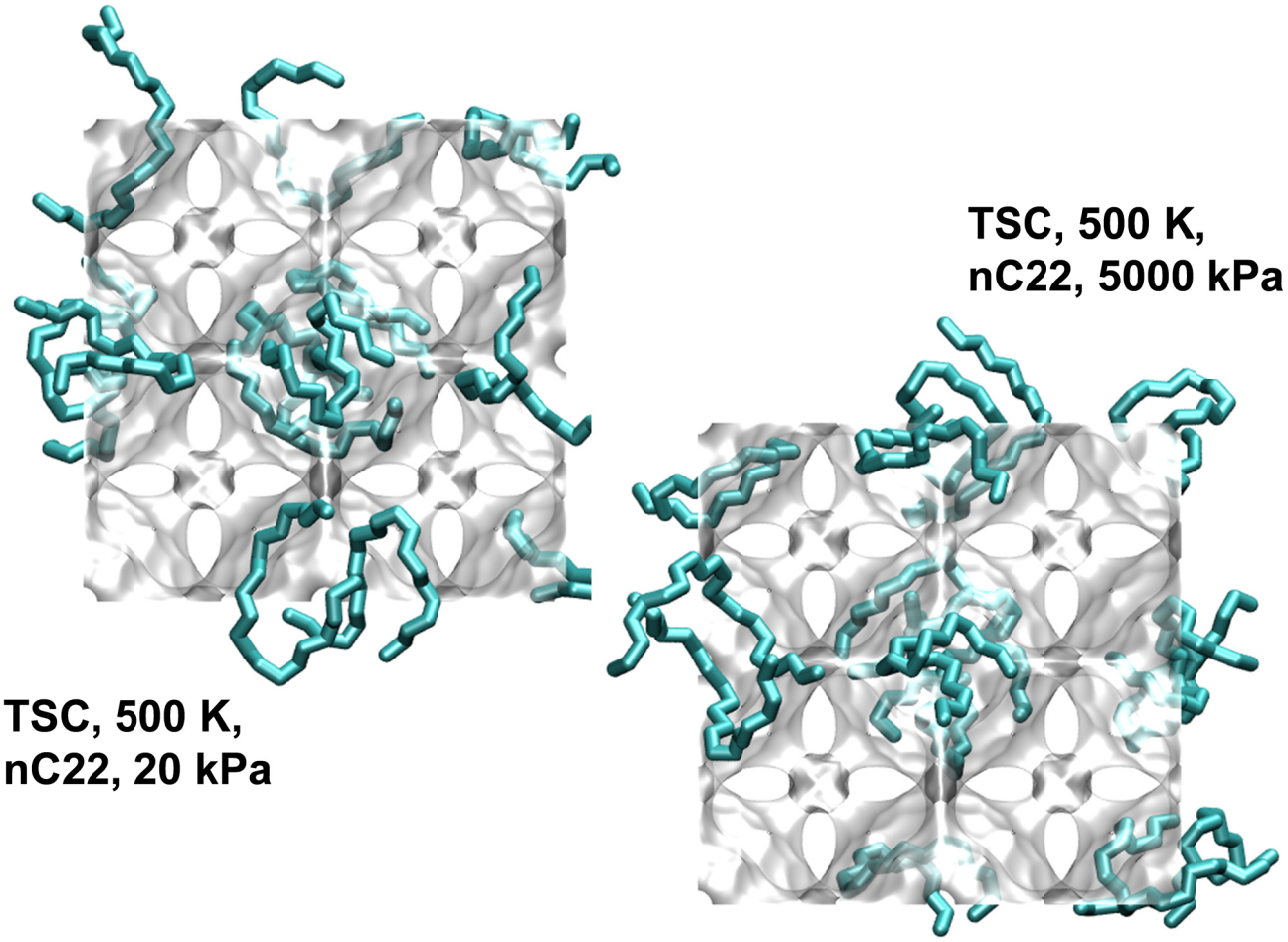

Figure 13-5. Snapshots showing the conformations and location of nC22 in TSC at 500 K.

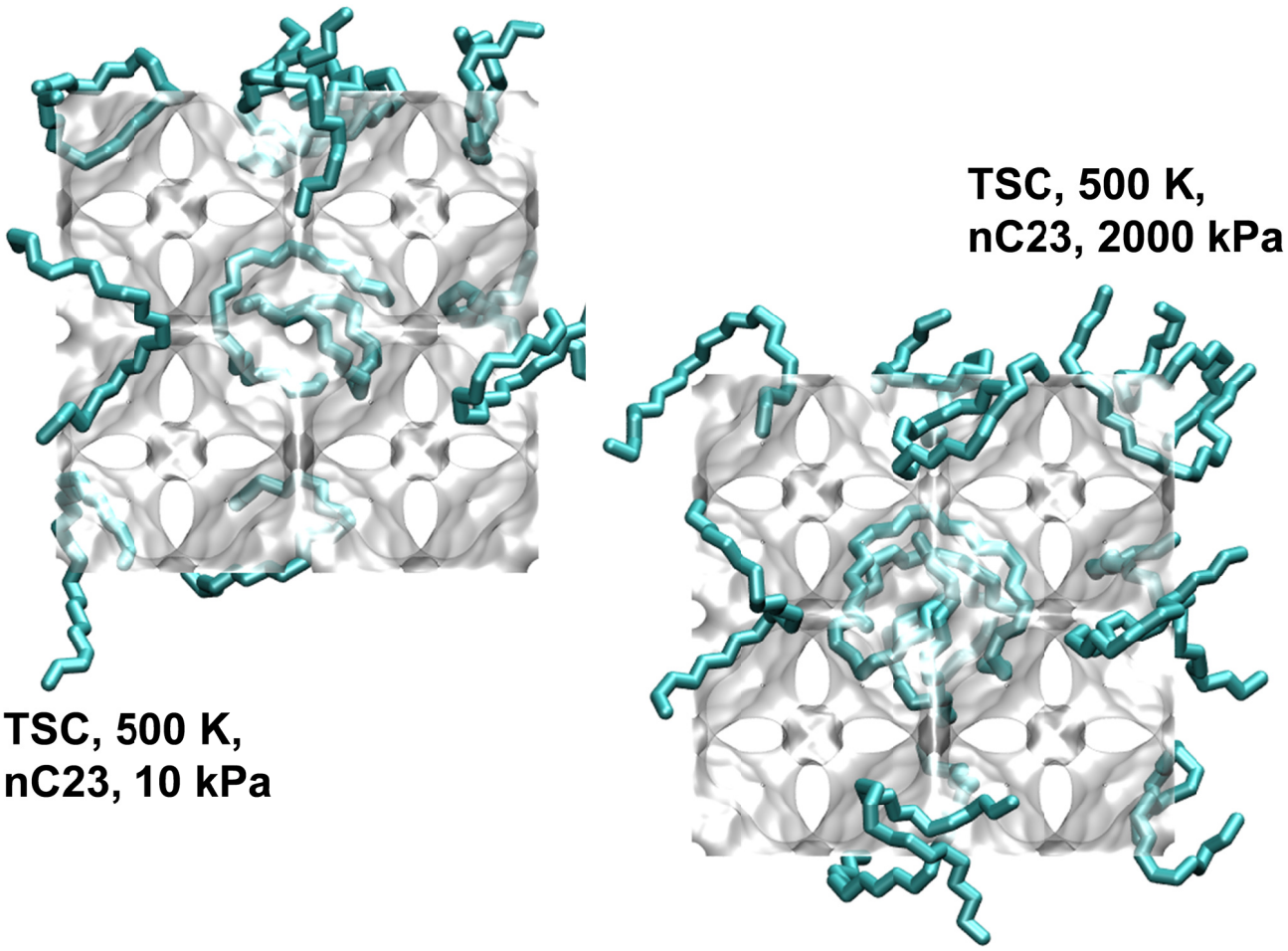

Figure 13-6. Snapshots showing the conformations and location of nC23 in TSC at 500 K.

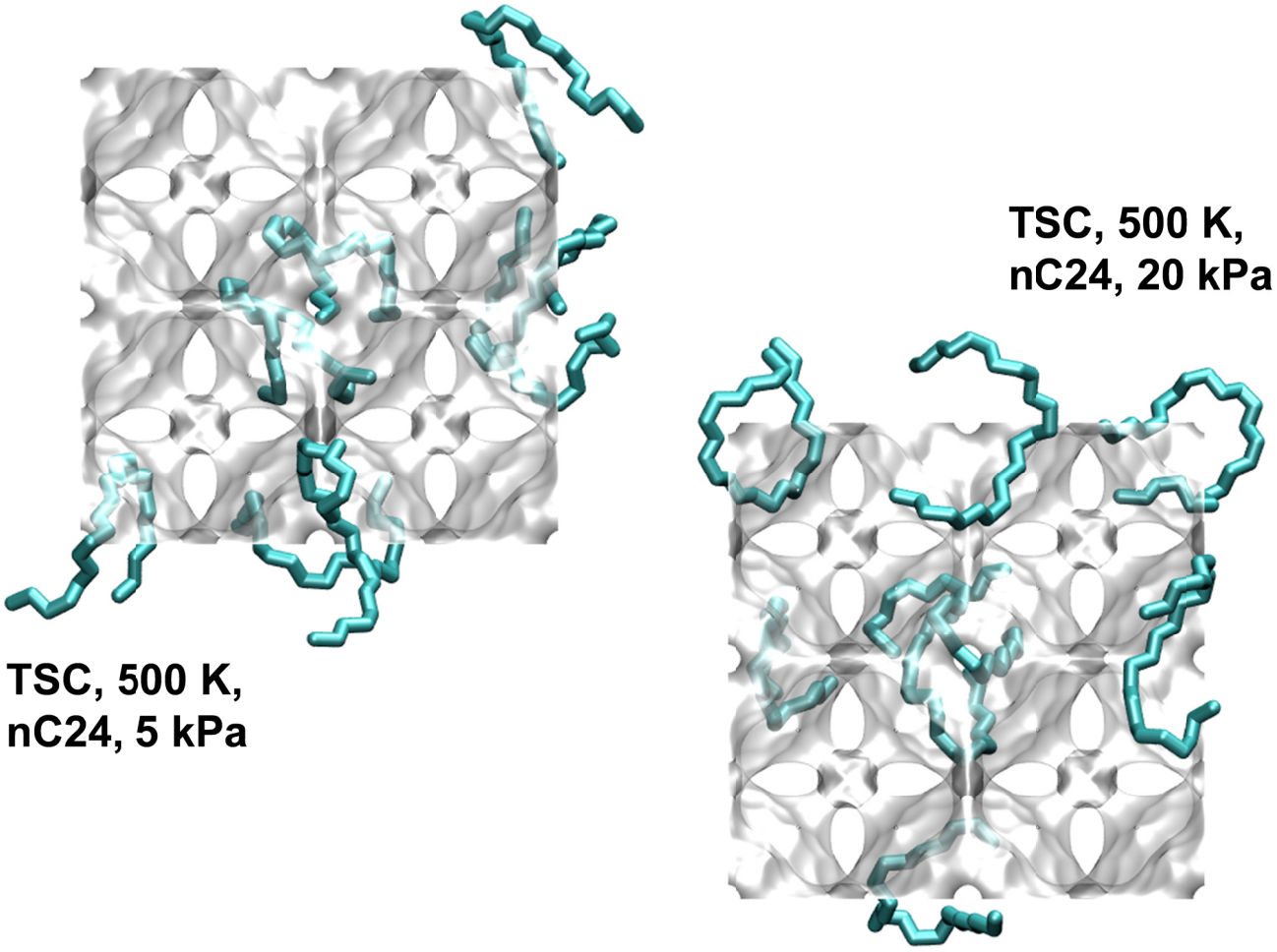

Figure 13-7. Snapshots showing the conformations and location of nC24 in TSC at 500 K.

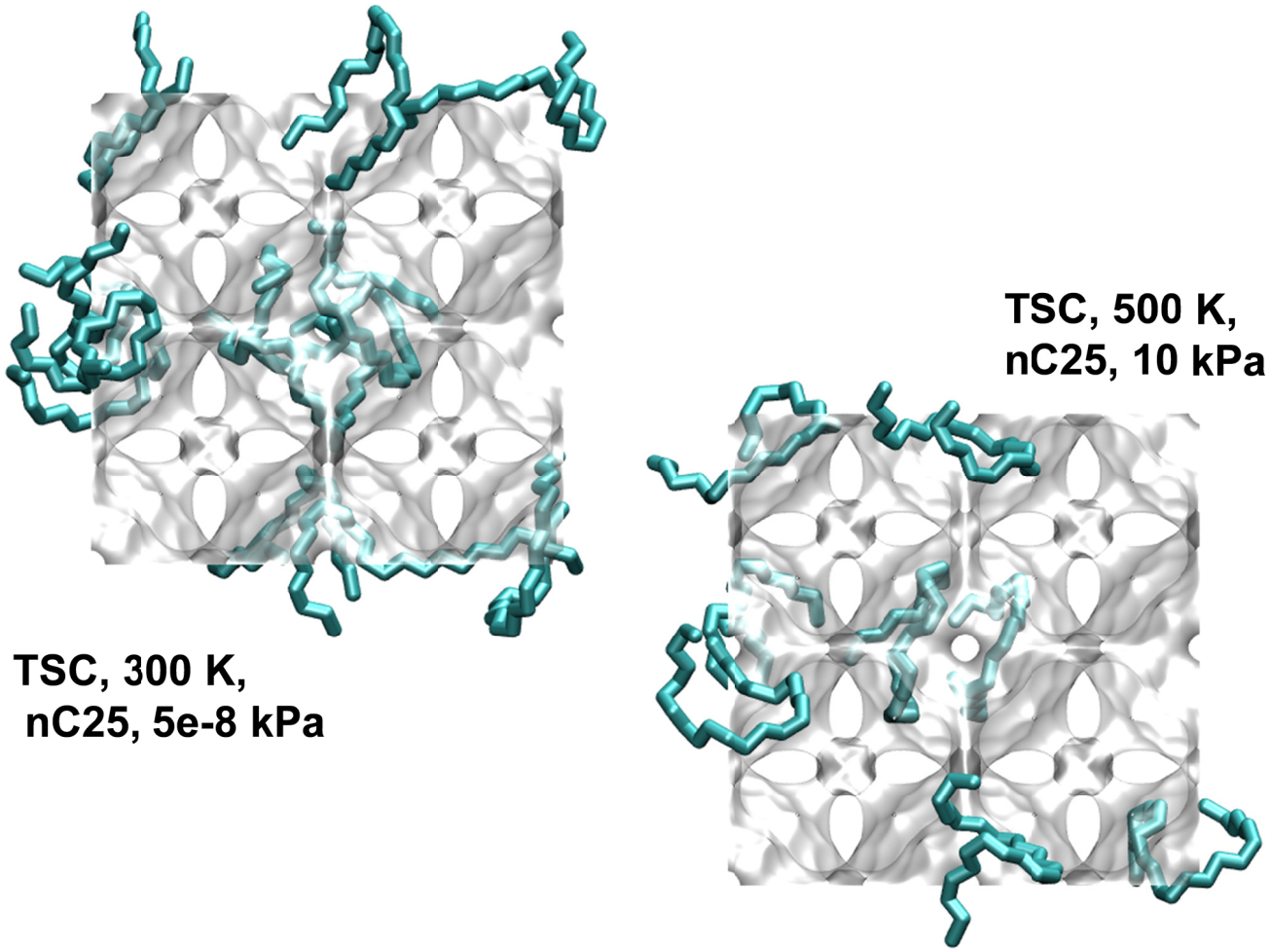

Figure 13-8. Snapshots showing the conformations and location of nC25 in TSC at 500 K.

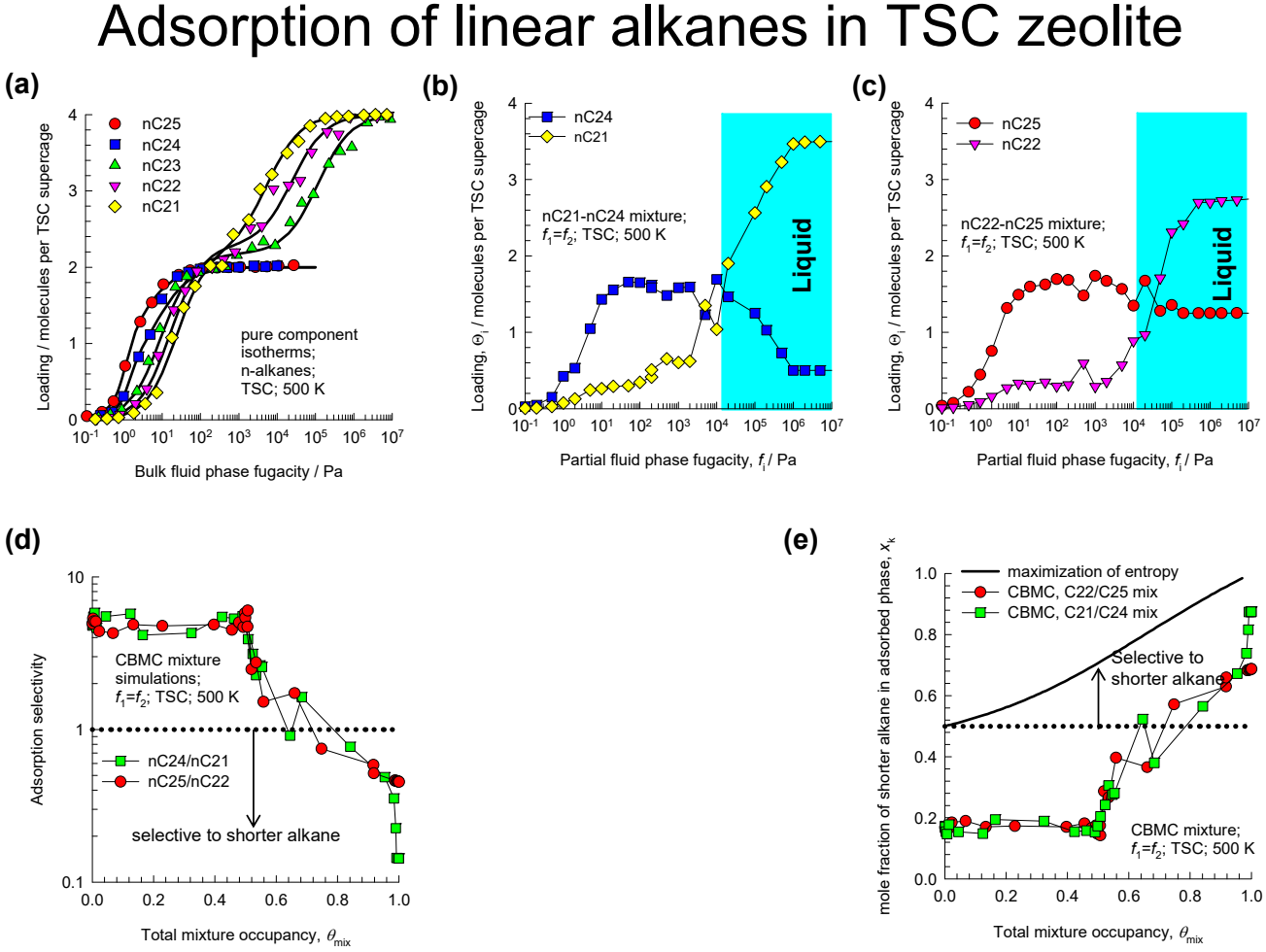

Figure 13-9. (a) CBMC simulations of pure component adsorption isotherms for n-alkanes in TSC at 500 K. (b, c, d, e) CBMC simulations of binary nC21/nC24, and nC22/nC25 mixture adsorption in TSC at 500 K. The partial fugacities in the bulk fluid phase, f_1=f_2. The range of liquid phase operation is indicated by the shaded region; the transition between vapor and liquid bulk phase is determined using the Peng-Robinson equation of state. The *x*-axes in (d, e) represents the the total occupancy of the mixture, θ_{mix} .

14 Separation of Mixtures of Aromatics

14.1 Background information on separation of xylene isomers

Mixtures of o-xylene, m-xylene, and p-xylene are most commonly obtained from catalytic reforming of naphtha. In a commonly used separation scheme used to recover p-xylene (cf. Figure 14-1), the xylenes rich stream from the bottom of the reformer splitter is routed to a xylenes splitter. Here, the heavier aromatics (C9+) are removed from the bottom of the column. The overhead stream from the xylenes splitter containing o-xylene, m-xylene, p-xylene, and ethylbenzene need to be separated for recovery of p-xylene, a valuable feedstock in the manufacture of polymers and fibres.

Due to the very small differences in boiling points, p-xylene recovery form o-xylene/m-xylene/p-xylene/ethylbenzene mixtures is not possible by use of distillation technology. There are, however, significant differences in the freezing points (see Figure 14-2) that allow fractional crystallization to be used for separations. The differences in the freezing points arise because of differences in the stacking efficiencies of molecules. Para-xylene has the highest freezing point because these molecules stack most efficiently; pure p-xylene crystals are the first to emerge from the solution upon cooling. However, the energy requirements for fractional crystallization are high because of the need to cool to temperatures of about 220 K. Selective adsorption of xylene isomers within the pores of ordered crystalline micro-porous materials is an energy-efficient alternative to fractional crystallization. In currently used technology the separation is carried out in a Simulated Moving Bed (SMB) adsorption separation unit. An SMB unit consists of a set of interconnected columns in series; countercurrent flow of the solid and liquid phases is simulated by the periodic shifting of the inlets and outlets in the direction of the liquid flow. Commonly used SMB technologies are UOP's Parex, Axens' Eluxyl, and Toray's Aromax.[67, 68]

The typical composition of a mixed xylenes feed to a simulated moving bed (SMB) adsorber is 19% ethylbenzene, 44% m-xylene, 20% o-xylene, and 17% p-xylene. Since the adsorbent particles are in

contact with a mixture in the *liquid* phase, the pores of the adsorbent material are practically saturated with guest molecules. The hierarchy of adsorption strengths is dictated by molecular packing, or entropy, effects. Binding energies of guest molecules with the framework walls or non-framework cations do not solely determine the separation performance. As pointed out by Peralta et al.,[69] adsorbents selective to p-xylene are desirable for high productivities; they need to adsorb only ~20% of the feed, whereas an adsorbent that rejects p-xylene would have to adsorb 80% of the feed. In current industrial practice the adsorbent used is BaX zeolite, that selectively adsorbs p-xylene. Typically, BaX zeolite also contains other cations such as K^+.

A common feature of all the aromatics separation is that the operation conditions are such that the pores are nearly saturated with guest molecules. Therefore, molecular packing and entropy effects are of primary importance in the separations. Aromatic molecules that pack, or stack, most efficiently within the zeolite or MOF channels are the ones that are selectively adsorbed. For any adsorbent material, the packing efficiencies of any aromatic molecule are dictated by a combination of two factors: (a) molecular dimensions, and (b) departures from planarity.

The discovery of MOFs that are selective to p-xylene and have higher separation potential than BaX zeolite will result in lower recirculation flows of eluent, and solids in the SMB unit and this will result in significant economic advantages.

The height and width of the C8 aromatic molecules are: o-xylene: 8 Å × 7.4 Å; m-xylene: 8.9 Å × 7.4 Å; p-xylene: 9.3 Å × 6.7 Å; ethylbenzene: 9.5 Å × 6.7 Å; styrene: 9.3 Å × 7 Å; see dimensions provided in Figure 14-2. A further point to note is that xylene isomers are flat; these isomers can align themselves parallel to the channel walls, affording better van der Waals interactions with the framework atoms. By contrast, ethylbenzene is not a flat molecule; the ethyl branch is not in the same plane as the benzene ring. Styrene is also a flat molecule. Due to the differences in the molecular dimensions of the xylene isomers, the efficiencies with which the xylene isomers stack within the channels of different dimensions are different. We can deliberately choose an adsorbent material with a specified channel

dimension in order to allow the optimum stacking of one or other of the xylene isomers. Stacking xylenes within 1D channels of MOFs is analogous to stacking books within bookshelves.[8, 70]

14.2 Exploiting entropy effects for separating xylenes

Consider the separation of xylenes using AFI zeolite, that has 1D channels of approximately 7.3 Å; see structural details and pore landscapes in Figure 14-3, and Figure 14-4. Let us first examine the experimental data reported by Chiang et al.[71] on the unary isotherms of o-, m-, and p-xylenes in aluminophosphate $AlPO_4$-5 (with AFI zeolite topology); see Figure 14-4(a). The hierarchy of saturation capacities is o-xylene > p-xylene ≈ m-xylene. CBMC simulations of Torres-Knoop et al.[72] for the unary isotherms of C8 aromatics confirm the experimentally observed hierarchy of saturation capacities; see Figure 14-4(b). The higher saturation capacity of o-xylene can be rationalized on the basis of the computational snapshots[72] in Figure 14-4(c). For m-xylene, and p-xylene, either the "height" or "width" is too large to allow vertical alignment; the orientation of these isomers occurs at an inclination. By contrast, the molecular dimensions of o-xylene allow the molecules to be stacked vertically within the 8.4 Å "grooves" of AFI zeolite; this face-to-face is akin to the packing of potato crisps in cylindrical tubes as marketed by Pringles. An important consequence of the differences in the orientation of isomers is that the "footprints" of o-xylene molecules is significantly shorter than the footprints of m-xylene, and p-xylene molecules. Shorter footprints result in higher saturation capacities, as evidenced in the isotherm data in Figure 14-4(a, b).

Differences in packing efficiencies can be exploited to adsorb the ortho isomer preferentially from a mixture of xylenes. CBMC simulations of the adsorption of 4-component o-xylene/m-xylene/p-xylene/ethylbenzene mixtures in AFI zeolite at 433 K are shown in Figure 14-5(a,b); the partial fugacities in the bulk fluid phase, f_i, are equal to one another. For mixture occupancies $\theta_{mix} > 0.6$ entropy effects cause the adsorbed phase to be predominatly occupied by o-xylene. Indeed, at pore saturation condtions, $\theta_{mix} \approx 1$, the adsorbed phase is almostly exclusively occupied by o-xylene. Hu et al.[73, 74] report transient breakthrough experiments to demonstrate that the breakthrough of o-xylene

occurs significantly later than that of either m-xylene or p-xylene, confirming the selectivity of AFI to o-xylene. It is also noteworthy that $AlPO_4$-5 zeolite has been patented by Exxon Research & Engineering for o-xylene selective separation of aromatic mixtures.[75]

Experimental data[26, 76, 77] for MIL-47 and MIL-53 with 1D rhombohedric channels of 8.5 Å show that these MOFs are selective to adsorption of o-xylene when operating at conditions close to pore saturation. The computational snapshots[70] in Figure 14-6, obtained from CBMC simulations, clearly show the optimal, commensurate, stacking of o-xylene within 8.5 Å channels of MIL-47.

Within the one-dimensional 10 Å channels of MAF-X8, we have commensurate stacking of p-xylene;[70] see snapshots in Figure 14-7(a). CBMC simulations for mixture adsorption show that the adsorbed phase is significantly richer in the para-isomer, suggesting a good potential for replacement of BaX zeolite.

Figure 14-8 presents snapshots of stacking of o-xylene, m-xylene, p-xylene, and ethylbenzene within the 1D zig-zag shaped channels of Co-CUK-1, which is comprised of cobalt(II) cations and the dianion of dicarboxylic acid $[Co_3(2,4\text{-pdc})_2(\mu 3\text{-}OH)_2]$ (2,4-pdc = pyridine-2,4-dicarboxylic acid dianion); the synthesis of this MOF is described by Yoon et al.[78] The p-xylene molecules can stack vertically, and this results in a higher saturation capacity for the para-isomer, as demonstrated by the experimental data on unary isotherms in Figure 14-8. IAST calculations of mixture adsorption, along with transient breakthrough simulations, show that the recovery of p-xylene is expected to be significantly superior to that of BaX zeolite. [78]

14.3 Entropy effects in ethylbenzene/styrene separations

Alkylation of benzene with ethene produces ethyl benzene (cf. Figure 14-1), which is dehydrogenated to styrene, a monomer used in the manufacture of many commercial polymers and co-polymers The conversion of ethylbenzene to styrene is only partial, and the reactor product contains a large fraction, in the range of 20%-40%, of unreacted ethylbenzene. Due to the small, 9 K, difference in their boiling

points, the distillation separation of styrene and ethylbenzene has to be carried out in tall distillation columns operating under vacuum and at high reflux ratios; the energy demands are therefore very high.

Maes et al.[79] and Remy et al.[80] have demonstrated that MIL-47 (V) and MIL-53 (Al) also have the potential for separation of mixtures of styrene and ethylbenzene. Styrene is a flat molecule; by contrast, ethylbenzene is not a flat molecule; the ethyl branch is not in the same plane as the benzene ring. Being flat, styrene molecules stack more efficiently within the 1D channels of MIL-47 (V) and MIL-53 (Al). The unary isotherms for MIL-47, determined from CBMC simulations, confirm that the saturation capacity of styrene is higher than that of ethylbenzene, due to commensurate stacking in the 1D channels; see Figure 14-9(a). Due to its higher packing efficiency of styrene, the mixture adsorption is strongly in favor of styrene; see CBMC simulations data for mixture adsorption in Figure 14-9(b, c, d). At pore saturation conditions, the pores are almost exclusively filled with styrene.

14.4 Entropy effects in separation of trichlorobenzene isomers

Torres-Knoop et al.[72, 81] have also provided other examples in which optimum face-to-face stacking of aromatic molecules can lead to uncommonly effective separations. Within triangular channels of a structure such as $Fe_2(BDP)_3$, but with larger channel dimensions, 1,3,5 tri-chlorobenzene (TCB) can be selectively separated from the 1,2,3 and 1,2,4 TCB isomers; the preferential adsorption of the 1,3,5 isomer is due to optimum face-to-face stacking; see computational snapshots in Figure 14-10. Figure 14-11(a) shows CBMC simulations for unary isotherms of 1,2,3 tri-chlorobenzene (TCB), 1,2,4 TCB, and 1,3,5 TCB in modified $Fe_2(BDP)_3$ at 433 K. Due to optimal face-to-face stacking, the 1,3,5 isomer has the highest saturation capacity. For adsorption of ternary mixtures of the three TCB isomers under saturation conditions, the adsorbed phase is practically devoid of the 1,2,3 and 1,2,4 isomers due to entropy effects that favor of 135 TCB, the component with the smallest footprint; see Figure 14-11(b,c).

14.5 List of Figures for Separation of Mixtures of Aromatics

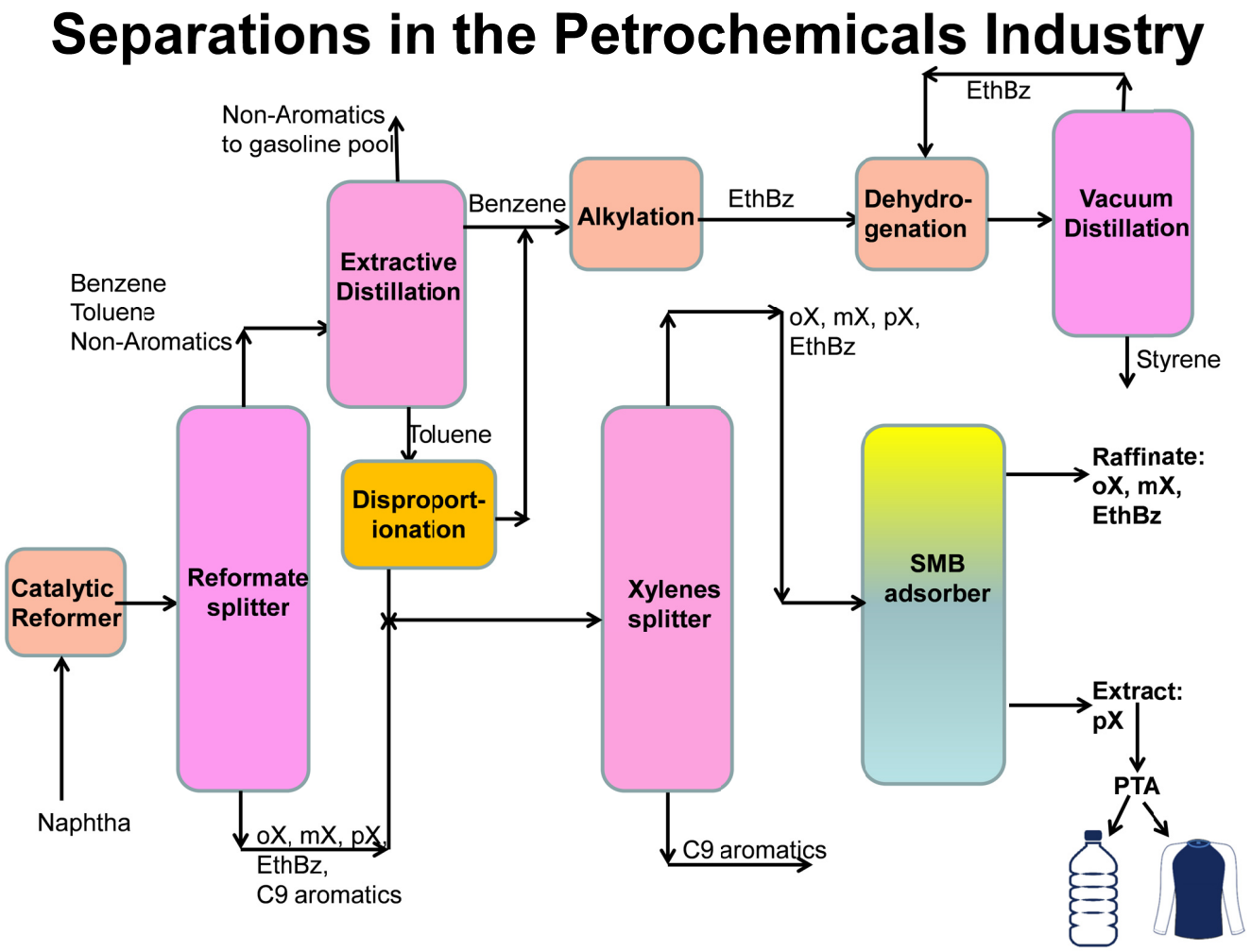

Figure 14-1. Schematic showing the separations of the products from a catalytic reforming unit.

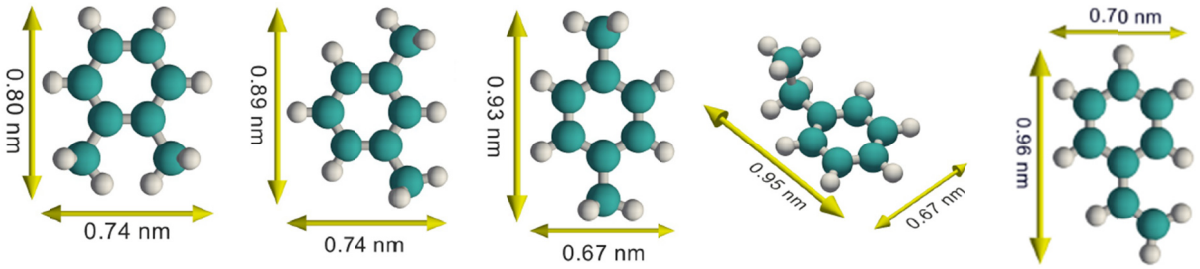

	o-xylene (oX)	m-xylene (mX)	p-xylene (pX)	Ethylbenzene (EtBz)	Styrene (St)
Boiling point	417.6 K	412.3 K	411.5 K	409 K	418.3 K
Freezing point	248 K	222 K	286 K	178 K	242.5 K

Figure 14-2. The molecular dimensions of xylene isomers, ethylbenzene and styrene culled from Torres-Knoop et al.[70]

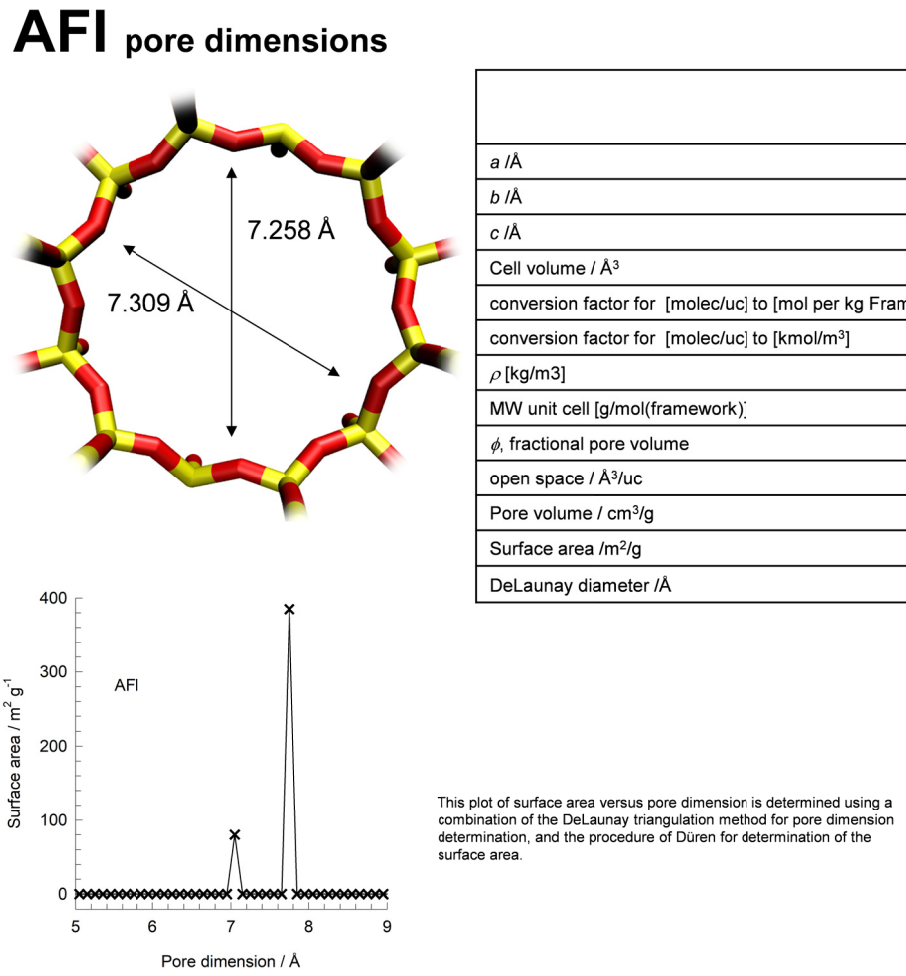

	AFI
a /Å	23.774
b /Å	13.726
c /Å	8.484
Cell volume / Å^3	2768.515
conversion factor for [molec/uc] to [mol per kg Framework]	0.3467
conversion factor for [molec/uc] to [kmol/m^3]	2.1866
ρ [kg/m3]	1729.876
MW unit cell [g/mol(framework)]	2884.07
ϕ, fractional pore volume	0.274
open space / Å^3/uc	759.4
Pore volume / cm^3/g	0.159
Surface area /m^2/g	466.0
DeLaunay diameter /Å	7.26

Figure 14-3. Pore dimensions and structural details of AFI zeolite.

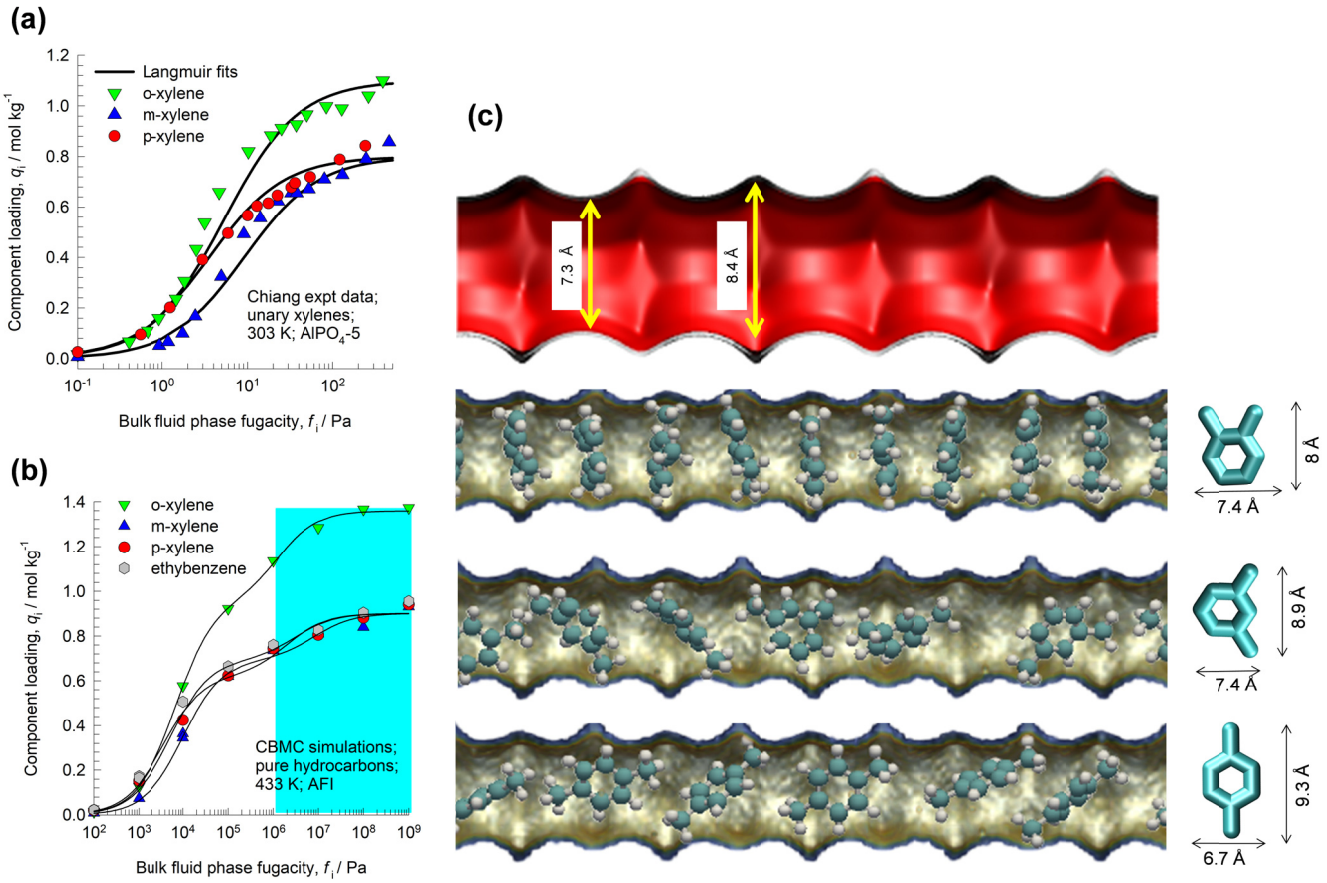

Figure 14-4. (a) Experimental data of Chiang et al.[71] for pure component isotherms for xylene isomers in $AlPO_4$-5 at 303 K. (b) CBMC simulations[72] of the unary isomers for C8 aromatics in AFI zeolite at 433 K.(c) Computational snapshots[72] showing the orientations of o-xylene, m-xylene, and p-xylene as they stack within the corrugated 1D channel of AFI zeolite.

AFI zeolite: Xylenes Mixture Adsorption

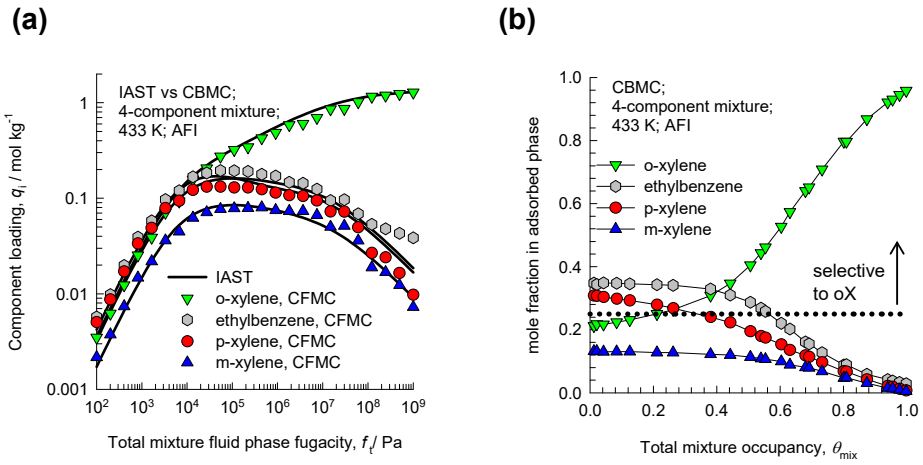

Figure 14-5. (a, b) CBMC simulations of the adsorption of 4-component o-xylene/m-xylene/p-xylene/ethylbenzene mixtures in AFI zeolite at 433 K; the partial fugacities in the bulk fluid phase, f_i, are equal to one another. In (a) the component loadings are plotted as a function of the total bulk fluid phase fugacity, f_t. Also shown by the continuous solid lines are the IAST calculations using the unary isotherm fits. In (b) the component mole fractions in the adsorbed phase are plotted as a function of the total occupancy of the mixture, θ_{mix} .

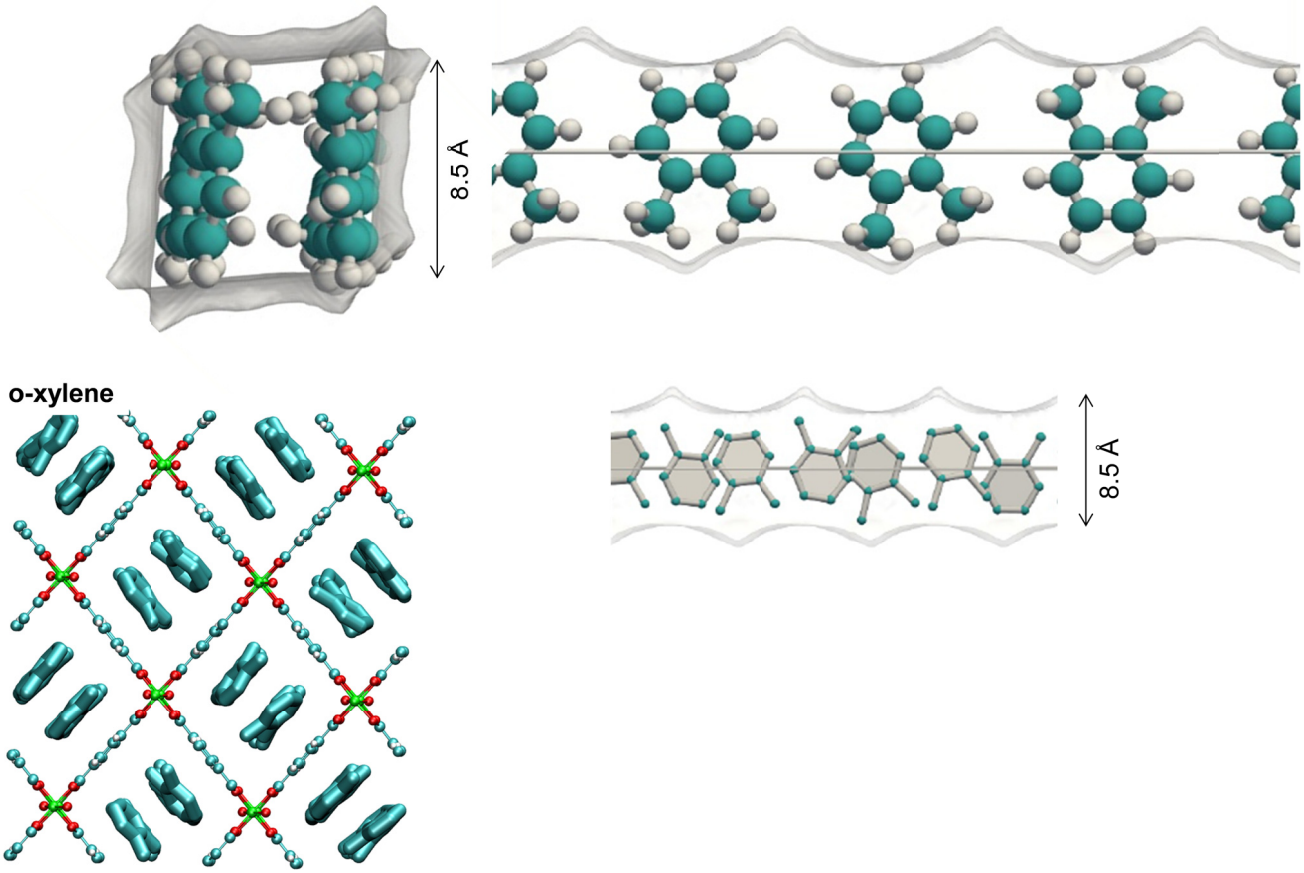

Figure 14-6. Computational snapshots [70] showing the stacking of o-xylene within 8.5 Å channels of MIL-47.

Commensurate stacking of p-xylene in MAF-X8

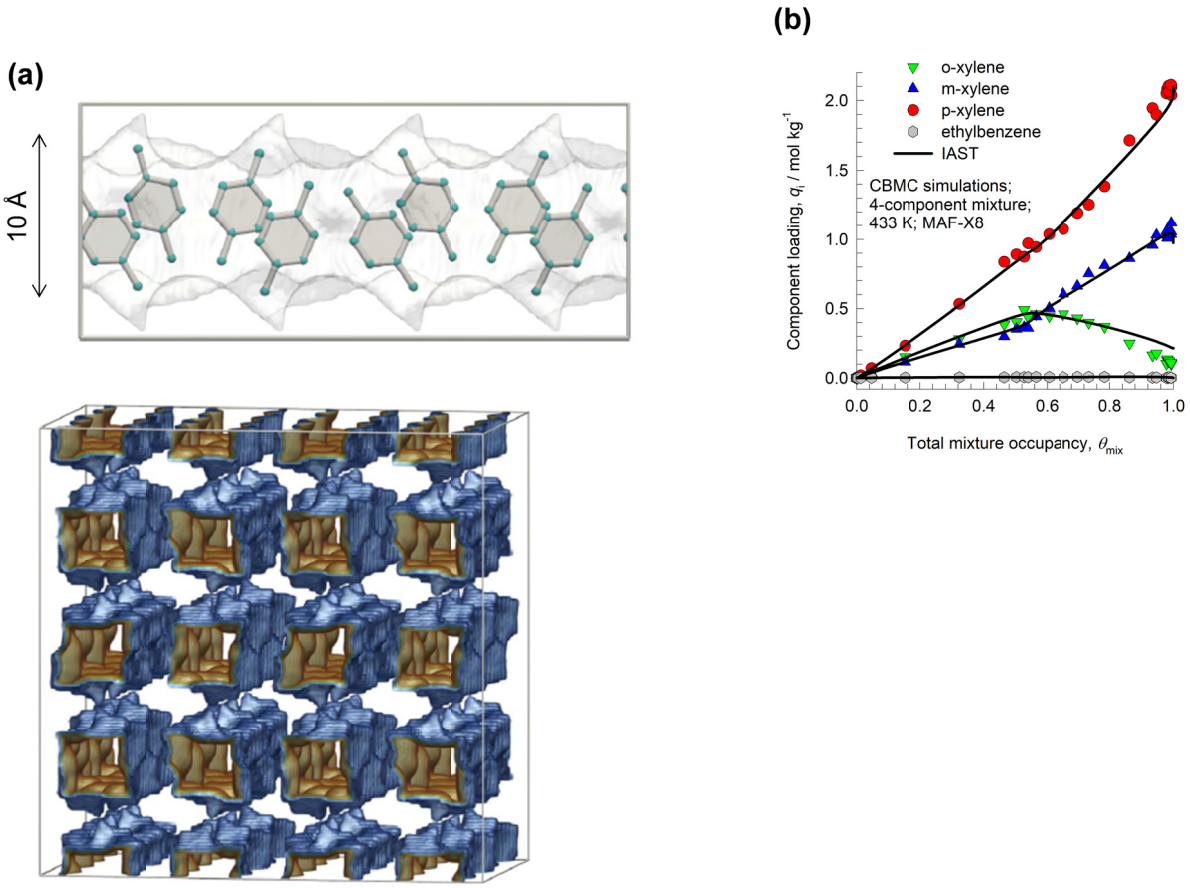

Figure 14-7. (a) Computational snapshots [70] showing the stacking of *p*-xylene within 10 Å channels of MAF-X8. (b) CBMC simulations for adsorption of 4-component o-xylene/m-xylene/p-xylene/ethylbenzene mixtures in MAF-X8 zeolite at 433 K; the partial fugacities in the bulk fluid phase, f_i, are equal to one another.

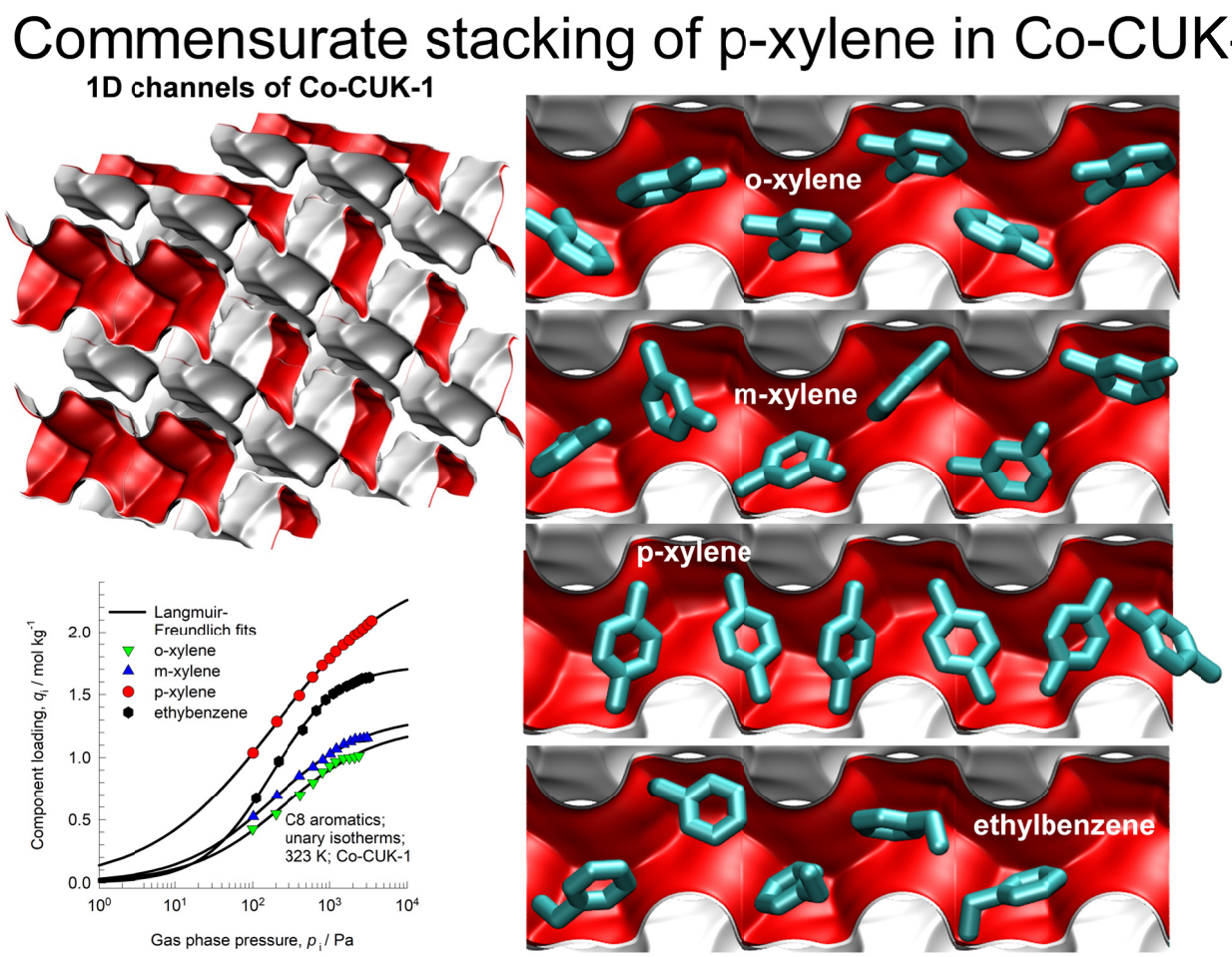

Figure 14-8. Snapshots, obtained from CBMC simulations, showing the stacking of *o*-xylene, *m*-xylene, *p*-xylene, and ethylbenzene within the 1D zig-zag shaped channels of Co-CUK-1. Also shown are the experimental data on unary isotherms presented by Yoon et al.[78]

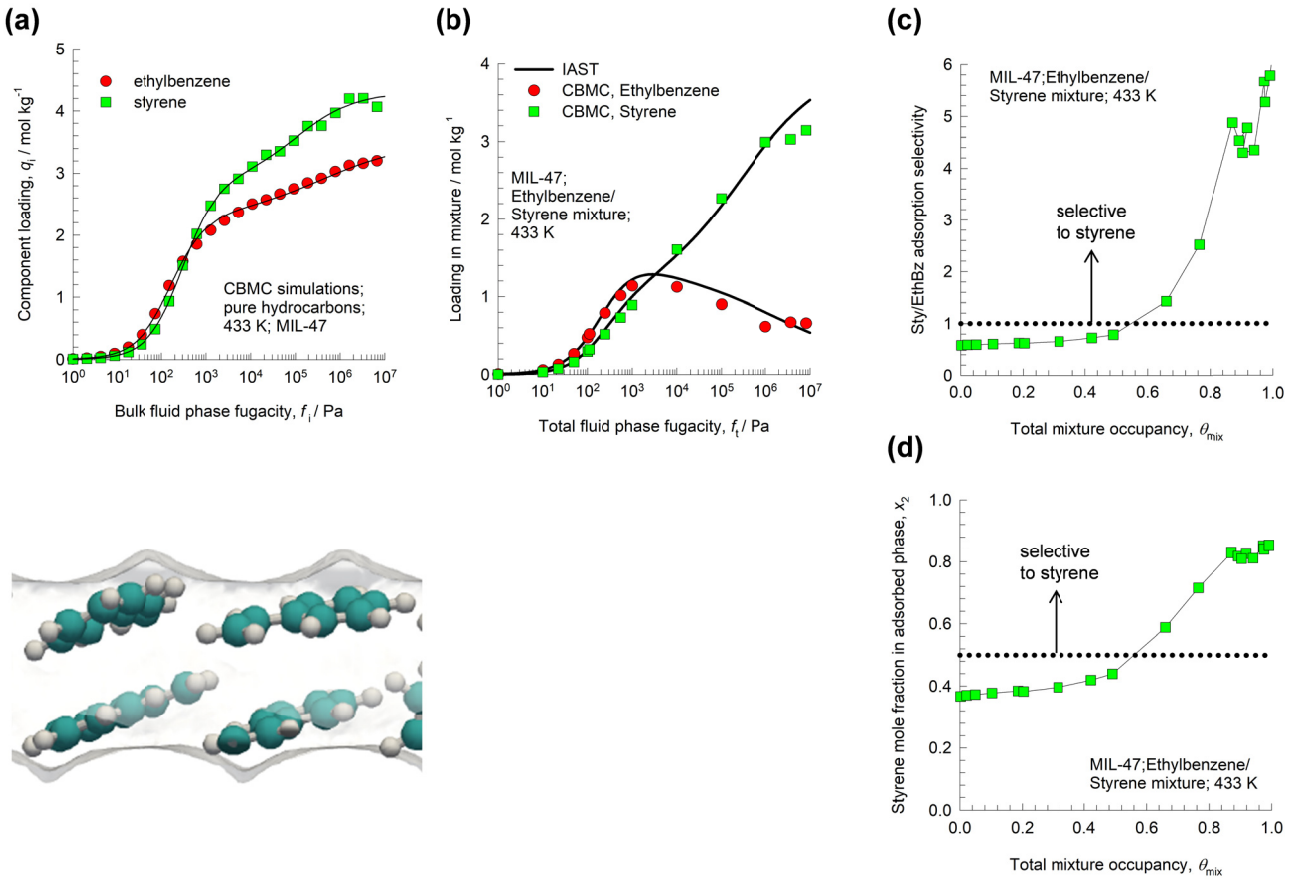

Figure 14-9. (a) CBMC simulations[82] of unary isotherms of ethylbenzene and styrene in MIL-47 at 433 K. (b, c, d) CBMC simulations[82] for adsorption of binary ethylbenzene/styrene mixtures in MIL-47 at 433 K; the partial fugacities in the bulk fluid phase, f_i, are equal to one another.

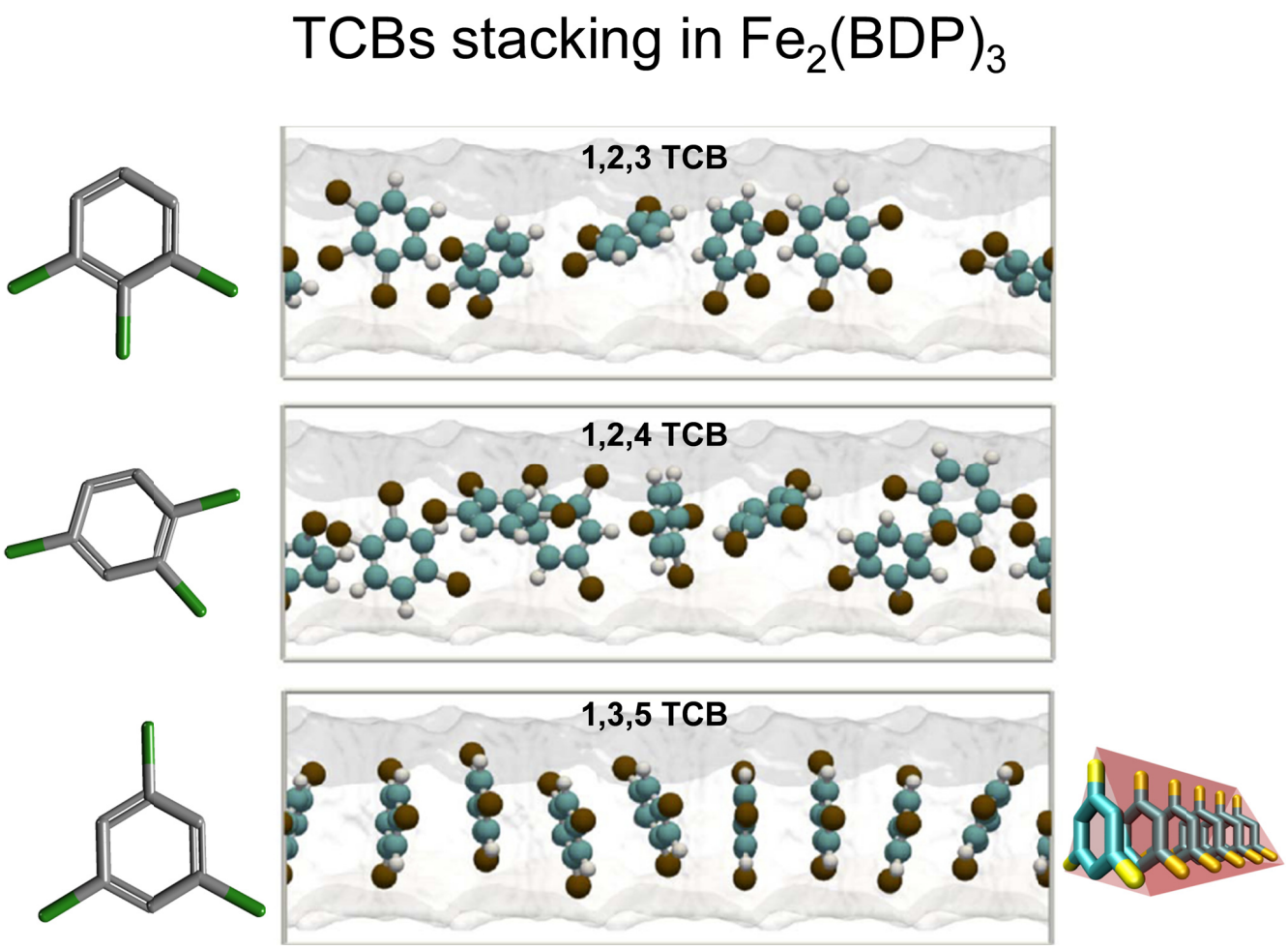

Figure 14-10. Computational snapshots showing conformations and stacking of 1,2,3 trichlorobenzene (TCB), 1,2,4 TCB, and 1,3,5 TCB within the triangular channels of modified $Fe_2(BDP)_3$. From Torres-Knoop et al. [72]

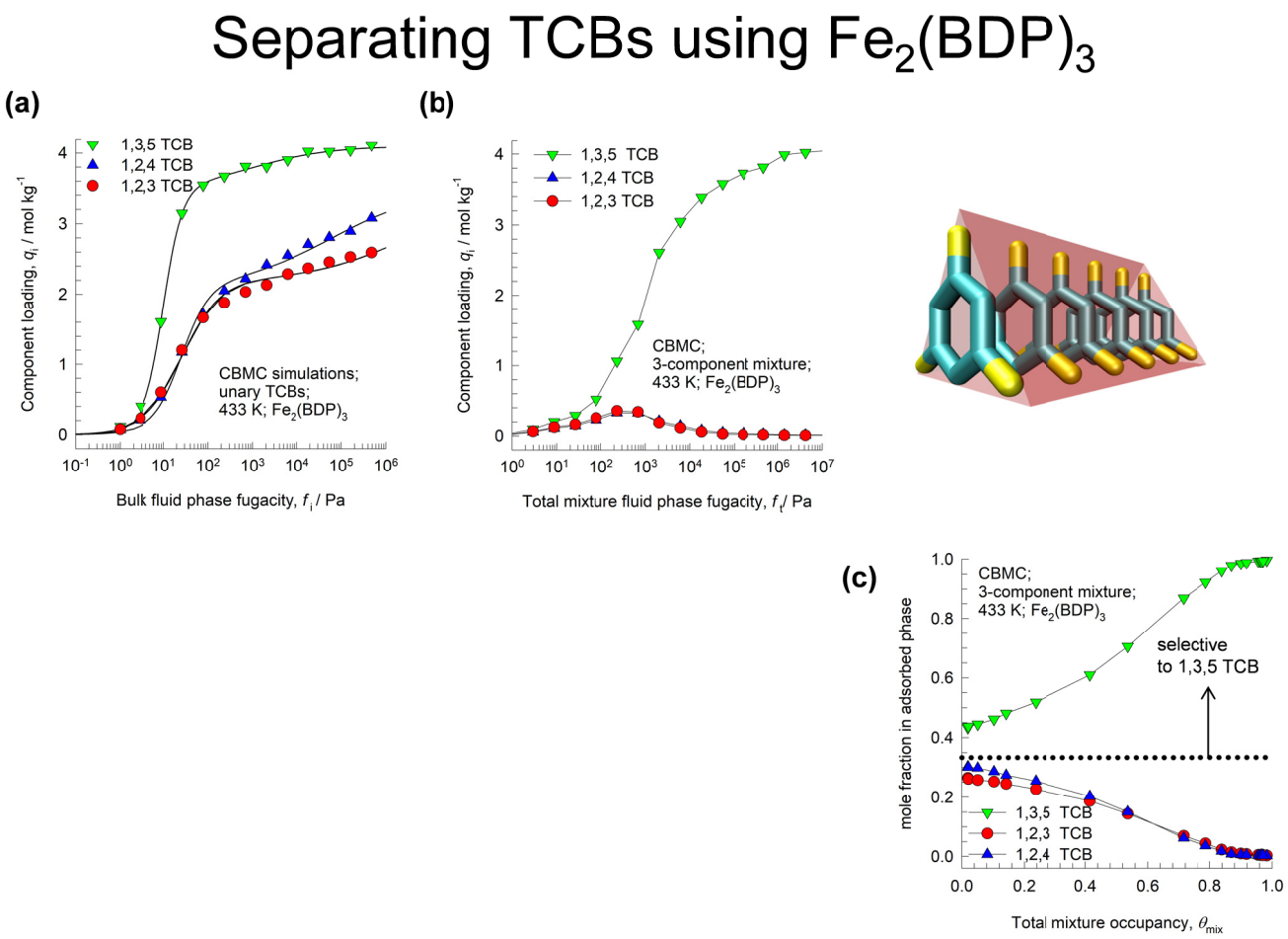

Figure 14-11. (a) CBMC simulations[72] for unary isotherms of 1,2,3 tri-chlorobenzene (TCB), 1,2,4 TCB, and 1,3,5 TCB in modified $Fe_2(BDP)_3$ at 433 K. (b, c) CBMC simulations[72] of (b) component loadings, and (c) adsorbed phase mole fractions for adsorption of equimolar ternary TCB mixtures in modified $Fe_2(BDP)_3$ at 433 K.

15 Separation of Mixture of Polar Compounds using CuBTC

CuBTC (= $Cu_3(BTC)_2$ with BTC = 1,3,5-benzenetricarboxylate, also known as HKUST-1) framework is composed of copper atoms connected by benzene-1,3,5-tricarboxylate (BTC) linkers, which form a characteristic paddle-wheel structure: two copper atoms bonded to the oxygen atoms of four BTC linkers, generating four-connected square-planar vertexes; see Figure 15-1, and Figure 15-2. The framework contains two types of large cavities (9 Å diameter) and small cavities (of 5 Å diameter). The larger cavities (L_2 and L_3) are similar in size and shape but as a result of the paddle-wheel, the copper atoms are only accessible from the L_3 cages. L_2 and L_3 cavities are connected through triangular-shaped windows. The small cavities (T_1) are tetrahedral pockets enclosed by the benzene rings; these are connected to L_3 cages by small triangular windows (3.5 Å in size), as shown in Figure 15-3.

Figure 15-4 presents CBMC simulated unary isotherms[46, 47] for water, methanol, ethanol, 1-propanol, and benzene in CuBTC at 298 K. These isotherms are not amenable to fitting by the simple Langmuir model; the continuous solid lines are the dual-site or 3-site Langmuir-Freundlich model fits; the unary isotherm fit parameters are specified in Table 15-1, and Table 15-2. The saturation capacities are: water = 54 mol kg^{-1}; methanol = 19.9 mol kg^{-1}; ethanol = 13 mol kg^{-1}; 1-propanol = 10 mol kg^{-1}; benzene = 6.7 mol kg^{-1}.

Figure 15-5 presents CBMC simulations[83, 84] of binary mixture adsorption in CuBTC at 298 K: (a) water/ethanol, (b) water/1-propanol, (c) methanol/ethanol, (d) methanol/benzene, (e) ethanol/benzene, and (f) water/benzene mixtures, with equal partial fugacities in the bulk fluid phase, $f_1=f_2$. The *y*-axes represent the mole fraction in the adsorbed phase of the component with the higher saturation capacity. The *x*-axes represent the total occupancy of the mixture $\theta_{mix} = \frac{q_1}{q_{1,sat}} + \frac{q_2}{q_{2,sat}}$. For all six mixtures, the adsorption favors the component with the higher saturation capacity at mixture occupancies, θ_{mix} approaching pore saturation.

15.1 List of Tables for Separation of Mixture of Polar Compounds using CuBTC

Table 15-1. 3-site Langmuir-Freundlich isotherm fits for adsorption of water in CuBTC at 298 K.

	Site A			Site B			Site C		
	$q_{A,sat}$ / mol kg^{-1}	b_A / Pa$^{-\nu_{iA}}$	ν_A	$q_{B,sat}$ / mol kg^{-1}	b_B / Pa$^{-\nu_{iB}}$	ν_B	$q_{C,sat}$ / mol kg^{-1}	b_C / Pa$^{-\nu_C}$	ν_C
water	22	5.48 $\times 10^{-4}$	1	22	6.24 $\times 10^{-32}$	10	10	2.51 $\times 10^{-4}$	0.6

Table 15-2. Dual-site Langmuir-Freundlich parameters for adsorption of methanol, ethanol, and benzene at 298 K in CuBTC.

Adsorbate	Site A			Site B		
	$q_{A,sat}$ mol kg^{-1}	b_A Pa$^{-\nu_A}$	ν_A dimensionless	$q_{B,sat}$ mol kg^{-1}	b_B Pa$^{-\nu_B}$	ν_B dimensionless
methanol	8.4	3.82×10^{-4}	1.03	11.5	9.3×10^{-16}	6.5
ethanol	5	2.29×10^{-3}	0.97	8	6.41×10^{-7}	3.2
1-propanol	8	4.83×10^{-4}	2.7	2	2.07×10^{-2}	0.5
benzene	4.6	2.76×10^{-6}	3.1	2.1	3.96×10^{-3}	1

15.2 List of Figures for Separation of Mixture of Polar Compounds using CuBTC

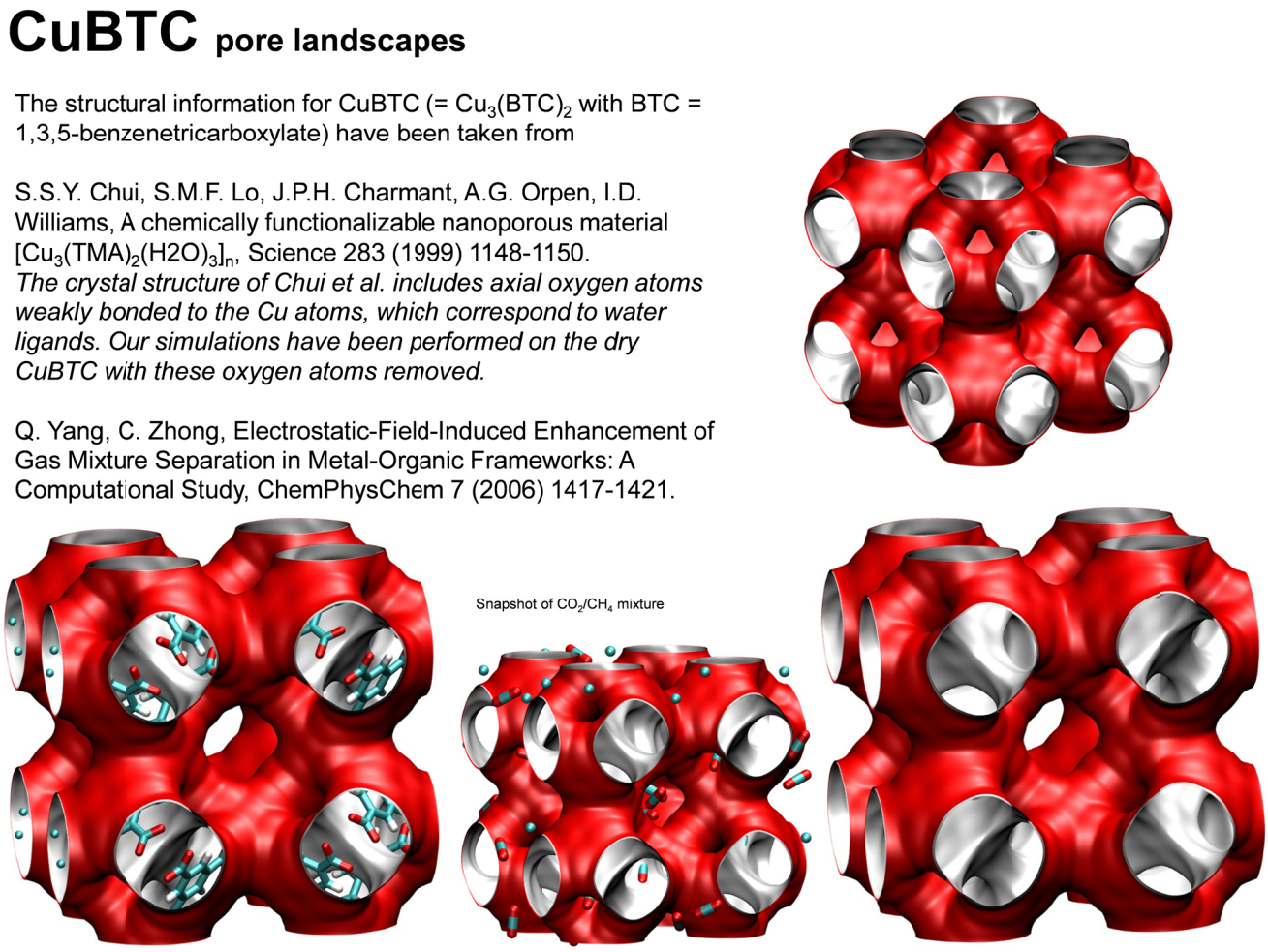

Figure 15-1. Pore landscape of CuBTC.

CuBTC pore dimensions

	CuBTC
a /Å	26.343
b /Å	26.343
c /Å	26.343
Cell volume / Å^3	18280.82
conversion factor for [molec/uc] to [mol per kg Framework]	0.1034
conversion factor for [molec/uc] to [kmol/m^3]	0.1218
ρ [kg/m3]	878.8298
MW unit cell [g/mol(framework)]	9674.855
ϕ, fractional pore volume	0.746
open space / Å^3/uc	13628.4
Pore volume / cm^3/g	0.848
Surface area /m^2/g	2097.0
DeLaunay diameter /Å	6.23

The CuBTC structure consists of two types of “cages” and two types of “windows” separating these cages. Large cages are inter-connected by 9 Å windows of square cross-section. The large cages are also connected to tetrahedral-shaped pockets of ca. 6 Å size through triangular-shaped windows of ca. 4.6 Å size

Figure 15-2. Structural details of CuBTC.

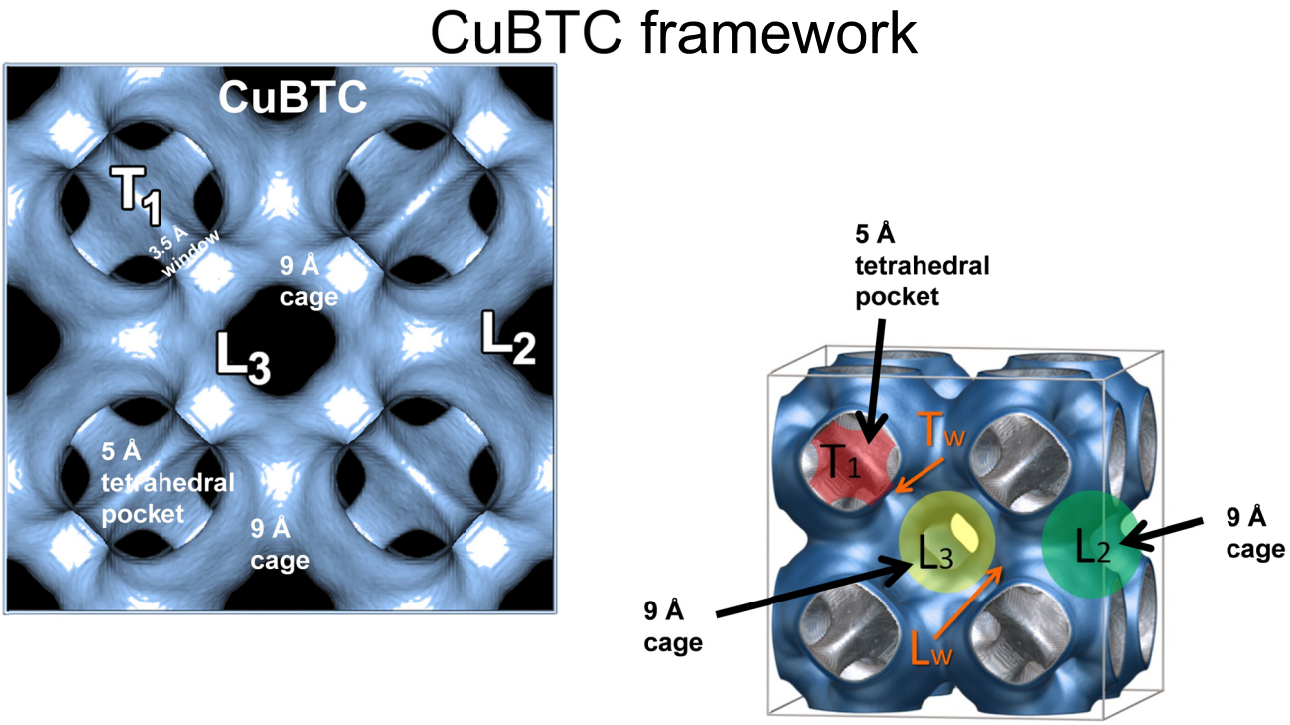

Figure 15-3. Cage connectivity of CuBTC.

Unary isotherms of polar molecules in CuBTC

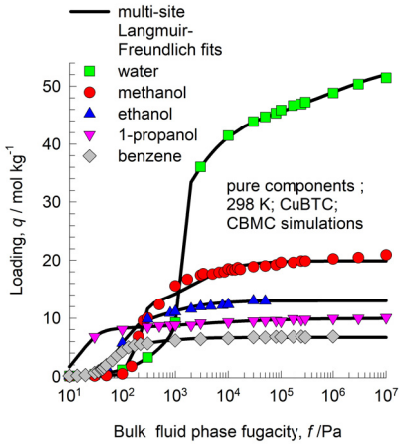

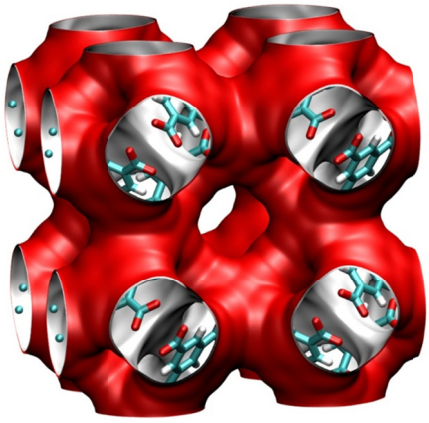

Figure 15-4. CBMC simulations[83, 84] for unary isotherms of water, methanol, ethanol, 1-propanol, and benzene in CuBTC at 298 K with 3-site (for water) or 2-site Langmuir-Freundlich isotherm fits. For CuBTC, the unary isotherm fit parameters are specified in Table 15-1, and Table 15-2.

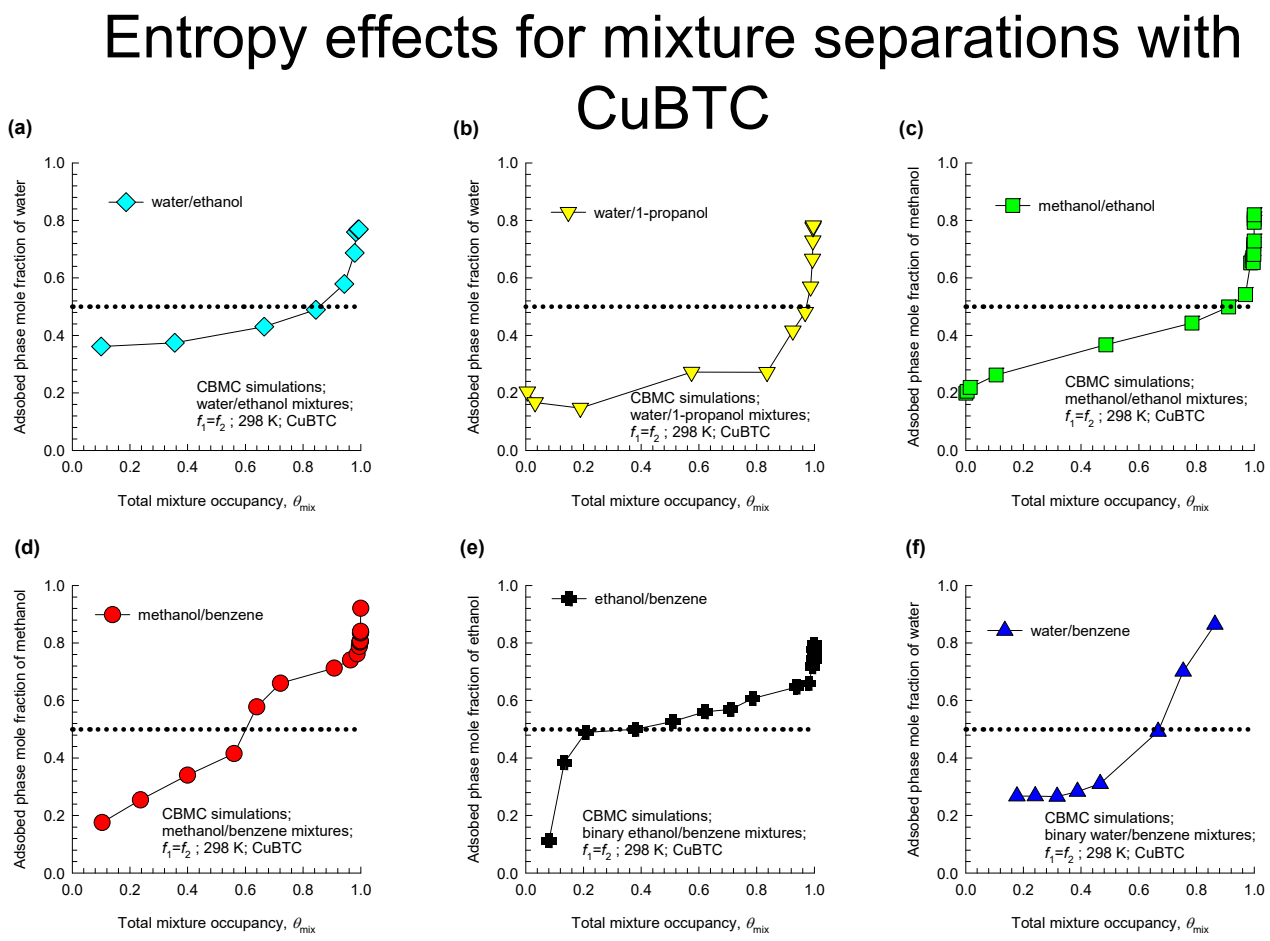

Figure 15-5. CBMC simulations[83, 84] of binary mixture adsorption in CuBTC at 298 K: (a) water/ethanol, (b) water/1-propanol, (c) methanol/ethanol, (d) methanol/benzene, (e) ethanol/benzene, and (f) water/benzene mixtures, with equal partial fugacities in the bulk fluid phase, $f_1=f_2$. The *y*-axes represent the mole fraction in the adsorbed phase of the component with the higher saturation capacity. The *x*-axes represent the total occupancy of the mixture $\theta_{mix} = \frac{q_1}{q_{1,sat}} + \frac{q_2}{q_{2,sat}}$.

16 Nomenclature

Latin alphabet

A	surface area per kg of framework, $m^2\ kg^{-1}$
b	binding constant, Pa^{-1}
b_k	binding constant of k-mer, Pa^{-1}
b_l	binding constant of l-mer, Pa^{-1}
b_A	dual-Langmuir-Freundlich constant for species i at adsorption site A, $Pa^{-\nu_i}$
b_B	dual-Langmuir-Freundlich constant for species i at adsorption site B, $Pa^{-\nu_i}$
f_i	partial fugacity of species i, Pa
f_t	total fugacity of bulk fluid mixture, Pa
F	Helmholtz free energy, $J\ mol^{-1}$
k	number of identical units occupied by k-mer, dimensionless
k_B	Boltzmann constant, $1.38\times10^{-23}\ J\ molecule^{-1}\ K^{-1}$
l	number of identical units occupied by l-mer, dimensionless
M	number of sites on lattice, dimensionless
N_k	number of k-mers, dimensionless
N_l	number of l-mers, dimensionless
n	number of species in the mixture, dimensionless
P_i^0	sorption pressure, Pa
q_i	component molar loading of species i, $mol\ kg^{-1}$
q_t	total molar loading for mixture adsorption, $mol\ kg^{-1}$
$q_{i,sat}$	molar loading of species i at saturation, $mol\ kg^{-1}$

Nomenclature

R	gas constant, 8.314 J mol^{-1} K^{-1}
S	entropy, J mol^{-1} K^{-1}
T	absolute temperature, K
W	probability (= *Wahrscheinlichkeit*), dimensionless
x_i	component mole fraction in adsorbed phase, *i*, dimensionless
x_k	mole fraction of *k*-mer in adsorbed phase, dimensionless
x_l	mole fraction of *l*-mer in adsorbed phase, dimensionless
y_i	component mole fraction in bulk fluid phase, *i*, dimensionless

Greek alphabet

μ_i	molar chemical potential of component *i*, J mol^{-1}
π	spreading pressure, N m^{-1}
θ_i	fractional occupancy of component *i*, dimensionless
θ_k	fractional occupancy of *k*-mer, dimensionless
θ_l	fractional occupancy of *l*-mer, dimensionless
θ_{mix}	occupancy of adsorbed mixture, $\theta_{mix} = \frac{\theta_k}{k} + \frac{\theta_l}{l}$, dimensionless
Θ_i	loading of species *i*, molecules per unit cage, or per unit cell
$\Theta_{i,sat}$	saturation loading of species *i*, molecules per unit cage, or per unit cell
Θ_t	total mixture loading, molecules per unit cage, or per unit cell
ν	exponent in dual-Langmuir-Freundlich isotherm, dimensionless
ρ	framework density, kg m^{-3}
Ω	entropy factor, dimensionless

Subscripts

Nomenclature

1	referring to component 1
2	referring to component 2
i	referring to component *i*
k	referring to component *k*
l	referring to component *l*
t	referring to total mixture

17 References

(1) Kärger, J.; Ruthven, D. M.; Theodorou, D. N. *Diffusion in Nanoporous Materials*. Wiley - VCH: Weinheim, 2012.

(2) Krishna, R.; van Baten, J. M. In Silico Screening of Zeolite Membranes for CO_2 Capture. *J. Membr. Sci.* **2010**, *360*, 323-333.

(3) Krishna, R.; van Baten, J. M. In silico screening of metal-organic frameworks in separation applications. *Phys. Chem. Chem. Phys.* **2011**, *13*, 10593-10616.

(4) Thomas, A. Functional Materials: From Hard to Soft Porous Frameworks. *Angew. Chem. Int. Ed.* **2010**, *49*, 8328 – 8344.

(5) Baerlocher, C.; Meier, W. M.; Olson, D. H. *Atlas of Zeolite Framework Types*. 5th Edition, Elsevier: Amsterdam, 2002.

(6) Baerlocher, C.; McCusker, L. B. Database of Zeolite Structures. http://www.iza-structure.org/databases/, International Zeolite Association, 10 January 2002.

(7) Krishna, R. Diffusion in Porous Crystalline Materials. *Chem. Soc. Rev.* **2012**, *41*, 3099-3118.

(8) Krishna, R. The Maxwell-Stefan Description of Mixture Diffusion in Nanoporous Crystalline Materials. *Microporous Mesoporous Mater.* **2014**, *185*, 30-50.

(9) Krishna, R. Describing the Diffusion of Guest Molecules inside Porous Structures. *J. Phys. Chem. C* **2009**, *113*, 19756-19781.

(10) Krishna, R.; van Baten, J. M. Investigating the Relative Influences of Molecular Dimensions and Binding Energies on Diffusivities of Guest Species Inside Nanoporous Crystalline Materials *J. Phys. Chem. C* **2012**, *116*, 23556-23568.

(11) Krishna, R.; van Baten, J. M. Investigating the Influence of Diffusional Coupling on Mixture Permeation across Porous Membranes *J. Membr. Sci.* **2013**, *430*, 113-128.

(12) Krishna, R.; van Baten, J. M. Influence of Adsorption Thermodynamics on Guest Diffusivities in Nanoporous Crystalline Materials. *Phys. Chem. Chem. Phys.* **2013**, *15*, 7994-8016.

(13) Krishna, R.; van Baten, J. M. Insights into diffusion of gases in zeolites gained from molecular dynamics simulations. *Microporous Mesoporous Mater.* **2008**, *109*, 91-108.

(14) Krishna, R.; van Baten, J. M. Diffusion of alkane mixtures in MFI zeolite. *Microporous Mesoporous Mater.* **2008**, *107*, 296-298.

(15) Krishna, R.; van Baten, J. M. Describing Mixture Diffusion in Microporous Materials under Conditions of Pore Saturation. *J. Phys. Chem. C* **2010**, *114*, 11557-11563.

(16) Krishna, R.; van Baten, J. M. Diffusion of alkane mixtures in zeolites. Validating the Maxwell-Stefan formulation using MD simulations. *J. Phys. Chem. B* **2005**, *109*, 6386-6396.

(17) Ryckaert, J. P.; Bellemans, A. Molecular dynamics of liquid alkanes. *Faraday Discuss. Chem. Soc.* **1978**, *66*, 95-106.

(18) Dubbeldam, D.; Calero, S.; Vlugt, T. J. H.; Krishna, R.; Maesen, T. L. M.; Smit, B. United Atom Forcefield for Alkanes in Nanoporous Materials. *J. Phys. Chem. B* **2004**, *108*, 12301-12313.

(19) Skoulidas, A. I.; Sholl, D. S. Transport diffusivities of CH_4, CF_4, He, Ne, Ar, Xe, and SF_6 in silicalite from atomistic simulations. *J. Phys. Chem. B* **2002**, *106*, 5058-5067.

(20) Talu, O.; Myers, A. L. Reference Potentials for Adsorption of Helium, Argon, Methane and Krypton in High-Silica Zeolites. *Colloids Surf., A* **2001**, *187-188*, 83-93.

(21) Makrodimitris, K.; Papadopoulos, G. K.; Theodorou, D. N. Prediction of permeation properties of CO_2 and N_2 through silicalite via molecular simulations. *J. Phys. Chem. B* **2001**, *105*, 777-788.

(22) García-Pérez, E.; Parra, J. B.; Ania, C. O.; García-Sánchez, A.; Van Baten, J. M.; Krishna, R.; Dubbeldam, D.; Calero, S. A computational study of CO_2, N_2 and CH_4 adsorption in zeolites. *Adsorption* **2007**, *13*, 469-476.

(23) Chui, S. S. Y.; Lo, S. M. F.; Charmant, J. P. H.; Orpen, A. G.; Williams, I. D. A Chemically Functionalizable Nanoporous Material $[Cu_3(TMA)_2(H2O)_3]_n$. *Science* **1999**, *283*, 1148-1150.

(24) Yang, Q.; Zhong, C. Electrostatic-Field-Induced Enhancement of Gas Mixture Separation in Metal-Organic Frameworks: A Computational Study. *ChemPhysChem* **2006**, *7*, 1417-1421.

(25) Alaerts, L.; Kirschhock, C. E. A.; Maes, M.; van der Veen, M.; Finsy, V.; Depla, A.; Martens, J. A.; Baron, G. V.; Jacobs, P. A.; Denayer, J. F. M.; De Vos, D. Selective Adsorption and Separation of Xylene Isomers and Ethylbenzene with the Microporous Vanadium(IV) Terephthalate MIL-47. *Angew. Chem. Int. Ed.* **2007**, *46*, 4293-4297.

(26) Finsy, V.; Verelst, H.; Alaerts, L.; De Vos, D.; Jacobs, P. A.; Baron, G. V.; Denayer, J. F. M. Pore-Filling-Dependent Selectivity Effects in the Vapor-Phase Separation of Xylene Isomers on the Metal-Organic Framework MIL-47. *J. Am. Chem. Soc.* **2008**, *130*, 7110-7118.

(27) Barthelet, K.; Marrot, J.; Riou, D.; Férey, G. A Breathing Hybrid Organic - Inorganic Solid with Very Large Pores and High Magnetic Characteristics. *Angew. Chem. Int. Ed.* **2007**, *41*, 281-284.

(28) Coombes, D. S.; Corà, F.; Mellot-Draznieks, C.; Bell, R. G. Sorption-Induced Breathing in the Flexible Metal Organic Framework CrMIL-53: Force-Field Simulations and Electronic Structure Analysis. *J. Phys. Chem. C* **2009**, *113*, 544-552.

(29) Rappé, A. K.; Casewit, C. J.; Colwel, K. S.; Goddard, W. A.; Skiff, W. M. UFF, A Full Periodic Table Force Field for Molecular Mechanics and Molecular Dynamics Simulations. *J. Am. Chem. Soc.* **1992**, *114*, 10024-10035.

(30) Mayo, S. L.; Olafson, B. D.; Goddard, W. A. DREIDING: A Generic Force Field for Molecular Simulations. *J. Phys. Chem.* **1990**, *94*, 8897-8909.

(31) Myers, A. L.; Monson, P. A. Adsorption in Porous Materials at High Pressure: Theory and Experiment. *Langmuir* **2002**, *18*, 10261-10273.

(32) Babarao, R.; Hu, Z.; Jiang, J.; Chempath, S.; Sandler, S. I. Storage and separation of CO_2 and CH_4 in silicalite, C_{168} schwarzite, and IRMOF-1: A comparative study from Monte Carlo simulation. *Langmuir* **2007**, *23*, 659-666.

(33) Babarao, R.; Jiang, J. Exceptionally high CO_2 storage in covalent-organic frameworks: Atomistic simulation study. *Energy Environ. Sci.* **2008**, *1*, 139-143.

(34) Frenkel, D.; Smit, B. *Understanding Molecular Simulations: From Algorithms to Applications*. 2nd Edition, Academic Press: San Diego, 2002.

(35) Talu, O.; Myers, A. L. Molecular Simulation of Adsorption: Gibbs Dividing Surface and Comparison with Experiment. *A.I.Ch.E.J.* **2001**, *47*, 1160-1168.

(36) Düren, T.; Millange, F.; Férey, G.; Walton, K. S.; Snurr, R. Q. Calculating Geometric Surface Areas as a Characterization Tool for Metal-Organic Frameworks. *J. Phys. Chem. C* **2007**, *111*, 15350-15356.

(37) Foster, M. D.; Rivin, I.; Treacy, M. M. J.; Friedrichs, O. D. A geometric solution to the largest-free-sphere problem in zeolite frameworks. *Microporous Mesoporous Mater.* **2006**, *90*, 32-38.

(38) Ruthven, D. M. *Principles of Adsorption and Adsorption Processes*. John Wiley: New York, 1984.

(39) Myers, A. L.; Prausnitz, J. M. Thermodynamics of Mixed Gas Adsorption. *A.I.Ch.E.J.* **1965**, *11*, 121-130.

(40) Siperstein, F. R.; Myers, A. L. Mixed-Gas Adsorption. *A.I.Ch.E.J.* **2001**, *47*, 1141-1159.

(41) PTC MathCad 15.0. http://www.ptc.com/, PTC Corporate Headquarters, Needham, 3 November 2015.

(42) Rao, M. B.; Sircar, S. Thermodynamic consistency for binary gas adsorption equilibria. *Langmuir* **1999**, *15*, 7258-7267.

(43) Nitta, T.; Shigetomi, T.; Kuro-Oka, M.; Katayama, T. An Adsorption Isotherm of Multi-site Occupancy Model for Homogeneous Surface. *J. Chem. Eng. Japan.* **1984**, *17*, 39-45.

(44) Bai, R.; Deng, J.; Yang, R. T. Improved Multisite Langmuir Model for Mixture Adsorption Using Multiregion Adsorption Theory. *Langmuir* **2003**, *19*, 2776-2781.

(45) Dávila, M.; Riccardo, J. L.; Ramirez-Pastor, A. J. Exact Statistical Thermodynamics of Alkane Binary Mixtures in Zeolites: New Interpretation of the Adsorption Preference Reversal Phenomenon from Multisite-Cccupancy Theory. *Chem. Phys. Lett.* **2009**, *477*, 402-405.

(46) Matoz-Fernandez, D. A.; Ramirez-Pastor, A. J. Adsorption Preference Reversal Phenomenon from Multisite-Occupancy Theory for Two-Dimensional Lattices. *Chem. Phys. Lett.* **2014**, *610-611*, 131-134.

(47) Azizian, S.; Bashiri, H. A New Isotherm for Multisite Occupancy Adsorption of Binary Gaseous Mixtures. *Langmuir* **2009**, *25*, 2309-2312.

(48) Van Assche, T. R. C.; Baron, G. V.; Denayer, J. F. M. An Explicit Multicomponent Adsorption Isotherm Model: Accounting for the Size-effect for Components with Langmuir Adsorption Behavior. *Adsorption* **2018**, *24*, 517-530. https://doi.org/10.1007/s10450-018-9962-1.

(49) Krishna, R.; van Baten, J. M. Entropy-based Separation of Linear Chain Molecules by Exploiting Differences in the Saturation Capacities in Cage-type Zeolites. *Sep. Purif. Technol.* **2011**, *76*, 325-330.

(50) Remy, T.; Saint-Remi, J. C.; Singh, R.; Webley, P. A.; Baron, G. V.; Denayer, J. F. M. Adsorption and Separation of C1-C8 Alcohols on SAPO-34. *J. Phys. Chem. C* **2011**, *115*, 8117-8125.

(51) Krishna, R.; van Baten, J. M. A molecular simulation study of commensurate – incommensurate adsorption of n-alkanes in cobalt formate frameworks. *Molecular Simulation* **2009**, *35*, 1098-1104.

(52) van Baten, J. M.; Krishna, R. Entropy effects in adsorption and diffusion of alkane isomers in mordenite: An investigation using CBMC and MD simulations. *Microporous Mesoporous Mater.* **2005**, *84*, 179-191.

(53) Vlugt, T. J. H.; Zhu, W.; Kapteijn, F.; Moulijn, J. A.; Smit, B.; Krishna, R. Adsorption of linear and branched alkanes in the silicalite-1. *J. Am. Chem. Soc.* **1998**, *120*, 5599-5600.

(54) Vlugt, T. J. H.; Krishna, R.; Smit, B. Molecular Simulations of Adsorption Isotherms for Linear and Branched Alkanes and Their Mixtures in Silicalite. *J. Phys. Chem. B* **1999**, *103*, 1102-1118.

(55) Krishna, R.; Smit, B.; Calero, S. Entropy effects during sorption of alkanes in zeolites. *Chem. Soc. Rev.* **2002**, *31*, 185-194.

(56) Schenk, M.; Vidal, S. L.; Vlugt, T. J. H.; Smit, B.; Krishna, R. Separation of alkane isomers by exploiting entropy effects during adsorption on silicalite-1: A configurational-bias Monte Carlo simulation study. *Langmuir* **2001**, *17*, 1558-1570.

(57) Titze, T.; Chmelik, C.; Kärger, J.; van Baten, J. M.; Krishna, R. Uncommon Synergy Between Adsorption and Diffusion of Hexane Isomer Mixtures in MFI Zeolite Induced by Configurational Entropy Effects *J. Phys. Chem. C* **2014**, *118*, 2660-2665.

(58) Krishna, R.; Smit, B.; Vlugt, T. J. H. Sorption-induced Diffusion-selective Separation of Hydrocarbon Isomers Using Silicalite. *J. Phys. Chem. A* **1998**, *102*, 7727-7730.

(59) Dandekar, H. W.; Funk, G. A.; Gillespie, R. D.; Zinnen, H. A.; McGonegal, C. P.; Kojima, M.; Hobbs, S. H., Process for alkane isomerization using reactive chromatography. UOP, Des Plaines, Illinois, USA., *U.S. Pat.*, US 5763730, 1999.

(60) Dandekar, H. W.; Funk, G. A.; Zinnen, H. A., Process for separating and recovering multimethyl-branched alkanes. UOP LLC, Des Plaines, Illinois, USA., *U.S. Pat.*, US 6069289, 2000.

(61) Carr, R. W.; Dandekar, H. W. *Adsorption with reaction*. Reactive Separation Processes; 2nd, Edited by S. Kulprathipanja, Taylor & Francis: New York, USA, 2001.

(62) Krishna, R. Methodologies for Evaluation of Metal-Organic Frameworks in Separation Applications. *RSC Adv.* **2015**, *5*, 52269-52295.

(63) Krishna, R.; van Baten, J. M. Loading dependence of self-diffusivities of gases in zeolites. *Chem. Eng. Technol.* **2007**, *30*, 1235-1241.

(64) Krishna, R.; van Baten, J. M. Separating n-alkane mixtures by exploiting differences in the adsorption capacity within cages of CHA, AFX and ERI zeolites. *Sep. Purif. Technol.* **2008**, *60*, 315-320.

(65) Daems, I.; Singh, R.; Baron, G. V.; Denayer, J. F. M. Length exclusion in the adsorption of chain molecules on chabazite type zeolites. *Chem. Commun.* **2007**, 1316-1318.

(66) Krishna, R.; van Baten, J. M. Commensurate-Incommensurate Adsorption and Diffusion in Ordered Crystalline Microporous Materials. *Phys. Chem. Chem. Phys.* **2017**, *19*, 20320-20337.

(67) Minceva, M.; Rodrigues, A. E. Modeling and Simulation of a Simulated Moving Bed for the Separation of *p*-Xylene. *Ind. Eng. Chem. Res.* **2002**, *41*, 3454-3461.

(68) Minceva, M.; Rodrigues, A. E. Understanding and Revamping of Industrial Scale SMB Units for p-Xylene Separation. *A.I.Ch.E.J.* **2007**, *53*, 138-149.

(69) Peralta, D.; Barthelet, K.; Pérez-Pellitero, J.; Chizallet, C.; Chaplais, G.; Simon-Masseron, A.; Pirngruber, G. D. Adsorption and Separation of Xylene Isomers: CPO-27-Ni vs HKUST-1 vs NaY. *J. Phys. Chem. C* **2012**, *116*, 21844-21855.

(70) Torres-Knoop, A.; Krishna, R.; Dubbeldam, D. Separating Xylene Isomers by Commensurate Stacking of p-Xylene within Channels of MAF-X8. *Angew. Chem. Int. Ed.* **2014**, *53*, 7774-7778.

(71) Chiang, A. S. T.; Lee, C.-K.; Chang, Z.-H. Adsorption and diffusion of aromatics in $AlPO_4$-5. *Zeolites* **1991**, *11*, 380-386.

(72) Torres-Knoop, A.; Balestra, S. R. G.; Krishna, R.; Calero, S.; Dubbeldam, D. Entropic Separations of Mixtures of Aromatics by Selective Face-to-Face Molecular Stacking in One-Dimensional Channels of Metal–Organic Frameworks and Zeolites. *ChemPhysChem* **2015**, *16*, 532-535.

(73) Hu, E.; Derebe, A. T.; Almansoori, A.; Wang, K. Xylene Separation on Plate-Like SAPO-5 Zeolite Molecular Sieves. *Int. Journal. Materials Sci. Eng.* **2014**, *2*, 10-14.

(74) Hu, E.; Lai, Z.; Wang, K. Adsorption Properties of the SAPO-5 Molecular Sieve. *J. Chem. Eng. Data* **2010**, *55*, 3286-3289.

(75) Rosenfeld, D. D.; Barthomeuf, D. M., Separation of Ortho Aromatic Isomers by Selective Adsorption with an Aluminophosphate. Exxon Research & Engineering Co., Florham Park, N.J., *U.S. Pat.*, US 4482776, 1984.

(76) El Osta, R.; Carlin-Sinclair, A.; Guillou, N.; Walton, R. I.; Vermoortele, F.; Maes, M.; De Vos, D.; Millange, F. Liquid-Phase Adsorption and Separation of Xylene Isomers by the Flexible Porous Metal−Organic Framework MIL-53(Fe). *Chem. Mater.* **2012**, *24*, 2781-2791.

(77) Remy, T.; Baron, G. V.; Denayer, J. F. M. Modeling the Effect of Structural Changes during Dynamic Separation Processes on MOFs. *Langmuir* **2011**, *27*, 13064-13071.

(78) Yoon, J. W.; Lee, J. S.; Piburn, G. W.; Cho, K. H.; Jeon, K.; Lim, H.-K.; Kim, H.; Jun, C.-H.; Humphrey, S. M.; Krishna, R.; Chang, J.-S. Highly Selective Adsorption of p-Xylene over other C8 Aromatic Hydrocarbons by Co-CUK-1: A Combined Experimental and Theoretical Assessment. *Dalton Trans.* **2017**, *46*, 16096-16101. http://dx.doi.org/10.1039/C7DT03304D.

(79) Maes, M.; Vermoortele, F.; Alaerts, L.; Couck, S.; Kirschhock, C. E. A.; Denayer, J. F. M.; De Vos, D. E. Separation of Styrene and Ethylbenzene on Metal-Organic Frameworks: Analogous Structures with Different Adsorption Mechanisms. *J. Am. Chem. Soc.* **2010**, *132*, 15277-15285.

(80) Remy, T.; Ma, L.; Maes, M.; De Vos, D. E.; Baron, G. V.; Denayer, J. F. M. Vapor-Phase Adsorption and Separation of Ethylbenzene and Styrene on the Metal−Organic Frameworks MIL-47 and MIL-53(Al). *Ind. Eng. Chem. Res.* **2012**, *51*, 14824-14833.

(81) Torres-Knoop, A.; Dubbeldam, D. Exploiting Large-Pore Metal–Organic Frameworks for Separations through Entropic Molecular Mechanisms. *ChemPhysChem* **2015**, *16*, 2046-2067.

(82) Torres-Knoop, A.; Heinen, J.; Krishna, R.; Dubbeldam, D. Entropic Separation of Styrene/Ethylbenzene Mixtures by Exploitation of Subtle Differences in Molecular Configurations in Ordered Crystalline Nanoporous Adsorbents. *Langmuir* **2015**, *31*, 3771-3778.

(83) Gutierrez-Sevillano, J. J.; Calero, S.; Krishna, R. Selective Adsorption of Water from Mixtures with 1-Alcohols by Exploitation of Molecular Packing Effects in CuBTC. *J. Phys. Chem. C* **2015**, *119*, 3658-3666.

(84) Gutierrez-Sevillano, J. J.; Calero, S.; Krishna, R. Separation of Benzene from Mixtures with Water, Methanol, Ethanol, and Acetone: Highlighting Hydrogen Bonding and Molecular Clustering Influences in CuBTC. *Phys. Chem. Chem. Phys.* **2015**, *17*, 20114-20124.